Creating an Open Source Electromagnetic Tracking Platform

Herman Alexander Jaeger
BEng, MEngSc
110380277

Thesis submitted for the degree of Doctor of Philosophy



NATIONAL UNIVERSITY OF IRELAND, CORK

SCHOOL OF ENGINEERING

October 2018

Head of School: Prof Liam Marnane

Supervisor: Dr Pádraig Cantillon-Murphy

Creating an open source electromagnetic tracking platform

Herman Alexander Jaeger

5th October 2018

This thesis was typeset using LaTeX with the `book` class. Images were edited and processed in Inkscape* and imported using the `svg`† package. Times New Roman acts as both the text and display typeface. Courier is used for formatting hyperlinks and code snippets throughout the text.

Creating an open source electromagnetic tracking platform

October 5, 2018, Herman Alexander Jaeger

*Available at `https://inkscape.org`

†Available at `https://ctan.org/pkg/svg`

Declaration

I hereby declare that I am the sole author of this thesis and all of the work undertaken in this thesis is original in content and was carried out by the author. Work carried out by others has been duly acknowledged in the thesis.

Herman
Alexander Jaeger

Digitally signed by Herman Alexander Jaeger
DN: cn=Herman Alexander Jaeger, o=University College Cork, ou, email=h.jaeger@umail.ucc.ie, c=IE
Date: 2019.01.15 14:35:55 Z

Herman Alexander Jaeger
October 5th, 2018

Abstract

This thesis describes the design, development and testing of Anser, the world's first open electromagnetic tracking (EMT) platform for use in minimally invasive and image-guided interventions; Anser EMT. The goal of this work is to advance the state of the art of electromagnetic tracking systems by creating an open-source electromagnetic tracking platform for pre-clinical research and development. The specific application of this work is in bronchoscopy, where accurate navigating and targeting in the outer airways for the diagnosis and staging of lung cancer using endoscopic technology is a key unmet clinical need.

A review of electromagnetic navigation and its use in bronchoscopy is included. Different imaging modalities are compared and discussed, which give rise to the need for electromagnetic tracking for navigation in the outer airways. Commercially available bronchoscopy systems are highlighted and their current drawbacks are discussed. A review of the underlying principles of electromagnetic tracking is then performed. The review enables the partitioning of an electromagnetic tracking system into independent modules. The modules are implemented as a general software framework in the Python programming language. The framework is applied to the Anser EMT platform with accuracy and performance experiments described.

The hardware composition of Anser is then described in detail. A previous system design is summarised and an improved circuit design is presented. The area footprint of the revised system is reduced by approximately 75%, with significant improvements in power supply efficiency also described. The Anser system is used to address some shortcomings of commercially available electromagnetic tracking systems. Detection of metallic distortion in the clinical environment is successfully demonstrated. Experimental results show that the modified field generator is capable of detecting the severity, material type and approximate location of distorters near the field generator, a feature which commercially available systems do not provide. An exploration of modular field generator designs is then performed by combining two Anser systems. Extended tracking and enhanced accuracy is demonstrated using combined field generator configurations.

The integration of electromagnetic in surgical instruments is explored through the design of custom electromagnetic tracking coils for use with the Anser system. A number of hand-wound coils were designed and tested to successfully track laparoscopic and endoscopic instruments with accuracies on-par with commercially available sensors. Lastly, Anser is demonstrated in a live, pre-clinical setting for electromagnetic navigation bronchoscopy. An electromagnetically tracked catheter was used with Anser to successfully target phantom tumours with minimum and maximum targeting errors of 7.2mm and 19.6mm respectively.

This thesis provides a platform which may accelerate research and development of electromagnetic tracking at the pre-clinical stage and lead to future innovation to address bottlenecks and drawbacks with existing technology. Supporting documentation and resources are available at `http://openemt.org`

Acknowledgements

I would like to take this chance to thank all the individuals who have helped guide my work over the last number of years. I would like to thank my supervisor, Dr. Pádraig Cantillon-Murphy for all the guidance, support and opportunities he has provided over the course of my graduate studies. I wish to thank Dr. John Hayes and Prof. Terry Peters for examining this thesis as well as Dr. Marcus Kennedy and Dr. Kashif Ali Khan for their engagement and collaboration during the various studies and experiments. I would also like to thank Kilian O'Donoghue and Pietro Nardelli for sharing their knowledge with me over the course of my PhD.

I would like to thank all the staff of the Department of Electrical and Electronic Engineering in University College Cork. I would like to sincerely thank Michael O'Shea and Tim Power for their assistance and the mechanical insights they have provided over the course of my masters and PhD studies. All the experimental prototypes described in this thesis would not have been possible without their assistance. I would also like to thank James Griffiths for the all the electronic design help, tips and tricks that made learning circuit board design a breeze. I also wish to thank Ralph O'Flaherty and Niamh O'Sullivan for receiving the never-ending supply of Farnell orders on my behalf!

I would like to thank the students in the power electronics lab: Conor, Diarmaid, Yeny, Brendan, Ed, Jaspar, Sean, Kevin, Patrick, Adrian, Robby, Tim, Stephen, Philip and Oliwier. I am now fully convinced that a rigidly scheduled tea and banter break is an integral part of the PhD process! A special shout out to Fabian for his critical design feedback and insights on all things mechanical, particularly during our year in Strasbourg.

I would like to thank my parents and grandparents for all their encouragement, interest and belief in me over all these years. Finally I would like to thank Alex for all of her patience, kindness and motivation these last few months. This thesis is yours, as well as mine!

List of Publications

Journal Papers

1. **H. A. Jaeger** and P. Cantillon-Murphy, "Electromagnetic Tracking using Modular, Tiled Field Generators," *IEEE Transactions on Instrumentation & Measurement*, 2018, *(under review)*.

2. **H. A. Jaeger**, F. Trauzettel, P. Nardelli, F. Daverieux, E. F. Hofstad, H. O. Leira, M. P. Kennedy, T. Langø and P. Cantillon-Murphy, "Peripheral tumour targeting using open-source virtual bronchoscopy with electromagnetic tracking: a multi-user pre-clinical study," *Minimally Invasive Therapy & Allied Technologies*, DOI: 10.1080/13645706.2018.1544911, 2018.

3. **H. A. Jaeger** and P. Cantillon-Murphy, "Distorter Characterisation Using Mutual Inductance in Electromagnetic Tracking," *Sensors*, vol. 18, no. 9, 3059, 2018.

4. **H. A. Jaeger**, A. M. Franz, K. O'Donoghue, A. Seitel, F. Trauzettel, L. Maier-Hein and P. Cantillon-Murphy, "Anser EMT: the first open-source electromagnetic tracking platform for image-guided interventions," *International Journal of Computer Assisted Radiology and Surgery*, vol. 12, no. 6, pp. 1059–1067, 2017.

5. **H. A. Jaeger**, P. Nardelli, C. O'Shea, J. Tugwell, K. A. Khan, T. Power, M. O'Shea, M. P. Kennedy and P. Cantillon-Murphy, "Automated Catheter Navigation With Electromagnetic Image Guidance," *IEEE Transactions on Biomedical Engineering*, vol. 64, no. 8, pp. 1972–1979, 2017.

6. P. Nardelli, **H. A. Jaeger**, C. O'Shea, K. A. Khan, M. P. Kennedy and P. Cantillon-Murphy, "Pre-clinical validation of virtual bronchoscopy using 3D Slicer," *International Journal of Computer Assisted Radiology and Surgery*, vol. 12, no. 1, pp. 1–14, 2016.

7. K. A. Khan, P. Nardelli, **H. A. Jaeger**, C. O'Shea, P. Cantillon-Murphy and M. P. Kennedy, "Navigational Bronchoscopy for Early Lung Cancer: A Road to Therapy," *Advances in Therapy*, vol. 33, no. 4, pp. 580–596, 2016.

8. C. O'Shea, K. A. Khan, P. Nardelli, **H. A. Jaeger**, M. P. Kennedy and P. Cantillon-Murphy, "Evaluation of Endoscopically Deployed Radiopaque Tumor Models in Bronchoscopy," *Journal of Bronchology & Interventional Pulmonology*, vol. 23, no. 2, pp. 112–122, 2016.

Conference Papers

1. **H. A. Jaeger**, S. Hinds, T. Langø, E. F. Hofstad, O. V. Solberg, H. O. Leira, J. Scheltes and P. Cantillon-Murphy, "Novel Instrument Design for Electromagnetic Navigation Bronchoscopy," submitted to IPCAI 2019.

2. E.P. de Kater, O. McVeigh, S. Hinds, **H. A. Jaeger**, J. van den Dobbelsteen and P. Cantillon-Murphy, "6-DoF Sensor Design for Electromagnetic Tracking," submitted to IPCAI 2019.

3. S. Hinds, **H. A. Jaeger**, R. Burke, B. O'Sullivan, J. Keane, F. Trauzettel, B. Marques, S. Cotin, B. Bird, H. O. Leira, T. Langøand P. Cantillon-Murphy, "Electromagnetic Tracking for Deep Liver Targets: A preliminary feasibility study," submitted to IPCAI 2019.

4. M. P. Kennedy, **H. A. Jaeger**, F. Trauzettel, P. Nardelli, C. F. Davrieux, E.F. Hofstad, H. O. Leira, T. Langø and P. Cantillon-Murphy, "Endobronchial Tumour Targeting using a Novel Alignment of an Open-Source Virtual Bronchoscopy Platform with Electromagnetic Tracking: A Multi-user Preclinical Study," *CHEST*, vol 154, no. 4, p. 869A, 2018.

5. **H. A. Jaeger**, S. Hinds and P. Cantillon-Murphy, "An Open Framework Enabling Electromagnetic Tracking in Image-Guided Interventions," *Medical Image Computing and Computer Assisted Intervention - MICCAI*, MICCAI 2018, Lecture Notes in Computer Science, vol 11073, pp. 168–175, 2018.

6. **H. A. Jaeger**, F. Trauzettel, E. F. Hofstad, M. P. Kennedy, H. O. Leira, T. Langø and P. Cantillon-Murphy, "Open source airway navigation: initial experiences with CustusX and Anser EMT," *Annual Meeting of the International Society for Medical Innovation and Technology (iSMIT)*, Torino, Italy, 2017.

7. F. Trauzettel, **H. A. Jaeger**, E. F. Hofstad, M. P. Kennedy, H. O. Leira, T. Langø and P. Cantillon-Murphy, "Mechanical catheter navigation with electromagnetic tracking to peripheral airway targets," *Annual Meeting of the International Society for Medical Innovation and Technology (iSMIT)*, Torino, Italy, 2017.

8. F. Trauzettel, **H. A. Jaeger** and P. Cantillon-Murphy, "Development of a testing apparatus for an omni-directionally steerable EM-guided bronchoscopy catheter," *Annual Meeting of the International Society for Medical Innovation and Technology (iSMIT)*, Torino, Italy, 2017.

9. **H. A. Jaeger**, F. Trauzettel, M. P. Kennedy and P. Cantillon-Murphy, "Image-guided catheter navigation with electromagnetic tracking," *Annual Meeting of the International Society for Medical Innovation and Technology (iSMIT)*, Delft, The Netherlands, 2016.

List of Figures

1.1 Bronchoscopy with a bronchoscope and CT scan. 2
1.2 SuperDimension navigation system for ENB 4

2.1 Diagram of the the human airways. 10
2.2 Introduction of bronchoscope into the airways. 12
2.3 Bronchoscope camera and CT scan view of carina and bronchi. 13
2.4 An Olympus Medical BF-1TQ290 bronchoscope. 13
2.5 Olympus EBUS ultrasound kits for TBNA. 15
2.6 OCT images of lung tissue. 16
2.7 Commericially available C-arm X-ray platforms. 17
2.8 NDI Polaris and Aurora tracking systems. 18
2.9 Electromagnetic navigation bronchoscopy on a patient. 19
2.10 Operation of a CT scanner. 21
2.11 Axial, sagittal and coronal views of a chest CT scan. 21
2.12 3D Slicer visualisation of lung airway segmentation. 22
2.13 CustusX visualisation of markup selection process. 23
2.14 SuperDimension navigation catheters and locatable guide 26
2.15 Veran Medical optical probe and tracked instruments. 26
2.16 Monarch bronchscopy robot developed by Auris Health. 27

3.1 Hardware/software interface for clinical applications. 30
3.2 Photograph of the Anser EMT system. 32
3.3 Processing steps for electromagnetic tracking 32
3.4 Continuous and discrete waveform at a single frequency. 33
3.5 Continuous and discrete waveform at multiple frequencies. 33
3.6 Commercially available data acquisition systems. 35
3.7 Data acquisition unit data pipeline. 36
3.8 Discrete Fourier tranform visualisation. 39
3.9 Acquisition update rate as a function of frame size. 40
3.10 An example of coherent sampling. 41
3.11 An example of incoherent sampling. 42

3.12 The effects of incoherent sampling due to frequency mismatch. 44
3.13 Applying a window function to an acquisition frame. 47
3.14 Hamming and Blackman window frequency response. 48
3.15 Rectangular, Hamming and Blackman windows results. 49
3.16 Magnetic dipole model. 51
3.17 Magnetic current filament model 52
3.18 Magnetic due to a multiple straight line current filaments. 53
3.19 5-DoF sensor model. 54
3.20 Position and orientation with respect to origin. 56
3.21 Tracking system software framework. 59
3.22 Position plot comapring Python to Matlab. 60

4.1 Processing steps for Anser EMT 64
4.2 AD9833 waveform generator diagram. 65
4.3 Non-inverting amplifier buffer. 67
4.4 Passive RC bandpass filter. 68
4.5 Basic current source op-amp topology. 69
4.6 Current source with transmitter coil. 70
4.7 Frequency response of open-loop current source. 71
4.8 Original class AB current buffer. 72
4.9 LMH6321 current buffer diagram 75
4.10 Transmitter coil load analysis test circuit. 76
4.11 Maximum current bode plot. 77
4.12 Closed loop current source schematic. 80
4.13 Small-signal model for coupling capacitor analysis. 81
4.14 Effect of different coupling capacitor values. 82
4.15 DC versus AC coupled system response. 84
4.16 Closed-loop frequency response. 86
4.17 Closed-loop response versus coil inductance. 87
4.18 Closed-loop response versus coil resistance. 87
4.19 Induction sensor circuit model. 89
4.20 Noise versus source impedance for INA128 and INA163 91
4.21 Instrumentation amplifier design. 92
4.22 Photograph of a Teensy 3.2 microcontroller. 93
4.23 National instruments USB-6212 OEM PCB 94
4.24 Linear and switch-mode power supplies. 95
4.25 Texas Instruments -15 V DC-DC converter. 96
4.26 Magnitude response of input CLC filter. 96
4.27 Anser EMT field generator PCB 99
4.28 Anser EMT enclosure. 100
4.29 Anser EMT field generator enclosure. 101

4.30 D rendering of the field generator enclosure 101
4.31 Current driver startup transient. 102
4.32 Current source temperature drift versus time. 103
4.33 Current waveform of the system. 105
4.34 FFT plot of the current sense signal. 106
4.35 FFT plot of the sensor induced voltage signal post-amplification. . . . 107
4.36 Hummel protocol experimental setup 110
4.37 Hummel board diagram 110
4.38 The effect of metal cylinders on sensor positioning error. 112
4.39 MITK visualisation of acquired test positions. 113

5.1 Diagram illustrating the effects of distortions on EMT. 116
5.2 Magnetic coupling between two coupled inductors. 119
5.3 Arrangement of transmitter coils in Anser EMT. 122
5.4 3D model of current filaments. 123
5.5 Diagram of field sensing circuitry. 127
5.6 Photograph of distorters and their locations. 128
5.7 Illustration of distorter experimental setup 130
5.8 Block diagram of the experimental setup. 131
5.9 Photograph of experimental setup. 132
5.10 Mutual inductance error for planar sheet distorters. 137
5.11 Mutual inductance error for the small aluminium section distorters . . 138
5.12 Phase error for planar sheet distorters. 140
5.13 Phase error for small aluminium block distorters. 141
5.14 Mean error and standard deviation for sheet metal distorters 143
5.15 Mean error and standard deviation for aluminium section distorter. . . 143
5.16 Point cloud plot showing error from sheet distorter. 144

6.1 Electromagnetic tracking field generator designs. 148
6.2 Coil locations in Anser EMT field generator. 150
6.3 Spatial relationship between adjacent field generators. 151
6.4 Proposed tiling strategy for multiple field generator array. 153
6.5 Experimental setup diagram for two field generators. 154
6.6 Experimental setup of two field generators 155
6.7 3D ploint plot showing grid regitration procedure. 156
6.8 Experimental setup for planar field generator array. 158
6.9 Fiducial registration error versus inclicnation angle. 160
6.10 Jitter error versus inclicnation angle. 161
6.11 FFT frequency spectrum for inclinations of 0° and 9-°. 161
6.12 Point cloud of errors due to seperation distance. 162
6.13 Position errors versus field generator seperation distance. 163

7.1 Diagram and photo of commerical induction sensors. 166
7.2 Photograph of hand-wound induction coil sensors. 170
7.3 Impedance characteristic of air/ferrite core sensors. 171
7.4 Diagram of calibration point on field generator. 171
7.5 Experimental setup for calibrating sensors. 172
7.6 Sensor position plots over two heights. 181
7.7 Bronchoscope and laparaoscope with attached ait-core sensors. 182
7.8 Error plots for coils *A* and *B*. 182
7.9 Error plots for coils *C*, *D* and *E* with air/ferrite cores 183
7.10 Error plot for the NDI coil. 184
7.11 FFT plot showing effect of ferrite core. 184
7.12 3D plot showing instrument trajectory tracking. 185

8.1 Generalised block diagram of a surgical navigation system 188
8.2 Commercial electromagnetic tracking systems. 189
8.3 CustusX virtual bronchoscopy screenshot 191
8.4 Illustration of bronchoscope, catheter and instrument. 192
8.5 Diagram of bronchial catheter dimensions. 193
8.6 Screenshots of CloudCompare during registration. 198
8.7 CustusX screenshot showing tumour locations. 199
8.8 Annotated catheter handle design. 200
8.9 Screenshot of CustusX during airway navigation. 201
8.10 Photograph and X-ray image of embolisation coil. 201
8.11 Photograph of the clinical setup of the animal study. 202

A.1 Mutual inductance error plots for planar sheet distorters. 212
A.2 Mutual inductance error plots for steel block distorter. 213
A.3 Mutual inductance error plots for aluminium section distorter. 214
A.4 Mutual inductance error plots for aluminium cylinder distorter. 215
A.5 Mutual inductance error plots for steel slab distorter. 216
A.6 Phase error for planar sheet distorters 218
A.7 Phase error for planar steel block distorters 219
A.8 Phase error for aluminium section distorter. 220
A.9 Phase error for aluminium cylinder distorter. 221
A.10 Phase error for steel slab distorter. 222
A.11 Position error plots for sheet metal distorters. 223
A.12 Position error plots for the steel block distorter. 224
A.13 Position error plots for aluminium section distorter. 225
A.14 Position error plots for aluminium cylinder distorter. 226
A.15 Position error plots for steel slab distorter. 227

List of Tables

3.1 NI-USB 6212/6216 specifications 35
3.2 Transmitter frequencies used in Anser EMT 44
3.3 Comparison of different windowing functions 46
3.4 Anser EMT performance on Matlab 60
3.5 Anser EMT performance on Python 61

4.1 Swept transmitter coil parameters 88
4.2 INA128 and INA163 specifications 90
4.3 Teensy 3.2 versus Arduino Uno 93
4.4 USB-6212/6216 specifications 93
4.5 Anser EMT precision and accuracy results 111
4.6 Anser EMT rotational error results 111
4.7 Anser EMT versus commercial systems 112

5.1 Simulated field generator inductance matrix. 125
5.2 Simulated induced voltages on field generator. 125
5.3 Properties of EMT transmitter coils. 127
5.4 Properties of distorters used in experiments. 129
5.5 Experimentally calculated mutual inductance matrix 135

7.1 Properties of designed EMT sensor coils 169
7.2 Static accuracy of coils *A* and *B* with air-cores. 174
7.3 Static accuracy of coils *C*, *D* and *E* with air-cores. 174
7.4 Static accuracy of coils *C*, *D* and *E* with ferrite cores 175
7.5 Static accuracy test results for the NDI coil. 175

8.1 Tumour targeting accuracy results 204

Contents

Abstract i

Acknowledgements iii

List of Publications v

List of Figures ix

List of Tables xiii

List of Abbreviations xxi

List of Symbols xxv

1 Introduction 1
- 1.1 Lung cancer . . . 1
- 1.2 Limitations of Bronchoscopy . . . 2
- 1.3 Electromagnetic Navigation Bronchoscopy . . . 3
- 1.4 Shortcomings of ENB . . . 4
- 1.5 Thesis Objectives . . . 6
- 1.6 Thesis Structure . . . 7

2 Clinical Background 9
- 2.1 Introduction . . . 9
- 2.2 The Lung . . . 9
  - 2.2.1 Lung Cancer . . . 11
- 2.3 Bronchoscopy . . . 11
- 2.4 Imaging in Bronchoscopy . . . 13
  - 2.4.1 Preoperative imaging . . . 14
  - 2.4.2 Intraoperative imaging . . . 14
- 2.5 Electromagnetic Navigation in Bronchoscopy . . . 18
- 2.6 ENB Procedure . . . 20

2.6.1 Airway Imaging and Segmentation . . . 20
2.6.2 Airway Mark-up . . . 22
2.6.3 Airway Registration . . . 23
2.6.4 Airway Navigation . . . 25
2.7 The Future of Bronchoscopy . . . 27
2.8 The Future of ENB . . . 28

3 An Open Framework for EMT System Development 29
3.1 Introduction . . . 29
3.2 Framework Design . . . 31
3.3 Acquisition . . . 32
3.3.1 Acquisition in Anser EMT . . . 34
3.4 Filtering . . . 36
3.4.1 Sampling parameters . . . 39
3.4.2 Spectral leakage . . . 40
3.4.3 Coherent sampling . . . 42
3.4.4 Window sampling . . . 45
3.5 Model . . . 50
3.5.1 Dipole approximation model . . . 50
3.5.2 Large circular coil model . . . 51
3.5.3 Current filament model . . . 52
3.5.4 Sensor Model . . . 53
3.6 Solver . . . 56
3.7 Framework Implementation . . . 57
3.8 Experiments and Results . . . 58
3.8.1 Performance benchmark . . . 59
3.8.2 Accuracy benchmark . . . 59
3.9 Discussion . . . 61

4 EMT system design 63
4.1 Introduction . . . 63
4.2 Previous transmitter driver . . . 64
4.2.1 Waveform generation . . . 65
4.2.2 Signal conditioning . . . 66
4.2.3 Design critique . . . 73
4.3 Optimised transmitter driver . . . 74
4.3.1 AC coupled driver design . . . 77
4.3.2 Open-loop transmitter analysis . . . 83
4.3.3 Closed-loop transmitter analysis . . . 85
4.4 Sensor amplifier design . . . 88
4.4.1 Noise analysis . . . 90

4.4.2 Amplifier circuit design . . . 91
4.5 Microcontroller . . . 92
4.6 Data acquisition unit . . . 93
4.7 Power delivery . . . 94
4.7.1 Mains power . . . 94
4.7.2 Input filtering . . . 95
4.7.3 Split rail design . . . 95
4.7.4 Linear regulation . . . 97
4.8 Field generator design . . . 98
4.9 Enclosure design . . . 98
4.9.1 Driver PCB enclosure . . . 98
4.9.2 Field generator PCB enclosure . . . 100
4.10 System operation . . . 102
4.10.1 System start-up . . . 102
4.10.2 Current settling . . . 103
4.10.3 Steady state . . . 104
4.10.4 Frequency programming . . . 108
4.11 Accuracy evaluation . . . 109
4.11.1 Testing protocol . . . 109
4.11.2 Results . . . 109
4.12 Summary . . . 114

5 Detection and localisation of distortions in EMT 115
5.1 Background . . . 118
5.1.1 Magnetic Field Generator . . . 118
5.1.2 Mutual Inductance . . . 118
5.1.3 Field Generator Inductance Matrix . . . 120
5.1.4 Summary . . . 121
5.2 Field Generator Inductance Simulation . . . 121
5.3 Experimental Setup . . . 125
5.3.1 Modified Field Generator Design . . . 125
5.3.2 Distorter Selection . . . 126
5.3.3 Acquisition Hardware . . . 128
5.4 Acquisition Methods . . . 133
5.4.1 Mutual Inductance Measurement . . . 133
5.4.2 Position acquisition . . . 133
5.5 Results . . . 134
5.5.1 Mutual Inductance Matrix . . . 134
5.5.2 Inductance Error . . . 135
5.5.3 Phase response . . . 139
5.5.4 Position Error . . . 142

5.6 Discussion . . . 142
5.6.1 Error versus Distance . . . 143
5.6.2 Phase Angle versus Material . . . 144
5.6.3 Inductance and Phase Error versus Distorter Location . . . 145
5.7 Summary . . . 145

6 Modular and Tiled Field Generator Design 147
6.1 Introduction . . . 147
6.2 Planar EM Tracking . . . 149
6.2.1 Multi Field Generator Design . . . 150
6.3 Field Generator Hardware . . . 152
6.4 Experimental Methods . . . 154
6.4.1 Angle Experiment . . . 155
6.4.2 Scribble Experiment . . . 157
6.5 Results . . . 159
6.5.1 Error versus Angle β Results . . . 159
6.5.2 Scribble Test Results . . . 159
6.6 Discussion . . . 159
6.7 Summary . . . 163

7 Bespoke Tracking Sensor Design 165
7.1 Introduction . . . 165
7.2 Materials and Methods . . . 169
7.2.1 Sensor Design . . . 169
7.2.2 Sensor Calibration . . . 170
7.2.3 Static Accuracy Testing . . . 172
7.2.4 Instrument Trajectory Tracking . . . 173
7.3 Results . . . 174
7.3.1 Static Accuracy Testing . . . 174
7.3.2 Instrument Trajectory Tracking . . . 175
7.4 Discussion . . . 177
7.4.1 Coil Design Theory and Practice . . . 177
7.4.2 Static Accuracy Testing . . . 177
7.4.3 Instrument Trajectory Tracking . . . 179
7.5 Summary . . . 179

8 Pre-clinical Evaluation with Anser EMT 187
8.1 Open Navigation System Design . . . 187
8.1.1 Tracking Hardware . . . 188
8.1.2 Visualisation Software . . . 189

8.1.3 Communication Interface 190
8.2 Tracked Instrument Design 190
8.2.1 Bronchial Catheter Specification 192
8.3 Experimental Procedure 194
8.3.1 Tumour Model Deployment 194
8.3.2 Segmentation, Registration and Mark-up 195
8.3.3 Virtual navigation 195
8.3.4 Measuring targeting accuracy 196
8.4 Results 196
8.4.1 Tumour model results 196
8.4.2 Targeting accuracy results 203

9 Summary and Future Work **205**
9.1 Proposals for Future Work 207
9.1.1 A scalable and robust field generator topology 207
9.1.2 Integration with toolkits 208
9.1.3 Distortion detection and compensation 208
9.1.4 Improved sampling 208
9.1.5 Simplified calibration using machine learning 209
9.1.6 Persistent calibration 210
9.1.7 Miniaturised sensor design 210

A Extended Results **211**
A.1 Inductance Error Plots 211
A.2 Phase Angle Plots 217
A.3 Position Error Plots 223

Bibliography **229**

List of Abbreviations

2D . . . . . Two-dimensional

3D . . . . . Three-dimensional

5-DoF . . . . . 5 degree-of-freedom

6-DoF . . . . . 6 degree-of-freedom

AC . . . . . Alternating current

ADC . . . . . Analogue to digital converter

API . . . . . Application programming interface

CCD . . . . . Charge-coupled device

CLC . . . . . Capacitor-inductor-capacitor

CO_2 . . . . . Carbon dioxide

CP-EBUS . . . . . Convex probe endobronchial ultrasound

CPU . . . . . Central processing unit

CT . . . . . Computed tomography

DAC . . . . . Digital to analogue converter

DAQ . . . . . Data acquisition unit

DC . . . . . Direct current

DDS . . . . . Direct digital synthesis

DFT . . . . . Discrete Fourier transform

DSP . . . . . Digital signal processing

DTFT . . . . . Discrete time Fourier transform

EBUS . . . . . Endobronchial ultrasound

EM . . . . . Electromagnetic

EMN . . . . . Electromagnetic navigation

EMT . . . . . Electromagnetic tracking

ENB . . . . . Electromagnetic navigation bronchscopy

ESD . . . . . Electrostatic discharge

EWC . . . . . Extended working channel

FFT . . . . . Fast Fourier transform

FG . . . . . Field generator

FIFO . . . . . First-in first-out

FPGA . . . . . Field-programmable gate array

FRE . . . . . Fiducial registration error

GPS . . . . . Global positioning system

IC . . . . . Integrated circuit

ICP . . . . . Iterative closest point

IEEE . . . . . Institute of electrical and electronics engineers

IGI . . . . . Image-guided intervention

IGSTK . . . . . Image-guided therapy toolkit

IGT . . . . . Image-guided therapy

IHU . . . . . L'Institut hospitalo-universitaire

IRCAD . . . . . Research Institute against Digestive Cancer

ITK . . . . . The Insight Segmentation and Registration Toolkit

LDO . . . . . .Low-dropout regulator

LM/LMA . . . . . .Levenburg-Marquard algorithm

LMB . . . . . .Left main bronchus

MAE . . . . . .Mean absolute error

MDR . . . . . .Miniature delta ribbon

ME . . . . . .Mean error

MITK . . . . . .The Medical Interaction Toolkit

MOOP . . . . . .Means of patient protection

MRI . . . . . .Magnetic resonance imaging

MUX . . . . . .Multiplexer

NDI . . . . . .Northern Digital Inc.

NF . . . . . .Noise figure

NI . . . . . .National Instruments

NIH . . . . . .National Institutes of Health

OCT . . . . . .Optical coherence tomography

OEM . . . . . .Original equipment manufacturer

OS . . . . . .Operating system

P&O . . . . . .Position and orientation

PC . . . . . .Personal computer

PCB . . . . . .Printed circuit board

PET . . . . . .Positron emission tomography

PLUS . . . . . .Public library for ultrasound

PXI . . . . . .PCI eXtensions for instrumentation

R-EBUS . . . . . .Radial endobronchial ultrasound

RAM . . . . . Random-access memory

RC . . . . . Resistor-capacitor

REG . . . . . Register

RMB . . . . . Right main bronchus

RMS . . . . . Root mean square

ROM . . . . . Read-only memory

RX . . . . . Receiver

SCPI . . . . . Standard commands for programmable instruments

SFDR . . . . . Spurious-free dynamic range

SLAM . . . . . Simulataneous localisation and mapping

SMT . . . . . Surface-mount technology

SNR . . . . . Signal-to-noise ratio

SPICE . . . . . Simulation program with integrated circuit emphasis

TBNA . . . . . Transbronchial needle aspiration

THD . . . . . Total harmonic distortion

TNM . . . . . TNM Classification of Malignant Tumours

TR/TRF . . . . . Trust region algorithm

TX . . . . . Transmitter

US . . . . . Ultrasound

USB . . . . . Universal serial bus

VTK . . . . . The Visualization Toolkit

List of Symbols

Sign	Description	Unit
A	Cross sectional area	mm^2
A_{OL}	Open-loop gain	-
C	Capacitance	F
F_s	Sampling frequency	Hz
F_{MCLK}	AD9833 master clock frequency	Hz
F_{in}	Analogue input frequency	Hz
F_{out}	AD9833 output frequency	Hz
F_{system}	Tracking system update frequency	Hz
G	Amplifier gain factor	-
I	Electric current	A
J	Waveform periods per acquisiton frame	-
L	Inductance	H
L	Number of samples per acquisition frame length	-
M	Mutual inductance matrix	H
N_{FG}	Number of field generators in user	-
$N_{P/S}$	Number of transformer primary/secondary turns	-
N_{cloud}	Number of points in a point cloud	-
N_{coil}	Number of transmitter coils in field generator	-
N_{ft}	Number of samples in Fourier tranform calculation	-
N_{turn}	Number of turns on an inductive sensor coil	-
P	Matrix of points $\boldsymbol{p}$	-
R	Resistance	Ω
R_G	Programming resistor for setting amplifier gain	Ω
T_L	Latency delay	s
T_s	Sampling period	s
T_{ad}	Acquisition delay	s
Z	Impedance	Ω

Sign	Description	Unit
ΔF_{ML}	Main lobe width	Hz
Φ	Magnetic flux	Wb
$\boldsymbol{B}$	Magnetic flux density	T
$\hat{\boldsymbol{n}}$	The normal unit vector	-
$\boldsymbol{m}$	Magnetic moment	$\mathrm{N\,m\,T^{-1}}$
$\boldsymbol{r}$	Vector distance from origin	m
λ	Flux linkage	Wb
$\mathbf{E}$	Discrete fourier transform matrix	-
$\mathbf{R}$	Rigid rotation matrix	-
$\mathbf{T}_R$	Homogenous tranformation matrix	-
$\mathbf{W}$	Vector of window functiion coefficients	-
$\mathbf{X}$	Vector of waveform samples	-
$\mathbf{Y}$	Vector of frequency magntitudes	-
$\mathbf{p}$	Cartesian (x,y,z) coordinate	m
$\mathbf{t}_R$	Translation vector	m
$\mathscr{F}$	Fourier operator	-
μ_0	Magnetic permeability of free space	$\mathrm{H\,m^{-1}}$
μ_a	Apparent magnetic permeability	$\mathrm{H\,m^{-1}}$
μ_e	Mean error measurement	mm
μ_r	Relative magnetic permeability	-
ω	Angular frequency	$\mathrm{rad\,s^{-1}}$
π	A mathematical constant	-
σ_e	Standard deviation of error measurement	mm
σ_z	Standard deviation in z	m
θ	Spherical elevation angle	$^\circ$
φ	Spherical azimuthal angle	$^\circ$
d	Sensor diameter	m
e_n	Voltage noise	$\mathrm{nV}/\sqrt{\mathrm{Hz}}$
e_z	Position error in z	m
f_n	Normalised sampling frequency	$\mathrm{Hz\,S^{-1}}$
i	The current signal	A
i_n	Voltage noise	$\mathrm{pA}/\sqrt{\mathrm{Hz}}$
j	Imaginary unit	-
k	Frequency index in DFT	-
k_B	Boltzmann constant	$\mathrm{J\,K^{-1}}$
k_d	Demagnetisation factor	-
l	Sensor length	m
n	Discrete time sample index	-

Sign	Description	Unit
s	Complex frequency variable in Laplace domain	-
t	Time.	s
v	A voltage signal	V
w	DFT bin width	Hz
x	Cartesian x coordinate	m
y	Cartesian y coordinate	m
z	Cartesian z coordinate	m

Chapter 1

Introduction

This chapter provides a summary of the work presented in this thesis. The primary motivations for the work are initially explained followed by a brief description of the structure of the thesis.

1.1 Lung cancer

Lung cancer is the world's deadliest cancer with over 2 million deaths annually, a number which is rising each year [1, 2]. The standard of care for the diagnosis and treatment of lung cancer is through *bronchoscopy*; a minimally invasive procedure used to navigate a patient's airway using the patient's mouth for entry as shown in Fig. 1.1(a). A device called a *bronchoscope* is used for navigation and consists of a long flexible tube whose tip can be controlled using the handle as shown in Fig. 1.1(b). Traditional bronchoscopy uses a computer tomography scan acquired before the procedure (pre-operative CT) to provide the clincian with a static visual map of the airway as shown in Fig. 1.1(c). The bronchoscope contains an open lumen called a *working channel* which allows the clinician to insert biopsy and therapy tools through the scope into the airway.

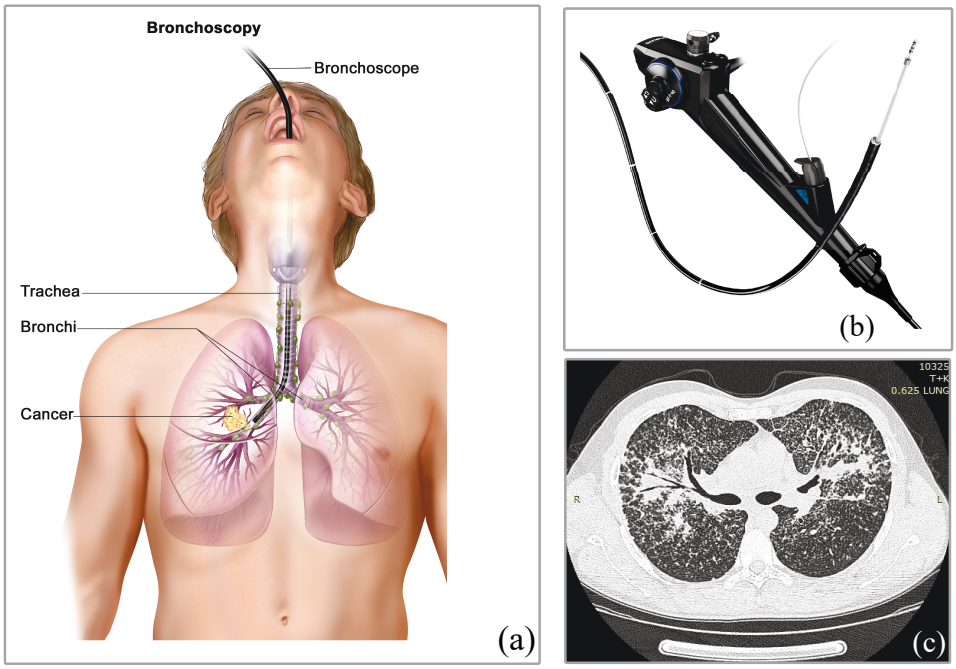


Figure 1.1: (a) Illustration depicting a bronchoscopy procedure showing the tip of a bronchoscope navigating within the lung [3]. (b) A model BF-P190 diagnostic bronchoscope (Olympus Medical, Shinjuku, Tokyo, Japan) with a outer diameter of 4.2 mm specifically designed for investigating the outer airway [4]. (c) Axial slice of a CT scan used to guide the clinician when navigating the airways [5].

1.2 Limitations of Bronchoscopy

Flexible bronchoscopy is currently the standard procedure for the diagnosis and treatment of pulmonary disease. While the technique is beneficial to both patients and clinicians in terms of procedure speed and patient comfort, the minimal invasiveness leads to limitations when investigating the outer airways. Similar to the roots of a tree, the branching structure of the airways results in smaller and smaller airway diameters as one travels deeper into the lung towards the outer airways. The limit occurs when the bronchoscope diameter exceeds that of the airway, from which point the scope is unable to navigate further without risking damage to the patient's airway. Obtaining access to the outer airways is becoming increasingly important in the diagnosis and staging of lung cancer as many young cancers start in these hard to reach areas [6, 7]. Bronchoscope manufacturers are addressing the need to extend the reach of their de-

vices by creating specialist diagnostic bronchoscopes such as that shown in Fig. 1.1(b) with an outer tube diameter as narrow as 4.2 mm. However, the complex branching structure and increasing airway density pose navigational difficulties to the clinician which has led to the development of electromagnetic navigation bronchoscopy.

1.3 Electromagnetic Navigation Bronchoscopy

The navigation challenge described in section 1.2 is currently being addressed by applying electromagnetic sensing principles to bronchoscope devices and instruments through electromagnetic navigation bronchoscopy (ENB) [8]. The technique provides a radiation-free alternative for guiding instruments through the airway using low-frequency electromagnetic fields. External camera tracking techniques are ineffective for airway navigation as they require line-of-sight in order to operate. An illustration of the procedure is shown in Fig 1.2. The patient lies on a magnetic transmitter from which a magnetic tracking volume is created. The clinician guides ENB-enabled tools through the airways via a standard bronchoscope. The position and orientation of the guided instruments are displayed in the guidance software in the context of the patient's chest CT scan. Performing bronchoscopy in this manner allows the clinician to reach the outer airways without using real-time X-ray. Electromagnetic navigation bronchoscopy relies on the use of an electromagnetic tracking (EMT) system, a commercially available technology which provides a global high-speed precision position and orientation reference using compatible magnetic tracking sensors. The magnetic sensors are typically embedded into the tips of bronchoscopy instruments or probes allowing them to be tracked within the patient. EMT operates on the principle of Faraday's law (1.1) which states that the induced voltage on a magnetic coil, v, is proportional to the rate of change of the magnetic flux intersecting the coil $\Phi(t)$.

$$v(t) = -\frac{d\Phi}{dt} \tag{1.1}$$

EMT utilises this induced voltage to resolve the position and orientation of the magnetic sensor.

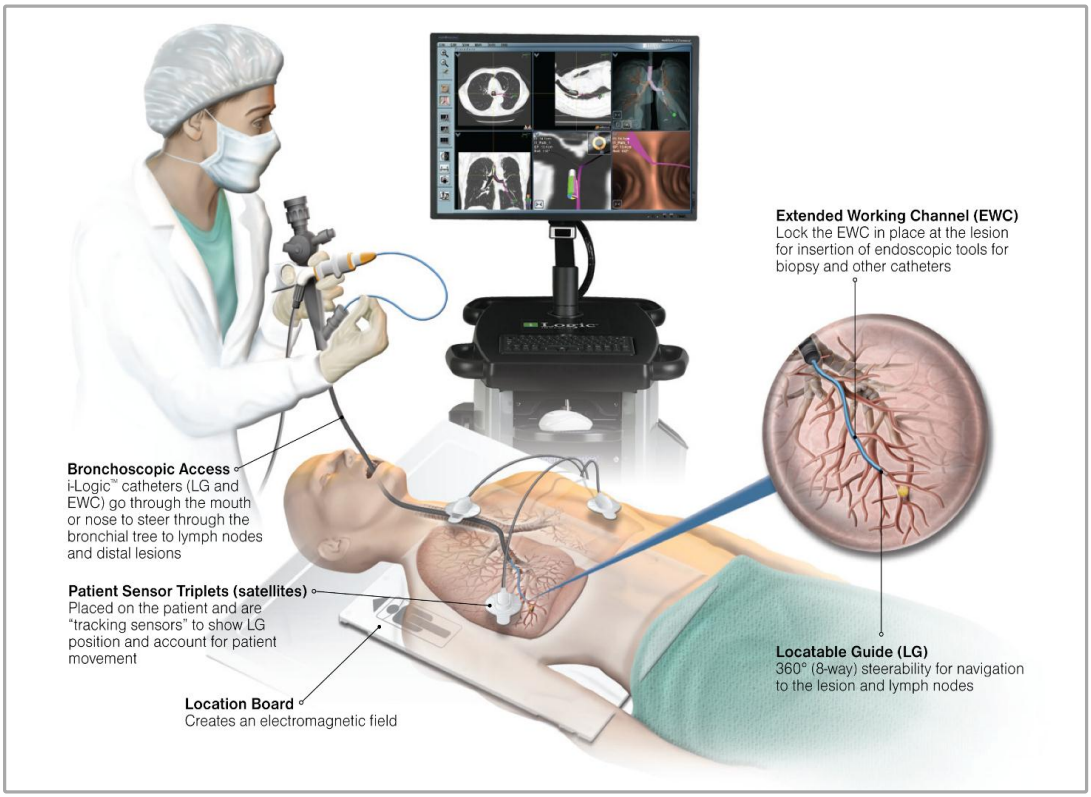


Figure 1.2: Illustration depicting electromagnetic navigation bronchoscopy being performed on a patient using the SuperDimension Navigation System (Medtronic, Dublin, Ireland) [9].

1.4 Shortcomings of ENB

Currently available commercial electromagnetic tracking systems used in medical navigation systems suffer from a number of shortcoming which this thesis aims to address.

- *Magnetic distortion detection*. The principles of electromagnetism result in electromagnetic tracking systems being susceptible to distorters comprising of ferrous and non-ferrous objects. Any deviations in the voltage due to these external distorters can result in errors in the sensors' position and orientation reported by the system [10]. Medical instruments and procedure tables make up the largest source of disturbances in the clinical setting. However, commercially available systems cannot directly detect magnetic disturbances or sense their

whereabouts. Position error compensation techniques have previously been developed, but these are purely numerical in design. [11–14], although there are some researchers tackling the problem by analysing the underlying physics of the magnetic signals [15, 16].

- *Fixed sensor geometries*. Commercially available tracking systems such as the Aurora system (*Northern Digital Inc, Waterloo, Ontario*) provide a catalogue of tracking sensors of fixed dimensions [17]. As a corporate customer one can indeed develop custom sensors in partnership with these companies. However, as a researcher developing novel tracking applications, the required upfront costs of such a partnership can pose a barrier to entry.

- *High cost*. The cost of entry for using electromagnetic tracking in research is high at approximately $10,000. This initial high cost can be a barrier to entry for potential research. Electromagnetic tracking in the clinical setting is currently dominated by Northern Digital which may be one of the reasons for such a high system cost.

- *Lack of underlying physics models*. The physical models and algorithms used by commercial tracking systems are not available to the public (closed-source). This is a completely understandable strategy from a commercial standpoint, however, no open-source tracking alternative exists. This can cause innovation in the area to stagnate.

1.5 Thesis Objectives

The work presented in this thesis aims to address some of the shortcomings of current electromagnetic tracking system technology by developing:

An open software framework for EMT. Implementation details of the software and algorithms governing the operation of commercial EMT systems are not publicly disclosed. This thesis describes a reference implementation which researchers can adapt and modify by breaking down EMT into several separate processing steps. In this way researchers may understand, modify and apply, part, or all of the framework within a larger EMT application.

Anser EMT - An open EMT hardware platform. The creation of an open-source electromagnetic tracking system will allow researchers to understand, customise and apply magnetic tracking to their specific application. While the initial focus of this work is for enhancing the accuracy of ENB, it is envisioned that the technology can be readily applied to research in other clinical disciplines where electromagnetic tracking is beneficial.

Custom magnetic sensors. In providing an open tracking system design, this thesis also proposes techniques for the creation of customised magnetic tracking sensor coils. This work aims to facilitate the integration of electromagnetic tracking into other tracking applications otherwise incapable of using EMT due to the fixed geometries and sensitivities of commercially available sensors.

Redundant transmitter topologies. The tracking volume of EMT systems are limited by the size of the magnetic field produced by the system field generator. Future applications of EMT may require larger tracking volumes of different sizes. This work proposes a low-cost method for scaling EMT field generator designs to provide tracking volumes of arbitrary size.

Distortion analysis techniques. The effect of metal on the accuracy of magnetic tracking is a well documented phenomenon although the majority of compensation

techniques are purely numerical or use redundant data sources. Direct characterisation of the effects of different metal distorters can reveal information about the type of metal and location of the distorter with respect to the transmitter as well as the degree of positioning error experienced by the tracking system as a result.

Reference ENB Platform. ENB is a relatively novel procedure and many innovations in the field are currently being developed in the areas of robotics and motion compensation [18]. This thesis presents an implementation of ENB using only open-source hardware and software tooling. This work demonstrates that fully open-source hardware and software can be effectively applied to ENB research in the pre-clinical setting.

1.6 Thesis Structure

This thesis is broken into eight main chapters which investigate the different aspects of the work. Chapter 2 investigates the clinical background of lung cancer, chest imaging and electromagnetic navigation in bronchoscopy and provides a primer for the preclinical work described in chapter 8. The chapter provides a motivation for further development in the electromagnetic tracking and a brief outlook on the future of the procedure.

Chapter 3 introduces the concepts of electromagnetic tracking and the construction of an open electromagnetic tracking system framework from a top-down perspective. Justifications for the creation of an open system are discussed. Each subsystem of the system is presented in a separate section, starting with the hardware-software boundary of the sampling electronics and finishing with the numerical techniques used to for resolving tracking sensor positions and orientations. The framework is applied to Anser EMT with experimental accuracy and speed results recorded.

Chapter 4 describes the hardware implementation of the open electromagnetic tracking system, Anser EMT, from a bottom-up perspective. The reference design is built to operate with the framework discussed in chapter 3. Current control, amplifier design and power supply implementation details are simulated, discussed and their

performance evaluated.

Chapter 5 builds upon the work of chapter 4 to investigate the effect of metal distorters when placed near the system magnetic field generator. The physical principles of distorters are discussed followed by the design, implementation and experimental validation of a novel magnetic field generator capable of detecting the location and severity of static magnetic distortions proximal to the magnetic field generator.

Chapter 6 builds upon chapters 3 and 4 to define a novel low-cost method of scaling the effective tracking volume of electromagnetic tracking systems. A tiling structure is introduced allowing an arbitrary number of field generators to form a larger aggregate tracking volume. An implementation is designed and implemented using two planar field generators. Experimental results are reported for planar and angled configurations of the two tiled field generators.

Chapter 7 investigates the design and development of customised tracking sensors for electromagnetic tracking applications. The physical principles governing the design of induction sensors are initially discussed, followed by physical implementations using hand-wound coil sensors with both air and ferrite magnetic cores. The accuracy metrics of the hand-wound sensors are compared with a commercial off-the-shelf electromagnetic sensor. Finally, surgical instrument tracking is experimentally validated using endoscopic and laparoscopic devices.

Chapter 8 validates the clinical applications of the presented electromagnetic tracking system in electromagnetic navigation bronchoscopy. A custom tracked catheter is presented along with the supporting software utilised to visualise the tip position within the airway. An *in vivo* study is performed on porcine models with two qualified pulmonologists. Accuracy in targeting peripheral lung lesions is demonstrated using a novel tumour modelling technique and post-operative CT scan validation. The work demonstrates the first fully-open source ENB suite for pre-clinical research.

Chapter 9 reviews the key findings of the thesis and some recommendations for future work on electromagnetic tracking are presented.

Chapter 2

Clinical Background

2.1 Introduction

This chapter provides an overview of the medical technologies and techniques discussed in this thesis. We begin by describing bronchoscopy in the context of lung disease and endoscopic navigation. Software tooling for navigation research are described along with commercially available navigation systems for applying electromagnetic navigation in bronchoscopy.

2.2 The Lung

The lungs are a central part of the human respiratory system. Located in the chest cavity, their primary function is the extraction of oxygen from the airway and removal of carbon dioxide (CO_2) from the body in a gas exchange process. A diagram of the lungs is illustrated in Fig. 2.1 with all major structures labelled. The right lung has three lobes (*superior, inferior* and *middle*) and is slightly larger than the left lung which has only two lobes (*superior* and *inferior*). The trachea is the flexible tube which extends from the *larynx* to the *carina* and forms the main airway. Air enters and leaves the lungs through the main bronchi, which branch off from the *trachea* at the *carina*. The *tracheal* and *bronchi rings* are C-shaped rings of cartilage that hold these main airways open. The bronchi successively divide into bronchioles and are terminated

with the alveolar sacks. These sacks contain a fine network of blood vessels called *capillary beds* in which the gaseous exchange occurs. The pulmonary artery brings oxygen-depleted, CO_2 rich blood to the lungs *alveoli* while the pulmonary vein returns the re-oxygenated blood from the lungs back to the heart [19].

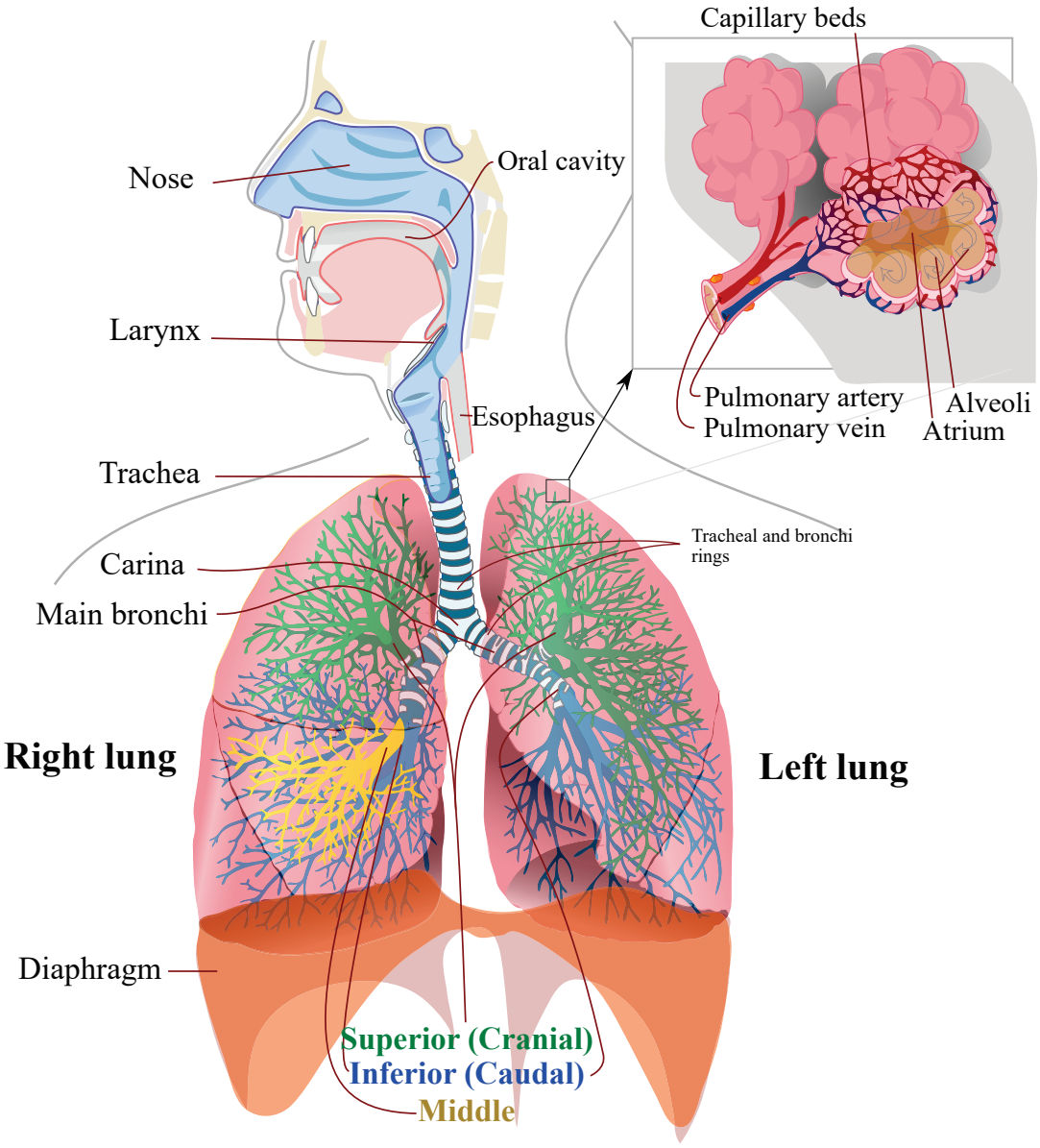


Figure 2.1: Diagram of the the human airways with main anatomical structures labelled [20].

2.2.1 Lung Cancer

Cancer is the uncontrolled growth of abnormal cells in bodily tissues. Lung cancer was a fairly rarely diagnosed condition in the 20th century, but is now the most deadly cancer in the world with over 2 million deaths annually [1, 2] and is rising each year. The carcinogenic ingredients of tobacco smoke are the primary cause of lung cancer, with about 85-90% of all lung cancer patients being smokers. That being said, people who have never smoked in their lives can also suffer from lung cancer due to environmental factors. These include air pollution, radon exposure, viruses and an individual's genetic predisposition to the disease [21].

The most difficult lung cancers to diagnose and treat are those which express themselves as tumours in the outer airways of the lung. The localisation, targeting and treatment of these tumours remains a the most challenging clinical need. Despite advances in technology, typically less than 30% of primary lung nodules beyond the reach of the conventional bronchoscope are diagnosed [22]. With the advent of lung cancer screening, small peripheral lung cancers are being detected which often require tissue confirmation [23]. Conventional biopsy techniques for lung cancer require the use of a bronchoscope to navigate to the tumour site to obtain a physical tissue biopsy.

2.3 Bronchoscopy

Flexible bronchoscopy (commonly referred to as *bronchoscopy*) is one of the most commonly performed procedures for the investigation of the human lung, allowing visualisation of the inside of the airways for the diagnosis and treatment of lung disease. The procedure is performed with a bronchoscope: a long thin, steerable tube with integrated camera optics. The first commercially available bronchoscope was invented by Shigeto Ikeda in 1966 in association with Pentax (Pentax Medical, Tokyo, Japan). A diagram illustrating the technique is shown in Fig. 2.2. The clinician navigates the tip of the scope past the carina into the lungs [24]. The operating clinician, called a bronchoscopist or pulmonologist, must have in-depth knowledge of the patient's lung structure in order to successfully navigate to a region of interest. A live camera view of the bronchoscope camera is typically used alongside a pre-operative computed

tomography (CT) scan, allowing the clinician to successfully navigate the scope using the pre-operative scan as a guiding map. The clinician must mentally correlate the position on the CT image to the live video feed in order to navigate the complex structure of the airway, which is quite a cognitively heavy task.

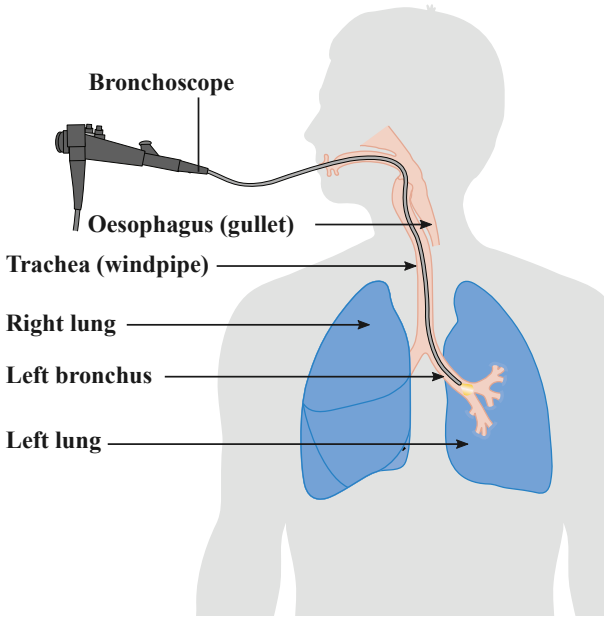


Figure 2.2: Simplified illustration showing the introduction of a bronchoscope into a patient's airways.

Different models of bronchoscopes exist depending on the clinical need. Variable features among designs are the scope's outer diameter and the working channel diameter. For diagnostic bronchoscopy deep within the lung, a small scope diameter is desirable as it allows the clinician to access the narrowest bronchi. One example of such a scope is the BF-MP290F bronchoscope (*Olympus, Shinjuku, Tokyo, Japan*) which is specifically designed to access the peripheral airways; it features a 3.0mm outer scope diameter and an 1.7mm working channel. Conversely, a therapeutic scope features much larger dimensions. The Olympus BF-1TQ290 scope shown in Fig. 2.4 has a 6mm scope outer diameter and a 3.0mm working channel. Therapeutic scopes are used for treatment of lung disease as their relatively large working channel enables the passage of large therapeutic instruments such as probes for the ablation of airway tumours [25]. Other well-known bronchoscope manufacturers include Fujifilm, Pentax

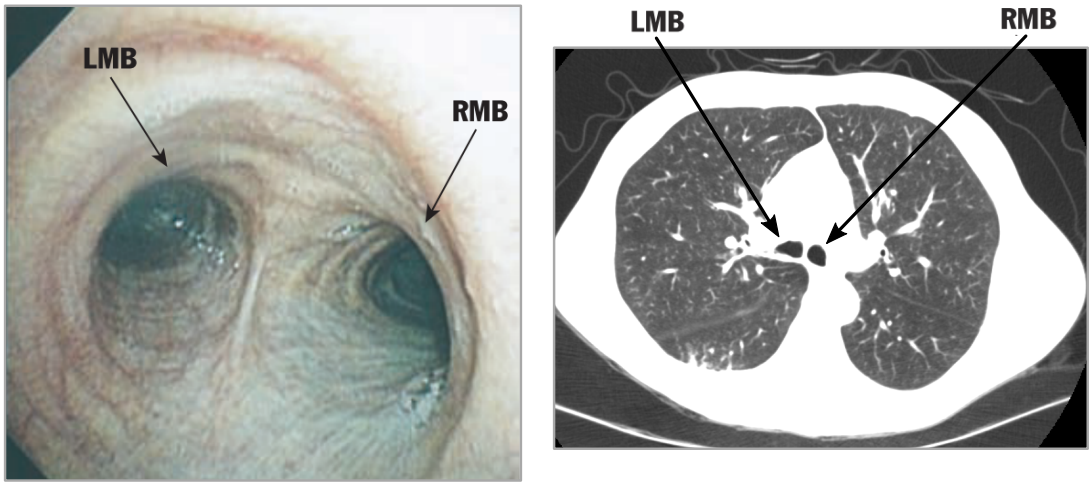


Figure 2.3: Bronchoscope camera view of the carina whilst in the trachea (left). The outline of the bronchial and tracheal cartilage rings can be seen. Computed tomography (CT) scan of the lungs (right). Right-main-bronchus (RMB) and left-main-bronchus (LMB) are labelled in each case [24].

and Karl-Storz.



Figure 2.4: An Olympus Medical BF-1TQ290 bronchoscope. This scope features a large 3.0mm working channel allowing for the insertion of therapeutic instruments into the lung.

2.4 Imaging in Bronchoscopy

The clinician has three techniques to assist him/her during bronchoscopic navigation: (i) preoperative imaging, (ii) intraoperative imaging and (iii) virtual imaging.

2.4.1 Preoperative imaging

Preoperative imaging consists of well established imaging modalities including computed tomography (CT), magnetic resonance imaging (MRI) and positron emission tomography (PET). CT is the preferred imaging technique for planning airway navigations due its fast acquisition time and high-contrasting images it provides of the airway. The longer acquisition times required by MRI result in blurry images due to patient motion due to breathing and pulsing artefacts. The limited susceptibility difference between delicate pulmonary tissues and airway cavities make obtaining highly-contrasting MRI images difficult, although when combined with matching CT images, MRI can provide the clinician with more insight of the tissue structure [26,27]. There has been an increased clinical uptake of PET in tandem with CT for the treatment of lung cancer, as PET provides insight into the metabolic process of cancerous lesions [28] while CT/MRI provides a structural context [29].

2.4.2 Intraoperative imaging

During the bronchoscopy procedure, the clinician may use a number of real-time imaging techniques. These intraoperative imaging techniques are numerous and consist of four main methods;

- Endoscopic imaging
- Endobronchial ultrasound
- Optical coherence tomography
- Cone beam computed tomography

Endoscopic imaging is the classic form of visualisation within the airway as it provides the clinician with a real-time view of the airway from the perspective of the tip of the bronchoscope, as shown in Fig. 2.3, using camera optics located at the scope's tip. Modern bronchoscopes use chip-on-the-tip camera technology where a charge coupled device (CCD) converts incident light into an array of pixels which are displayed on a screen after processing. Traditional bronchoscopes instead used

bundled glass fibres to transmit light from the scope tip to the scope eyepiece. For illumination inside the airway, fibre bundles in combination with a xenon arc lamp are still used as a light source. Difficulties arise due to the large bronchoscope diameter and the limited field of view offered by the camera, but visual imaging is still the only direct means of viewing the inner airway for navigation and tissue inspection. Imaging capabilities can be enhanced when used in combination with narrow-band-imaging (NBI) which has been found useful for detecting and staging lung cancer [30, 31].

Endobronchial ultrasound imaging (EBUS) uses high-frequency sound waves to provide localised imaging through tissues within the airway, enabling clinicians to navigate, diagnose and treat airway diseases without the use of ionising radiation [32]. EBUS can be either fixed to the tip of the bronchoscope as a convex probe (Cp-EBUS) or take the form of an endoluminal radial catheter probe (Rp-EBUS). The former has been found to be effective for locating and targeting cancerous lesions outside of the main airway. Transbronchial needle aspiration (TBNA) uses a needle to puncture and biopsy suspect lesions which lie outside of the airway for which Cp-EBUS provides greatly increased targeting accuracy [33, 34]. Rp-EBUS has been shown to be effective at detecting cancer in cases where sufficient biopsy material cannot be extracted from a lesion [35, 36]. The radial probe is inserted into the lesion to localise targets prior to biopsy. The resulting images provide diagnosis and staging information to the clinician.

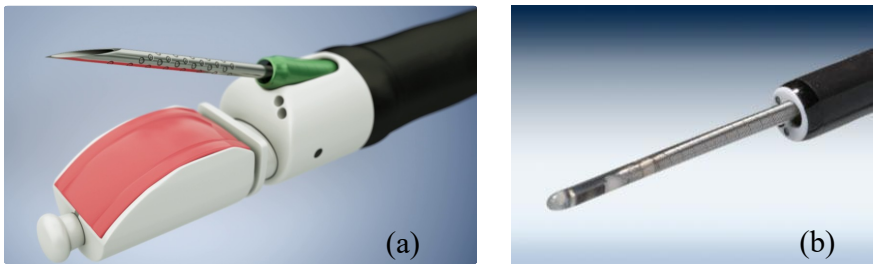


Figure 2.5: (a) Olympus ViziShot EBUS-TBNA kit. The convex ultrasound probe is rigidly mounted to the tip of the bronchoscope. The needle is then visualised using ultrasound guidance on a screen for the clinician. (b) Olympus Rp-EBUS probe. The probe can pass freely through the working channel of the bronchoscope using the Olympus Guide Sheath Kit. The Rp-EBUS probe is removed to allow for the passage of biopsy instruments [37].

Optical coherence tomography (OCT) is a relatively new imaging modality being applied to bronchoscopy which uses low-coherence interferometry to capture high-resolution images of the optical scattering from tissue structures [38–40]. The technology provides depth-resolved, non-invasive, non-destructive imaging features which are similar to EBUS in many respects except at a significantly magnified scale [41]. 2D OCT images can be combined to form 3D reconstructions of tubular structures within the body. The ability of OCT to provide optical biopsy information in the form of functional imaging of blood flow and tissue structure has led to its successful use diagnosing and staging of lung cancer [42–45].

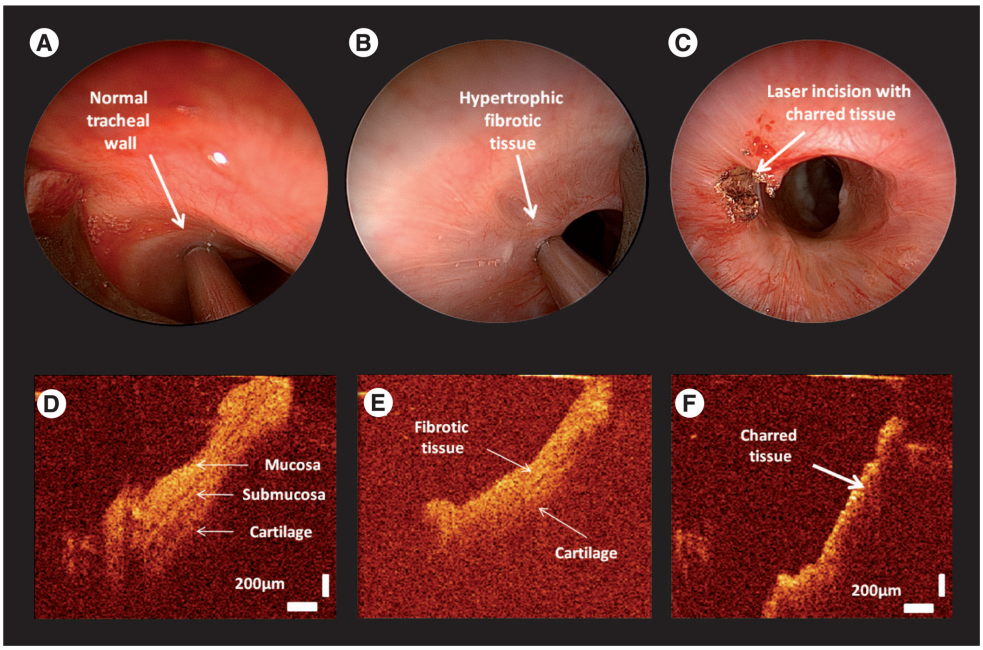


Figure 2.6: 2D OCT images within the lung obtained from Hou *et al.* [46]. The probe images can easily discriminate different lung tissue types and the effects of therapy.

Intraoperative X-ray fluoroscopy and cone-beam computed tomography (CBCT) are two radiological imaging modalities that can provide the clinician with a global context of the location of instruments within the patient. Fluoroscopy and CBCT are extremely useful for navigation through complex anatomy and confirming placement of instruments for biopsy and therapy. The real-time nature of the imaging also allows the clinician to capture motion of the airways due to breathing, allowing for increased

accuracy during targeted biopsy and when providing radiation therapy [47, 48]. While providing the clinician with a global view of the procedure site, imaging in this manner exposes clinicians and patients to ionising radiation which is always best minimised.

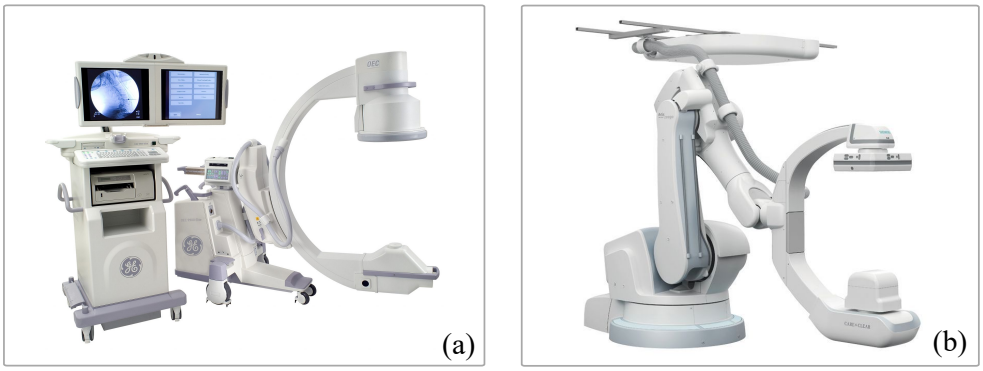


Figure 2.7: (a) General Electric OEC 9900 Elite C-arm. The device can provide real-time X-ray footage of the patient during medical procedures. (b) Siemens Artis Zeego robotic cone beam CT platform. The system is capable of producing 3D volumes of the target site in a matter of seconds using its DynaCT protocol.

Global navigation

Of these four imaging modalities discussed (endoscopy, EBUS, OCT and X-ray/CBCT), only real-time X-ray/CT can provide the clinician with a global contextual view of the target site within the lung. In many cases successful application of EBUS and OCT require X-ray in order to confirm successful navigation to a region of interest. In all cases this exposes both the patient and clinician to ionising radiation which as been proven to increase their risk of cancer [49]. Therefore, external tracking methods have been created that are capable of providing a reference to the clinician without radiation in order to reduce exposure. Optical and electromagnetic varieties of these systems exist which, when combined with pre-operative patient imaging, can provide the clinician with effective real-time *virtual* navigation within the patient in a global patient context. Clinically approved systems include the Polaris Spectra for optical tracking and the Aurora and Trakstar electromagnetic systems (Northern Digital Inc., Waterloo, Ontario, Canada) shown in Fig. 2.8. Optical tracking systems are ideally suited for tracking rigid instruments where the user interface is within line-of-sight of

the tracking camera. Optical tracking is therefore unsuited to bronchoscopy as the instruments are flexible and used deep within the lung. Electromagnetic tracking (EMT) has proven effective for navigating the airways as the sensors can be readily embedded in endoscopic tools and probes. The use of electromagnetic tracking in bronchoscopy will remain the focus of this chapter and will be discussed in sections 2.5 and 2.6.

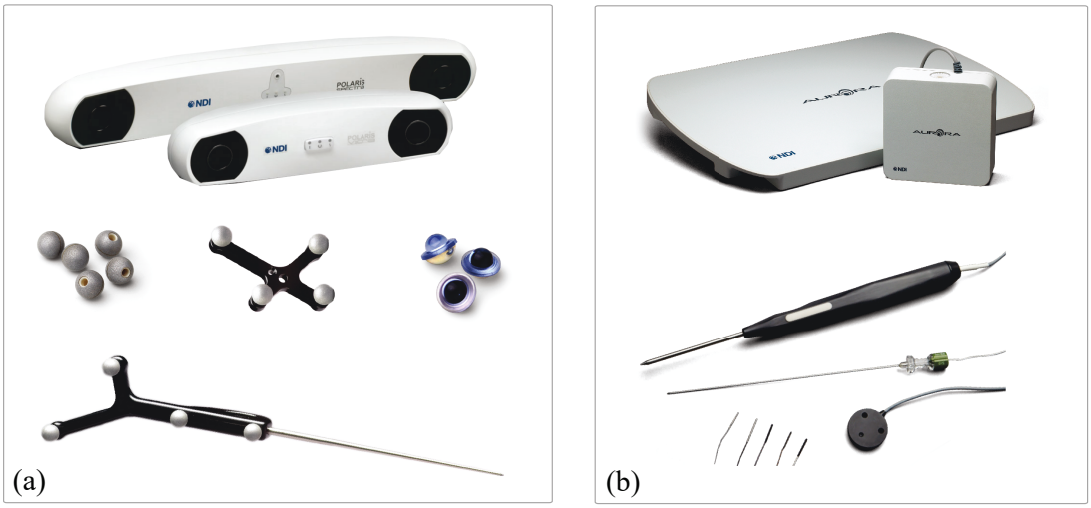


Figure 2.8: (a) NDI Polaris Spectra optical navigation system. The system uses stereoscopic infrared cameras to locate the position optical markers. Multiple optical markers may be attached to surgical tools to behave as a position and orientation reference. (b) NDI Aurora electromagnetic tracking system showing planar and table-top field generators. Small magnetic sensors can be embedded into surgical instruments to produce a position and orientation reference for clinical applications.

2.5 Electromagnetic Navigation in Bronchoscopy

EMT provides the position and orientation (pose) of the bronchoscope and endobronchial instruments using miniaturised sensors. In combination with preoperative patient imaging, live instrument tracking within the context of the patient's scan can provide the clinician with the ability to navigate to parts of the body inaccessible by cameras. These areas correspond to the outer airways of the lung where the diameter of the bronchoscope exceeds the diameter of the bronchi. Camera guidance is no longer effective from this point onwards as the target lies beyond the camera's field of view.

EMT has enabled the development of electromagnetic navigation in bronchoscopy (ENB) [50] to increase diagnostic yield in outer airway navigation by allowing the clinician to visualise their position within the airway without camera optics. Similar to an automobile's global positioning guidance system (GPS), ENB systems guide the clinician through the complex branching structure of the human airway using magnetic fields. Examples of commercial ENB systems are the *superDimension Navigation System* (Medtronic, Dublin, Ireland) and *SPiN Drive* (Veran Medical, St. Louis, MO) systems. The SuperDimension system is shown in use in Fig. 2.9

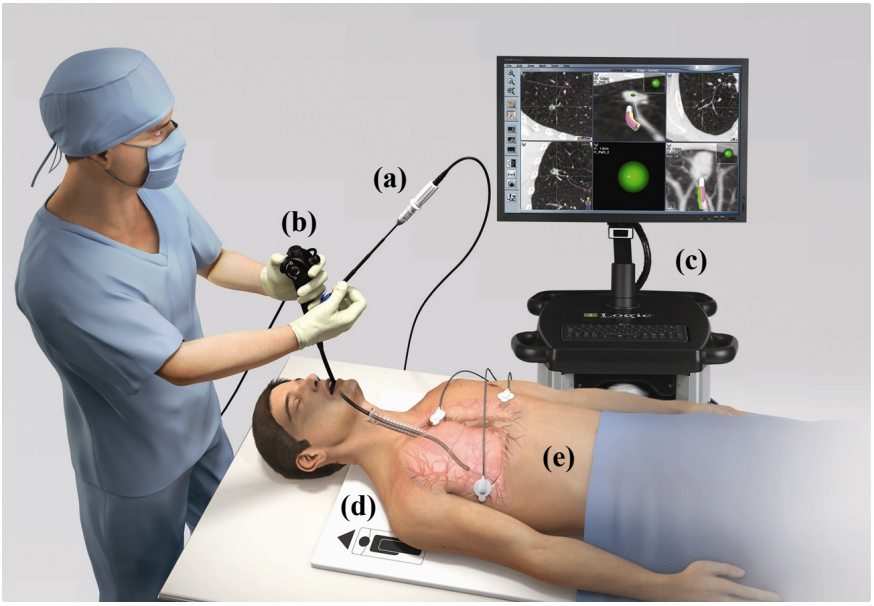


Figure 2.9: Electromagnetic navigation (EMN) applied to bronchoscopy [9]. A tracked instrument (a) is inserted through the working channel of the bronchoscope (b) into the patient's airway. The navigation system (c) combines the pose data of the instrument with pre-operative patient imaging to provide the clinician a camera-less map of the airway. The system field generator (d) lies beneath the patient (e) and produces the magnetic field. The patient wears three reference sensors which allow the navigation system to compensate for motion due to breathing.

2.6 ENB Procedure

The workflow of an electromagnetic navigation bronchoscopy procedure can be summarised in four steps:

1. *Airway Imaging and Segmentation*. A pre-operative patient CT scan is used to generate a 3D rendering of the airway in a process called *segmentation*. The rendering is visualised on-screen and used by the clinician as an airway map during the navigation process.

2. *Airway Mark-up and Planning*. Mark-up target regions of interest (ROI) on the 3D model for navigation and generate routes to the airway targets through the model.

3. *Airway Registration*. Register the 3D airway model to the patient's coordinate system in order to align the pre-operative CT imaging to the sensor location within the patient's airway.

4. *Airway Navigation*. Navigate to the target ROI using ENB-enabled instruments and the path planning features of the navigation software. The 3D model can provide a virtual endoscopy imaging view.

2.6.1 Airway Imaging and Segmentation

Accurate patient imaging data is crucial in bronchoscopy as it provides the clinician with a map of the patient's airway and tumour locations. Computed tomography (CT) is the gold standard for chest imaging due to the high contrasting 3D images it can produce for low-density structures such as the lung [51]. CT operates similarly to a traditional X-ray, except that the X-ray source and detector are mobile and rotate around the patient in a known configuration to produce a series of X-ray images as shown in Fig. 2.10. Individual images are formed based on the amount of projected radiation absorbed by the patient's tissue. The resulting images are combined using a *reconstruction kernel* to produce a three dimensional volumetric image of the patient

[52,53]. The type of kernel used can be adjusted in order to highlight different anatomical structures. Manufacturers of CT scanners generally provide a *lung* kernel that is most suited for diagnosing pulmonary disease. In traditional bronchoscopy, clinicians interpret the resulting scan using orthogonal cross-sectional views of the reconstructed 3D volume as shown in Fig. 2.11 and then mentally construct the instrument location during the procedure.

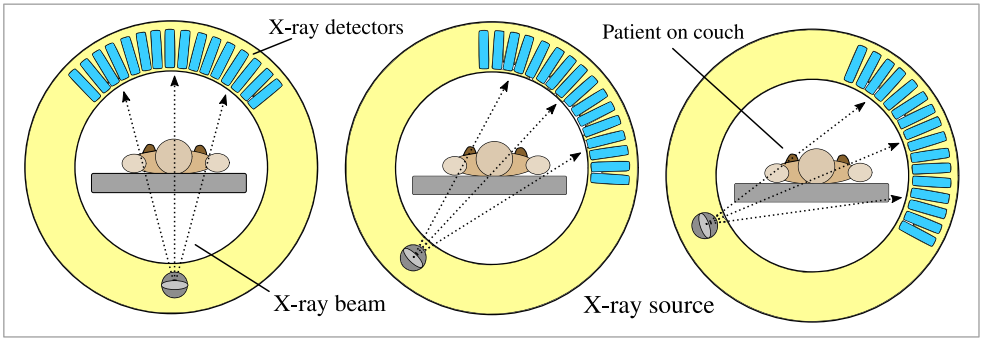


Figure 2.10: Operation of a computed tomography (CT) scanner [54]. Multiple X-ray images are acquired to create a three dimensional volume.

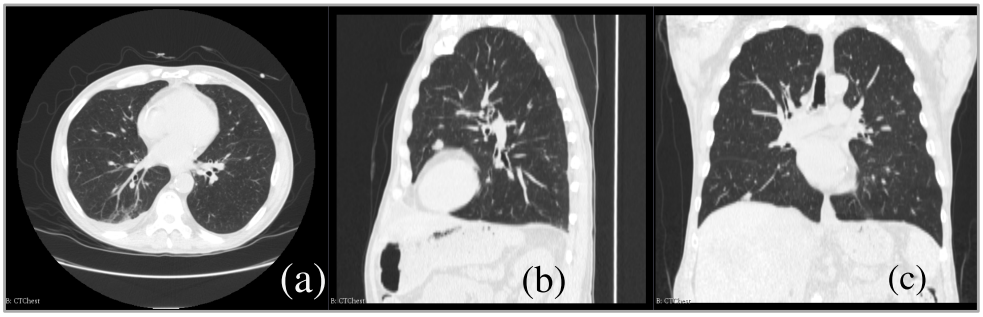


Figure 2.11: Chest CT image showing (a) axial, (b) sagittal and (c) coronal slices of the human chest cavity.

ENB procedures utilise the resulting CT imaging as source data for creating a 3D representation of the airway tree, in a process called *segmentation*. Segmentation refers to the detection and extraction of anatomical regions of interest from sets of 2D pixels or 3D voxels [56,57]. In ENB, the region of interest consists of the airway from which segmentation generates a *label map* of all voxels belonging to the airway. Classical segmentation implementations utilise a technique called *region-growing* where the

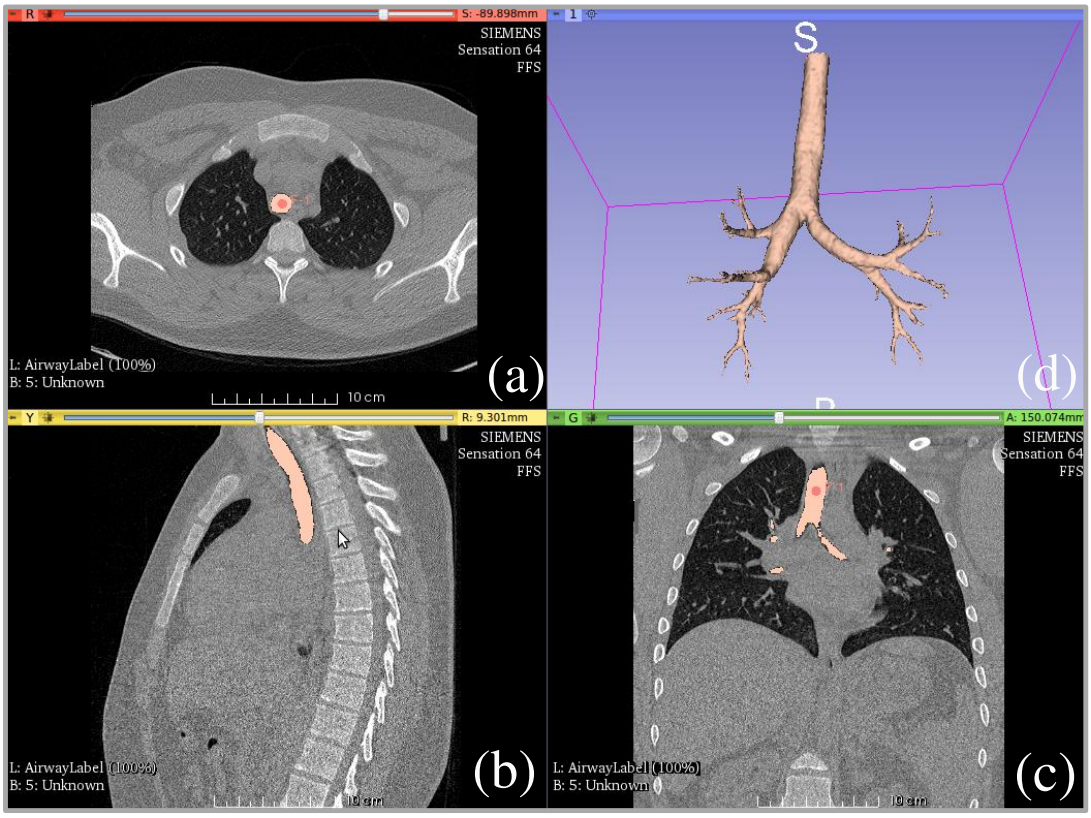


Figure 2.12: Chest CT image showing (a)-(c) slice views with segmentation overlay. (d) 3D visualisation of the airway segmentation showing the branching trachea and bronchial tree [55]. CT scan was acquired on a Somotom Sensation 64 scanner (Siemens Healthineers, Erlangen, Germany).

segmented airway grows from an initial seed point [58–60]. Recent work has shown that machine learning techniques can offer improved segmentation performance compared to classical approaches [61, 62]. Segmentation can provide an additional 3D airway model as shown in Fig. 2.12. The resulting airway model is used to provide the clinician with a global, 3D visualisation of the airway for the purposes of ENB.

2.6.2 Airway Mark-up

Once a 3D model of the airway is generated, the clinician must highlight regions of the airway for navigation. This is performed using the graphical user interface of the ENB software. After all regions of interest have been highlighted, the software generates a

virtual path to each target [63]. Highlighting these regions allows the ENB software to generate a visualisation of the path from the trachea main airway to the regions of interest as shown in Fig. 2.13.

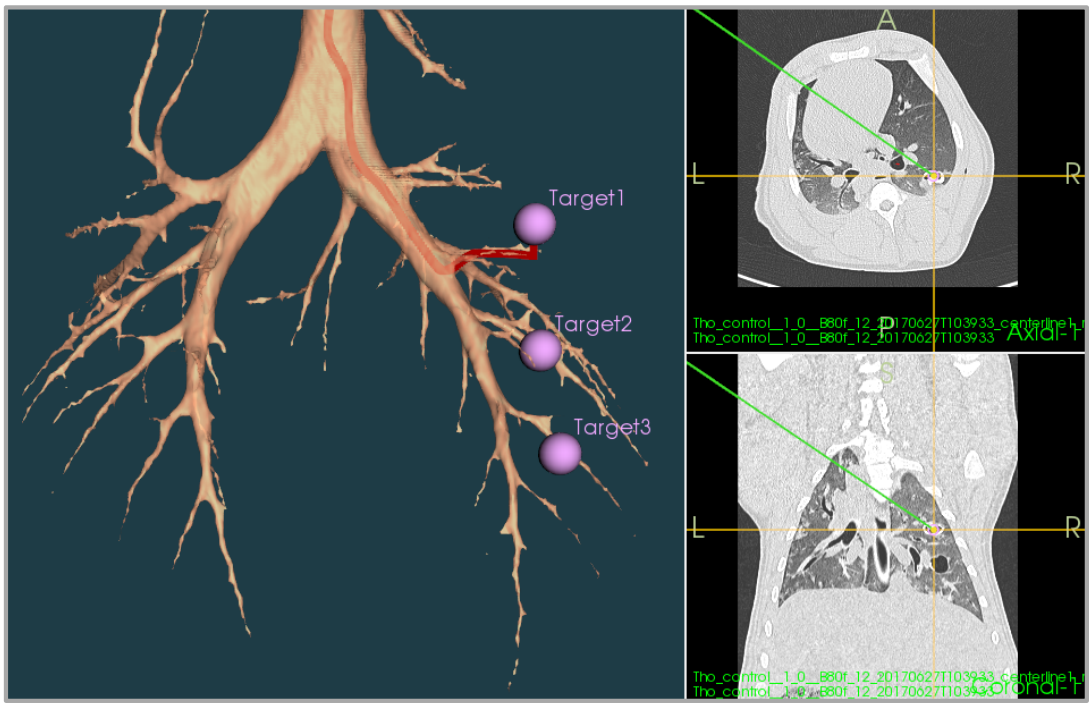


Figure 2.13: Screenshot showing three navigation targets highlighted in the 3D virtual model. The path to *Target1* (red) is generated by CustusX medical visualisation software [64, 65].

2.6.3 Airway Registration

Registration is the process of aligning two or more sets of data into a single coordinate system. Standard ENB procedures have two data source reference frames which require alignment in order to allow the clinician to navigate the airway using the virtual 3D model.

- *The patient frame*. The frame in which the patient rests during the ENB procedure. This frame is generally referenced to the origin of the electromagnetic tracking system being used.

- *The image frame*. The reference frame of the CT scanner from which the patient imaging was obtained. The resulting airway segmentation will be in this reference frame.

Coordinates obtained using an electromagnetic sensor within a patient's airway will not readily correspond to the 3D airway model unless a mathematical transformation of coordinates is performed. In the simplest case, the registration can be defined as a rigid transformation matrix, $\mathbf{T}_R$. Defining the electromagnetic system reference frame as the *patient* frame and the CT scan frame as the *image* frame, the mapping from the *patient* to the *image* can be expressed in (2.1)

$$\mathbf{p}_{image} = \mathbf{T}_R \mathbf{p}_{patient} \tag{2.1}$$

where $\mathbf{p}_{patient}$ and $\mathbf{p}_{image}$ are corresponding sets of positions recorded in both the *patient* and *image* frames. $\mathbf{T}_R$ is a homogeneous transformation matrix comprising of a rotation matrix and a translation vector given by (2.2), where $\mathbf{R}_R$ is an orthogonal rotation matrix with $\det(\mathbf{R}_R) = 1$ and $\boldsymbol{t_R}$ is a translation vector pointing from the origin of the *patient* frame to the origin of the *image* frame. Applying the resulting transformation to the electromagnetic tracking coordinates in the *patient* frame allows visualisation of an electromagnetically tracked instrument within the context of the patient's CT scan.

$$\mathbf{T}_R = \begin{bmatrix} \mathbf{R}_R & t_R \\ \mathbf{0} & 1 \end{bmatrix} \tag{2.2}$$

The most basic method of obtaining the $\mathbf{T}_R$ registration matrix uses the method of *landmarks* [66, 67], in which a number of predefined points in the 3D model are navigated and identified within the patient using an electromagnetic sensor. These landmarks are usually easily accessible via traditional bronchoscopy. The corresponding sensor coordinates are recorded at these landmarks and the mapping transform is calculated using a closed-form approach [68]. This landmark registration technique can be tedious and requires meticulous acquisition of landmarks, as any error in positioning directly affects the accuracy of the registration [69]. Registration techniques utilising *iterative-closest-point* (ICP) [70] provide an easier and more robust method of calculat-

ing the registration $\mathbf{T}_R$ by instead calculating the best-fit transformation between two sets of point-clouds in a least-squares sense [71]. Unlike landmark based techniques, ICP registration does not require the two sets of points clouds to be the same size. Time dependant registration techniques [72, 73] have also been developed which are capable of compensation for patient motion during interventions.

2.6.4 Airway Navigation

Once successful registration has been achieved then navigation can proceed. Initially the clinician uses a standard bronchoscope to enter and navigate the main airway. Once the bronchoscope reaches an airway that is too narrow, the clinician may proceed further to the target using ENB-enabled tools and instruments.

The use of ENB requires that the probes and instruments used are capable of sensing the magnetic field from the system field generator located either beside or beneath the patient (see Fig. 2.9(d)). Commercial systems have different methods of achieving sensing. The SuperDimension system use a dual-instrument approach by combining a pre-curved *Edge* sheath with a removable locatable electromagnetically tracked guide catheter inside, as shown in Fig 2.14. The sheath and guide are inserted through the instrument channel of the bronchoscope and used for airway navigation. Once a region of interest has been reached, the guide catheter is removed while the sheath is left in situ to act as an extended working channel allowing for the passage of biopsy instruments to the region of interest. No tracking takes place during the biopsy procedure.

Veran Medical's SPiN System uses integrated tracking sensors in all of their instruments as shown in Fig. 2.15. Tracking is not lost during the procedure, as the catheter, forceps, brushes and guidewires all contain their own independent tracking sensor. This *Always-On Tip Tracked* approach claims to reduce errors during biopsy when compared to the SuperDimension system [74]. The single-use design of the tracked instruments results in a high consumable costs for hospitals using the system.

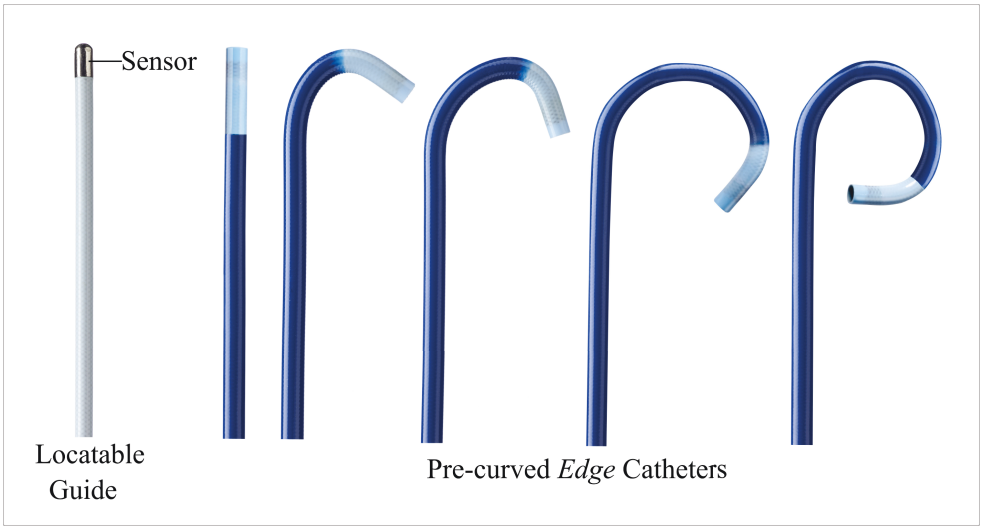


Figure 2.14: Medtronic SuperDimension catheters [75]. A range of tip curvatures achievable available between 0° and 190° enabling access to all lung lobes. The inner diameter of the catheters is 2.0mm and do not contain tracking sensors.

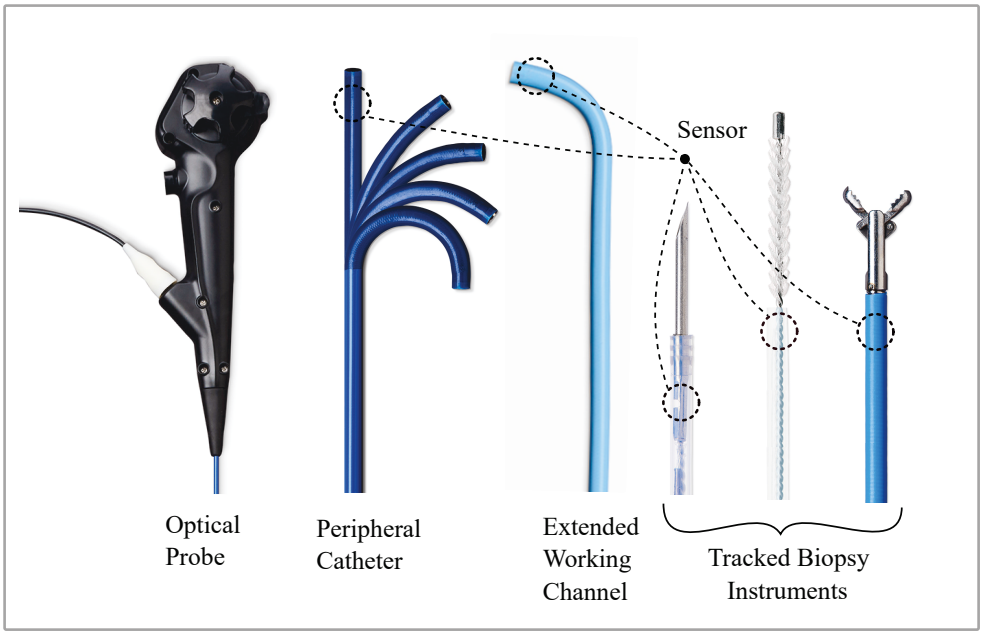


Figure 2.15: Tracked bronchoscopy instruments available for Veran Medical's SPiN System [76]. All tools contain embedded tracking sensors enabling consistent tracking throughout the bronchoscopy and biopsy procedure.

2.7 The Future of Bronchoscopy

Bronchoscopy is currently experiencing major clinical developments in imaging and therapy. The most prominent advancement is that of robotisation of the entire bronchoscopy procedure which has been shown to be effective at targeting peripheral lung lesions [77]. Development of a commercial robotic system is currently underway by the developers of the Monarch platform (Auris Health Inc., Redwood City, CA) and has been shown to be effective in preliminary studies [78, 79] following its recent FDA clearance and market approval.

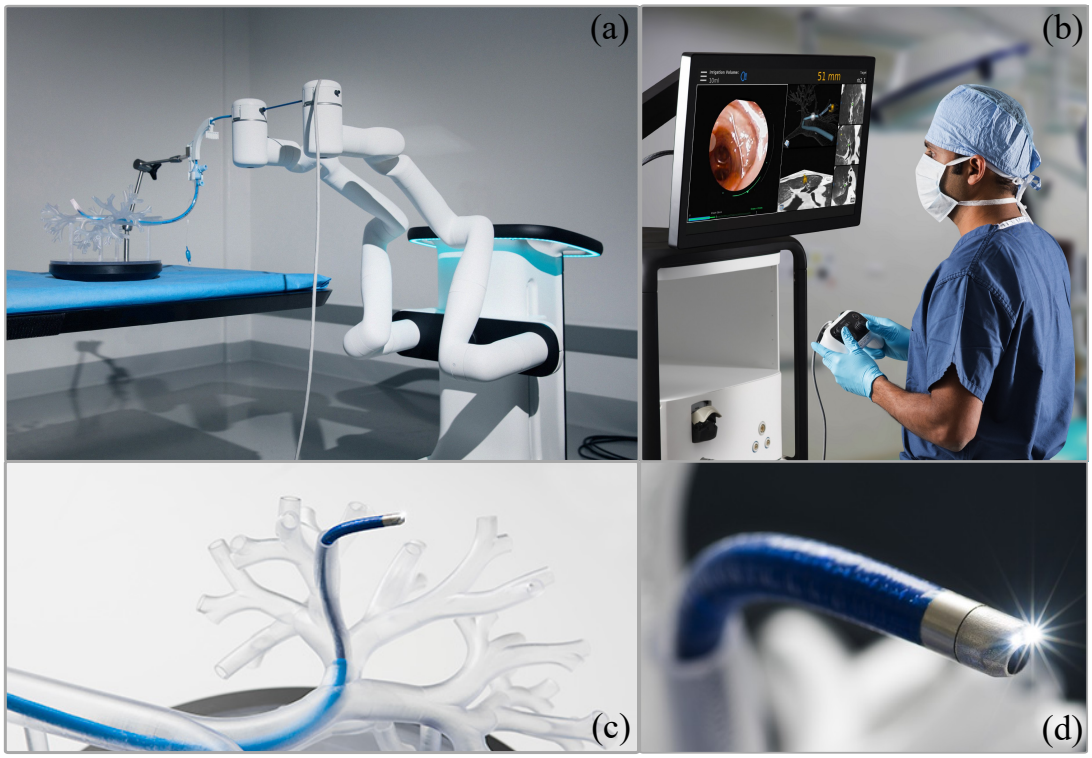


Figure 2.16: The Monarch robotic endoscopy platform (Auris Health Inc., Redwood City, CA) [18]. (a) Two robotic limbs guide and control an EMT enabled robotic endoscopic catheter. (b) The catheter is controlled by the clinician using a joypad and a head-up display (HUD). (c) The flexible catheter can conform to the shape of the airway and provide illumination and a working channel to the target site (d).

Innovations in the area of histological imaging are also taking place. Confocal laser endomicroscopy has been shown to provide histology of tissue changes within the

airways without the need for biopsy [22, 80]. Endocytology is another optical biopsy technique which uses a high magnification fixed focus objective lens for inspection of the respiratory tract at a cellular level, although the precise role of this technique has not been clearly defined [41].

2.8 The Future of ENB

Electromagnetic navigation in bronchoscopy is still a new field and the absolute effectiveness of the technique when compared to standard bronchoscopy approaches has not yet been conclusively shown in clinical practice [81]. While initial single-centre studies in an expert setting indicated that ENB could increase clinical yield for endobronchial biopsy in the outer airways by up to 88% when combined with radial EBUS probe (miniature ultrasound probe through the bronchoscope working channel) [82], these initial results were not replicable elsewhere [83], [84–87]. Currently, manufacturer-sponsored studies are seeking to address repeatability in a multi-centre study [88]. However, the combination of inconclusive clinical performance and high operating costs means that ENB currently remains limited to select centres. Technical drawbacks, primarily in the accuracy of current registration procedures also exist while ongoing efforts seek to compensate for lung deformation and patient movement during the procedure [89].

In the context of these current shortcomings, this thesis aims to create an open platform for the design and development of electromagnetic tracking systems suitable for bronchoscopy as well as other image guided interventions. Building on the group's prior work on bronchoscopy software [59] and electromagnetic tracking [90], this thesis aims to integrate both to provide an open framework for future research into image guided interventions, while also addressing some of the key shortcomings inherent in current electromagnetic tracking system designs.

Chapter 3

An Open Framework for EMT System Development

This chapter discusses the design and development of an open-source library for use with the Anser electromagnetic tracking system. The name of the system is inspired by the greylag goose *Anser anser*, which uses the earth's magnetic field for navigation during its annual migration. The framework was originally designed to overcome the limitations of using Anser on Matlab (The Mathworks, Natick, MA). In particular, this implementation [90, 92] used the proprietary Data Acquisition Toolbox which is only compatible with Windows at the time of writing. The framework discussed in this chapter uses free software and can be executed on all major OS platforms (including Apple MacOS and Linux) and aims to provide a template for future tracking system developers and users.

3.1 Introduction

The development of new image guided therapies relies heavily on intelligently combining data from multiple hardware sources. New techniques combining ultrasound and

This chapter is based on H. A. Jaeger, S. Hinds and P. Cantillon-Murphy, "An Open Framework Enabling Electromagnetic Tracking in Image-Guided Interventions", MICCAI 2018, LNCS 11073, pp. 168-175, Granada, Spain, 16-20 September 2018. [91].

electromagnetic tracking (EMT) [93, 94] are among techniques which combine multiple data sources to enhance the safety and accuracy of procedures. Progress in these areas is made possible by the standardised open protocols [95, 96] that govern how hardware and software should interact with one another. Fig. 3.1 shows the generalised design flow of many image guided interventions. Applications interact with hardware through vendor authored application programming interfaces (APIs) or interface toolkits such as the Public software library for Ultrasound (PLUS) [95] and Image-Guided Therapy Toolkit (IGSTK) [97]. Such toolkits provide standardised software interfaces through which applications and hardware can interact. From a software perspective, this standardised approach enables developers to prototype and apply their work in a manner that can be distributed and replicated. That said, these types of software development typically fall short of incorporating custom innovations in tracking hardware. The proprietary nature of medical tracking devices results in the developed libraries being tied to closed, vendor specific application programming interfaces.

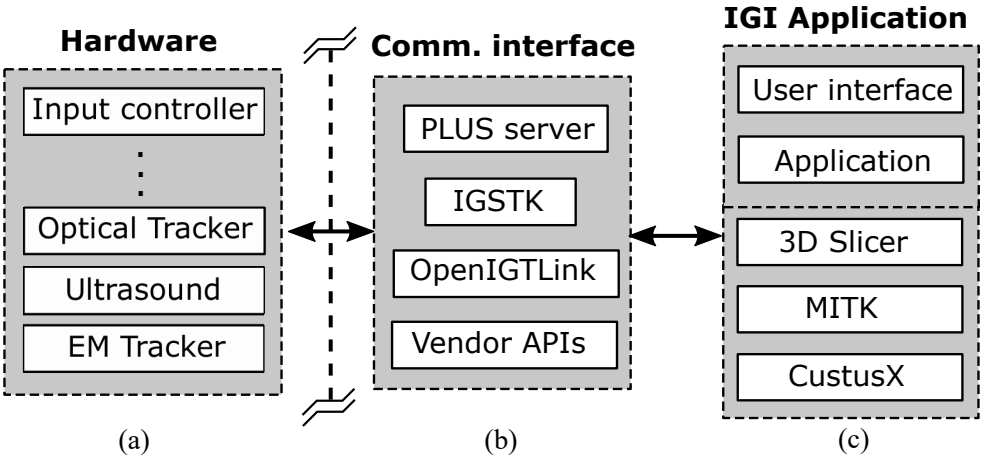


Figure 3.1: A standard approach for developing cross-platform IGI applications. (a) Proprietary hardware is interfaced using an API or open communications interface (b). (c) Guided therapy applications use this interface to ensure cross-platform compatibility.

Electromagnetic tracking systems in particular are very much considered 'black-boxes' when developing clinical applications and cannot be directly modified by the end-user or system integrator. This is understandable from a regulatory perspective as

any modifications to either hardware or software may necessitate re-validation by regulatory bodies for clinical approval. On the other hand, those researchers who focus on medical hardware development can find it difficult to interface their work as part of the clinical workflow, as no template exists which unites the fundamental device operation with the interfaces required by medical imaging software. An open-source hardware magnetic tracking system was proposed by the National Alliance for Medical Image Computing (NA-MIC) and details an overview of the design and implementation of a magnetic tracking system using tri-axial transmitter and receiver coils [98]. While the project provides a detailed overview of the design of the system architecture, it does not provide the necessary implementation details required for rapid construction of a system. Component specifications, circuit schematics and mathematical derivations are scattered over multiple websites and paper, and although references are made to relevant papers in the field [99], the resource may be insufficient for an engineer to build a bespoke tracking design. The time investment required may also be too large for engineers focussing on developing a clinical application. In order to accelerate and bridge the gap between novel tracking hardware and clinical applications, this chapter outlines a framework to encourage integration of new electromagnetic tracking hardware into the clinical setting. By modelling a tracking system in terms of its functional blocks and communication interfaces it is hoped that other researchers can accelerate integration of new EMT hardware into their own applications. The resulting framework was implemented in the Python programming language and applied to the open-source Anser EMT system [100] shown in Fig. 3.2. The corresponding reference hardware enabling rapid construction of the system is described in chapter 4.

3.2 Framework Design

Electromagnetic tracking systems are complex electronic systems that incorporate advanced analog circuit design, signal processing and numerical optimisation techniques. The specific topology of such systems will vary depending on the core design and manufacturer, but in general all EMT systems can be distinguished by four common processing steps outlined in Fig. 3.3: *acquisition*, *filtering*, *modelling*, and *solving*.

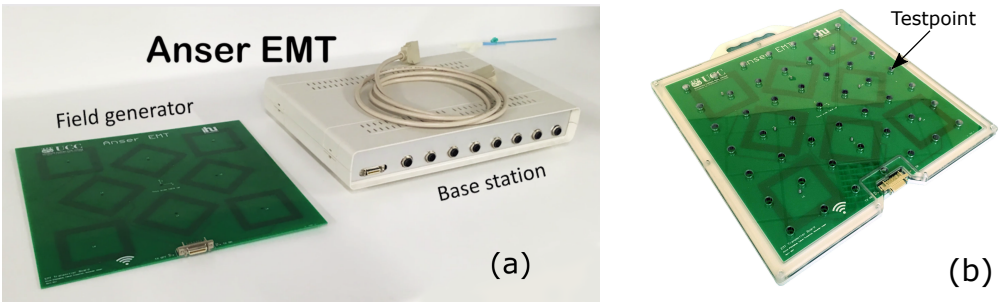


Figure 3.2: (a) The Anser EMT system v1.0. (b) Field generator enclosure with testpoint sockets.

Each of these processing steps can be treated as a discrete and independent stage in the tracking system software pipeline. The designed framework is structured according to these stages.

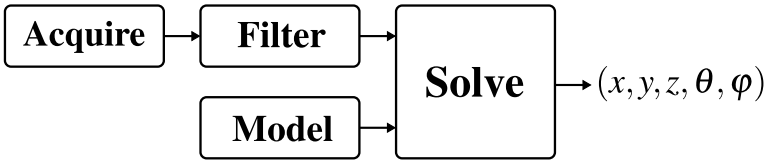


Figure 3.3: The basic components which comprise all electromagnetic tracking systems are shown. The 5 degree-of-freedom magnetic sensor coordinate $(x, y, z, \theta, \varphi)$ is the most basic case for a symmetrical sensor coil, where θ and φ correspond to yaw and pitch angles respectively.

3.3 Acquisition

The most fundamental step in any measurement system is data acquisition. It is the process by which physical signals are digitised into forms suitable for manipulation by a computer. In the case of EMT systems, the signals being measured are typically voltages induced on a tracking sensor. Such signals are induced on a tracking sensor coil when it is placed in the tracking volume of an EMT system. Acquisition hardware in the form of an analogue-to-digital converter (ADC) converts the electrical signal into a digital data stream by sampling at fixed periodic intervals as shown in Fig. 3.4 and 3.5. Manufacturers of analogue-to-digital converters which form the foundation

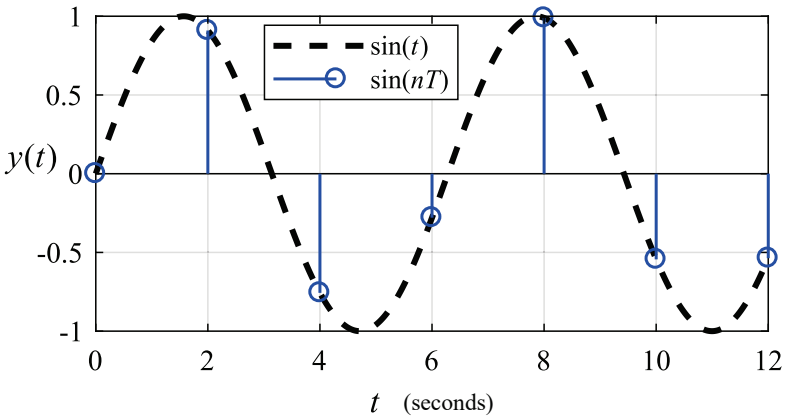


Figure 3.4: A single frequency continuous time signal $y = \sin(\omega t)$ where $\omega = 1\,\mathrm{rad\,s^{-1}}$ sampled with a sampling interval $T = 1\,\mathrm{s}$, where n is the sampling index. The points marked in blue are the acquired digital samples of the signal.

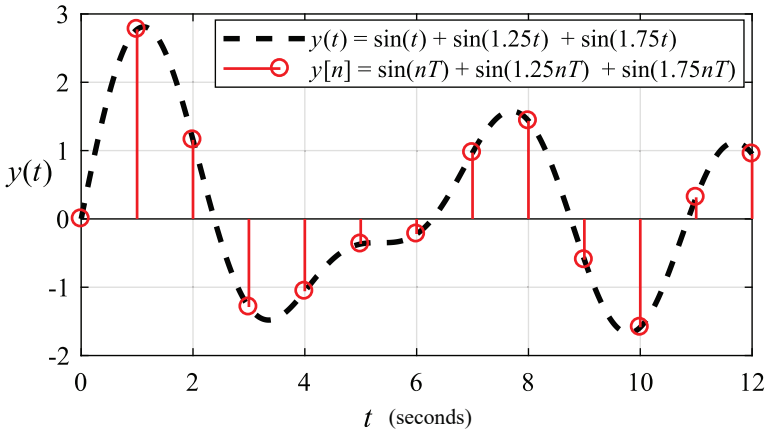


Figure 3.5: A continuous time signal $y(t)$ consisting of a sum of sinusoidal waveforms sampled at a rate of $F_s = 2\mathrm{Hz}$. The points marked in red are the digital samples of the signal. A tracking sensor's induced voltage signal may contain many more frequency components, depending on the type of field generator used.

of these acquisition systems include Analog Devices (*Norwood, MA, USA*), Texas Instruments (*Dallas, TX, USA*), and Microchip (*Chandler, AZ, USA*). The rate at which a continuous signal is sampled is known as the *sampling frequency* of the ADC and is commonly denoted as F_s. The sampling frequency is the inverse of the sampling

period, T_s, as indicated in (3.1).

$$F_s = \frac{1}{T_s} \tag{3.1}$$

Most ADCs feature configurable sampling rates which the user can adjust to meet the requirements of their application. Increasing Generally F_s is selected such that all signals of interest lie below $F_s/2$ (Shannon's sampling theorem). This is discussed in section 3.4.

Instrumentation hardware manufacturers such as National Instruments (NI) and Measurement Computing use ADCs to construct acquisition systems for industrial research and development. Systems such as the PXI (PCI eXtensions for Instrumentation) chassis and NI-USB platform, shown in Fig. 3.6, provide an all-in-one data acquisition solution that is controllable from the user's PC. The main advantage of using such acquisition systems is that the sampling hardware is abstracted from the user through software, allowing the user to focus purely on developing the application. This standardisation leads to further advantages in community and software support resulting in many researchers using these systems for the development of electromagnetic tracking systems [15, 16, 101–104]. In particular [15, 16] have demonstrated the use of PXI for interacting with field programmable gate arrays (FPGAs) in order to create customised coil excitation and sampling conditions. The USB acquisition system shown in Fig. 3.6b is used in the Anser EMT system [92, 100]. The main disadvantage of these systems is the cost of purchase, with systems starting at approximately 1000 USD which limits their use to research and development.

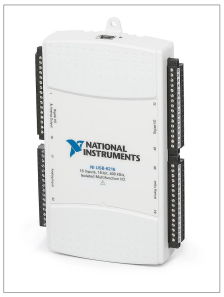
3.3.1 Acquisition in Anser EMT

The Anser EMT system uses an NI-USB 6212/6216 data acquisition system (DAQ) [105]. The plug-n-play functionality and wide software driver support make it very suitable for building and prototyping portable instrumentation. A summary of the DAQ features are outlined in Table 3.1.

Universal Serial Bus (USB) communication introduces latencies which prevent deterministic, real-time streaming of sample data from a device's internal ADC to the end-user application. This is a result of the multiple layers of software that run



(a)



(b)

Figure 3.6: (a)A NI PXI system. The chassis can house a number of modular expansion cards for signal generation, acquisition and protocol decoding. Different options of chassis are available depending on desired features and the maximum bandwidth requirements. (b) An NI-USB data acquisition system. The device is portable and powered directly from the host computer's power rail. Maximum data bandwidth is limited by the USB 2.0 bus.

Table 3.1: NI-USB 6212/6216 specifications [105]

Specification	*Value*
Analog Inputs	16
ADC resolution	16-bits
Max. Sampling Freq.	400 kHz
Digital I/Os	32
Driver support	Windows, MacOS, Linux

concurrently on the host computer system. Any real-time USB acquisition system will suffer if the demanded update latency is below a few milliseconds [106]. One therefore cannot rely on software-timed events on the host computer to schedule ADC acquisitions, where the effective sampling rate can be in the orders of MHz. The NI-USB DAQ overcomes this problem by implementing a buffered topology, as shown in Fig. 3.7. The ADC samples are acquired at a fixed sampling rate and are stored on the DAQ's internal first-in-first-out (FIFO) buffer. Storing samples in this manner ensures deterministic behaviour and uniform spacing between data samples. The Bus negotiates with the host PC's driver to transfer each *frame* of FIFO data in bulk to main memory. The user application may then access and process the sample data. The size of the FIFO buffer and sampling rate of the ADC are configurable from the PC

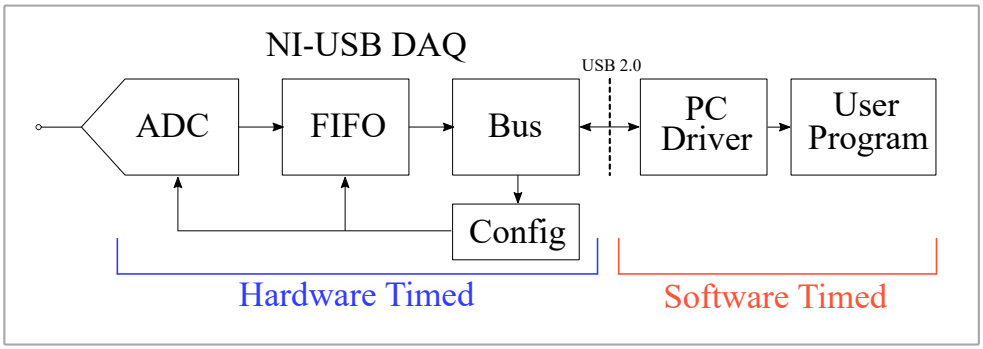


Figure 3.7: Simplified illustration of the data pipeline inside NI-USB 621X acquisition systems. The hardware timed components of the DAQ operate independently of host computer software.

Driver. Acquiring data in this manner has some very important repercussions from the perspective of the Anser tracking system:

- The FIFO frame must be full before the frame is transferred to the host PC. This introduces a finite length of time required to fill the FIFO frame with ADC data. The length of the delay is proportional to the length of the configured FIFO frame length L and inversely proportional to the ADC sampling frequency F_s. Ignoring USB data transfer times which are in the order of microseconds, the acquisition delay $T_{ad} = T_s N$, where T_s is the ADC sampling period.

- All FIFO data samples are available simultaneously. This allows efficient applications of many filtering and spectral analysis techniques such as the discrete Fourier transform (DFT) and fast Fourier transform (FFT).

Anser EMT provides the user with the option to adjust the FIFO size. The amount of latency can therefore be controlled to suit the end-user application. Section 3.4 will discuss how the size of this FIFO impacts the overall system performance.

3.4 Filtering

Filtering is the process of conditioning and extracting useful information from a signal. A typical EM tracking algorithm uses the frequency content of the induced voltage

signal to resolve the position and orientation of the sensor. Assuming that the original signal is band-limited (i.e. has a finite bandwidth of BWHz), then the frequency content of the sampled signal can be perfectly represented in its sampled form. In order to ensure a continuous signal is sampled correctly, the Nyquist-Shannon sampling theorem [107] must be obeyed: "*If a function y(t) contains no frequencies higher than BW hertz, it is completely determined by giving its ordinates at a series of points spaced 1/(2BW) seconds apart*"

In equation form (3.2):

$$F_s > 2BW \tag{3.2}$$

In other words, the sampling frequency, F_s, of the data acquisition must be greater than twice the bandwidth of the signal being analysed. Tracking system field generators typically transmit their magnetic signals over a range of frequencies, with each transmitter coil on the system field generator producing a magnetic field at a single frequency. For example, the Anser tracking system is capable of transmitting eight distinct frequencies between 10kHz and 50kHz on its eight coil field generator. In general, the frequency ranges of AC-field based EM tracking systems span from 1kHz [104] all the way to 400kHz [108]. Therefore the minimum sampling rate of the system is determined by the highest possible frequency of interest, which in this case is 50kHz. If (3.2) is not obeyed, then any signal components with frequencies higher than $F_s/2$ will be aliased and appear as a lower frequency in the resulting digital frequency spectrum. That said, aliasing can be utilised effectively when using low-cost ADC devices [109], although noise performance and overall system sensor position update rates can suffer.

The correctly sampled sensor signal contains all the necessary information required to resolve the sensor's position and orientation in space. Since EMT systems operate at multiple frequencies, the sampled sensor signal will be a superposition of the individual frequency components generated by each transmitting coil as illustrated in Fig. 3.5. The filtering stage extracts the relevant signal content. Fourier transform methods such as the discrete Fourier transforms (DFT) and the optimised fast Fourier transform (FFT) are common methods for extracting frequency components from a sampled

signal. The discrete Fourier transform (DFT) of a sampled signal is given by (3.3).

$$\mathscr{F}\{x[n]\} = \sum_{n=0}^{N_{ft}-1} x[n] e^{-\frac{2\pi j}{N_{ft}} kn} \tag{3.3}$$

where N_{ft} is the total number of samples in the DFT calculation, $x[n]$ is the value of the n^{th} sample of the acquisition, $e^{2\pi j}$ is a complex exponential and k is the frequency index. Anser EMT applies the summation of (3.3) in the form of a DFT matrix [110] due to all acquisition samples being available simultaneously. For a discrete time signal containing $N_{ft} = L$ samples from the data acquisition buffer (see section 3.3.1), the DFT matrix, E, can be written in (3.4) as

$$\mathbf{E} = \frac{1}{L} \begin{bmatrix} 1 & 1 & 1 & 1 & \dots & 1 \\ 1 & \omega & \omega^2 & \omega^3 & \dots & \omega^{N-1} \\ 1 & \omega^2 & \omega^4 & \omega^6 & \dots & \omega^{2(N-1)} \\ 1 & \omega^3 & \omega^6 & \omega^9 & \dots & \omega^{3(N-1)} \\ 1 & \vdots & \vdots & \vdots & \ddots & \vdots \\ 1 & \omega^{L-1} & \omega^{2(L-1)} & \omega^{4(L-1)} & \dots & \omega^{(L-1)(L-1)} \end{bmatrix} \tag{3.4}$$

where $\omega = e^{-2\pi j/L}$ and $j^2 = -1$. The vector of complex frequency magnitudes, $\mathbf{Y}$, is then extracted by post-multiplying $\mathbf{E}$ by the vector of sample data, $\mathbf{X}$, of length L, as the matrix product indicated by (3.5).

$$\mathbf{Y} = 2(\mathbf{EX}) \tag{3.5}$$

where the factor of 2 is required to recover the original signal amplitude of the frequency component. This is due to the two-sided nature of the Fourier Transform [112]. An illustration of this multiplication is shown in Fig. 3.8. In effect, $\mathbf{E}$ in (3.4) can be interpreted as a bank of DFT filters. In order to reduce spectral leakage due to discontinuities in the acquisition dataframe, a windowing function may be applied. In this case, (3.5) is changed to incorporate the coefficients of a windowing function, $\mathbf{W}$, in (3.6).

$$\mathbf{Y} = 2 \cdot \mathbf{E}(\mathbf{X} \cdot \mathbf{W}) \tag{3.6}$$

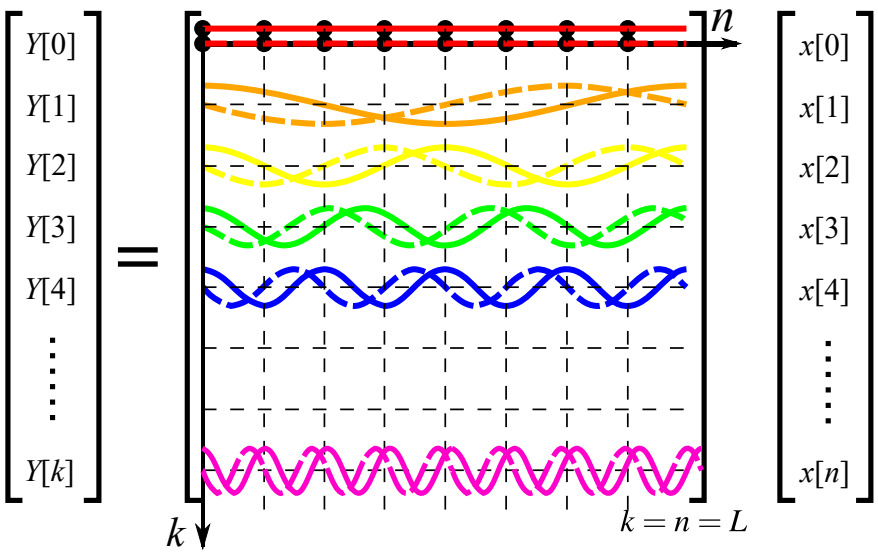


Figure 3.8: Illustration of the DFT matrix multiplication procedure [111]. Each row of the DFT matrix can be visualised as a complex exponential waveforms. Each reference waveform is multiplied by the acquired sample data to yield a vector of complex frequency magnitudes. The resulting values of Y represent the strength of each of the k frequency components.

where '$\cdot$' indicates the vector dot product. The absolute magnitude of a the resulting frequency components can recovered by taking the absolute value of each complex entry as shown in (3.7)

$$|\mathbf{Y}| = \sqrt{\mathbf{Y} \cdot \mathbf{Y}^*} \tag{3.7}$$

where $\mathbf{Y}^*$ is the element-wise complex conjugate of $\mathbf{Y}$.

3.4.1 Sampling parameters

The two main parameters governing the calculation of the DFT are acquisition frame size L and the acquisition sampling frequency F_s. The frequency resolution in Hz of the DFT result (also known as *bin width*), w, is given by (3.8)

$$w = \frac{F_s}{L} \qquad \text{(Hz)} \tag{3.8}$$

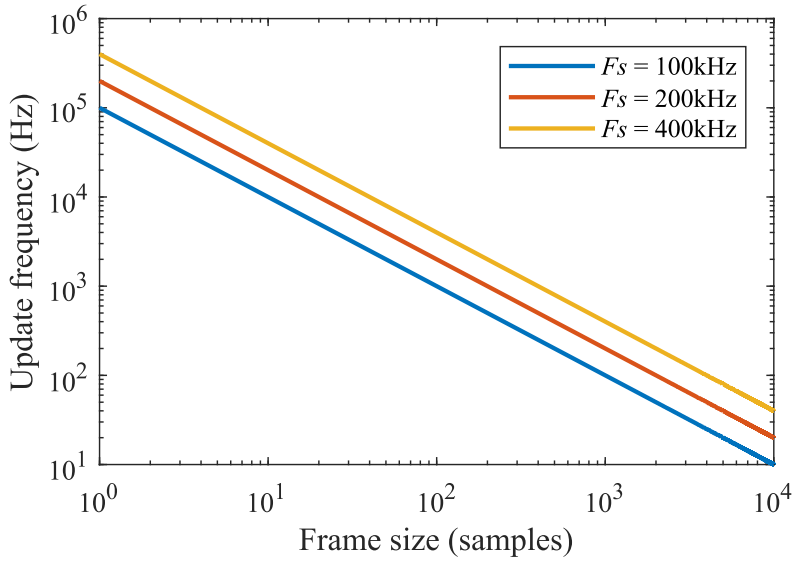


Figure 3.9: Acquisition frame update rate as a function of the number of samples acquired per frame for different sampling frequencies F_s. The relationship is log-linear.

For example, taking an F_s of 100kHz and frame length L of 5000 results in a bin width of 20Hz. For a fixed L, increasing F_s has the effect of increasing the maximum sampling bandwidth, but also increases w thereby reducing the resolution of the DFT result. Fixing F_s while increasing L increases the frequency resolution but increases the overall acquisition latency, T_L, in (3.9). This latency governs the overall DFT update rate, which in turn governs the overall tracking system position update rate, F_{system}, in (3.10).

$$T_L = F_s L \tag{3.9}$$

$$F_{system} = \frac{1}{T_L} \tag{3.10}$$

3.4.2 Spectral leakage

The DFT assumes that the sampled acquisition frame is periodic in nature. Spectral leakage is an artefact caused by sampling in the DFT process and occurs when an integer number of periods of a frequency component of a continuous-time signal do

not fit inside the acquisition frame [113]. Consider a continuous sinusoidal waveform of frequency $F_{in} = 5\,\text{kHz}$ sampled at a frequency of $F_s = 100\,\text{kHz}$ that oscillates for three periods as shown in Fig 3.10. Both the discrete time Fourier transform (DTFT) and discrete Fourier transforms of the signal are shown. The figure shows that precisely $N_{ft} = 20$ samples represent each period of the input waveform. In order words, precisely $1/20^{\text{th}}$ of the input waveform is represented by each digital sample. This is known as the normalised sampling frequency given by (3.11).

$$f_n = \frac{F_{in}}{F_s} \tag{3.11}$$

After performing the DFT on 20 samples of the waveform, the resultant frequency bins indicate an amplitude of 1 V at the 5 kHz frequency bin. The remaining bins show an amplitude of 0 V (-300 dB). This shows that the sampled 5 kHz waveform is perfectly represented by $N_{ft} = 20$ samples. Now consider what happens when input frequency

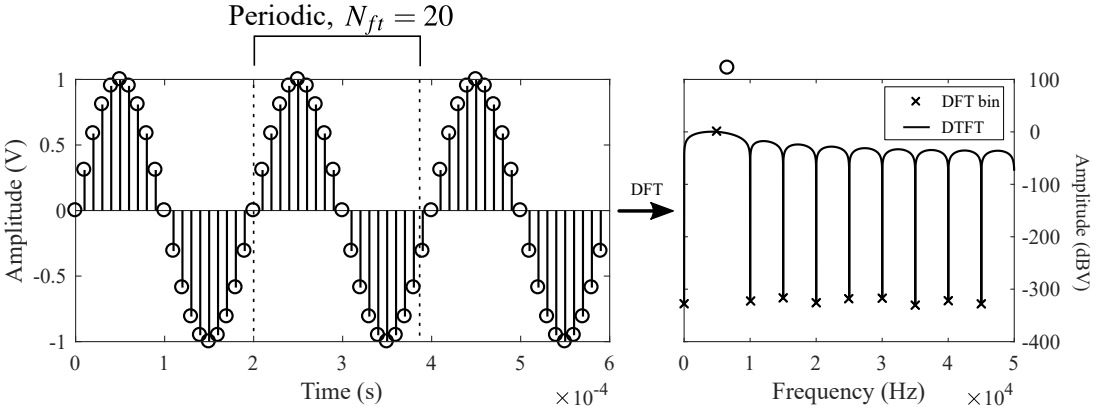


Figure 3.10: A 7 kHz sampled at 100 kHz. The resulting DFT and DTFT are shown for an $N_{ft} = 20$ sample acquisition frame. The DTFT is achieved by zero-padding the sample data before performing the DFT.

is changed such that $F_{in} = 7\,\text{kHz}$. The sampled waveform is no longer periodic. Taking the same DFT with $N_{ft} = 20$ samples results in spectral leakage as shown in Fig. 3.11. Instead of remaining in a single frequency bin, signal energy is now smeared across

The discrete time Fourier Transform (DTFT) is the continuous frequency spectrum of a discrete time signal. The discrete Fourier transform (DFT) is the sampled spectrum of the DTFT whose frequency resolution depends on the acquisition length, L, and sampling frequency, F_s, as shown in (3.8).

all bins of the DFT. Even though a 5 kHz input signal is not present, the bin reports an amplitude of 0.83 V. Taking the DTFT value at 7 kHz results in an incorrect apparent signal amplitude of 1.035 V. Clearly a 7 kHz can not be represented accurately using $N_{ft} = 20$ samples. The effects of spectral leakage therefore must be considered when

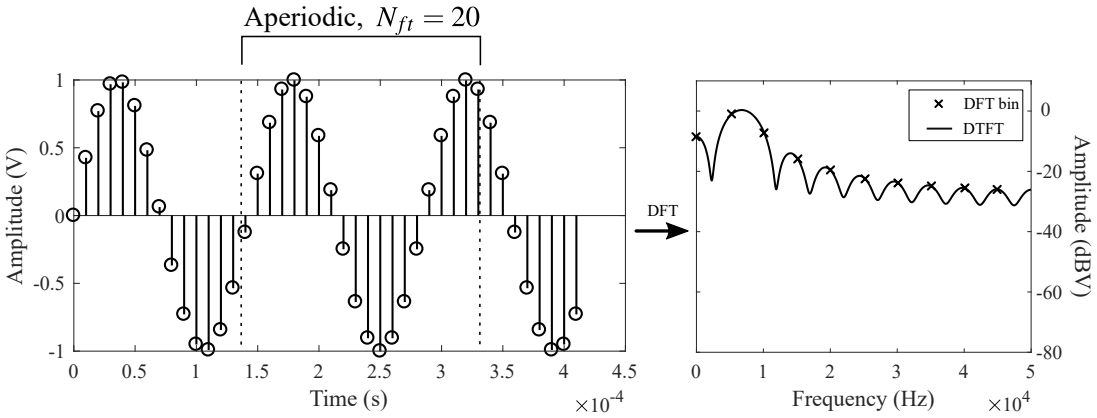


Figure 3.11: A 7 kHz sampled at 100 kHz. The resulting DFT and DTFT are shown for $N = 20$ samples. The DTFT is achieved by zero-padding the sample data FFT.

designing an EMT system. Neglecting these effects can lead to errors and incorrect measurements. Two methods can be used to ensure reliable data acquisition: They are coherent sampling and windowing.

3.4.3 Coherent sampling

Coherent sampling is a design constraint applied to acquisition systems to ensure frequency components of interest can be accurately measured using the DFT. The constraint forces periodicity of the signal of interest in the acquired acquisition frame. Coherent sampling can be implemented using (3.12)

$$f_n = \frac{J}{L} \tag{3.12}$$

where f_n is the normalised sampling frequency given by Eq. (3.11), J is an integer number of periods of the input waveform per acquisition frame and L is the size of the data acquisition frame in samples. Assuming a fixed normalised frequency f_n one must select a value of L to ensure J is an integer. Optimised coherence can be achieved

if L and J are even and odd integers respectively. Best coherence can be achieved if J is a prime number. Selecting N_{ft} and J in this manner prevents harmonics of F_{in} from appearing on the same frequency bin as F_{in}, which would result in harmonic distortion [114].

Returning to the case of Fig 3.10 and applying (3.12), an $f_n = 1/20$ and $N = 20$ produces $J = 1$, i.e., the continuous signal experiences exactly 1 period over the acquisition window, which by definition results in coherent sampling by default. The 2nd case of Fig 3.11 results in incoherent sampling unless $N = 100$ samples are acquired, resulting in $J = 3$ for sampling to be coherent. Three times as many samples are needed in order to calculate an accurate DFT for the 2nd case. In the context of EMT, an increased sample count can result in lower position update rates according to (3.10). The frequencies of the field generator must be carefully chosen to avoid incoherence as a result.

Anser EMT uses eight transmitter frequencies from 20 to 34 kHz separated by a spacing ΔF of 2 kHz. Utilising a sampling frequency F_s of 100 kHz results in a theoretical minimum frame size of $L_{min} = 50$ which obeys the coherence relation of (3.12) whilst also obeying satisfying the frequency resolution requirement of (3.8) ($w = \Delta F = 2000$ Hz). This results in coherent sampling of all transmitter frequencies used in the field generator. In practice an acquisition frame size of $N = 250$ samples is required to achieve good performance. The transmitter frequencies are shown in Table 3.2 alongside the J cycles of each component acquired during a single frame. The effect of the size of L is demonstrated in Fig. 3.12. Smearing of the voltage peaks is observed for $L = 50$. The effect is less pronounced for $L = 250$ samples as the peaks can be easily distinguished, although leakage still clearly exists in the DFT bins when compared to the DFT bins of Fig 3.10.

The spectral leakage evident in Fig. 3.12 is due to imperfect sampling hardware: Achieving perfect coherent sampling in practice is difficult due to frequency mismatch between the ADC and waveform generator. This can be remedied by synchronising both systems with a common clock signal [115]. Spectral leakage can be totally avoided in this case, and is the standard practice when evaluating the noise performance and precision of analogue-to-digital converters. This method of achieving coherent

Coil No.	F_{in} *(kHz)*	f_n *(cycles/sample)*	*J [L=250] (cycles)*	*J [L_{min}=50] (cycles)*
1	20	0.20	50	10
2	22	0.22	55	11
3	24	0.24	60	12
4	26	0.26	65	13
5	28	0.28	70	14
6	30	0.30	75	15
7	32	0.32	80	16
8	34	0.34	85	17

Table 3.2: Transmitter frequencies used in Anser EMT and their corresponding properties when in discretised form.

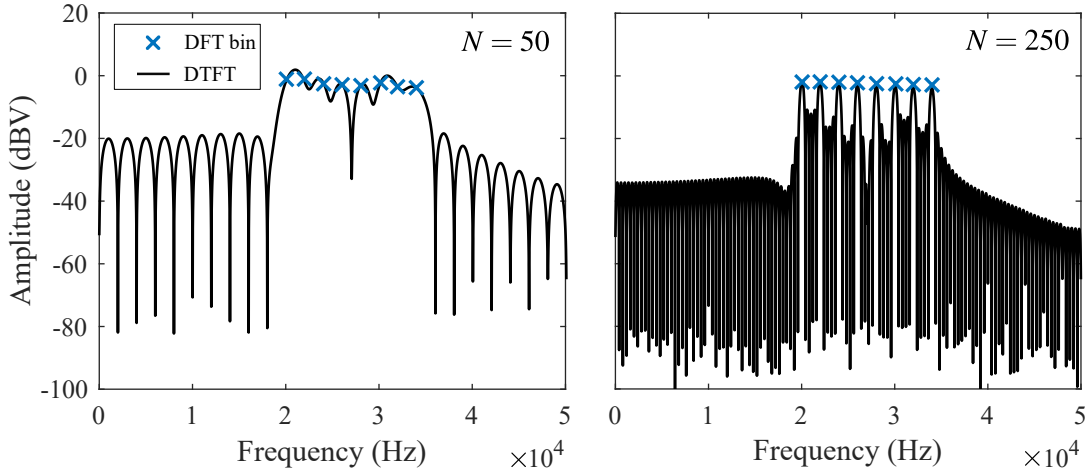


Figure 3.12: DTFT of the sampled current sense waveform of the field generator using $N = 50$ and $N = 250$. The DFT bins of frequencies of interest are highlighted. Even though the coherent sampling criterion are met in both cases, the DFT experiences spectral leakage throughout the spectrum.

sampling is not currently supported by Anser EMT as the data acquisition unit (DAQ) and waveform generator rely on separate clock signals. The performance is as close to coherent as possible with the current hardware configuration. Window sampling techniques can employed to improve the performance and further reduce leakage.

3.4.4 Window sampling

Sampling windows can be used to shape the frequency spectrum of a sampled signal by attenuating the beginning and end of an acquisition frame. This is achieved by multiplying an acquisition frame by a windowing function $w[n]$ [112, 113]. A finite data acquisition frame corresponds to multiplying by a rectangular window. The effect of windowing is shown in Fig 3.13. The act of multiplying $x[n]$ and $w[n]$ together is equivalent to convolving their frequency spectra, given by (3.13):

$$x[n] \times w[n] \equiv X[f] * W[f] \tag{3.13}$$

where f is the continuous normalised frequency variable.

Selecting an appropriate window

Selecting an appropriate sampling window depends on the demands of the application. It can be seen from Fig. 3.13 that windowing affects the frequency spectrum by decreasing the leakage at frequencies distant from the fundamental frequency of 7 kHz but at the cost of increasing the local spectral leakage close to the fundamental component. The degree of this shaping is determined by the window type. The degree of local leakage is captured by the width and height of the *main lobe*. The degree of distal attenuation is captured by the maximum height of a *side lobe*. A table of window functions and their attenuation characteristics is shown in Table 3.3. If a signal has strong unwanted components distant from the frequency of interest then a high roll-off (e.g. Hanning window) is desirable. On the other hand, if the interfering signals lie close to the frequency of interest, then a window with a small maximum side lobe level (e.g. flat-top window) should be used, although noise rejection can suffer in this case [116]. A waveform with adjacent frequency components of interest is best analysed with no window (i.e. rectangular). If only one frequency component is of interest then noise can be further minimised using a high-dynamic-range window such as the Blackman window [117, 118].

Window type	*-3dB Main Width*	*-6dB Main Width*	*Max Side Width*	*Roll off*
None (Rectangular)	0.89 bins	1.21 bins	-13.2	20 dB/decade
Hamming	1.3 bins	1.81 bins	-41.9 bins	20 dB/decade
Hanning	1.44 bins	2 bins	-31.6 bins	60 dB/decade
Blackman	1.68 bins	2.35 bins	-58 bins	60 dB/decade

Table 3.3: Comparison of different windowing functions [118]. Widths are normalised with respect to the number of bins of the DFT. Larger side lobe attenuation results in increased lobe width.

Window selection in Anser EMT

In its default configuration Anser EMT utilises eight frequencies between 20 and 34 kHz uniformly spaced $\Delta F = 2$ kHz apart. Careful consideration must be taken when selecting the windowing function since there exist eight fundamental frequencies of interest in proximity to one another. On the application of a windowing function, each fundamental will create its own main lobe. Ideally these main lobes should not intersect one another in order to avoid harmonic distortion in measurements. One can design a window to ensure adjacent main lobes do not intersect one another as shown in Fig 3.14. The window of choice is primarily dictated by the size of ΔF, the spacing between adjacent transmitter frequencies. If we constrain the main lobe width ΔF_{ML} to not exceed half the spacing $\Delta F/2$, then the main lobes will never intersect. For example. given a fixed acquisition frame size of $N = 250$, a Blackman windowing function has a main lobe width of approximately 1160 Hz, while a Hamming window has a width of 780 Hz. The resulting frequency spectrum of the field generator signal using Blackman, Hamming and rectangular windows is shown in Fig. 3.15.

$$\Delta F_{ML} < \frac{\Delta F}{2} \tag{3.14}$$

Anser EMT provides a user-adjustable windowing scheme. Anser EMT utilises a Hamming window in its default configuration, and in most use cases the window type does not require adjusting. The type and size of the applied window function should be considered only when selecting different transmitter frequencies and frequency separations ΔF.

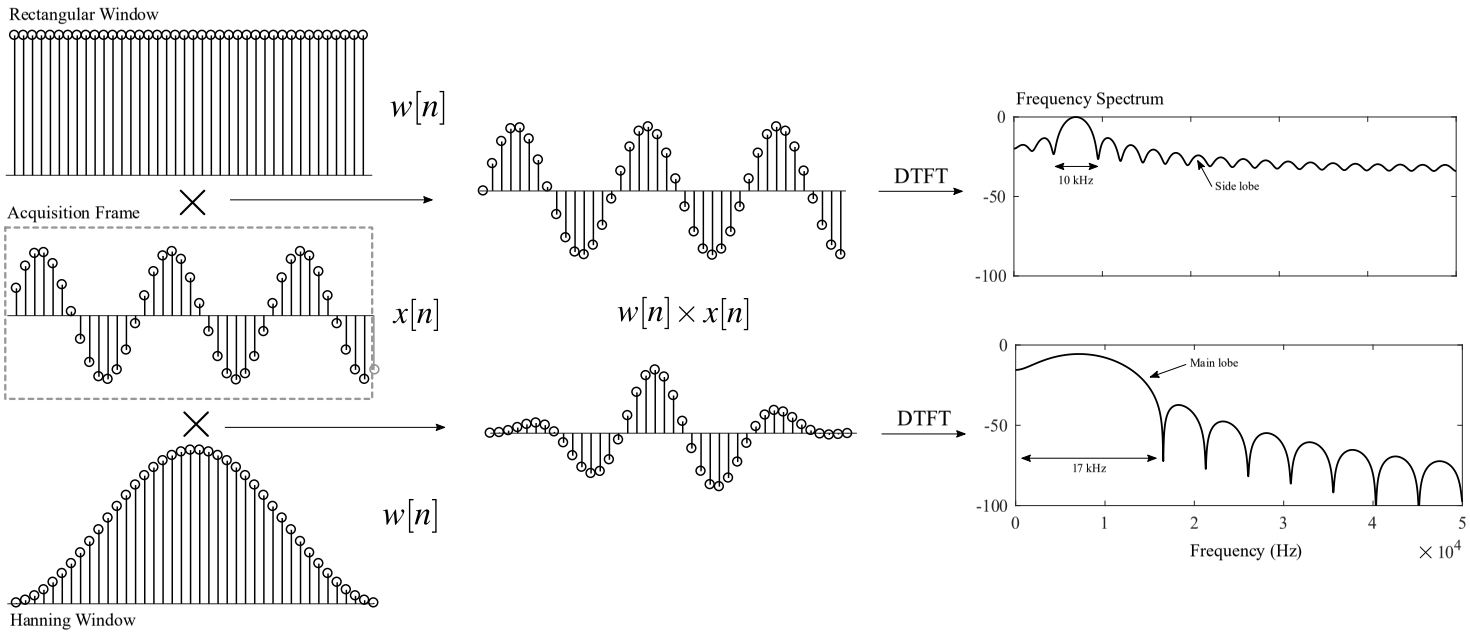


Figure 3.13: The process of applying a window function $w[n]$ to an incoherent acquisition frame $x[n]$ consisting of a 7 kHz fundamental signal sampled at 100 kHz previously shown in Fig 3.11. $L = 40$ samples are used in this case. The effect of the Hanning window is seen after multiplication where the beginning and end of the acquisition frame are tapered off. The resulting frequency spectra show significantly improved side lobe attenuation far from the fundamental with up to -70dB of attenuation at 70kHz, although the width of the main lobe increases from 10 kHz to 17 kHz.

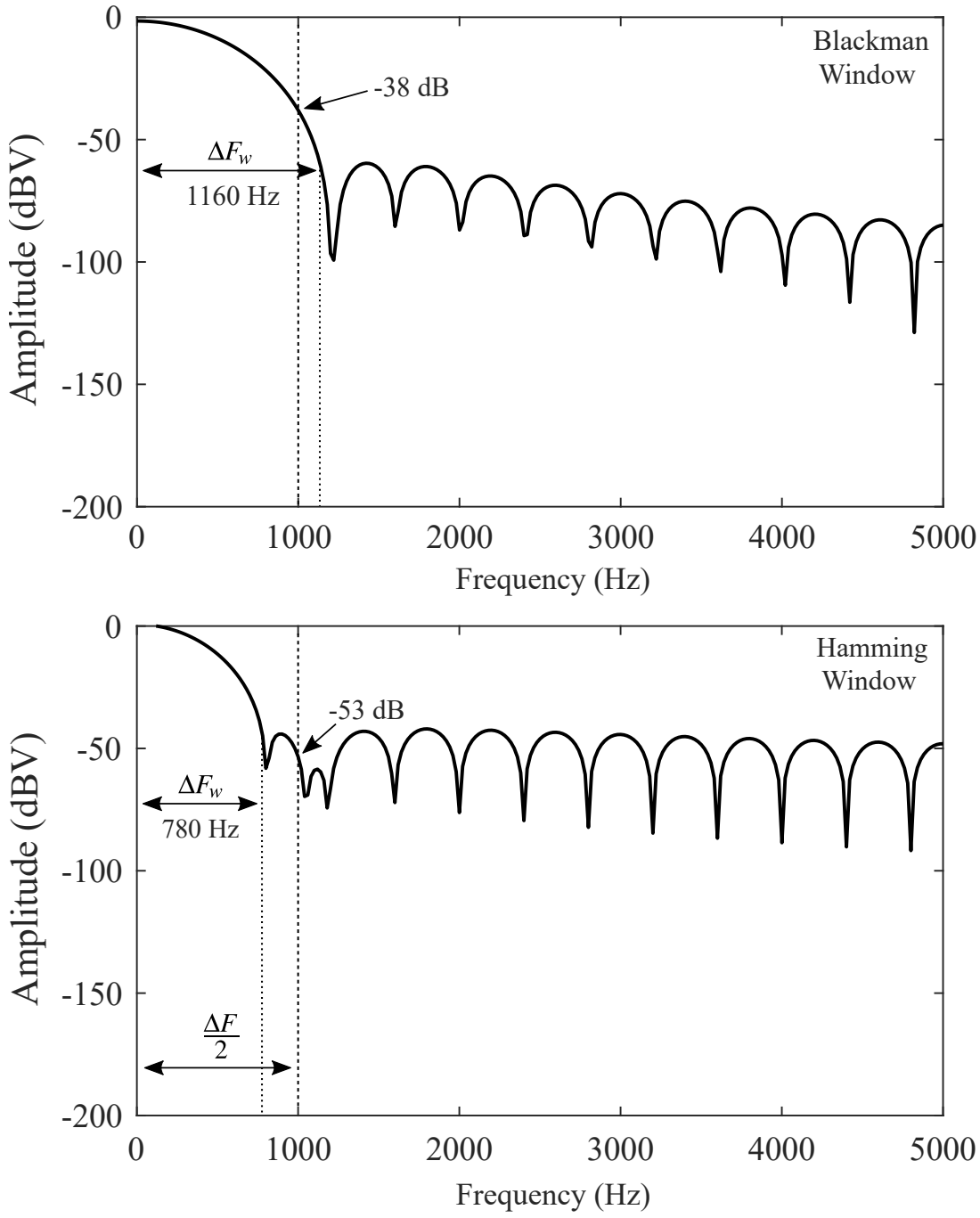


Figure 3.14: The effect of using Hamming and Blackman windows on an $L = 250$ sample acquisition frame. The application of a Blackman window significantly improves the SNR of the system at the cost of increased mainlobe width. Gain is in units of decibels (dB) with respect to 1V (dBV).

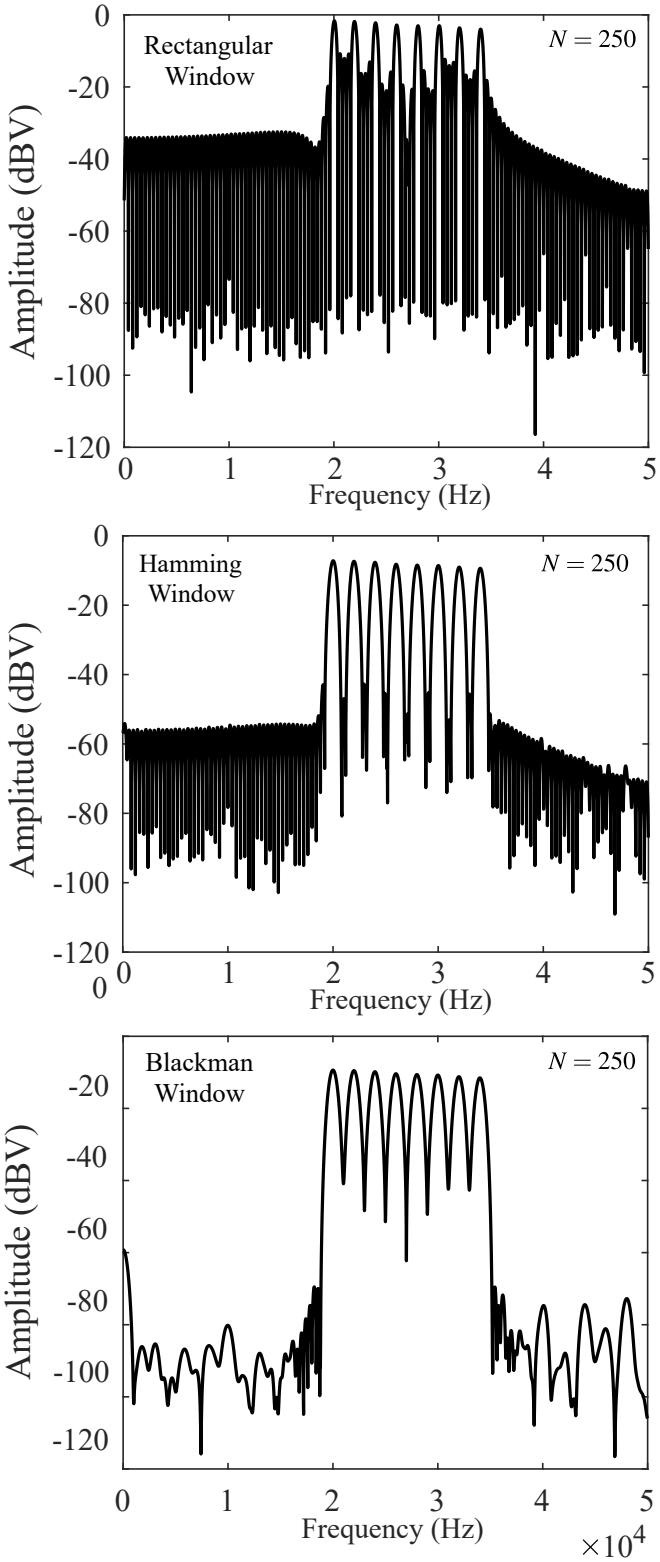


Figure 3.15: Frequency spectrum of the sampled current signal for rectangular, Hamming and Blackman window functions with $L = 250$ samples. Gain is in units of decibels (dB) with respect to 1V (dBV).

3.5 Model

An accurate mathematical model of the tracking system's generated magnetic field is a necessary component in all EMT system designs. Models are typically defined as analytical expressions which define the spatial distribution of magnetic fields in the volume around the tracking system field generator. Solving for the position and orientation of a tracking sensor generally involves fitting acquired sensor data to a magnetic field model. The type of model used in tracking systems depends on the design of coils that comprise the field generator.

3.5.1 Dipole approximation model

By far the most popular EMT model design is the dipole approximation model [119], in which the magnetic flux density $\boldsymbol{B}$ from a solenoidal coil (in Tesla) can be approximated using (3.15).

$$\boldsymbol{B}(\boldsymbol{r}) = \frac{\mu_0}{4\pi}\left(\frac{3\boldsymbol{r}(\boldsymbol{m}\cdot\boldsymbol{r})}{||\boldsymbol{r}||^5} - \frac{\boldsymbol{m}}{||\boldsymbol{r}||^3}\right) \tag{3.15}$$

where $\boldsymbol{m}$ is the magnetic dipole moment of the transmitter coil (in $\mathrm{N\,m\,T^{-1}}$), $\boldsymbol{r}$ is the displacement vector between the observation point (i.e. the tracking sensor) and the transmitter coil origin and μ_0 is the magnetic permeability of free space ($\mu_0 = 4\pi \times 10^{-7}$ in $\mathrm{H\,m^{-1}}$). This approximation only holds if the distance $\boldsymbol{r}$ is much larger than the dimensions of the generating coil as shown in Fig 3.16. The resulting $\boldsymbol{B}(\boldsymbol{r})$ is a vector denoting the strength and direction of the magnetic flux density (3.16)

$$\boldsymbol{B}(\boldsymbol{r}) = [B_x^r, B_y^r, B_z^r] \tag{3.16}$$

Variations of the dipole model are used in many research tracking systems [120–122] and formed the original model of the first magnetic tracking systems [99, 123], in which three orthogonal transmitter coils produced a spatially unique magnetic field. Commercial systems that use this coil configuration include the *Liberty* and *Patriot* from Polhemus Navigation Systems (*Colchester, VT, USA*), and the *AmfiTrack* system from Amfitech Systems (*Hjortsvang, Denmark*).

If the transmitting coils are large relative to the observation point, the dipole as-

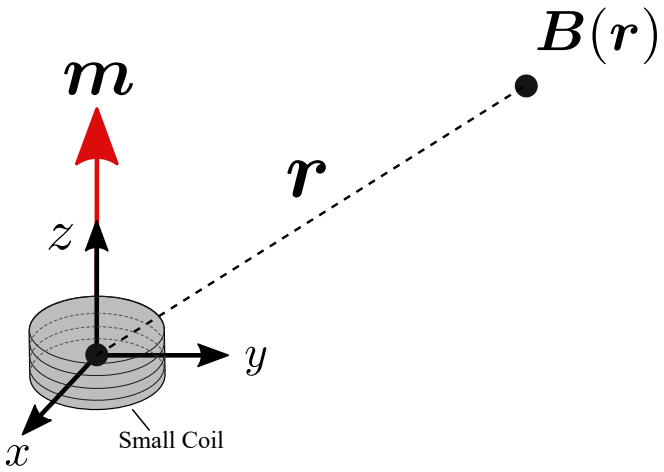


Figure 3.16: Magnetic dipole moment approximation for the field generated by a small coil described by (3.15).

sumption no longer holds and the tracking system will suffer from errors. In this case a discrete-source model based on Biot-Savart's law must be used as was demonstrated in [102]. The resulting field components require significantly increased computation due to the presence of elliptic integrals, but the result is a magnetic field model which holds at distances close to the field generator.

3.5.2 Large circular coil model

The use of large circular transmitter coils is another useful topology for field generator design [102,103]. The use of larger windings makes for easier construction of transmitter coils and enables larger tracking volumes to be constructed. The main consequence of using such a design is that the magnetic dipole model no longer holds as a valid approximation since the dimensions of the coil are relatively large with respect to the tracking distances. Accurate calculation of the resulting magnetic fields requires full integration of the Biot-Savart law around the coil [124] resulting in Cartesian expressions which can be found in [102]. The resulting equations require calculation of both elliptic integrals of the first and second kind, $E(k)$ and $K(k)$, and are computationally expensive, although updates rates of upwards of 650 Hz have been demonstrated with this method [102].

3.5.3 Current filament model

The magnetic model used in the Anser EMT system uses a piece-wise approach to calculate the magnetic field due a planar coil. Originally described in [125], the first EM tracking system to use this method was described in [92] using discrete printed-circuit-board coils. The model is based on the Biot-Savart Law and calculates the magnetic field due to single straight line of current as shown in (3.17) and Fig. 3.17

$$B(\boldsymbol{r}) = \frac{\mu_0 I}{4\pi}\left(\frac{\boldsymbol{c}\times\boldsymbol{a}}{|\boldsymbol{c}\times\boldsymbol{a}|^2}\right)\left(\frac{\boldsymbol{a}\cdot\boldsymbol{c}}{|\boldsymbol{c}|}-\frac{\boldsymbol{a}\cdot\boldsymbol{b}}{|\boldsymbol{b}|}\right) \tag{3.17}$$

where I is the current flowing through the filament, $\boldsymbol{a}$ is a vector representing the length and direction of the current filament, and $\boldsymbol{b}$ and $\boldsymbol{c}$ are vectors pointing from the observation point, $\boldsymbol{r}$, to the tip and tail of $\boldsymbol{a}$ respectively. A transmitter coil can comprise multiple filaments as shown in Fig. 3.18. In this case, the total magnetic field at an observation point, $\boldsymbol{r}$, is a superposition of the fields produced by all current filaments (3.18):

$$\boldsymbol{B}_{coil} = \sum_{i=1}^{k-1} \boldsymbol{B}(\boldsymbol{r}_i) \tag{3.18}$$

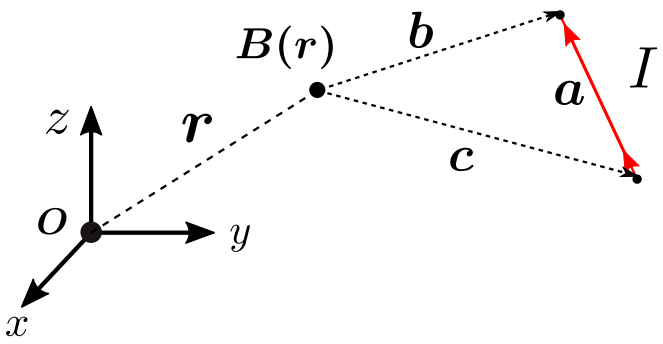


Figure 3.17: Magnetic due to a single straight line current filament.

This model provides is a satisfactory trade-off between accuracy and speed. The degree of approximation is reduced by considering each filament as an isolated individual magnetic element, resulting in a higher precision model at distances close to the coil. Linearity also allows each filament calculation to be performed in parallel on

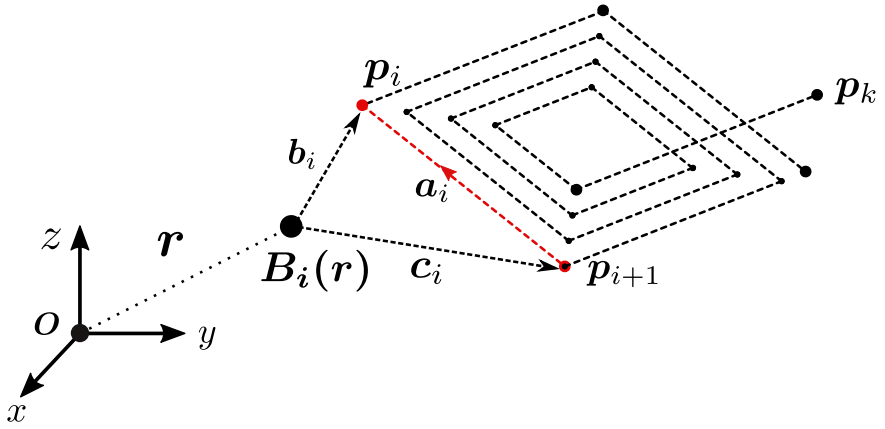


Figure 3.18: Magnetic due to a multiple straight line current filaments. The total magnetic field at a point $\boldsymbol{r}$ is the sum of the magnetic fields produced by all $k-1$ current filaments.

a computer. If multiple coils exist with each coil transmitting at a specific frequency, the magnetic field at $\boldsymbol{r}$ will be a superposition of all frequencies.

3.5.4 Sensor Model

The second aspect of the magnetic field model is the tracking sensor which detects the magnetic field produced by the field generator. The most basic form of tracking sensor for an AC magnetic tracking system is a solenoidal coil. The coil will experience an induced voltage on its terminals when placed in an time-varying magnetic field. Alternatively, DC-based tracking systems can also sense pulsed DC magnetic signals using fluxgate sensors, which are used in the Ascension Trakstar system [126]. Fig. 3.19 shows a solenoidal coil placed in a time varying magnetic field. The voltage in this case is produced by the changing magnetic flux inside the sensor. With reference to Fig. 3.19, the total instantaneous magnetic flux in the sensor at at an instant in time is given by (3.19):

$$\Phi(\boldsymbol{r},t) = \mu_a \boldsymbol{B}(\boldsymbol{r},t) A \cdot \hat{\boldsymbol{n}} \tag{3.19}$$

where Φ is the instantaneous magnetic flux through the sensor, $\boldsymbol{B}$ is the instantaneous magnetic flux density at a time t and position $\boldsymbol{r}$ with respect to the origin, A is the scalar cross-sectional area of the sensor, $\hat{\boldsymbol{n}}$ is a normal vector to the cross-sectional

area and points along the axis of the sensor and μ_a is the apparent permeability of the sensor's magnetic core, discussed in chapter 7. Eq. (3.19) is only valid for small sensor cross sections, where the magnetic flux density, $\boldsymbol{B}(\boldsymbol{r},t)$, can be assumed uniform over the cross-sectional area of the core as shown in (3.20).

$$\int \boldsymbol{B}(\boldsymbol{r},t)dA \cdot \hat{\boldsymbol{n}} = \boldsymbol{B}(\boldsymbol{r},t)A \cdot \hat{\boldsymbol{n}} \tag{3.20}$$

The induced voltage $v_s(t)$ is then found by taking the derivative of (3.19) in (3.21):

$$v_s(t) = \frac{d\Phi}{dt} = \mu_r \frac{d\boldsymbol{B}}{dt} A \cdot \hat{\boldsymbol{n}} \tag{3.21}$$

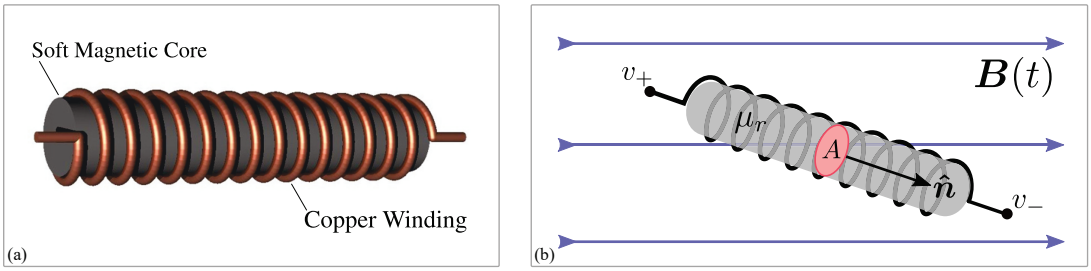


Figure 3.19: (a) 3D Illustration of a solenoidal coil sensor wrapped around a magnetic core. (b) Diagram showing a symmetrical solenoidal coil and magnetic core with cross sectional area A, normal vector $\hat{\boldsymbol{n}}$ and relative magnetic permeability μ_r placed in a time-varying magnetic flux density $\boldsymbol{B}(t)$.

From (3.21) we can see that the induced voltage of the sensor depends on both the position *and* orientation of the sensor as illustrated in Fig. 3.20, since $\boldsymbol{B}(\boldsymbol{r},t)$ is a function of x, y and z, while $\hat{\boldsymbol{n}}$ is a function of spherical the orientation angles θ and φ defined in (3.22), which are also defined with respect to the global origin $\boldsymbol{O}$ as shown in Fig 3.20.

$$\hat{\boldsymbol{n}} = \sin\theta\cos\varphi \cdot \hat{\boldsymbol{x}} + \sin\theta\sin\varphi \cdot \hat{\boldsymbol{y}} + \cos\theta \cdot \hat{\boldsymbol{z}} \tag{3.22}$$

where $\hat{\boldsymbol{x}}$, $\hat{\boldsymbol{y}}$, and $\hat{\boldsymbol{z}}$ are Cartesian unit vectors. The total instantaneous flux on the sensor can be written in expanded form by combining (3.19) and (3.22) to produce the

expression in (3.23)

$$\Phi(\boldsymbol{r},t) = \mu_a \boldsymbol{B}(\boldsymbol{r},t)A \cdot [\sin\theta\cos\varphi \cdot \hat{\boldsymbol{x}} + \sin\theta\sin\varphi \cdot \hat{\boldsymbol{y}} + \cos\theta \cdot \hat{\boldsymbol{z}}] \tag{3.23}$$

The flux density being a vector quantity in (3.16) results in a single scalar magnetic flux quantity shown in (3.24)

$$\Phi(\boldsymbol{r},t) = \mu_a A \left[B_x^r \sin\theta\cos\varphi + B_y^r \sin\theta\sin\varphi + B_z^r \cos\theta\right] \tag{3.24}$$

where B_x^r, B_x^r and B_x^r are the time-varying Cartesian components of $\boldsymbol{B}(\boldsymbol{r},t)$. Multiple time-varying magnetic fields from multiple field generator coils will produce independent magnetic fluxes at different frequencies within the sensor. For an arbitrary number of transmitting coils, N_{coil}, the induced voltages on the sensor can be expressed in vector form in (3.25).

$$\boldsymbol{V} = \begin{bmatrix} v_1 \\ v_2 \\ \vdots \\ v_N \end{bmatrix} = \begin{bmatrix} \frac{d\Phi_1}{dt} \\ \frac{d\Phi_2}{dt} \\ \vdots \\ \frac{d\Phi_{N_{coil}}}{dt} \end{bmatrix} \tag{3.25}$$

Anser EMT extracts each of these independent voltage signals from the sensor using the sampling and filtering techniques discussed in sections 3.3 and 3.4. This sensor model forms the basis for the solver discussed in the next section. For a planar magnetic tracking system like Anser EMT, a minimum of $N_{coil} = 8$ coils is required for successful tracking as proposed by [102] and [92]. An in-depth derivation of the model taking into account all sensor parameters can be found [92] and [90].

Anser EMT implements the magnetic system model in two stages. The field generator model, which defines the spatially varying magnetic field, is kept separate from the sensor model. The sensor model is implemented as part of the position and orientation solving process (discussed in section 3.6). This design allows different sensor models to be interchanged as will be demonstrated in chapter 7.

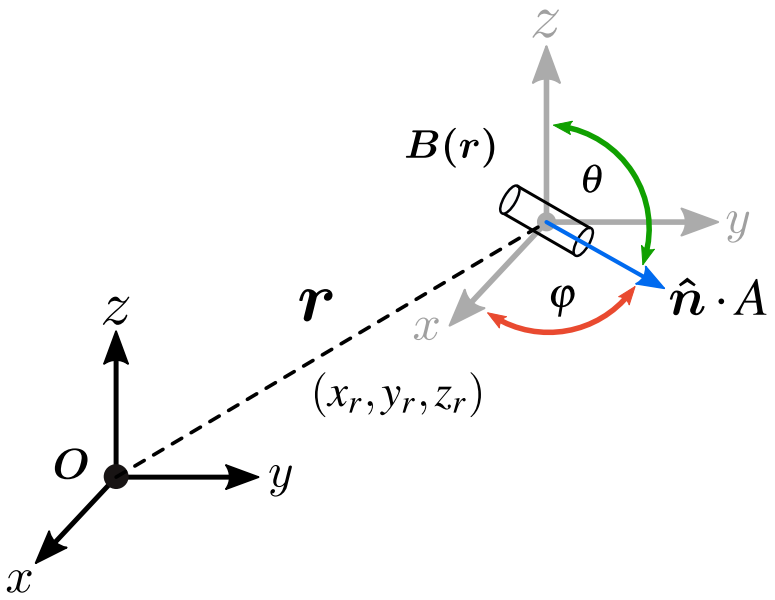


Figure 3.20: The magnetic flux through a 5-DoF sensor is a function of the sensor's position $r = (x, y, z)$ and the orientation (θ, φ) in spherical coordinates with respect to the global origin $\boldsymbol{O}$.

3.6 Solver

The solving stage is the final step in the tracking system process. Magnetic tracking systems resolve EM sensor position through a process of non-linear optimisation in which a cost function is minimised to yield the best-fit solution for the position and orientation of the tracking sensor. The cost function is generally formulated such that the squared difference between the magnetic model of the sensor coil and acquired sensor measurements is minimised. For the 5-DoF sensor shown in Fig. 3.20, the system cost function for the Anser EMT system is given by (3.26)

$$\boldsymbol{F}(x, y, z, \theta, \varphi) = \boldsymbol{V}_d - \boldsymbol{\kappa} \cdot \boldsymbol{V_m} \tag{3.26}$$

where $\boldsymbol{V}_d$ is a vector of voltage measurements acquired from the sensor from (3.25), $\boldsymbol{V}_m$ is a vector of corresponding voltages from the magnetic model and $\boldsymbol{\kappa}$ is a vector of scaling factors obtained during the calibration process which fits the magnetic model with the acquired sensor measurements. Electrically, each κ_i establishes the relationship between the current in a single transmitter coil and the corresponding

voltage induced on the tracking sensor. Linearity allows all these parameters to be lumped into a single scalar for each transmitter coil.

The minimisation problem to solve for the best fit sensor position and orientation can then be stated as (3.27)

$$\begin{aligned} &\underset{\boldsymbol{p}}{\text{minimise}} \quad \boldsymbol{F}(\boldsymbol{p})^2 \\ &\text{subject to} \quad lb \leq \boldsymbol{p} \leq ub \\ &\\ &\text{where} \;\; \boldsymbol{p} = (x, y, z, \theta, \varphi) \end{aligned} \tag{3.27}$$

where *lb* and *ub* are lower and upper bounds that define the minimum and maximum allowable values of $\boldsymbol{p}$ and $\boldsymbol{F}(\boldsymbol{p})^2$ is the vector of squared residuals to be minimised. The $\boldsymbol{p}$ which globally minimises $\boldsymbol{F}$ is the position and orientation of the tracking sensor, $\boldsymbol{p}_{min}$. The task of finding $\boldsymbol{p}_{min}$ is accomplished using iterative methods. A non-linear least-squares approach is usually required to yield accurate results. Examples of general solving methods include the well known Levenburg-Marquard (LM) [127] and trust-region (TRF) algorithms [128].

Anser EMT implements both solving LM and TRF solving algorithms which can be selected by the user. The tolerances that define the solving process are readily accessible and can be adjusted to meet the accuracy and speed demands of the application.

3.7 Framework Implementation

The proposed EMT framework is composed of four Python modules representing each of the signal processing steps shown in Fig. 3.1. An expansion of this design showing the data-flow between modules is shown in Fig. 3.21. The framework is divided into four modules labelled (i) to (iv). Analogue signals from the EMT sensing electronics are acquired through a data acquisition module *daq.py*. This module facilitates the abstraction of acquisition hardware APIs into a standard interface. The acquired digital samples are fed into the filter module *filter.py* where the frequency components of interest are conditioned and extracted from the digital waveform. The filter module allows easy configuration of filter parameters while providing routines for efficient matrix

multiplications required during filtering operations. The extracted signal information is then fed to the solver module *solver.py*. Simultaneously, the magnetic field model of the system, *model.py*, is compared with the extracted signal data to minimise the system cost function (3.26) according to (3.27). The solver module provides access to the tolerance and parameter settings for the minimisation process. The resulting sensor coordinates from the solver may be streamed to the user application using OpenIGTLink [96].

The framework was applied to the Anser EMT project [100]. The open-source codebase, which was initially implemented in Matlab, was fully converted to Python in order to conform with the framework. The PyDAQmx driver [129] was used to provide a cross-platform interface with the NI-DAQmx driver acquisition system (*National Instruments, Austin, Texas*). Filtering and solving operations were performed using NumPy and SciPy libraries [130]. OpenIGTLink connectivity was achieved using PyIGTLink [131].

3.8 Experiments and Results

EMT framework's performance and accuracy were tested relative to the original Windows-only Matlab implementation. Testing of the framework was performed on three operating systems: Windows 10, MacOS 10.13 and Cent-OS 7.0 Linux. All reported metrics result from tests performed on a laptop PC configured with an Intel i7 4810HQ 3.5GHz CPU and 16GB of RAM, utilising both a Windows 10 and CentOS 7.0 installation. Compatibility with the MacOS 10.13 operating system was confirmed using a separate machine, but comparative results were not possible due to significant differences in the laptop hardware configuration. The variable sampling frequency of the data acquisition system, F_s, as indicated in section 3.3, was set at 100kHz for all experiments.

Framework code implementation available at `https://openemt.org`

The experimental MacOS laptop featured a much slower CPU (approx. 2.2 GHz) compared to the Windows testing machine. Differences in the NI-DAQ kernel driver performance can also play a significant role which were not studied in this work.

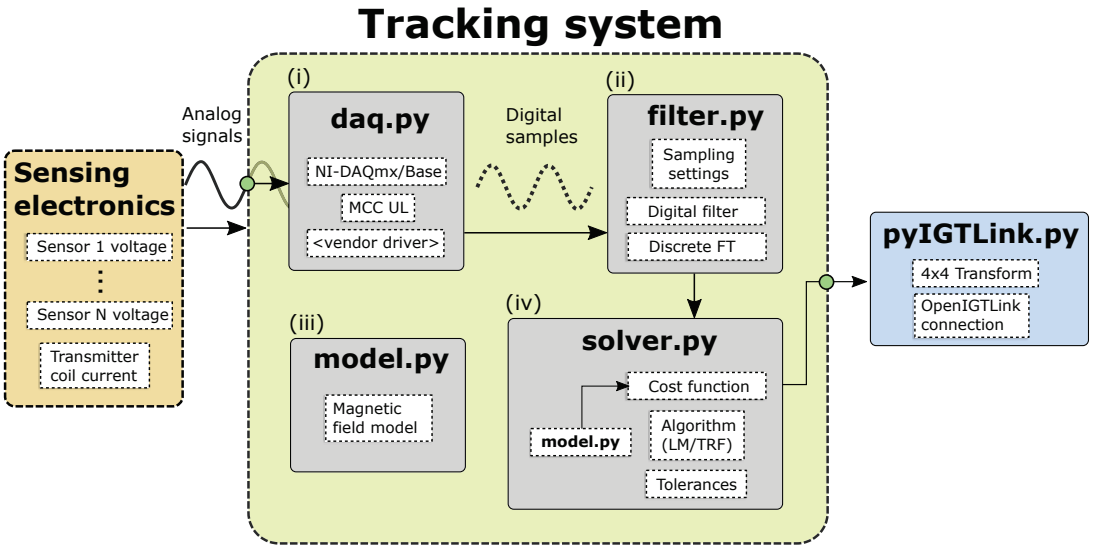


Figure 3.21: (i) Analogue signals are sampled by the data acquisition module. (ii) The samples are filtered in software with relevant frequency components extracted. (iii)-(iv) A cost function utilises the component magnitudes to yield a position vector which can be transmitted using OpenIGTLink as a 4x4 transformation matrix.

3.8.1 Performance benchmark

Performance testing measured the framework's ability to stream position measurements as quickly as possible with minimal latency over an OpenIGTLink connection to CustusX [64] and 3DSlicer [132], two open-source medical imaging and visualisation tools used for pre-clinical research. Acquisition latency, maximum update frequency (with both a stationary and moving sensor) were recorded for multiple acquisition frame sizes shown in Tables 3.4 and 3.5. An acquisition frame, L, constitutes the number of samples gathered by the acquisition system per single resolved position. A finite acquisition time for each frame puts a limit on the minimum latency figure as discussed in section 3.3. Static measurement refers to a slow moving sensor speeds of $<$5cm per second while 'Dynamic' measurements refers to speeds $>$50cm per second.

3.8.2 Accuracy benchmark

Accuracy testing consisted of comparing errors between sensor positions obtained from a 7x7 plane test x-y grid providing a total of 49 points. One hundred and fifty

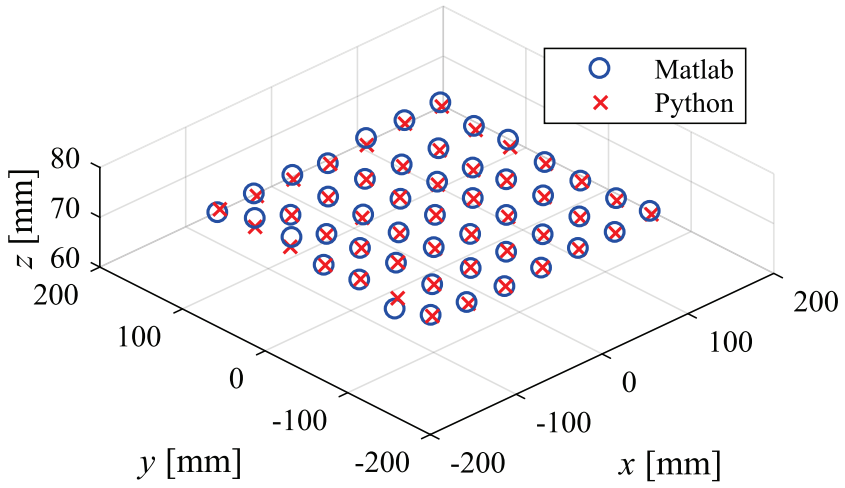


Figure 3.22: 3D Plot showing positions from both Matlab and Python software implementations. Performance is comparable with increased errors observed at the boundary of the tracking volume.

Table 3.4: Performance measurements using Matlab on Windows.

Matlab	Frame size	Acq. Latency (ms)	Max. Static (Hz)	Max. Dynamic (Hz)
-	250	2.5	72	64
-	500	5	70	61
-	1000	10	65	62
-	2000	20	50	50
-	5000	50	20	20

position acquisitions at an approximate height of $z = 70$mm from the transmitter board (Fig. 3.2 (b)) were recorded per grid point from which the mean x, y and z coordinate of each point was calculated. Measurements were obtained from both Matlab and Python implementations. Maximum, minimum and root-mean-square (RMS) errors were calculated between the two obtained point grids, using the Matlab measurements as the ground-truth. The grid obtained using the Matlab implementation was used as the reference since its performance has already been characterised in [100]. Maximum and minimum grid errors were measured as 3.1mm and 0.1mm respectively with an RMS error of 0.9mm and a standard deviation of 0.75mm.

Table 3.5: Performance measurements using Python framework (Windows/Linux).

Python	Frame size	Acq. Latency (ms)	Max. Static (Hz)	Max. Dynamic (Hz)
-	250	2.5/5000+*	138/120	84/70
-	500	5/2000+	142/115	95/83
-	1000	10/1000+	102/80	66/62
-	2000	20/100	51/45	52/45
-	5000	50/50	20/21	20/20

* Due to operating system driver, see discussion.

3.9 Discussion

Table 3.5 shows how performance of the Anser EMT system varies with acquisition sample size over Windows and Linux operating systems. Benchmark results on Windows are clearly favourable to Linux particularly at low sample sizes. The high latencies in Linux were found to be related to a low-level buffer issue caused by limitations in the NI-DAQmx Base kernel driver for Linux. Forcing the acquisition time to be greater than the solving time prevents this latency issue occurring. Empirically setting the acquisition frame L to 2000 (i.e. a frame acquisition delay time of T_{ad} =20 ms) mitigates the issue, although this approach limits the maximum effective position update rate F_{system}.

It can also be seen that the update speeds vary significantly depending on the movement speed of the sensor. This is due to the previous sensor position being used as the initial condition for the solver during each position update. A moving sensor causes previous sensor positions to lie further from the current true sensor position, resulting in the solver requiring more iterations to converge to the global minimum. Artificially forcing periodicity by limiting the update rate of the system prevents this issue from occurring. This approach must be implemented with care in order to avoid increasing the overall system latency.

The purpose of the accuracy benchmark is to identify any significant differences between the two EMT software implementations. The accuracy of the benchmark is limited since it uses the previous Matlab implementation results as reference rather than a gold standard comparison such as optical tracking. The reported mean error value of 0.9mm falls within the mean error value of the Matlab implementation which

was recorded as 1.14mm [100]. From this we can conclude that the Python implementation is of similar accuracy to the original implementation. Characterisation of this system according to the previously reported Hummel test protocol [133, 134] is necessary in order to fully validate the accuracy of the system under the new framework.

Summary

An open source framework for designing electromagnetic tracking systems has been designed and implemented. The framework was applied to a previously characterised tracking system with performance results reported. The source code of the Anser EMT implementation is publically available on `https://openemt.org`. It is hoped that this work will assist in the translation of new EMT developments from research into the clinical setting.

Chapter 4

EMT system design

This chapter describes the design and development of an open-hardware electromagnetic tracking (EMT) system, Anser EMT. Originally based on the work of [92], the goal of this work was to refine the original tracking system design and create a development kit for image-guided intervention research. We start with a brief overview of electromagnetic tracking and the fundamental components of these systems. System design criteria is then developed using the original system implementation as a reference. Finally, design features of the new system and performance metrics are discussed.

4.1 Introduction

Electromagnetic tracking systems operate by detecting magnetic fields to resolve the position and orientation of a magnetic field sensor. Tracking consists of three fundamental steps from a hardware standpoint: Transmission, Reception and Solving. Transmission refers to how the EMT system generates and transmits its magnetic field locally in space. Reception is performed by an inductive sensor, whose induced voltage is a function of its position in space. If the induced voltage response is unique

This chapter is based on H. A. Jaeger et al. "Anser EMT: the first open-source electromagnetic tracking platform for image-guided interventions", *Int. J. Comput. Assist. Radiol. Surg.*, vol. 12, no. 6, pp. 1059–1067, 2017.

with respect to the sensor's position and orientation (P&O) then it is possible to resolve the P&O based purely on this measurement through the process of cost function minimisation, described in chapter 3. Solving the resulting set of equations requires iterative techniques in order to achieve the sufficient accuracy. Examples of solvers include the well known Levenberg-Marquardt [127] and Trust-Region [128] methods. The solving process is discussed in more detail in chapter 3. A block diagram of the system components is shown in Fig. 4.1.

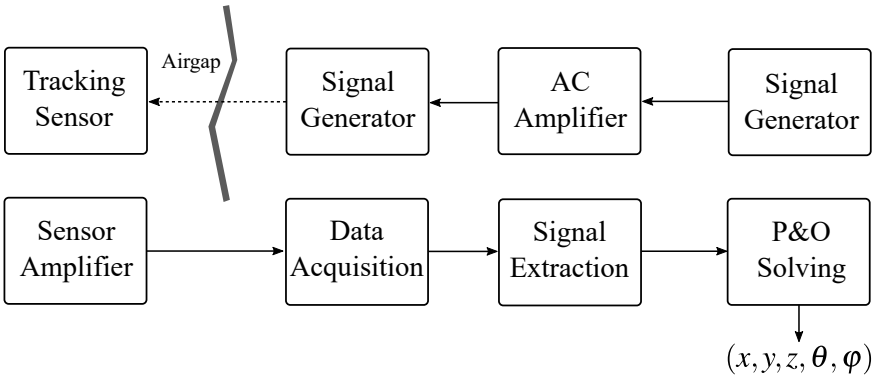


Figure 4.1: General processing stages in an electromagnetic tracking system.

Innovations in the tracking system design occurred in all stages of the system with major changes occurring in power design, signal generation, amplification field generator stages. This resulted in a more power efficient system with a significantly reduced printed circuit area footprint. The software tooling used in the work included Altium Designer 16 , LTSpice and National Instruments Multisim.

4.2 Previous transmitter driver

The Anser EMT system utilises eight transmitter coils in its default configuration. Each coil is driven by a user-programmable signal generator subsystem. Advantages of this signal generator include its programmability and closed-loop current sensing features. The original implementation of the signal generator [90, 92] will now be briefly discussed. This will provide a design background when discussing the design improvements in section 4.3.

4.2.1 Waveform generation

Waveform generation was replicated as the original design [92], and provides the reference signal for the generation of a time-varying magnetic field. The Analog Devices (*Norwood, MA, USA*) AD9833 programmable waveform generator system-on-a-chip was used to provide the user with the ability to select different transmitter frequencies. The waveform generator utilises a Direct Digital Synthesis engine to reconstruct an analogue waveform according to the desired frequency. A block diagram of the system internals is shown in Fig. 4.2. Programming takes place over the Serial Peripheral Interface (SPI) bus using a microcontroller, discussed in section 4.5. A 6 MHz crystal oscillator is used as a reference signal for the IC's synthesis engine. The equation relating the desired output frequency to the reference clock is given by (4.1) [135] where f_{OUT} and f_{MCLK} is the waveform generator's output and master clock input frequencies respectively in Hz.

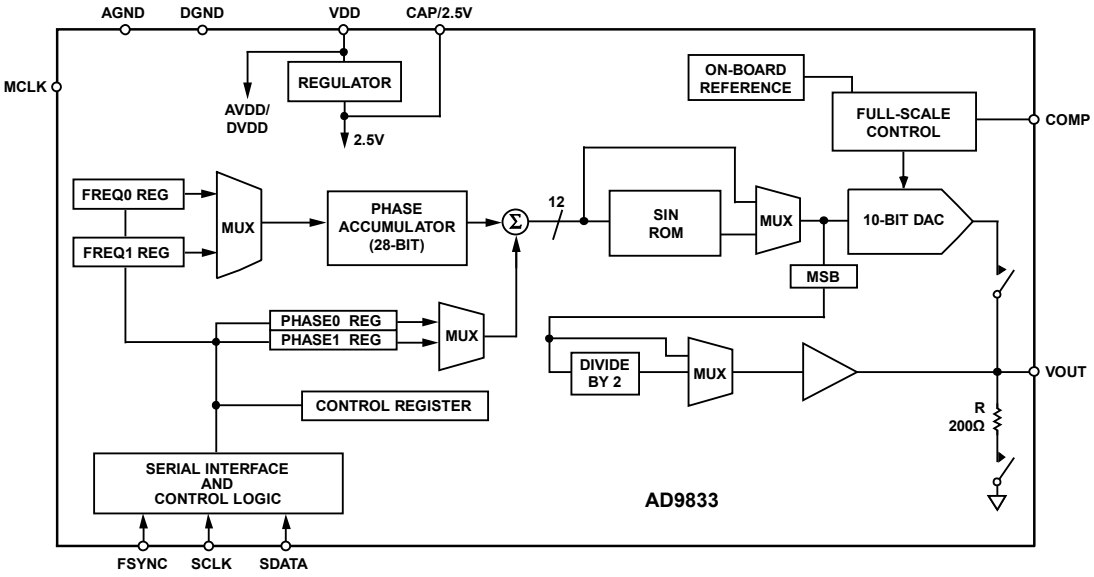


Figure 4.2: Block diagram of the AD9833 waveform generation system [135]. The device utilises direct digital synthesis (DDS), in which an analogue waveform is reconstructed from internal read-only memory (ROM). The output frequency is controlled using a pair of user-programmable registers.

$$FreqReg = \frac{F_{OUT} \times 2^{28}}{F_{MCLK}} \tag{4.1}$$

The resulting binary word, *FreqReg*, is written to the frequency register of the device. Further details of the programming process can be found in the AD9833 application note [136]. The output analogue waveform has an amplitude of 0.6 V. A Teensy 3.2 microcontroller is used interface with the AD9833 and is described in more detail in section 4.10.4.

4.2.2 Signal conditioning

The waveform generator's output amplitude of 0.6 V is too low to be of any practical use in a tracking system when used in isolation and must first undergo conditioning and amplification in order to drive a field generator transmitter coil. The device's output signal is generated by the AD9833's internal DAC current source output stage across the output 200 Ω resistor as shown in Fig. 4.2. The output impedance can therefore be approximated as a 200 Ω resistance.

Signal conditioning and amplification is broken into four stages: (i) amplification, (ii) passive filtering, (iii) closed-loop current control and (iv) a current boosting stage. The original coil driver is a DC coupled design [90,92] and utilises a discrete AB class current booster stage. The improved design is AC coupled which uses an efficient discrete current boosting stage to reduce quiescent power dissipation and is discussed in section 4.3.

Waveform amplifier

A gain stage is initially needed to buffer and amplify the high impedance 0.6 V reference waveform. An adjustable non-inverting amplifier stage was designed as shown in Fig. 4.3. The gain G of the op-amp stage is given by (4.2) where G is the resulting gain factor and R_G is the programming resistance in ohms.

$$G = \left(1 + \frac{R_G}{1000}\right) \tag{4.2}$$

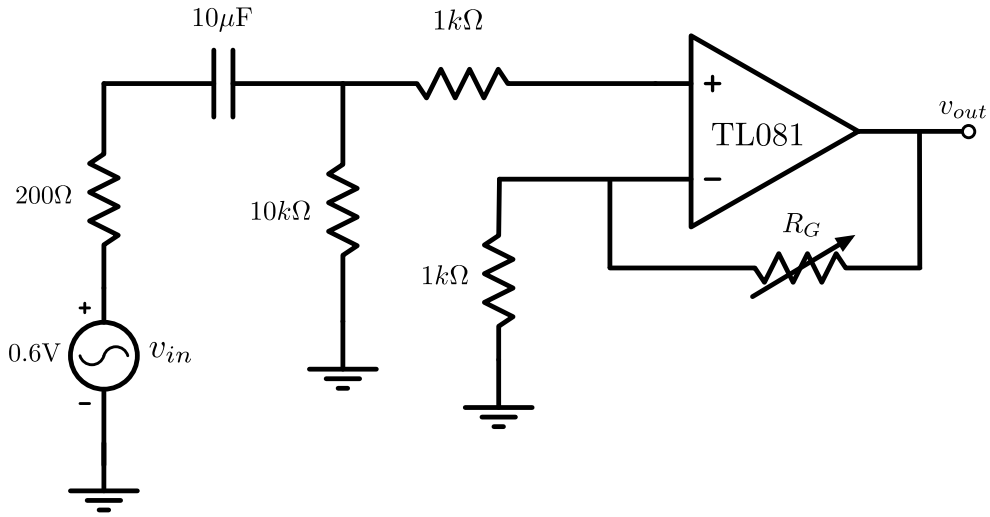


Figure 4.3: Non-inverting amplifier configuration used to buffer the signal generator output. The AD9833's output is modelled by a 0.6 V source in series with a 200 Ω resistor. A 10 µF capacitor provides a low-impedance AC coupled connection to the gain stage. R_G was chosen as a 10 kΩ ten-turn potentiometer to provide a maximum gain of 11 according to (4.2).

Passive filtering

Following amplification, a filtering stage is required to attenuate the undesired harmonic components of the amplified waveform signal caused by the AD9833. The Anser system is designed to transmit frequencies in the tens of kilohertz band. An appropriate passive bandpass filter was designed as shown in Fig. 4.4(a). The filter passband lies between 820 Hz and 30 kHz as shown in Fig. 4.4(b).

Closed-loop current control

AC electromagnetic tracking systems rely on accurately sensing a spatially varying magnetic field in the working volume of the field generator using an induction coil sensor. The stability of the magnetic field is therefore of critical importance as any deviation over time can result in position and orientation errors in the reported sensor position. The physics of the magnetic fields and sensors is discussed in chapter 3. A fast, closed-loop control scheme was devised in the previous implementation [92] in order to ensure a stable magnetic field is generated by each transmitter coil. This

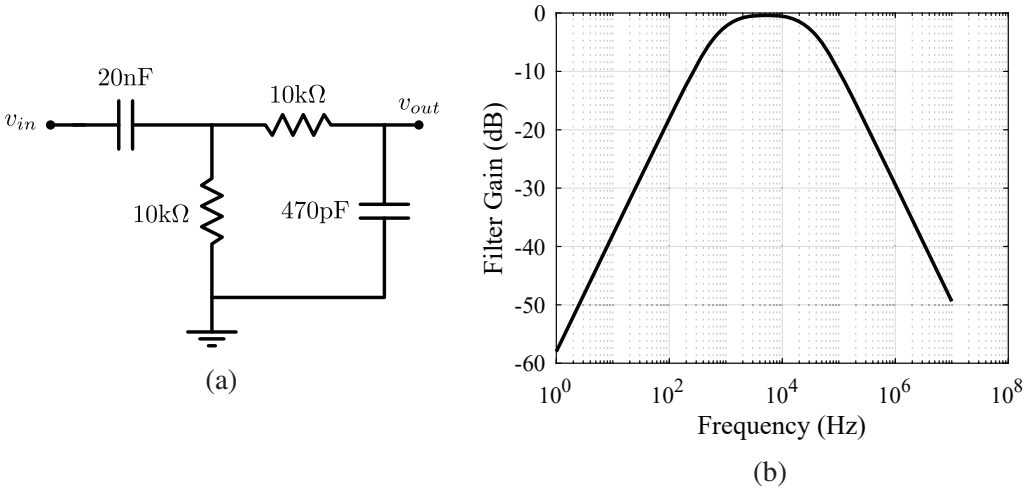


Figure 4.4: (a) Passive RC bandpass filter circuit (b) The frequency response of the passive bandpass filter. The filter has a bandwidth of 32 kHz with corner frequencies of 820 Hz and 33 kHz respectively.

section briefly reviews the original control scheme before describing the modifications made for the Anser system.

An ideal constant current control scheme can be constructed using an operation amplifier (op-amp) as shown in Fig. 4.5. This non-inverting negative feedback configuration results in the op-amp driving the voltage on the v^- pin being equal to v_{ref}. This property gives relation (4.3) where the current through the sense resistor R_s is determined by the reference voltage applied to the non-inverting input pin.

$$i_{out} = \frac{v_{ref}}{R_s} \tag{4.3}$$

Modelling the transmitter coil as a purely resistive circuit element is not sufficient as the coil will have a relatively large inductance associated with its design due to its purpose of generating a time-varying magnetic field. The magnetic properties of the transmitter coil is described in greater detail in chapter 3, but its circuit parameters can be estimated with by a lumped 70 µH inductor, L_{coil} , in series with a 3 Ω resistor, R_{coil}, as shown in Fig. 4.6. The current sense resistor R_s of 1 Ω was used to generate the feedback voltage to the amplifier. Taking the Laplace transforms of the system and rearranging terms results in the admittance relation between the output coil current and

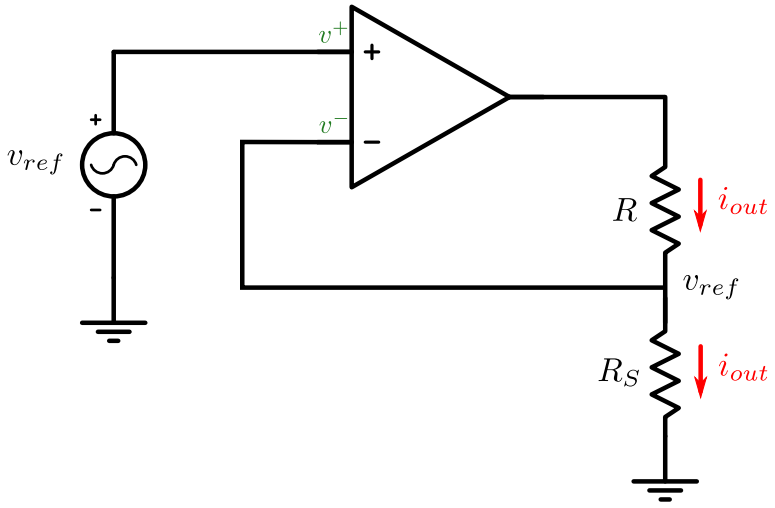


Figure 4.5: Basic current source op-amp topology.

input reference voltage in (4.4) where L_{coil} is the lumped transmitter coil inductance (in Henries), R_{coil} is the lumped coil series resistance (in ohms) and s is the complex frequency variable of the Laplace transform, where in sinusoidal steady state $s = j\omega$.

$$Y(s) = \frac{i_{out}}{v_{out}} = \frac{1}{R_{coil} + R_s + sL_{coil}} \tag{4.4}$$

At low frequencies where $s = j\omega \ll (R_{coil} + R_s)$, the output admittance is approximately constant as $Y = {}^{1}/_{(R_{coil}+R_s)}$, but as input signal frequency increases, the admittance reduces as the sL term in the denominator begins to dominate. An LM7171 operation amplifier was used in the design with a transfer function (4.5) where τ_1 and τ_2 are the two internal time constants of the op-amp and A_{OL} is the op-amp's open-loop gain which were estimated in [92] from the device datasheet [137].

$$A_{OL}(s) = \frac{A_{OL}}{(1+s\tau_1)(1+s\tau_2)} = \left(\frac{3\times 10^6}{1+0.01s}\right)\left(\frac{1}{1+1.6\times 10^{-8}s}\right) \tag{4.5}$$

The open-loop feedback signal of the current source can then be expressed by combining the transfer function of the coil with (4.5) in (4.6)

$$\frac{v_{fb}(s)}{v_{ref}(s)} = \frac{R_s}{R_s + R_{coil} + sL_{coil}} A_{OL}(s) \tag{4.6}$$

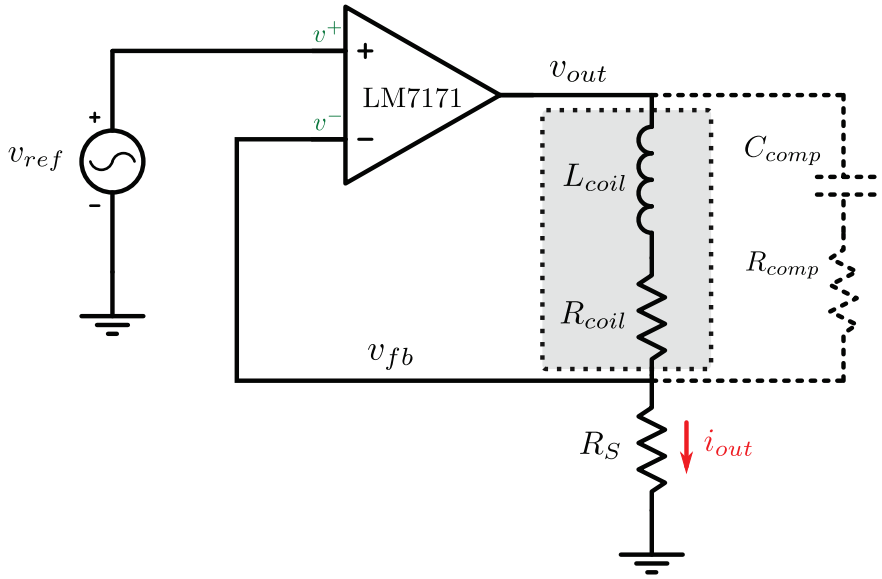


Figure 4.6: Ideal current source op-amp configuration with lumped transmitter coil parameters taken into consideration. L_{coil} and R_{coil} represent the transmitter coil's internal self inductance and resistance. R_s is the current sense resistor. C_{comp} and R_{comp} constitute a phase-lead compensation network to reduce amplifier ringing during closed loop operation.

where v_{fb} is the feedback voltage into the inverting input of the op-amp, v_{ref} is the reference waveform and $A_{OL}(s)$ is the transfer function of the LM7171 operational amplifier. The system open-loop response in Fig 4.7 shows the frequency response of the circuit of Fig. 4.6 using the LM7171. The sum of the phase lags introduced by both the op-amp's low-frequency pole and transmitter coil inductance results in a very low phase margin being present in the 1-30 of kHz band. This can potentially cause instability in closed loop configuration. This stability issue was solved using a phase-lead compensator resistor capacitor network composed of R_{comp} and C_{comp} shown in Fig. 4.6. The compensation network is discussed in terms of closed-loop performance of the new design in section 4.3.3.

Current boost stage

The system field generator requires a significantly large current driver in order to produce the 250 mA of current demanded by the design [92]. A final current boosting

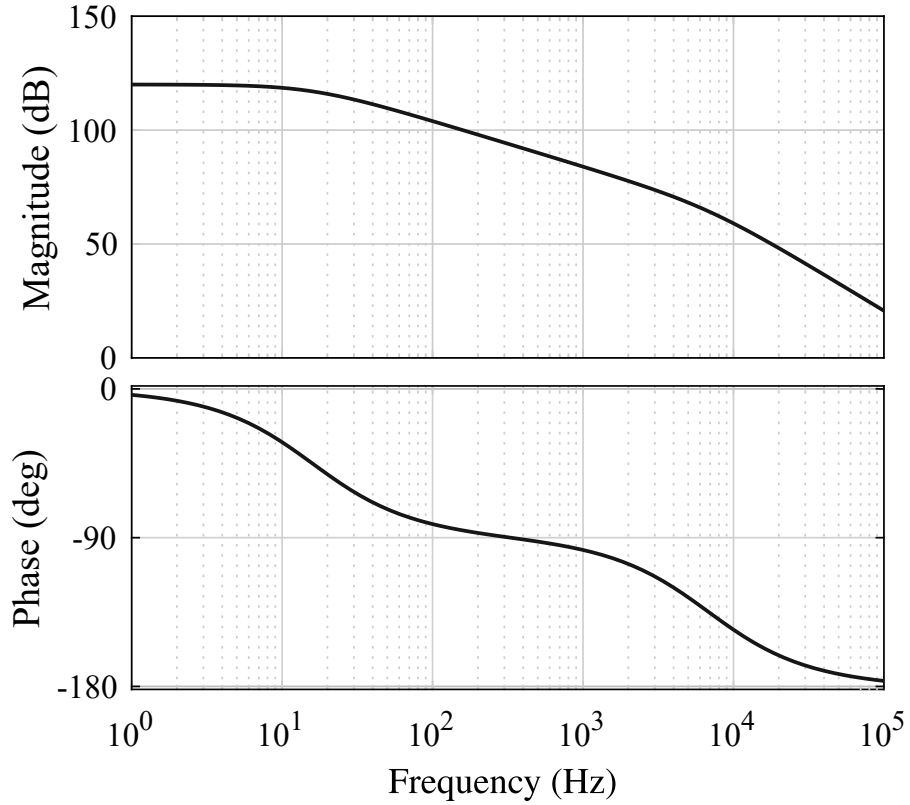


Figure 4.7: Open-loop frequency response of the LM7171 and transmitter coil as shown in Fig. 4.6. The phase angle of the feedback voltage v_{fb} approaches 180° in the kHz region of the response which can potentially lead to oscillation when the circuit loop is closed. A phase margin of 15° is present at a frequency of 30 kHz.

stage allows closed-loop current source to effectively source and sink up to a maximum of 500 mA of current [92]. The original topology used a discrete AB class amplifier design as shown in Fig. 4.8. This design provided a low-impedance output for connection to the transmitter coils. Further design details are provided in [90]. While this design provided very stable currents, it suffered performance drawbacks which are discussed in section 4.2.3.

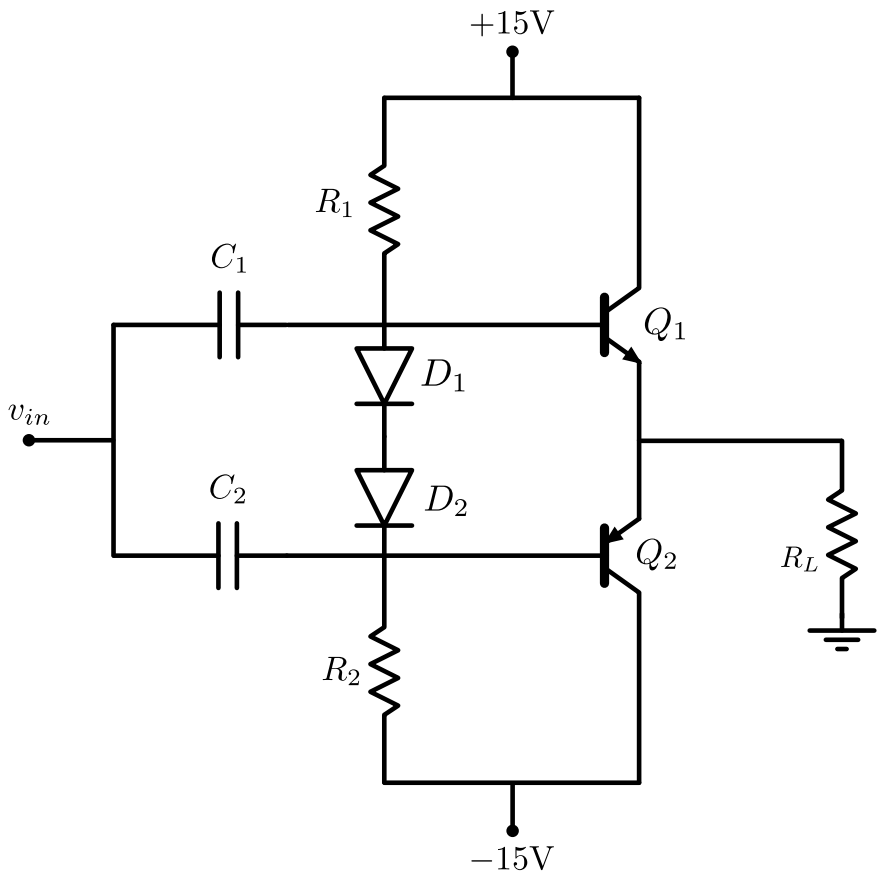


Figure 4.8: The class AB push-pull current amplifier stage used in the previous system implementation. R_L signifies a simplified circuit load which represents an ideal transmitter coil. Diodes D_1 and D_2 are matched diodes which serve to bias transistors Q_1 and Q_2 in order to minimise crossover distortion.

4.2.3 Design critique

Section 4.2 has so far discussed the design of the original current driver circuit for driving the field generator transmitter coils. Originating from a waveform generator IC, a reference waveform is generated, amplified, filtered and fed as an input into a closed-loop current control circuit. The resulting current is buffered using a discrete class AB amplifier. The original system design has a number of drawbacks which limit its ability for integration into a design suitable for replication, distribution and application in clinical settings.

- **Power consumption**. The AB class amplifier topology requires a quiescent current for biasing the output transistor pairs to the brink of conduction. This quiescent current is significant and when used with eight transmitter coils, causes an overall power consumption of 30 watts. This wasted power is dissipated as heat from the biasing diodes and output transistors. A large 3 kg heat sink is required in this case in order to conduct heat away from the electronics and prevent thermal runaway of the silicon. This heat sink adds significant volume and weight to the field generator enclosure.

- **Footprint area**. The original driver circuit footprint utilises discrete silicon for the current boost stage as well as large 1206 surface mount technology (SMT) components for the remaining circuitry. The resulting transmitter PCB had a total area of 660 cm^2, with each transmitter channel consuming 56 cm^2, making the design infeasible for integration in a small enclosure.

The solution to both of these issues is discussed in section 4.3. Power loss is minimised by modifying the closed-loop current source topology and current booster circuit designs. These modifications also significantly reducing the overall circuit footprint, which is further reduced by moving to 0603 surface-mount technology (SMT) components.

4.3 Optimised transmitter driver

The main design objectives of optimising the transmitter driver were to reduce circuit power consumption and heat dissipation while also consolidating the overall circuit layout to reducing the final PCB footprint area. This was achieved in three stages:

- **Integrated current buffer**. Replacing the discrete AB class current booster stage with a single buffer integrated circuit. Quiescent currents, heat and circuit footprint are significantly reduced as a result.
- **Single rail operation**. Operating the current buffer on the main 15 V supply reduces power-loss and current draw from the -15 V voltage rail.
- **SMT components**. Replacing all 1206 passive components with their equivalent 0603 variants resulted in a reduction in the overall circuit size. The resulting PCB footprint area of the current boosting circutry was reduced to 180 cm^2 from 660 cm^2.

Integrated current buffer

An integrated current buffer from Texas Instruments, the LMH6321, was chosen for replacing the discrete AB class current booster stage described in 4.2.2. The buffer is an integrated, open-loop, unity gain buffer circuit which can source and sink a maximum current of 300 mA. This figure can be increased if the current limiting feature of the device is disabled. Current buffer circuits such as the LMH6321 are designed to be inserted into the signal path in order to lower the output impedance of a circuit block, while minimising the noise and distortion caused by its insertion. A circuit diagram of the device internals can be seen in Fig. 4.9. The bandwidth the buffer is very high as a result, with the LMH6321 quoted as having a small signal bandwidth of 110 MHz and a large-signal bandwidth of 39 MHz from the device datasheet [138].

Single rail operation

The original tracking system design was entirely powered by a linear laboratory grade bench supply. This provided adequate current capabilities on both positive and negative

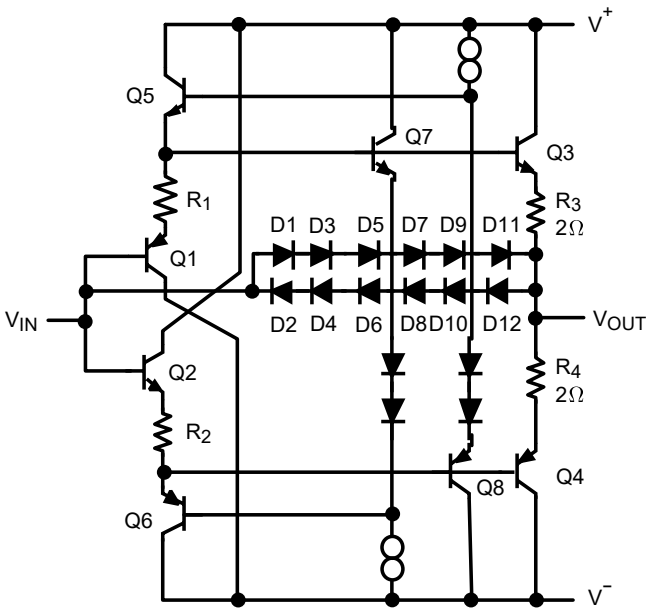


Figure 4.9: Simplified circuit topology of the LMH6321 current buffer [138]. The device uses an open-loop complementary follower design, where the bases of output transistors $Q3$ and $Q4$ are driven by their own push-pull stages. Transistors $Q7$ and $Q8$ are current mirrors for biasing. Diodes $D1$-$D12$ serve as input/output protection diodes.

15 V rails. All analogue circuit stages utilised this split-supply configuration in order to maximise the bandwidth and dynamic range specifications of the parts used. The revised system does not feature symmetry in its power delivery. The main source of power is a 15 V adapter capable of delivering up to 60 W of power, which is discussed further in section 4.7. The negative supply is generated on-board the system PCB by a buck-boost switching converter as described in section 4.7.3, and is capable of delivering a maximum current of 1.5 A. Since the switching converter delivers less power compared to the main 15 V power source, it was decided to partition the system power delivery into two functions:

- **Split supply**. $\pm$15 V rails are used for all low-power circuitry. This includes all voltage amplification and signal conditioning stages.

- **Single supply**. Any high current devices will be powered from the 15 V rail. This includes the LMH6321 current buffer circuitry.

Utilising a single supply for the current buffer design means reducing the potential voltage swing of the LMH6321 from ± 15 V (centred at 0 V) to 0-± 15 V (centred at 7.5 V). Reducing the voltage swing may negatively impact the current delivering capacity of the driver especially if the load impedance is large. Nominal current delivery for the tracking system is 250 mA [92]. A frequency analysis of the transmitter coil load was performed to confirm that utilising a single supply could achieve the required current drive.

The transmitter coil load impedance can be modelled as a series resistor-inductor network as shown in Fig. 4.10. The total complex impedance of the transmitter coil is given by (4.7) where L_{coil}, R_{coil} and R_s are the electrical coil parameters obtained previously from Fig. 4.7.

$$Z_{coil}(s) = sL_{coil} + R_{coil} + R_s \tag{4.7}$$

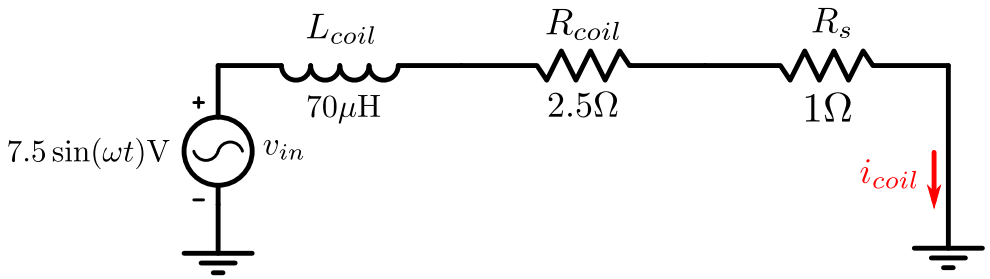


Figure 4.10: Circuit diagram of the transmitter coil and current sense resistor parameters. A test sinusoid with an amplitude of 7.5 V is used to simulate the theoretical maximum coil current conditions.

The maximum coil current can then be written as (4.8) where V_{coil}^{max} is the peak amplitude of the sinusoid and I_{coil}^{max} is the peak current through the coil impedance Z_{coil} resulting from V_{coil}^{max}.

$$I_{coil}^{max} = \frac{V_{coil}^{max}}{Z_{coil}(s)} \tag{4.8}$$

Equation (4.8) is plotted with respect to frequency in Fig. 4.11. The theoretical maximum coil current is always larger than the required nominal value until a frequency of 70 kHz is reached. While the absolute maximum currents shown are technically unachievable by the LMH6321 current buffer, it nonetheless shows that it is possible

to successfully drive the transmitter coil load with a reduced voltage range of 7.5 V.

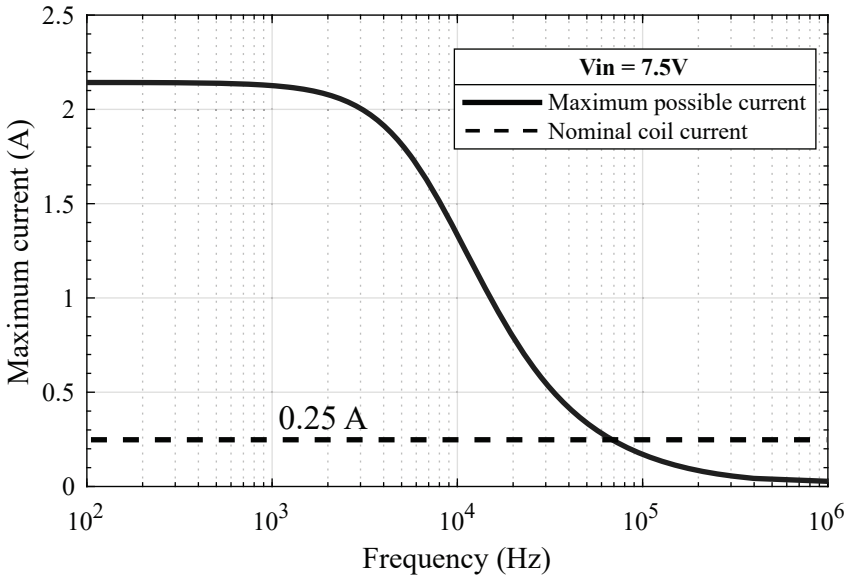


Figure 4.11: Magnitude bode plot showing the maximum possible current achievable through the transmitter coil given a 7.5 V voltage swing. The minimum required transmitter current is shown by the dotted 0.25 A line. This minimum current is achievable through the entire transmitter band (20-30 kHz) until the frequency reaches approximately 100 kHz at which point the load impedance $Z_{coil} \approx 47\,\Omega$.

4.3.1 AC coupled driver design

The transmitter driver was revised using an AC coupled design shown in Fig. 4.12. This design change from a DC system to an AC coupled design is a consequence of using a single supply rail to power the current booster circuitry. Having a directly coupled system is undesirable in this case as it would result in a constant DC current through the transmitter coil even when the waveform generator is inactive, since the output of the LMH6321 would be a constant 7.5 V.

Component functions

- R_1, R_2, R_3 and R_4 serve as resistor-divider pairs used to bias circuit nodes to the midrail voltage of 7.5 V. High precision 0.1 % resistors were used to ensure precise biasing.
- C_1 and C_2 serve as AC coupling capacitors. They allow the LMH6321 circuit to operate at a shifted DC operating point of 7.5 V while preserving the integrity of the reference voltage signal and preventing unwanted DC currents.
- The TL082 behaves as a unity-gain buffer in this configuration and provides a low-impedance bias voltage to the LMH6321, allowing it to operate at the midrail voltage.
- R_{comp} and C_{comp} form an optional shunt RC compensation network. This network inserts positive phase into the amplifier feedback signal in order to increase the system phase margin and reduce unwanted oscillations. This is discussed in section 4.3.3.
- L_{coil} and R_{coil} are the electrical transmitter coil parameters.
- R_s is the current sense resistor used to generate the feedback voltage signal.
- R_{fb1} and R_{fb2} are feedback resistors which feed the inverting input of the LM7171. R_{fb1} conducts the current feedback signal, while R_{fb2} provides a high impedance DC return path for the feedback loop. Without a DC feedback path, any slight DC offset between the inverting and non-inverting inputs will be multiplied by the open-loop gain of the op-amp and cause large undesired deviations in the output voltage.

Load analysis

Introducing an AC coupled load requires specifying the coupling capacitors, C_1 and C_2, such that they provide a low impedance current path in the frequency band of interest. A load analysis was performed to investigate which capacitor values should be considered in the circuit design. The critical capacitor is C_2 as this must conduct

sufficient current through the transmitter coil during operation. The simulated circuit is shown in Fig. 4.13. A dependant voltage source with unity gain is used to model the LMH6321 as an ideal high input impedance current buffer. R_1, R_2 and C_1 form the input *RC* coupling network to the buffer as shown previously in Fig. 4.12. C_2 is the output coupling capacitor to the transmitter coil.

C_1 was empirically chosen as 1 µF, in combination with R_1 and R_2 set to 10 kΩ to produce a high-pass *RC* filter network with $\omega_c = 200\,\mathrm{rad\,s^{-1}}$ which is sufficient to pass the transmitter's desired frequencies. The circuit was simulated with an input voltage of 7.5 V, equal to the maximum voltage swing provided by the design. Multiple orders of C_2 were simulated with their responses shown in Fig. 4.14. A coupling capacitance of 100 µF was chosen due to its flat gain response in the main field generator frequency band between 10 and 30 kHz. This larger capacitance value also allows the potential use of lower transmitter frequencies in the kHz range. This may be a desirable when minimising interference due to Eddy-current distorters [16]. A distortion-free low frequency field generator could be combined a distortion susceptible generator to produce an improved estimator-based tracking system design, in which the distortion-free field generator behaves as a reference measurement [12].

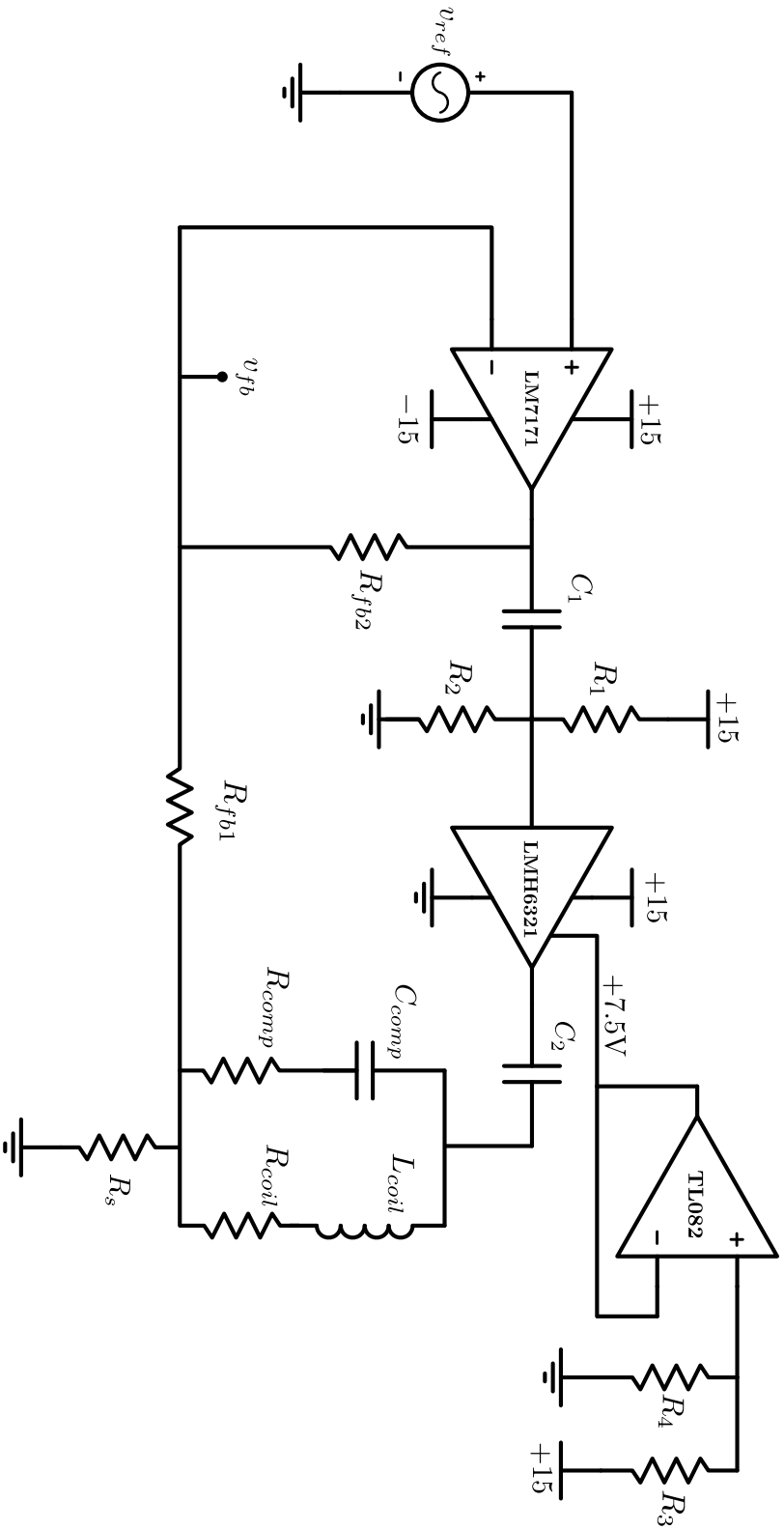


Figure 4.12: Simplified circuit schematic of the ac coupled closed loop transmitter drive with current booster circuit.

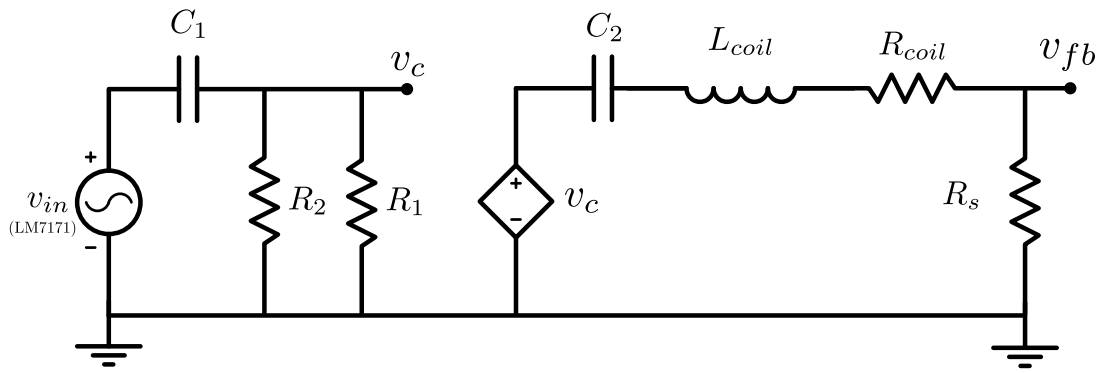


Figure 4.13: Small signal circuit model used to simulate the effects of coupling capacitor values in the ac coupled transmitter driver design.

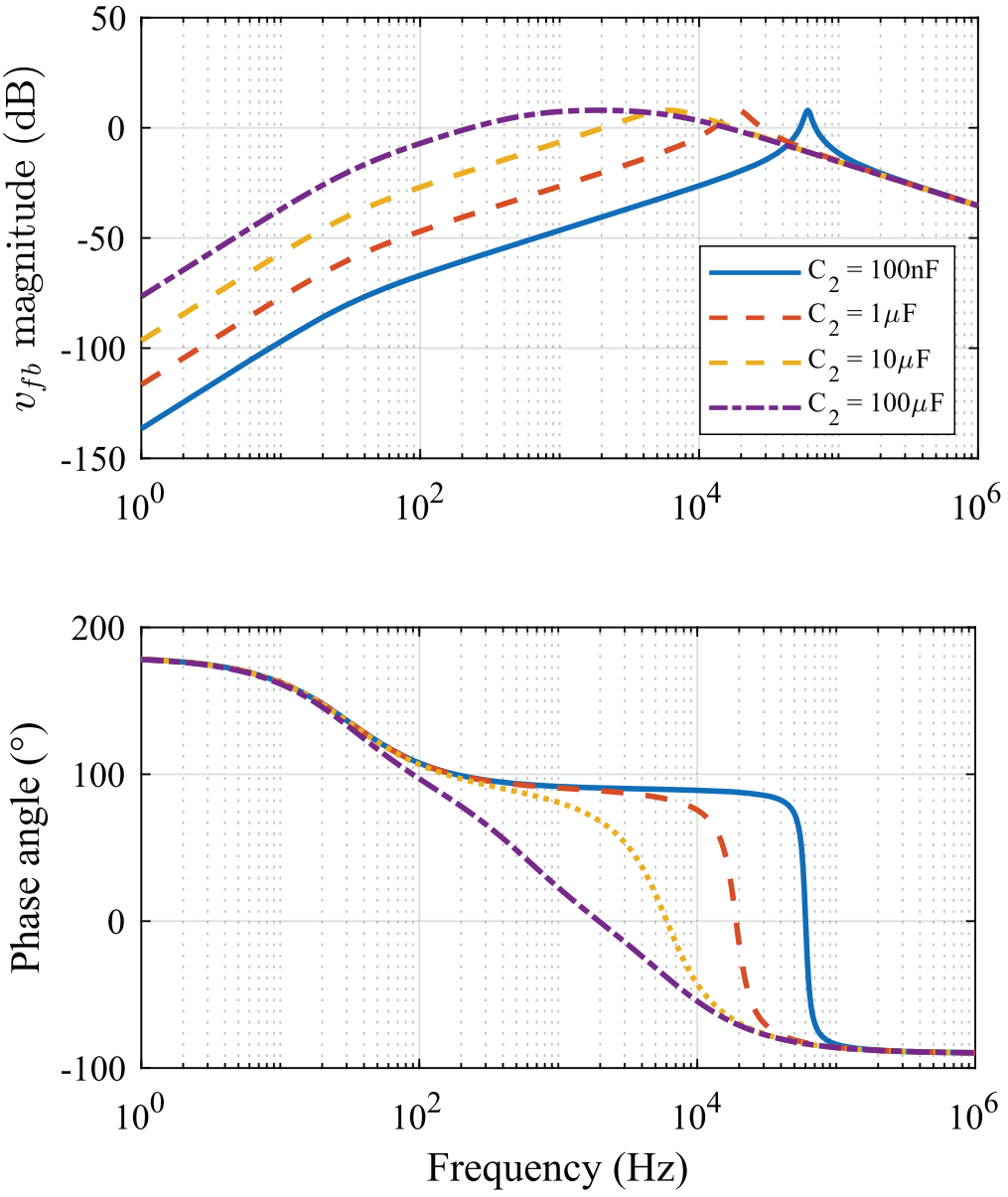


Figure 4.14: Bode diagram of the simulated open-loop frequency response using different coupling capacitor values.

4.3.2 Open-loop transmitter analysis

The response of the optimised current driver in Fig. 4.12 was simulated in SPICE using the part specific circuit models for all components provided by the manufacturer. AC analysis was performed in Multisim (National Instruments, TX, USA). The v_{fb} node was analysed. For simulations C_1 was set to 1 µF and C_2 set to 100 µF. An equivalent DC coupled split supply design was also simulated for reference. The frequency response of the circuit between 0 and 1 MHz is shown in Fig. 4.15. Significant differences between both AC and DC coupled designs are found throughout the first three decades of the frequency response in Fig. 4.15. For very low frequencies ($f < 10$ Hz) the phase angle approaches 180°. Moving towards the 10 kHz band, the responses converge to become identical. This difference in response is due to the coupling capacitors, C_1 and C_2, shown in Fig. 4.12. The impedance of each capacitor produces a large capacitive reactance, X_C, where the magnitude of the reactance is given by (4.9) and the phase angle given by (4.10)

$$|X_c| = \frac{1}{\omega C} \tag{4.9}$$

$$\arg(X_c) = \arctan(-\omega C) \tag{4.10}$$

where ω is the angular frequency. A low frequencies, Xc dominates the signal chain and produces a large positive phase contribution as shown in the lower frequencies in Fig. 4.15. The choices of C_1 and C_2 result in both AC and DC responses converging at the desired transmitter frequency band of 10 to 30 kHz.

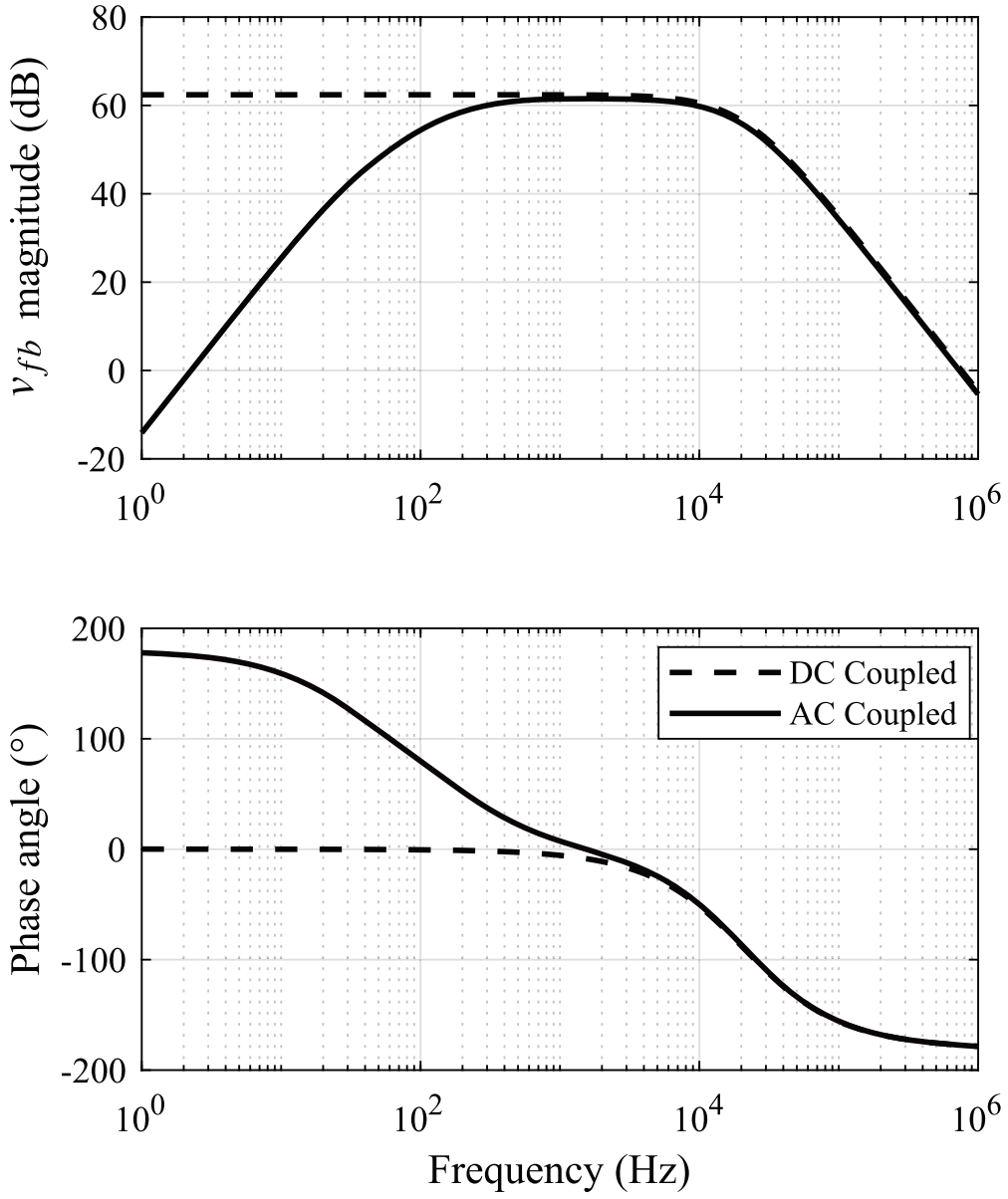


Figure 4.15: Frequency response of open-loop transmitter without RC compensation network. The initial positive phase shift at low frequencies is a consequence of the AC coupled design inserting +180° of positive phase. A phase margin of 65° is present at 30 kHz.

4.3.3 Closed-loop transmitter analysis

Closing the loop of the transmitter involves connecting v_{fb} to the inverting input of the LM7171. From to Fig. 4.7 we can see that the phase margin of the fully simulated system (65°) is considerably higher than that of the transfer function simulation shown in Fig. 4.7 (15°) developed from [90, p. 92]. This phase margin increase may be due to using the more accurate system SPICE model for the LM7171 amplifier which takes into account all the part specific circuit parasitics. Consequently potential for closed-loop oscillation is significantly reduced as a result, reducing the requirement for an *RC* compensation network. This is verified in section 4.10 where the start-up and steady-state current waveforms are analysed.

The closed loop frequency response of the transmitter driver is shown in Fig. 4.16. The transmitter exhibits a flat gain characteristic at the operational frequencies of the tracking system, with an overall unity-gain bandwidth between 5 kHz and 100 kHz. This flat characteristic is desirable as it allows the user to vary the transmission frequencies within a wide band without running the risk of saturating the current buffer.

Closed-loop current tracking performance

For the ideal current source, shown in Fig. 4.5, the current through the sensing resistor R_s should be independent of the load impedance Z_{coil}. Referring back to Fig. 4.5 and (4.3), it can be seen that the output current depends solely on the sensing resistor R_S. In reality, amplifiers have limited voltage swing and output current drive capability as discussed in section 4.3. However, a constant current design is desirable as it implies that the driving currents can be assumed constant within a certain range of Z_{coil}. In the context of electromagnetic tracking, this functionality would allow different field generators of different impedance characteristics to be connected without altering the coil current.

A parameter sweep analysis was performed to investigate how effectively the current drive circuit drive could react to various loads. Both transmitter coil resistance and inductance were swept over five discrete values using a 1 kHz to 1 MHz AC analysis. A reference voltage v_{ref} of 200 mV was used for the analysis. The magnitude plots for each sweep are shown in Fig. 4.17 and Fig. 4.18. It can be seen from both plots

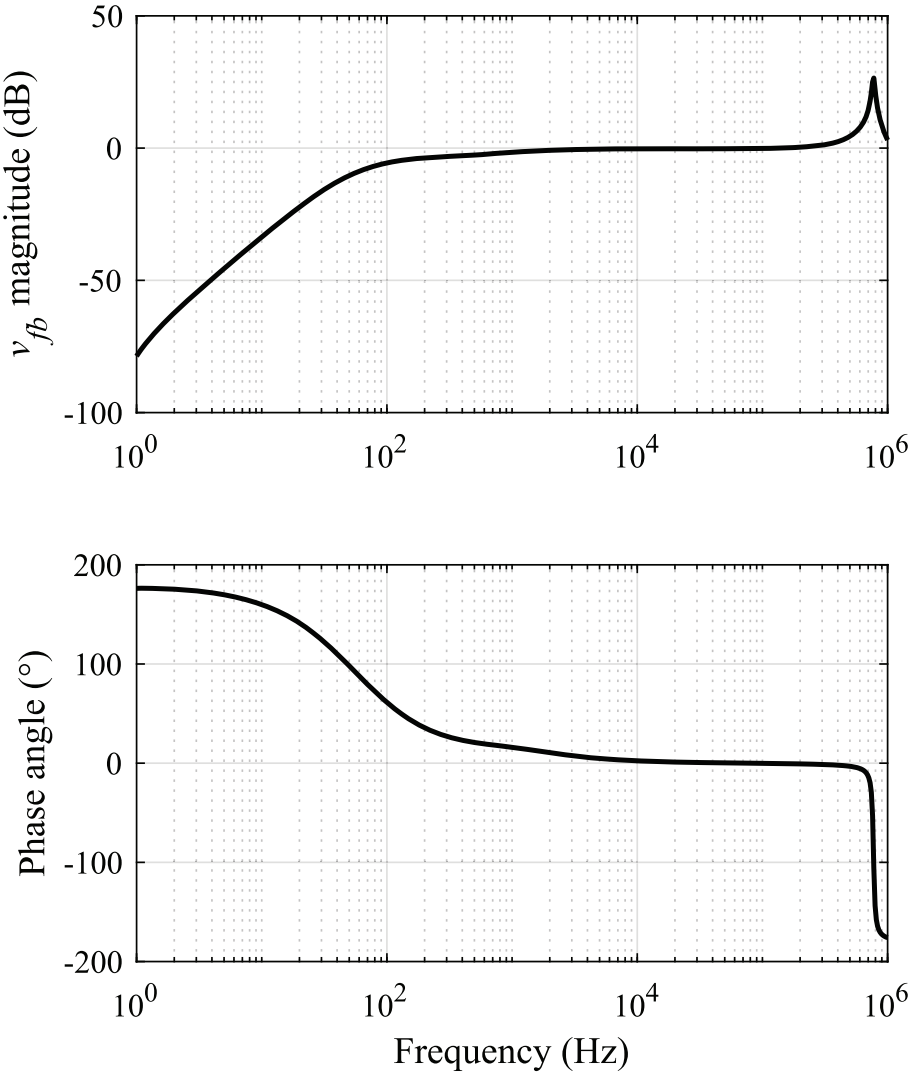


Figure 4.16: Bode diagram of the closed loop frequency response of the transmitter driver. A flat ≈ 0 dB gain response is observed between 5 kHz and 100 kHz. A resonant peak occurs at 800 kHz, but this is sufficiently distant from the operating frequencies of the tracking system to pose problems

that the coil current remains approximately constant for each parameter. The precise currents are shown in Table 4.1.

It can be observed from Table 4.1 that changing the coil inductance L_{coil} has a

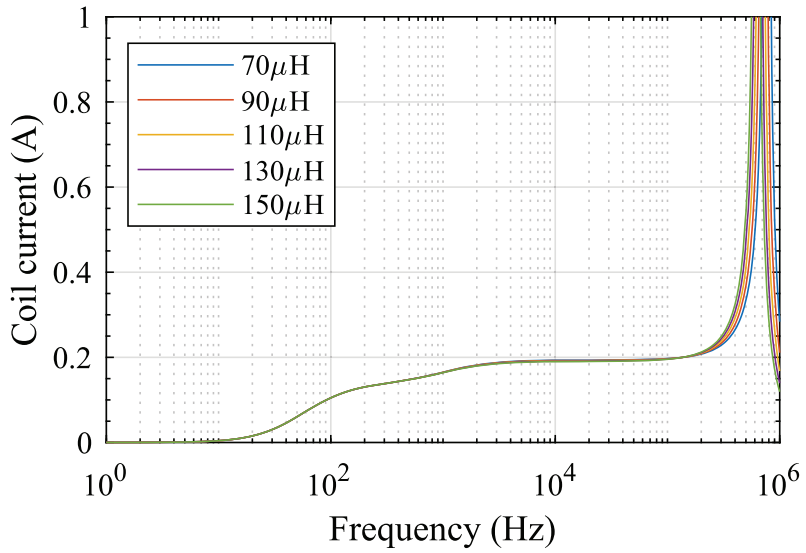


Figure 4.17: Magnitude response of transmitter coil current for different values of coil inductance.

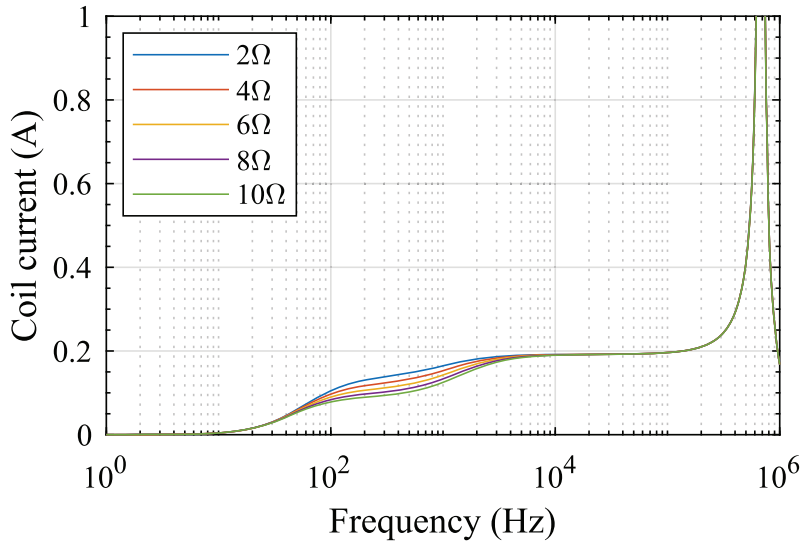


Figure 4.18: Magnitude response of transmitter coil current for varying values of coil inductance L_{coil} and resistance R_{coil}. Coil parameters were varied independently for each corresponding analysis.

much greater effect on the closed-loop performance when compared to scaling the resistance R_{coil}. The standard deviation of the current is approximately 2.54 mA dur-

L_{coil} (µH) ($R_{coil} = 2\Omega$)	Coil current (mA)
70	193.683
90	192.033
110	190.411
130	188.816
150	187.247
mean μ	190.44
std. dev. σ	2.54

R_{coil} (Ω) ($L_{coil} = 70\mu H$)	Coil current (mA)
2	192.032
4	191.915
6	191.789
8	191.655
10	191.512
mean μ	191.78
std. dev. σ	0.2057

Table 4.1: Transmitter coil current for different transmitter coil parameters. Parameters were var Simulated measurements were taken at a transmission frequency of 20 kHz.

ing the inductance sweep, but only 0.2057 mA for the resistance sweep. Assuming a constant current for different transmitter PCB designs is clearly incorrect in this case, particularly if the coil inductance changes significantly. Nonetheless the performance should be sufficient to account for small deviations in the manufacturing process of the PCB, including the slight variations in copper trace resistance that can occur during low-cost etching processes.

4.4 Sensor amplifier design

The developed tracking system uses electromagnetic induction in order to produce a voltage signal on a small inductive sensor coil. Induction sensors comprise primarily of a wound coil wrapped around a ferromagnetic core. A ferrite core is typically used, with the core increasing the overall sensitivity of the sensor by the apparent permeability of the material μ_a, discussed in chapter 7. This manufacturing process allows extremely small sensors to be fabricated while maintaining an acceptable signal-to-noise ratio whilst using low-energy magnetic fields. A full derivation of the sensor model can be found in chapter 3.

However, the induced sensor voltage a very weak, high-impedance signal in the order of microvolts. Amplification of the received sensor signal is required before any further signal processing steps can take place. Previous work [90, p. 70] saw the development of a 2nd-order sensor transfer function model, shown in (4.11), for a 5 degree-of-freedom induction sensor, where v_{in} is the induced voltage on the coil

and v_{out} is the apparent voltage at the sensor terminals. This sensor model enabled the design and implementation of a magnetic field detector circuit [90, p. 102]. The equivalent circuit model for an induction sensor from which the transfer function was derived is shown in Fig. 4.19 where R_s and L_s are the sensor's series resistance and inductance parameters, and C_s is the sensor's winding capacitance.

$$\frac{v_{out}}{v_{in}} = \frac{\dfrac{1}{L_s C_s}}{s^2 + \dfrac{R_s s}{L_s} + \dfrac{1}{L_s C_s}} \tag{4.11}$$

This section builds upon this previous work by describing the design of a refined magnetic field detector circuit for integration into the Anser EMT system which takes size, cost and electrostatic safety into consideration.

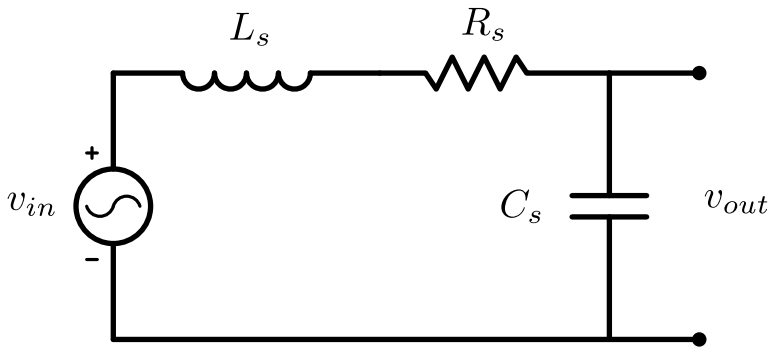


Figure 4.19: Equivalent circuit model for an induction sensor

The original detector circuit was an instrumentation amplifier design based around the INA128, a high performance amplifier from Texas Instruments [139]. The most critical characteristics for an amplifier in this sensor amplification role is its linearity and noise performance metrics. Replacing the INA128 with an INA163 amplifier [140] results in noise and cost improvements. Table 4.2 shows a comparison of the main specifications of the two amplifiers.

Table 4.2: Specifications of INA128 and INA163 instrumentation amplifiers taken from [141, p. 363] and the respective device datasheets [139, 140]. INA163 experience significantly reduced input stage voltage noise due to its increased input bias current requirements.

Datasheet Metric	INA128	INA163
CMRR (dB)	120	100
Input Bias Current (nA)	5	12000
Max. Gain (V/V)	10000	10000
-3dB BW, $G = 100$ (kHz)	200	800
Voltage Noise @ 1 kHz ($\mathrm{nV}/\sqrt{\mathrm{Hz}}$)	8	1
Current Noise @ 1 kHz ($\mathrm{pA}/\sqrt{\mathrm{Hz}}$)	0.3	0.8
Voltage Noise @ 10 kHz+, $G = 500$ ($\mathrm{pA}/\sqrt{\mathrm{Hz}}$)	8	1.1
Current Noise @ 10 kHz+, $G = 500$ ($\mathrm{nV}/\sqrt{\mathrm{Hz}}$)	0.3	0.8
Price per unit($)	~ 3.41	~ 2.90

4.4.1 Noise analysis

To estimate of the noise characteristics of the amplifiers, the noise figure was calculated assuming an operating frequency of 30 kHz and a sensor impedance of 377 Ω (based on R, L and C values of 70 Ω, 2 mH and 900 pF respectively from [90]). Both instrumentation amplifiers have bipolar junction transistor (BJT) input stages. The relevant noise figure equation is given in (4.12) [141].

$$\mathrm{NF} = 10\log_{10}\left(1 + \frac{e_n^2 + (i_n R_s)^2}{4k_B T R_s}\right)\mathrm{dB} \tag{4.12}$$

where e_n and i_n are the voltage and current noise parameters extracted from the device datasheets, R_s is the source impedance of the connected sensor, T is the ambient temperature and k_B is the Boltzmann constant. If the induction sensor is connected directly to the amplifier, (ignoring any input biasing resistors for the moment), then the noise figures using each amplifier would be:

$$\mathrm{NF}_{\mathrm{INA128}} = 20.93\,\mathrm{dB}, \quad \mathrm{NF}_{\mathrm{INA163}} = 5.44\,\mathrm{dB}$$

INA163 has a lower noise figure due to the relatively low sensor source impedance.

A low source impedance allows the voltage noise term, e_n, to dominate the noise figure equation. For sensors with high input impedances in the orders of kiloohms and upwards, the current noise value, i_n, becomes dominant and the INA128 would be a much better design choice. This is demonstrated in Fig. 4.20 where the noise figure of each amplifier is plotted with respect to source impedance.

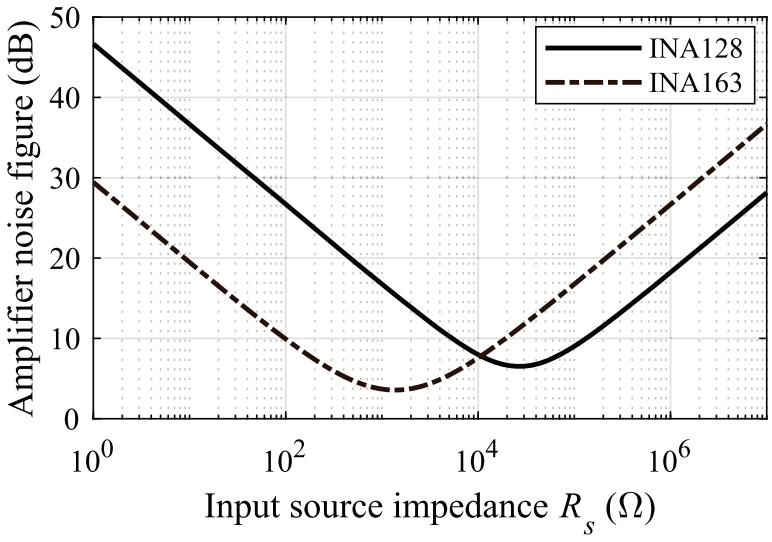


Figure 4.20: Simulated noise figures for both INA128 and INA163 instrumentation amplifiers with varying load impedance R_s with gain G set to 500. At approximately 10 kΩ source impedance, the noise figure of the INA128 becomes more favourable than that of the INA163.

4.4.2 Amplifier circuit design

An improved instrumentation amplifier circuit utilising the INA163 is shown in Fig. 4.21. Diodes D_z act as input protection for the amplifier input pins. These zener diodes have a reverse breakdown voltage of 15 V. R_{in} and C_{in} form an input low-pass filter. The filter impedance was designed such that the source impedance as seen from the input pins did not exceed 10 kΩ. High value R_B resistors provide the required biasing for the INA163 inputs since the induction sensor is a floating source. The gain of the circuit is adjusted using a potentiometer. The output voltage, v_{out}, connects to the system's data acquisition unit (DAQ).

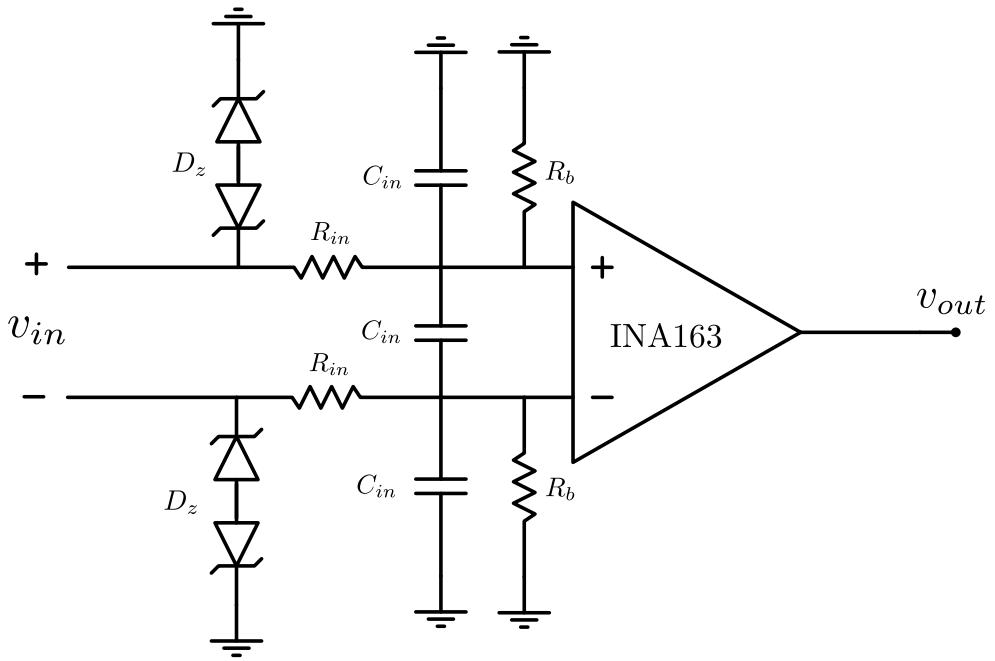


Figure 4.21: Simplified schematic of the implemented instrumentation amplifier circuit. For simplicity, programming gain potentiometer R_G is not shown.

4.5 Microcontroller

The waveform generators discussed in section 4.2.1 require programming each time the system is turned-on. The original system utilised an Arduino Uno microcontroller *(Scarmagno, Italy)* for this purpose. In this design, the controller was hard-programmed with the desired transmission frequencies which were downloaded to the corresponding waveform generators during the power-on-reset process. The initial system prototype did not provide a facility to alter these frequencies during operation and required the enclosure to be physically opened to reprogramme the microcontroller.

An improved microcontroller-based interface was developed to allow the system frequencies be modified in real-time during system operation. This new interface provides the user with the ability to alter the system frequencies with ease based on the desired application and will be discussed in section 4.10.4. A Teensy 3.2 microcontroller *(PJRC, Oregon, USA)* was used as the programmable platform due to its increased speed, smaller size and compatibility with the Arduino code ecosystem. Table 4.3

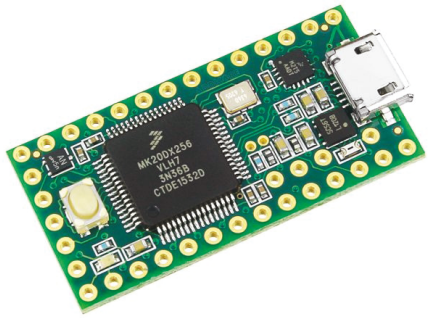


Figure 4.22: Photograph of a Teensy 3.2 microcontroller.

Specification	*Uno*	*Teensy 3.2*
CPU Type	8-bit	32-bit
CPU Freq. (MHz)	16	120
RAM (kB)	2	64
Program Mem. (kB)	32	256
Price per unit ($)	22	22.50

Table 4.3: Specifications comparing Uno and Teensy 3.2.

compares some of the basic specifications of both controller platforms.

4.6 Data acquisition unit

The original system implementation used a National Instruments USB-6216 acquisition device for sampling the current and sensor channels of the tracking system. In the revised system, the OEM variant of a similar device, the NI-USB-6212 was used instead. This board features identical specifications to the USB-6216 albeit with reduced electrical isolation on the analogue input channels, which are not required: It was decided to forego the isolation features since the analogue inputs are already buffered by the INA163 input stage which features electrostatic discharge input protection discussed in section 4.4.2.

Table 4.4: USB-6212/6216 specifications

Specification	NI USB-6212	NI USB-6216
Analog Inputs	16	16
ADC resolution	16-bits	16-bits
Max. Sampling Freq.	400 kHz	400 kHz
Digital I/Os	32	32
Unit Cost	€1350	€1610



Figure 4.23: National Instruments USB-6212 OEM PCB

4.7 Power delivery

The previous tracking system prototype did not feature on-board voltage conversion or regulation and thus required the use of a bench power supply. An EL302RT (*Fort Worth, TX, USA*) linear power supply shown in Fig. 4.24 was used to supply low-noise bipolar 15V power rails through banana plugs to the system. While this supply provides clean power, it is not suitable box-build product due to its large size and cost. A integrated dual rail power design was created to allow the system to operate from a single 15V wall adapter. The individual components of this design will in section 4.7.1.

4.7.1 Mains power

An off-the-shelf medical grade power supply was chosen as the main power delivery system for the tracking system. The ME60 60 Watt supply (SL Power Electronics, South Molton, UK) was chosen due to its compliance with isolation and EMC standards required by electronic medical devices; in particular the IEC 60601 and the Means of Patient Protection (MOOP) standards contained within [142]. A 5.5mm diameter barrel jack provides a standard connection for interfacing with the tracking system. The ME60 supply is suitable for use in all regions of the world and can accept a voltage input range of 90-264 Volts.



(a)



(b)

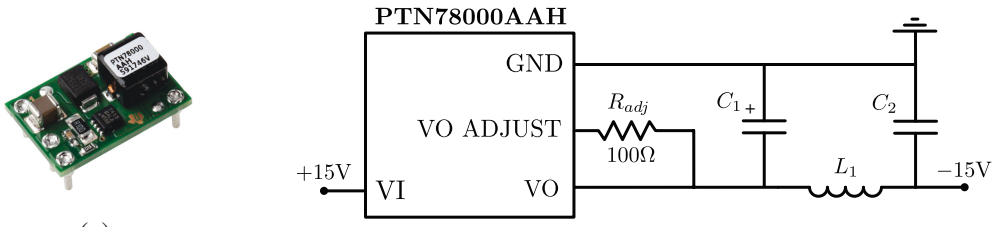
Figure 4.24: (a) A TTi EL302RT linear DC power supply. (b) General purpose medical grade power adapter.

4.7.2 Input filtering

The ME60 is a switching power supply and therefore produces significant switching noise compared to using a linear supply. A common mode choke (10 µH, *Wurth Elektronic, Niedernhall, Germany*) in combination with some electrolytic capacitors (100 µF, *Nichicon, Kyoto, Japan*) was designed to remove any common mode noise introduced by the barrel jack cable.

4.7.3 Split rail design

A bipolar supply is required for the majority the analogue circuitry in the tracking system. A DC/DC converter module was used to step the +15V rail to -15V. The Texas Instruments PTN78000AAH adjustable negative output converter was used to perform this conversion [143]. Output filtering is also required on this converter design. A capacitor-inductor-capacitor (CLC) filter (also known as a 'pi' filter) was implemented to attenuate switching noise from the converter. Fig. 4.25b shows the schematic of the converter circuit. The CLC behaves as a second order low-pass filter. The simulated response of the filter for various load current is shown in Fig. 4.26.



(a) (b)

Figure 4.25: (a) The Texas Instruments PTN78000AAH adjustable regulator module. The module measures 19 mm×13 mm and can deliver up to 1.5 A of current. (b) The schematic of the converter implementation. R_{adj} was chosen as 100 Ω according to the device datasheet to set the converter output to −15 V. Component value C_1 was set to 100 µF according to the datasheet, while C_2 and L_1 were empirically set to 22 µF and 10 µH respectively for attenuating the converter's nominal switching frequency of 440 kHz [143].

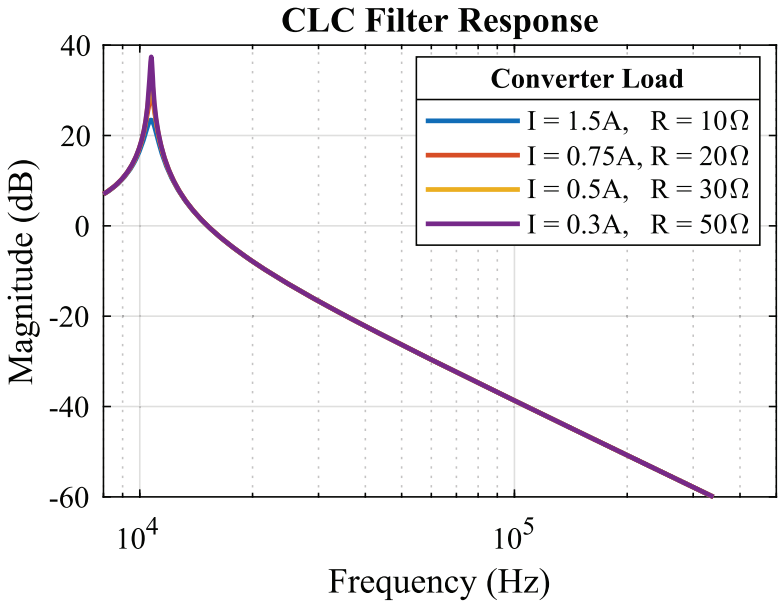


Figure 4.26: Simulated CLC filter responses for different load currents. Loads of 10 Ω, 20 Ω, 30 Ω and 50 Ω are simulated. A pole exists at approximately 10 kHz, but is sufficiently far from the converter's typical switching frequency of 400 kHz to cause stability issues.

4.7.4 Linear regulation

The $\pm 15\,\mathrm{V}$ rails may contain high frequency noise which cannot be fully eliminated by passive inductor-capacitor filters. Active regulation is still required to reduce this noise figure use with sensitive analogue amplification circuitry. A low drop-out (LDO) regulation stage was designed for both rails to achieve this goal. The Texas Instruments TPS7A33 [144] and TPS7A47 [145] were selected to regulate the -15 V and +15 V rails respectively.

4.8 Field generator design

The system field generator is responsible for emitting the alternating the magnetic field into the working volume. The original field generator was comprised of eight individual square transmitter coils of 25 turns each. The coils were housed in a custom machined polycarbonate housing and were individually wired to the transmitter driver using coaxial cable. The design is quite costly over multiple runs due to the machining required and can suffer variances in coil placement due to machine tolerances. The new design shown in Fig. 4.27 shows all transmitter coils integrated onto a single $30 \times 30\,\text{cm}$ printed circuit board (PCB). Manufacturing the field generator in this manner results in significant cost savings in terms of materials and assembly time, but it also reduces coil tolerating problems by taking advantage of the micron-level accuracy of PCB fabrication process [146]. For the purposes of tracking this means that the field generator can be interchanged without affecting the calibration accuracy of the system as discussed in section 4.3.3.

4.9 Enclosure design

A user-friendly enclosure was designed for both transmitter and driver PCBs. The designed enclosure allows the system to be transported and easily assembled/disassembled in a matter of minutes. An off-the-shelf enclosure was selected for the driver PCB while a custom housing was designed in-house for the field generator PCB.

4.9.1 Driver PCB enclosure

An off-the-shelf enclosure from a German enclosure manufacturer (*OKW, Buchen, Germany*) was used to mount the driver PCB for the tracking system. The Eurocase shown in Fig. 4.28 was chosen due to its large PCB capacity of $350 \times 220\,\text{mm}$ [147]. The layout of the driver PCB was performed according to these dimensions. Aluminium front and back panels are also provided with the enclosure which were machined separately in order to access all the external system connectors and buttons.

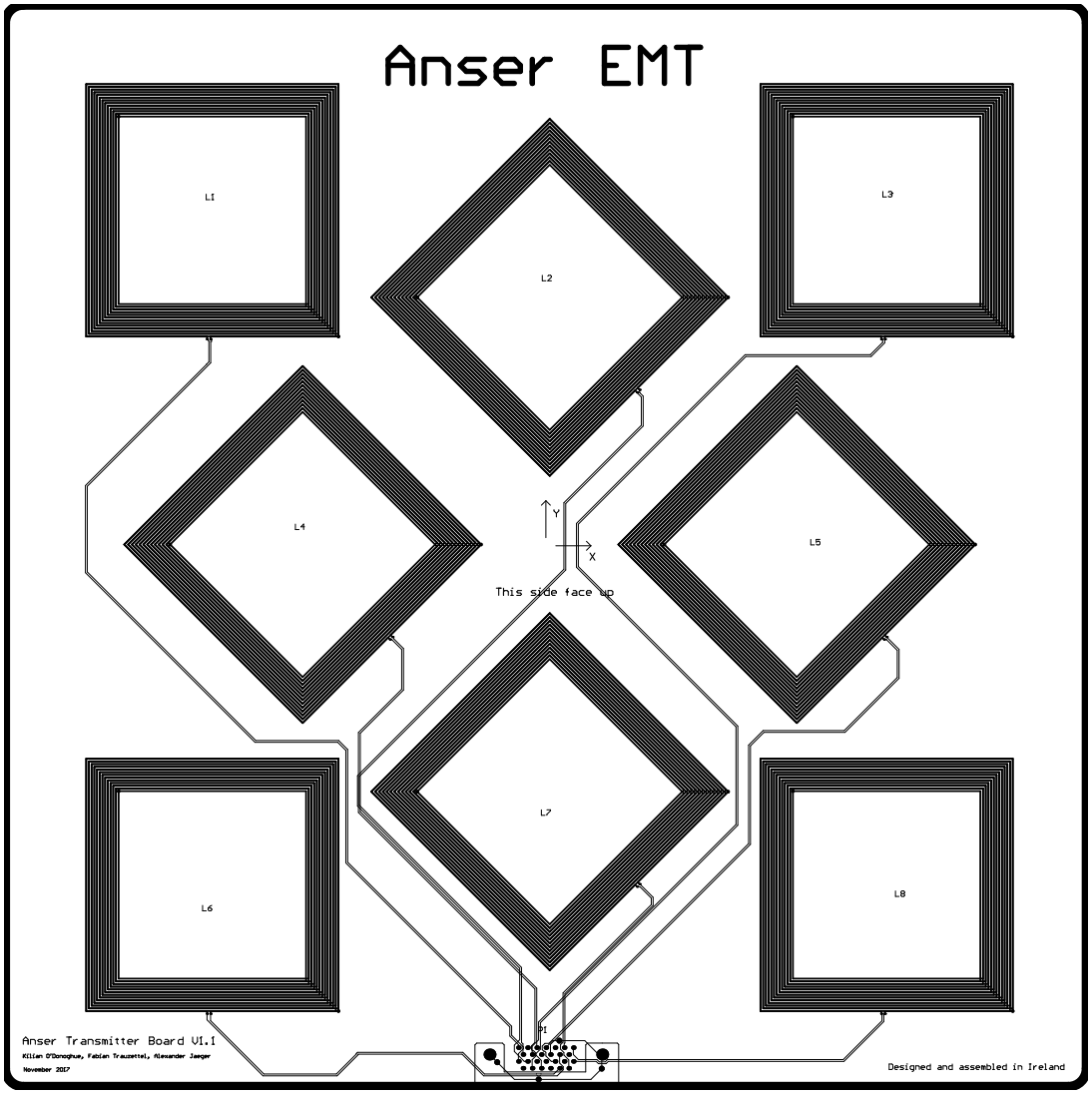
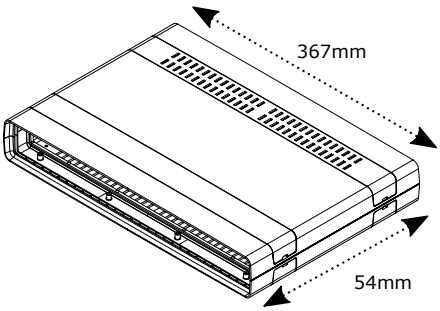


Figure 4.27: Single PCB field generator design for the Anser EMT system. The board measures precisely 30×30 cm, measures 1.6mm thick and is connected to the system base station with a 3M 26-position miniature delta ribbon (MDR) connector. The lead trace pairs between the connector and the respective coils we're designed to be as close to the coils and as narrow as possible in order to prevent unwanted magnetic coupling. The measured inductance value for each coil is 70µH with a series resistance of 2Ω. The coils furthest from the connectors have slightly larger resistance values due to their longer trace lengths. The origin of the tracking system is defined as shown at the centre of the PCB.



(a)



(b)

Figure 4.28: (a) Diagram of the main dimensions of the Eurocase enclosure. (b) 3D rendering of the enclosure with front panel machines for the field generator cable connector and sensor ports.

4.9.2 Field generator PCB enclosure

The field generator PCB shown in Fig. 4.27 is approximately 1.6mm thick and contains bare electrical contacts which require isolation. The PCB itself is made of fibreglass resin (FR4) and is prone to cracking and fracture if mishandle or if large external force is applied to it. The tracking system is designed for future use in medical procedures, therefore the field generator must be designed to support the weight of a patient. The tracking system also requires calibration before use, and this process necessitates that a number of test point positions be sampled above the field generator with a calibrating induction sensor [92]. Acquiring these points requires having a ground truth measurement of the sensor's position, a task which is very difficult to achieve using the bare PCB as a reference. The previous tracking system design used Duplo blocks (*The Lego Company, Billund, Denmark*) to precisely locate the test sensor in known positions for the calibration process [92]. An alternative approach was developed by integrating the test positions within the field generator enclosure as a uniform grid of holes as shown in Fig. 4.29. A plastic dowel containing the calibrating test sensor is then placed at each of these test positions during the calibration process and is shown in Fig. 4.30.

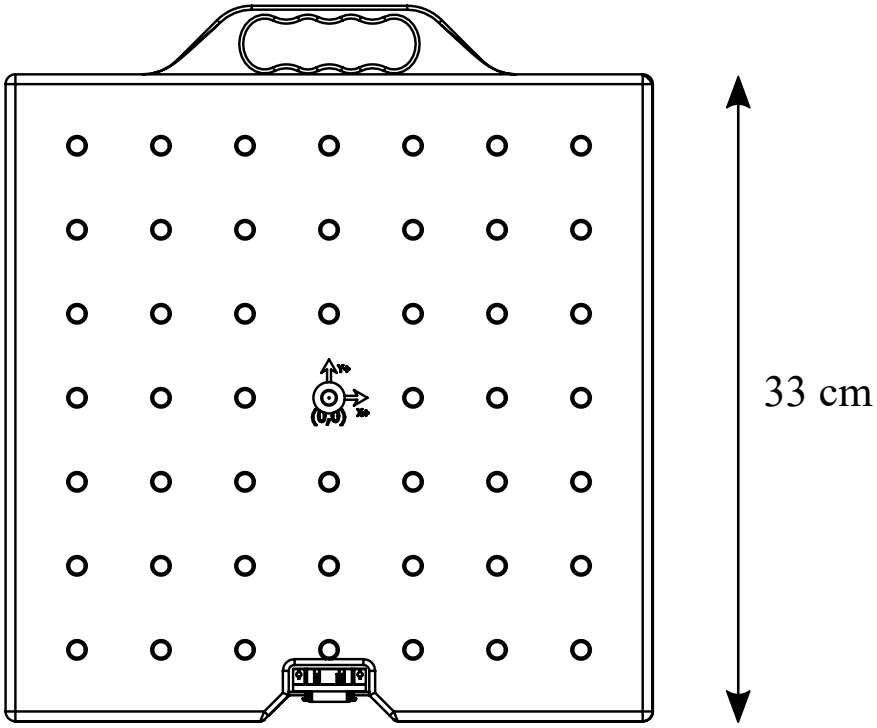


Figure 4.29: Plan view of the field generator enclosure showing the square 7x7 point grid of calibration test points positions.

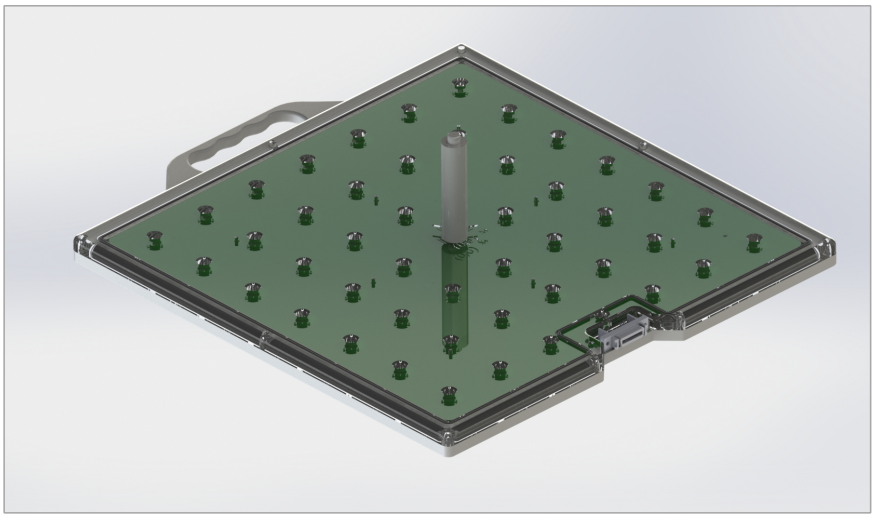


Figure 4.30: 3D rendering of the enclosure in Solidworks with PCB and calibration sensor in the central test position.

4.10 System operation

This section briefly explores the system behaviour on power-on and how the system may be programmed for different transmitting frequencies.

4.10.1 System start-up

The system start-up sequence occurs when the system is initially powered-on using the power switch. Fig. 4.31 shows the initialisation steps from the perspective of a single coil current driver. A reset signal is initially sent to all waveform generator circuits, followed by a byte sequence to programme each coils' desired frequency. Each waveform generator then begins producing the programmed frequency. A settling time of approximately 0.2 s is required.

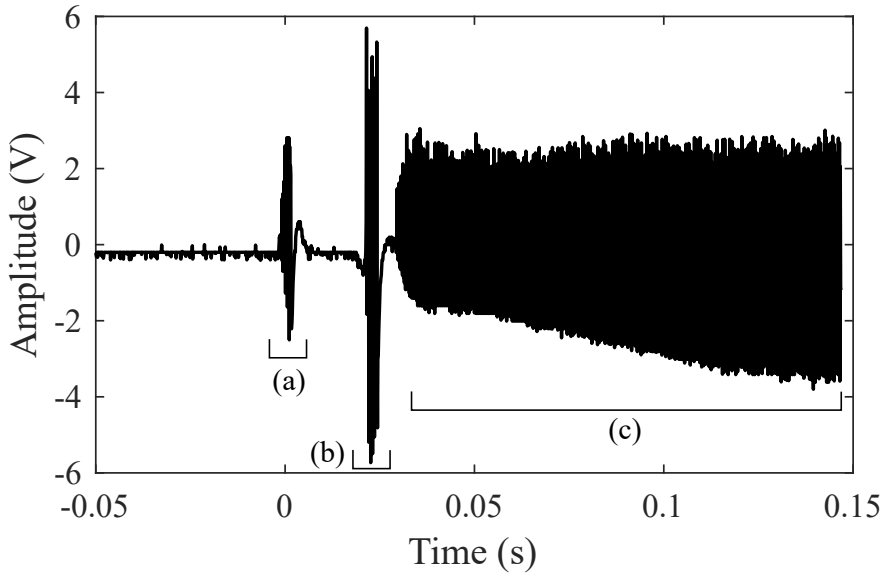


Figure 4.31: Zoomed-out view of a single coil driver's output voltage waveform envelope during the system start-up sequence. (a) The AD9833 waveform generator is reset. (b) Waveform generator is programmed via the Teensy microcontroller. (c) Waveform generator begins producing the programmed frequency and output settles to steady-state after a transient period of approximately 0.2 s

4.10.2 Current settling

All electronic components undergo temperature dependent drift when heated. This effect becomes noticable when the system is powered-on from ambient temperature (cold-start). The gradual heating of the components due to the power consumption of the system results in the transmitter current drifting over time as shown in Fig. 4.32. The LMH6321 current buffer reaches a maximum temperature of $\approx 55^{\circ}$C in steady state. The printed circuit board behaves as a heat sink which may, over time, cause the value of connected passive components' values to drift with temperature. Component value drift in the feedback loop will cause changes to the system's response, and is a drawback of using a densely populated PCB design. A maximum drift of 2 mA is observed. The system achieves constant current approximately 6 minutes after power-on. One should therefore let the system *warm-up* for this length of time in order to achieve the best calibration.

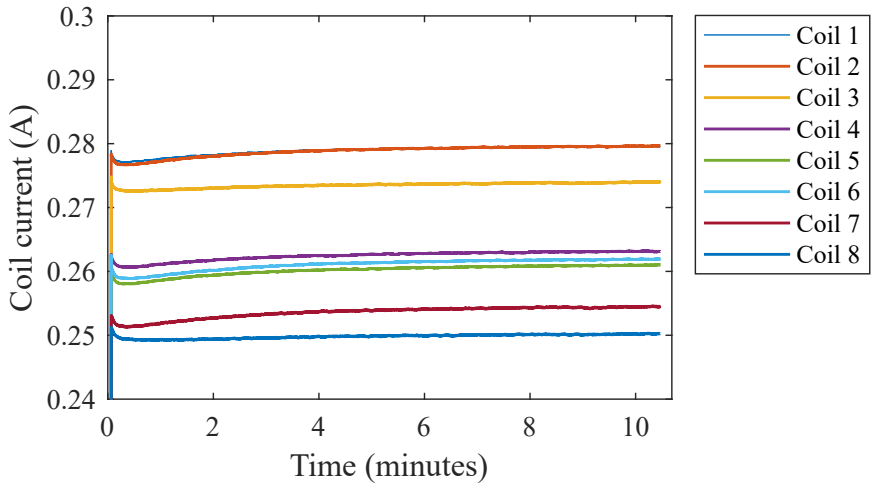


Figure 4.32: Current amplitude versus time for each transmitter coil when the system is turned on at ambient temperature. The coil currents take approximately 6 minutes to settle to steady state.

4.10.3 Steady state

Once powered-on, initialised and warmed-up, the system can be assumed to be operating in steady state: Each transmitter coil of the field generator produces an alternating current signal of constant amplitude to produce a spatially varying magnetic field in the tracking volume. The current through each coil is monitored using the DAQ in Fig. 4.23. The plot of the sensed field generator current signal is shown in Fig. 4.33 and the frequency spectrum of this signal is shown in Fig. 4.34. The spurious free dynamic range (SFDR) of the signal is defined as the strength of the fundamental signal to the highest undesired signal [141]. An SFDR of 40dB is observed using the 20 kHz fundamental frequency as reference. The total harmonic distortion (THD) is defined in (4.13) as the ratio of all powers of all N_H harmonic components to the fundamental frequency F.

$$\text{THD} = \frac{\sqrt{V_1^2 + V_2^2 + \ldots V_{N_H^2}}}{V_F} \tag{4.13}$$

$$\text{THD}_{Total} = \frac{\sqrt{V_1^2 + V_2^2 + \cdots + V_{N_H^2}}}{\sqrt{V_{F1}^2 + \cdots + V_{F8}^2}} \tag{4.14}$$

Taking the 20 kHz as the fundamental frequency, a THD of 1.3% is observed during normal operation. If all eight coil frequencies are considered, as fundamentals then the THD can be written as (4.14), where the calculated THD is approximately 0.35%. It should be noted that the magnitude of the low-frequency harmonics present in the current sense signal do not significantly impact the induced tracking sensor signal as shown in Fig 4.35. The natural high-pass filtering effect of Faraday's law in combination with passive circuit filtering produce a clean output signal which contains significantly fewer low-frequency tones. With the exception of the DC component, the observed SFDR is 57 dB (i.e. referenced to 1 V). A new THD of 0.2% found using (4.14).

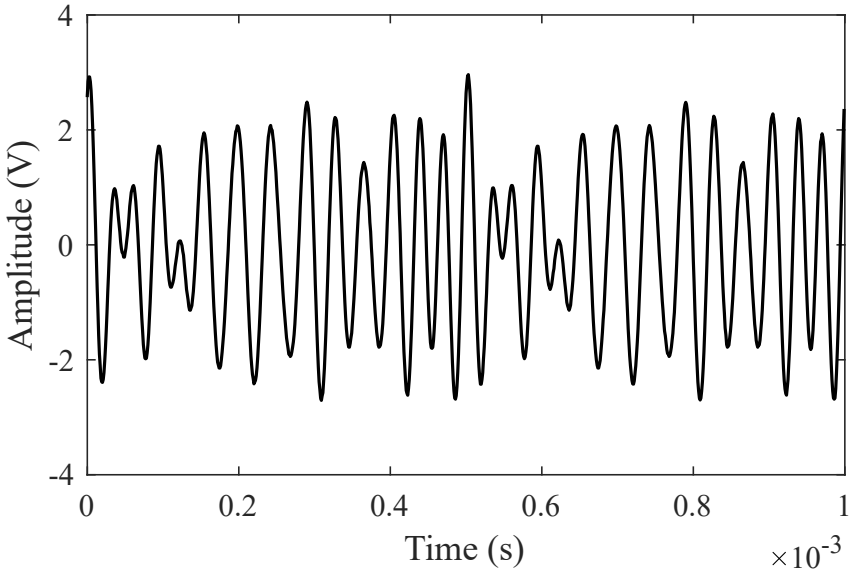


Figure 4.33: Current sense signal of the field generator. The resulting waveform is a superposition of the eight transmitter frequencies. Data acquired using an Agilent DSO-X3024A oscilloscope at a sampling frequency of 4 MegaSample per second (MSps). Signal amplitude units are in volts (V).

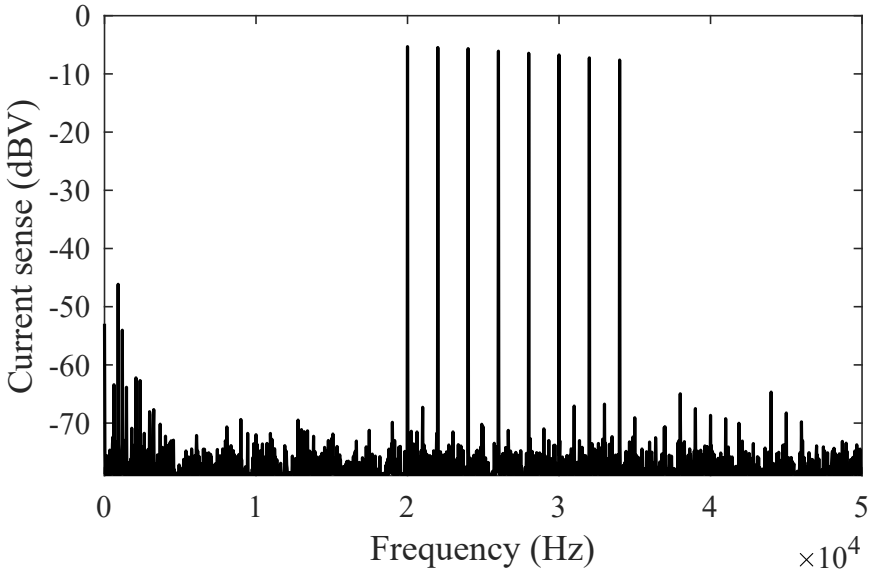


Figure 4.34: Fast Fourier transform (FFT) of the field generator current signal. Each peak represents a single transmitter coil. The 50k point FFT was generated using an Agilent DSO-X3024A oscilloscope at a sampling frequency of 4 MegaSample per second (MSps) using a Hanning window. Units are in decibels (dB) relative to 1 Volt, (dBV).

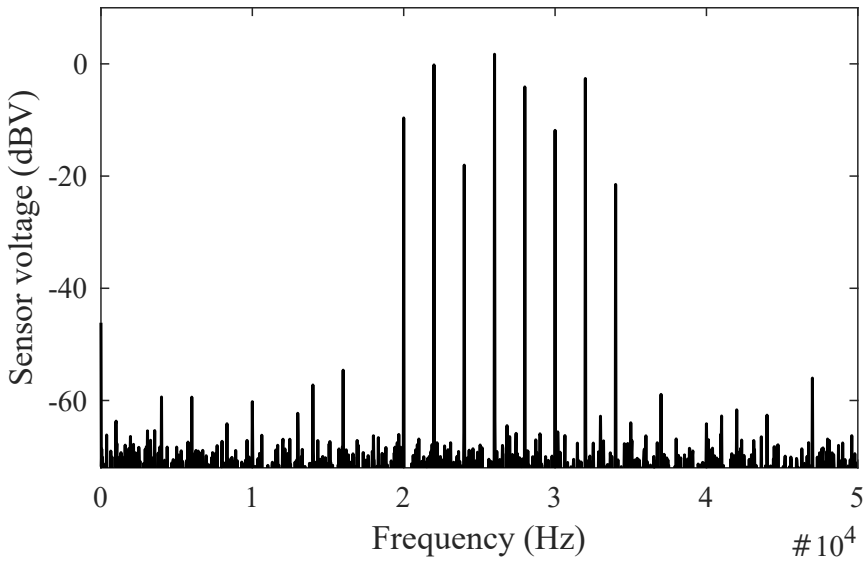


Figure 4.35: Fast Fourier transform (FFT) of the induced voltage on the tracking sensor due to the field generator after amplification and filtering. The sensor was placed vertically above the centre of the field generator at a height of 12cm. Each peak represents an induced frequency component due to a single transmitter coil. 50k point FFT generated using an Agilent DSO-X3024A oscilloscope at a sampling frequency of 4 MSps using a Hanning window.

4.10.4 Frequency programming

A USB-serial interface was designed for the Teensy microcontroller to allow system users to independently adjust the transmission frequencies of the field generator. The user can connect to the microcontroller over a virtual-serial terminal interface and issue commands to the microcontroller using a set of command strings. On receiving a valid command, the microcontroller decodes and programs the requested waveform generator. The command syntax draws inspiration from the Standard Commands for Programmable Instruments (SCPI) specified by IEEE 488.2 [148].

At the time of writing, four commands are currently supported:

`READ`: Queries the controller about which frequencies are currently being transmitted by the system. The user can query an individual coil number and the controller provides the corresponding frequency of that coil (in Hz) in response.

`FREQ`: Programs a specific coil to a desired transmitting frequency while leaving all other coils transmitting

`FREQR`: Similar to `FREQ`, but resets all other coil frequencies to 0 Hz. This is useful for debugging and testing.

`RESET`: Resets all coil frequencies to 0 Hz.

Formulating a command string to program a single transmission coil over the serial port takes the following form:

```
>>  FREQ:<coilno>@<frequency>
```

where the `<coilno>` is the number of the coil for programming, and `<frequency>` is the desired frequency in Hz. Multiple frequencies can be programmed at once by stringing together coil indices and frequencies:

```
>>  FREQ:<coilno>@<frequency>:<coilno>@<frequency> ...
```

4.11 Accuracy evaluation

The Anser EMT system subjected to a standardised testing assessment described in [100, 149, 150]. Standardised testing allows one to objectively compare Anser EMT to existing commercially available trackers. In this section, we aim to show that the Anser EMT system is comparable in performance to commercially available systems. The original implementation of the system by [92] was used for this work, as the optimised system detailed in this chapter was not fully constructed at the time when experiments took place. Both the original and revised system are identical in terms of magnetic design, so the results which follow can be assumed to apply to both systems. The revised system design is used for all other experimental work in this thesis.

4.11.1 Testing protocol

The Hummel protocol is a well-known standardised testing platform that is utilised to evaluate commercially available electromagnetic tracking systems [133, 134]. The protocol provides a method to quantitatively measure the error between a tracking sensor's resolved position and the sensor's actual position in space. The setup is shown in Fig. 4.36. The grid is used for positional error measurements $[x, y, z]$. The board contains a set of 32 holes arranged in a circle which are used for rotational error measurements $[\theta, \varphi]$. Two distinct angular displacements are also included and shown as Rotation 1 and 2 in Fig. 4.36b. The Hummel board was placed at three distinct heights of 11 cm (*bottom*), 16 cm (*middle*) and 21 cm (*top*) above the FG using the wooden stackable platforms shown in Fig. 4.36. For the position measurements $5 \times 5 =$ 25 points in the central area of the Hummel board were used, shown in Fig. 4.37. The FG was aligned in the middle of the covered volume before the measurements. The rotational measurements were taken at the middle height.

4.11.2 Results

Tables 4.5 and 4.6 display the results of the Anser system subjected to the Hummel protocol. One-hundred and fifty position samples were recorded and processed for

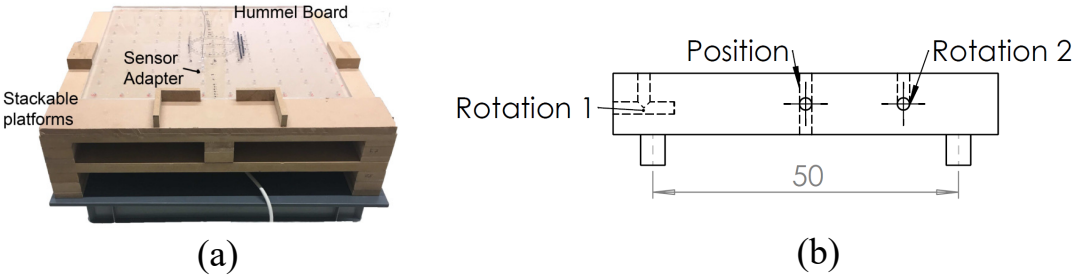


Figure 4.36: (a) Hummel board system setup [150]. The Hummel board is mounted on a set of stackable platforms. The field generator (not visible) is placed beneath the stacks on a metal-free surface. (b) The Hummel adapter for use with the Hummel board. Dimensions are in millimeters (mm)

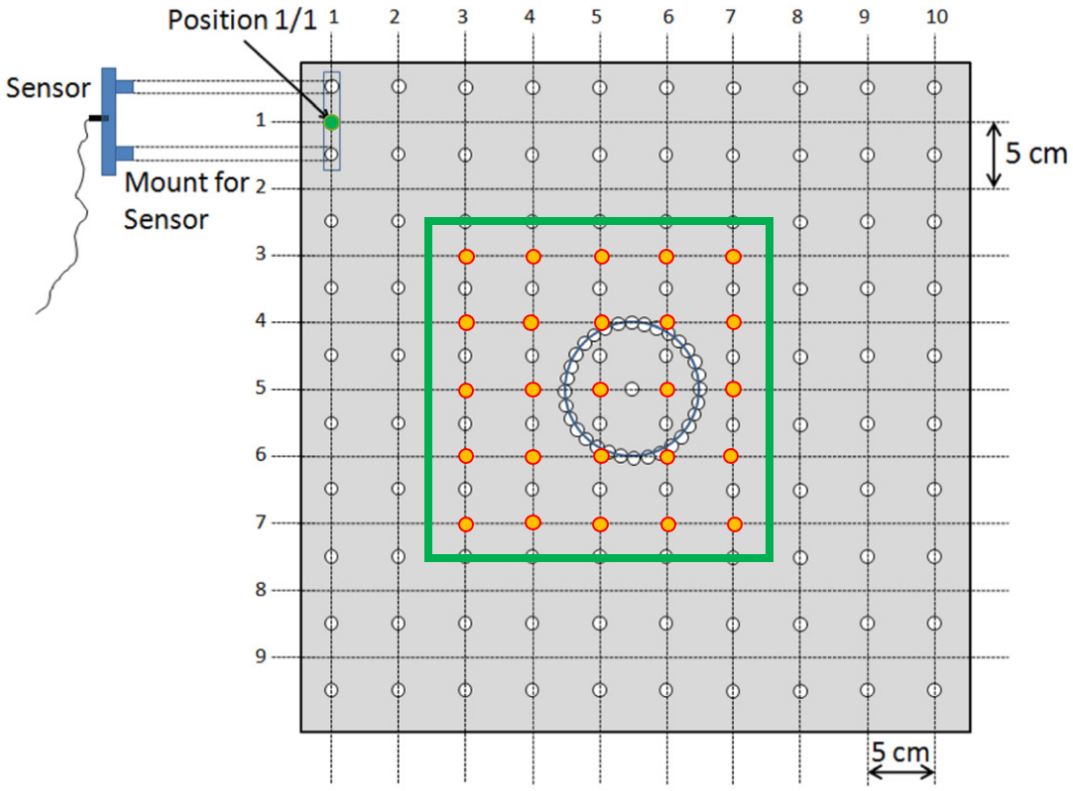


Figure 4.37: Diagram of the Hummel board. A 5×5 subsection of the grid, shown in green, was used for accuracy evaluation.

each measurement at an update rate of 15Hz. The precision measurement (also called jitter) describes how much variation exists in the sensor's resolved position whilst in a

fixed position. $N = 25$ locations were acquired for jitter measurements on each height of the setup. For each location the root mean square (RMS) error was calculated over all 150 positions samples. The accuracy measurement describes how well the resolved sensor position corresponds with the actual coordinates of the sensor in space. The sensor position was averaged over 150 position samples for each location. $N = 40$ distances (20 horizontal and 20 vertical) were acquired at each height (bottom, middle and top) with the relative distances between each point (5 cm) used as the reference. For determining the rotational accuracy, 31 measurement errors of 11.25° steps were recorded for each of the two rotation orientations. Position data was transferred to the MITK medical imaging environment [151] over the OpenIGTLink protocol [96]. A screenshot of the acquired points is shown in Fig. 4.39.

Distortion tests were also performed using a set of solid metal cylinders individually placed between the FG and tracking sensor. Five separation distances between each distorting cylinder and the tracking sensor were tested. A detailed description of the experimental setup can be found in Hummel's original paper describing the testing protocol [150]. Table 4.7 shows Anser's tests results alongside those from commercially available systems.

Separation	*Precision (mm)*	*Accuracy (mm)*
Top	0.29±0.34	1.98±1.47
Middle	0.15±0.1	1.14±0.8
Bottom	0.13±0.11	0.82±0.63

Table 4.5: Precision (jitter) and accuracy results for the Anser system ($\mu \pm \sigma$). The precision is averaged over 25 RMS errors on each height. The accuracy is averaged over 40 errors of 5cm distance measurements on the Hummel board.

Rotation type	*Rotation error (°)*
Perpendicular (Rotation 1)	0.04±0.02
Co-planar (Rotation 2)	0.09±0.05

Table 4.6: Rotational error ($\mu_e \pm \sigma_e$) results for the Anser system. For each rotation type, the error is averaged over 31 measurements of 11.25° steps.

Device	*FG Type*	*Ref.*	*Prec. (mm)*	*Acc. (mm)*	*Rot (°)*
NDI Aurora					
	Planar FG	[149]	0.20	0.80	1.2/1.0
	Tabletop FG	[149]	0.05	0.3	0.8/0.7
	Compact FG	[149]	0.05	0.5	1.0/0.8
Ascension microBird					
	Mid Range FG	[133]	0.14	0.69	0.04
Ascension 3D Guidance					
	Mid Range FG	[152]	0.15	0.24	0.05/0.06
	Flat FG	[152]	0.20	0.18	0.02/0.02
Anser EMT					
	Planar FG	–	0.15	1.14	0.04/0.09

Table 4.7: Test results commercial systems subject to the Hummel protocol taken from [134]. The mid-height Anser EMT results have been added for comparison.

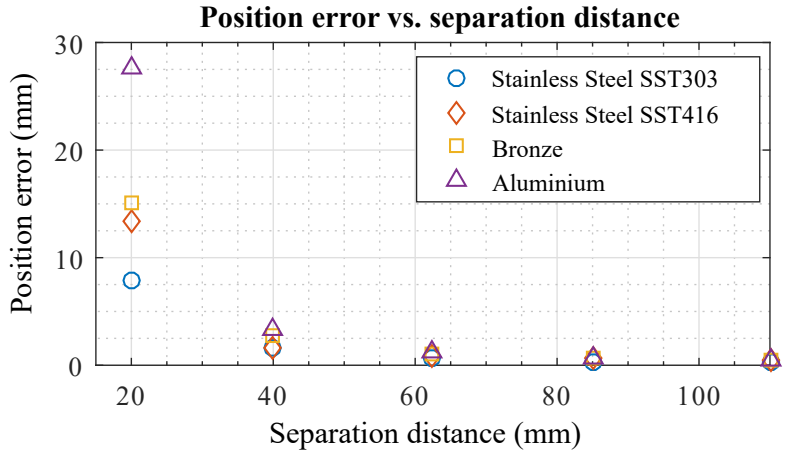


Figure 4.38: Position error vs. separation distance using four solid cylinders of different metals. The aluminium cylinder induces the largest positional error of 27mm.

Table 4.7 compares Anser with commercially available EMT trackers. The open-source tracker compares favourably to the *NDI* and *Ascension* system in terms of precision, accuracy and rotation. Precision (jitter) measures 0.15mm; similar to other systems. Positional accuracy is 1.14mm compared to 0.8mm for the Aurora planar field generator. Rotational accuracy compares favourably with errors of 0.04° and 0.09° for both rotation positions shown in Fig. 4.36(b). This rotational accuracy matches those of the *Ascension* system while significantly improving over the Aurora system. The sensor used in these experiments was an NDI 5-DOF sensor (model no. 610099)

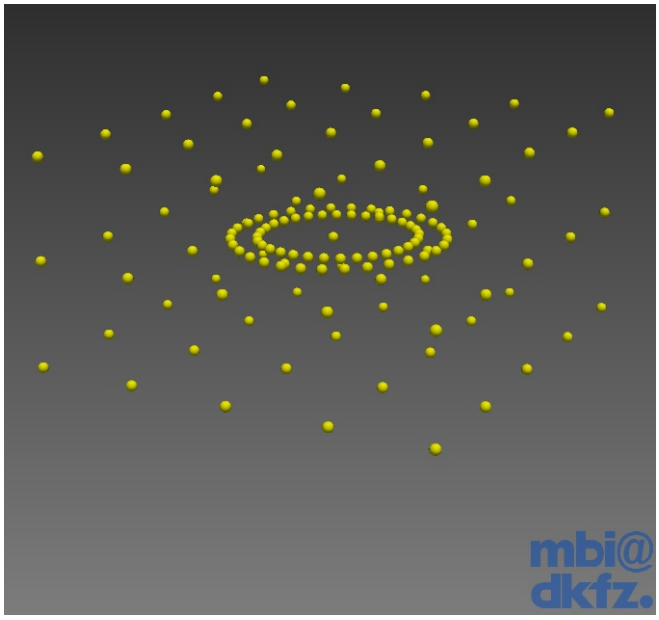


Figure 4.39: Screenshot of the acquired points visualised in the MITK medical imaging environment [151]. The three planar 5× 5 grids correspond to the *bottom*, *middle* and *top* heights of the Hummel board and was used for positioning error calculation. The circular array of points was captured in the *middle* layer and was used to calculate rotational errors.

which was rigidly glued into a 2.5mm diameter catheter to minimise rotation of the coil within the Hummel adapter during testing. Previous work reported cable orientation and sensor flipping impacting measurements [153], both of which did not occur in this experiment. Fig. 4.38 shows the distorting effects of metal on the tracking performance of the system. In all cases, an increase in position error is observed with decreasing separation between the distorting cylinders and the sensor. The aluminium cylinder caused the highest error of 27mm. This is expected as aluminium exhibits highest conductivity of the metals used in the experiment and will therefore produce the largest Eddy currents when placed in a time-varying magnetic field. The effects of metal distortions are studied in more detail in chapter 5.

4.12 Summary

This chapter described the design and implementation of an improved revision of the Anser electromagnetic tracking system. The design can now be fabricated as part of a system box-build as a result. Experiments we're then performed to evaluate the system's accuracy in light of commercially available tracking systems. Results show that Anser performs similarly to the NDI planar generator for accuracy measurements, and the Ascension 3D Guidance system for rotational measurements. The revised hardware design is a foundation for the experimental work carried in chapters 5, 6 and 7, while pre-clinical validation of the system is demonstrated in chapter 8.

Chapter 5

Detection and localisation of distortions in EMT

This chapter describes a novel method of detecting static magnetic distortions using only the magnetic field transmitting array. The existing field generator design described in chapter 4 is modified to enable simultaneous transmission and reception of the generated magnetic field. A mutual inductance model is developed for this field generator design in which deviations from control measurements indicate the location, magnitude and material of the field distorter to an approximate degree. Whilst not directly compensating for errors, this approach enables users of EMT systems to optimise placement of the magnetic field generator by characterising a distorter's effect within the tracking volume without the use of additional hardware. The discrimination capabilities of this method may also allow researchers to apply material-specific compensation techniques to minimise position error in the clinical setting.

All magnetic tracking systems experience error due to distorters in the operating environment [134, 155]. Distorters typically take the form of metallic objects which can be either static or moving with respect to the tracking system field generator. A distorter causes the redistribution of the generated magnetic field in their local envi-

This chapter is based on H. A. Jaeger and P. Cantillon-Murphy, "Distorter characterisation using mutual inductance in electromagnetic tracking", *Sensors*, 18(9), 2018. [154]

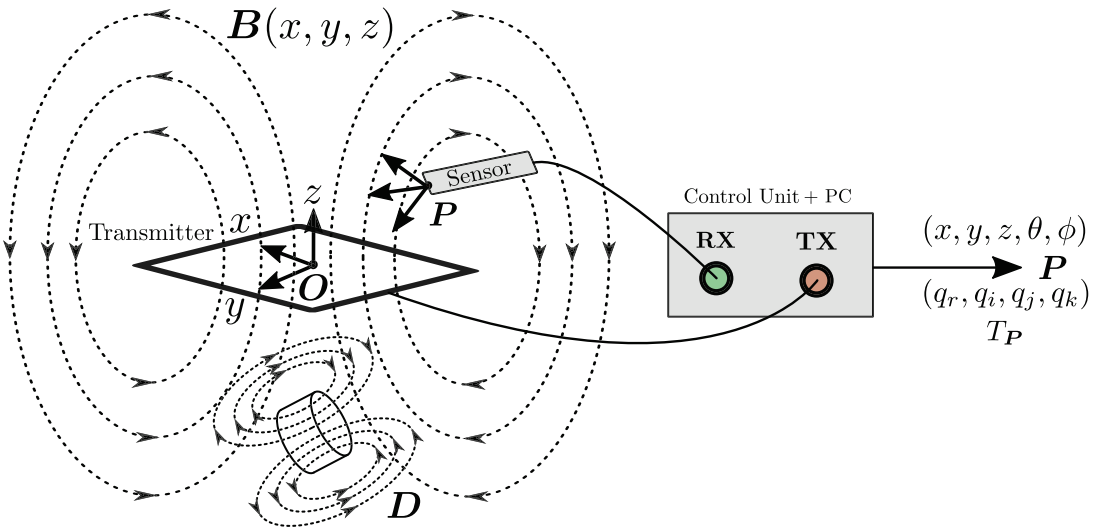


Figure 5.1: Generalised operation of an EM tracking system. A control unit is connected to a field generator board (TX) and magnetic sensor (RX). The sensor experiences an induced voltage from the generated time-varying magnetic field $\boldsymbol{B}$. The control unit measures this voltage and resolves the sensor position based on this measurement to yield the position and orientation of the sensor $\boldsymbol{P}$ with respect the origin $\boldsymbol{O}$. The orientation component take the form of a vector, quaternion or transformation. Distorters $\boldsymbol{D}$ in the region of the TX board distort the magnetic field and result in sensor positioning errors.

ronment as indicated in Fig. 5.1. Tables and surgical instruments make up the majority of distorters in the clinical setting as they are typically made from either aluminium or stainless steel due to sterility requirements. These metallic structures, when placed in the vicinity of the tracking system field generator, may affect the spacial distribution of the transmitted magnetic field which can cause significant errors in the reported sensor positions [13, 155]. Ferromagnetic distorters (those containing iron) change the shape of the local magnetic field distribution due to their relatively high magnetic permeability. Highly conductive non-ferromagnetic distorters such as aluminium produce opposing magnetic fields by induced Eddy-currents [156]. Commercial EMT systems such as the Aurora system (*Northern Digital Inc., Ontario, Canada*), trakSTAR (*Ascension Technologies, VT, USA*) and Fastrak (*Polhemus, VT, USA*) have been subject to standardised assessments to determine the effects of different distorter types [149, 150]. Some of these tracking systems contain compensation techniques, although

these methods remain proprietary and do not provide any localisation of the distorter location.

Compensation for the effects of metallic distorters has become a popular topic among researchers working on integrating EMT into the clinical setting. Intrinsic compensation techniques include manipulation of the underlying magnetics through the use of magnetic shielding [157] and novel field modulation methods [15, 16] which act to nullify the effect of local metallic objects. Other techniques rely on the use of redundant position measurements in order to characterise and map the nature of the distortion while simultaneously compensating for positioning error: EMT-only techniques utilise multiple magnetic sensors in fixed in relative orientation combination with simultaneous localisation and mapping (SLAM) to effectively reduce error by as much as 67% [11]. Optical tracking systems have also been used in combination with EMT to provide a position reference for sensor fusion algorithms [12].

While many of these compensation techniques are effective in reducing error from distorters, characterisation of the distortions themselves typically requires an undistorted sample of tracking system positions be obtained and analysed for baseline comparison. This approach provides distortion information purely from the perspective of the magnetic sensor and not from that of the field generator. It is also a relatively time-consuming process as a cloud of points needs to be acquired with respect to either a relative [11] or optical ground truth [12]. Procedural tables, trolleys and other medical equipment are the biggest distortion sources in the clinical setting, and their proximity to the field generator board has a large impact on overall system accuracy [157]. This chapter proposes a novel distortion detection scheme which utilises only the EMT field generator. The design is based on an existing field generator design for the open-source Anser EMT tracking system described in chapter 4 [92, 100]. The modified design allows calculation of distortion error from the perspective of the field generator based on measurements of the mutual inductance between constituent transmitting coils. Amplitude and phase measurements from the resulting signal waveforms allow discrimination between different distorting materials. The calculations can be performed autonomously allowing EM tracking systems to detect the presence, material type and approximate location of distortions without the need for position

acquisition or undistorted control data.

While this work does not attempt to compensate for position errors, the proposed technique can potentially be used in tandem with existing compensation methods. The proposed method can allow EMT users to quickly optimise placement of EMT field generators such that environmental errors can be minimised prior to the application of further compensation techniques.

5.1 Background

5.1.1 Magnetic Field Generator

All EMT systems use a magnetic field generator to produce a time-varying magnetic field as shown in Figure 5.1. The transmitting field must be spatially unique such that each position in space has a unique magnetic signature. Most field generator designs employ multiple transmitting coils with each generating a magnetic field at a different frequency to fulfil this requirement. EMT field generators come in a number of different arrangements including tri-axial [99], planar coil [103] and planar printed circuit board (PCB) [92, 100] such as shown in Fig. 3.2. In this chapter we alter the role of the magnetic field generator such that each transmitter coil can also behave as a receiver. The operation of the modified field generator and receiver coils is described in the following sections.

5.1.2 Mutual Inductance

Mutual inductance is the electrical property which relates how an electrical current in a conductor influences the voltage on another conductor. Consider the coil arrangement shown in Figure 5.2. The alternating current, $i_P(t)$, flowing through the primary coil creates a time-varying magnetic field. The resulting magnetic flux, $\Phi(t)$, interacts with a secondary coil in the vicinity and causes a voltage $v_S(t)$ to be induced across it. The extent of this interaction is captured by the mutual inductance coefficient, M, in (5.1)

and is the basic principle of an electrical transformer [158].

$$v_S(t) = N_S \frac{d\Phi(t)}{dt} = M \frac{di_P(t)}{dt} \tag{5.1}$$

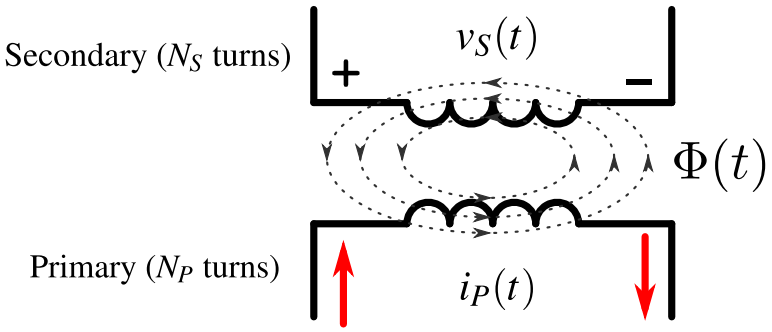


Figure 5.2: The interaction between two coupled inductors. A time varying current $i_P(t)$ in the primary coil establishes a time varying magnetic flux $\Phi(t)$, a portion of which links the secondary winding and causes a time-varying voltage to be induced at its terminals.

In the case of an EMT field generator containing multiple coils, the mutual inductances between all coils can be represented as a matrix $\mathbf{M}$ shown in (5.2). The diagonal entries represent the self inductances of each coil. The induced voltages on a particular coil can then be expressed as a superposition of its self-induced voltage and those induced by every coil in the field generator according to (5.3). Matrix representation of inductance is a commonly used tool in circuit analysis as it compactly defines the interaction between all current-carrying structures within a system, from the small scales of integrated circuit packages [159] to high powered electrical machine windings [160].

$$\mathbf{M} = \begin{bmatrix} L_1 & M_{12} & \dots & M_{1N} \\ M_{21} & L_2 & \dots & M_{2N} \\ \vdots & \vdots & \ddots & \vdots \\ M_{N1} & M_{N2} & \dots & L_N \end{bmatrix} \tag{5.2}$$

$$\mathbf{V} = \begin{bmatrix} v_1 \\ v_2 \\ \vdots \\ v_n \end{bmatrix} = \begin{bmatrix} L_1 & M_{12} & \dots & M_{1N} \\ M_{21} & L_2 & \dots & M_{2N} \\ \vdots & \vdots & \ddots & \vdots \\ M_{N1} & M_{N2} & \dots & L_N \end{bmatrix} \begin{bmatrix} di_1/dt \\ di_2/dt \\ \vdots \\ di_N/dt \end{bmatrix} = \mathbf{M}\frac{d\mathbf{I}}{dt} \tag{5.3}$$

Ideally the induction matrix is symmetric about the diagonal since the definition of mutual inductance implies that $M_{\alpha\beta} = M_{\beta\alpha}$. If an EMT magnetic field generator is capable of switching its coils between transmitter (TX) and receiver (RX) modes of operation, then the mutual inductance between every coil can be experimentally recovered in matrix form.

5.1.3 Field Generator Inductance Matrix

The mutual inductance matrix defines how effectively magnetic flux is coupled from one circuit to another and is therefore dependant on the intrinsic parameters of the circuits being analysed. The Anser EMT system field generator shown in Figure 5.3 uses eight identical transmitter coil circuits in a well known optimised planar arrangement [102]. According to (5.1), obtaining the mutual inductance between two coils requires applying a time-varying current to the primary coil whilst simultaneously measuring the induced voltage on the secondary coil. For a tracking system containing N_{coil} transmitter coils, $N!/(N-2)!$ mutual inductance measurements should be acquired, since two coils are utilised for a single inductance measurement. Generalising, the voltage induced on coil α due to a transmitting coil β is given by (5.4). This relation can be represented in matrix from in (5.5).

$$v_{\alpha\beta}(t) = M_{\alpha\beta}\frac{di_\beta(t)}{dt} \tag{5.4}$$

$$\begin{bmatrix} 0 & v_{12} & \dots & v_{1N_{coil}} \\ v_{21} & 0 & \dots & v_{2N_{coil}} \\ \vdots & \vdots & \ddots & \vdots \\ v_{N_{coil}1} & v_{N_{coil}2} & \dots & 0 \end{bmatrix} = \begin{bmatrix} 0 & M_{12} & \dots & M_{1N_{coil}} \\ M_{21} & 0 & \dots & M_{2N_{coil}} \\ \vdots & \vdots & \ddots & \vdots \\ M_{N_{coil}1} & M_{N_{coil}2} & \dots & 0 \end{bmatrix} \begin{bmatrix} di_1/dt & 0 & 0 & 0 \\ 0 & di_2/dt & \dots & 0 \\ \vdots & \vdots & \ddots & \vdots \\ 0 & 0 & \dots & di_{N_{coil}}/dt \end{bmatrix} \tag{5.5}$$

If both the source current and induced voltage can be measured, then the mutual inductance matrix can then be calculated using simple matrix inversion in (5.6):

$$\mathbf{M} = \begin{bmatrix} \ddots & & \\ & \frac{di_j}{dt} & \\ & & \ddots \end{bmatrix}^{-1} \mathbf{V} \tag{5.6}$$

5.1.4 Summary

The eight transmitter coils of the Anser tracking system result in a total of 56 mutual inductance measurements. Metallic objects in the vicinity of the transmitter will change the measured mutual inductance due to ferromagnetic and non-ferromagnetic (Eddy-current) effects, as they act to distort the shape and strength of the surrounding magnetic field. Detecting these changes in inductance is a commonly found design in very-low-frequency metal detecting circuits [161, 162]. Measuring this change in inductive coupling is the foundation of this work. Initially we simulate the inductive coupling between the field generator's transmitter coils from first principles. The experimental hardware is then discussed in detail followed by a thorough description of the experimental procedures performed. Finally the measured inductance error results are correlated with position errors experienced by the tracking system.

5.2 Field Generator Inductance Simulation

The mutual coupling between each coil of the transmitting field generator shown in Figure 5.3 was simulated to investigate whether detection of mutually induced voltages

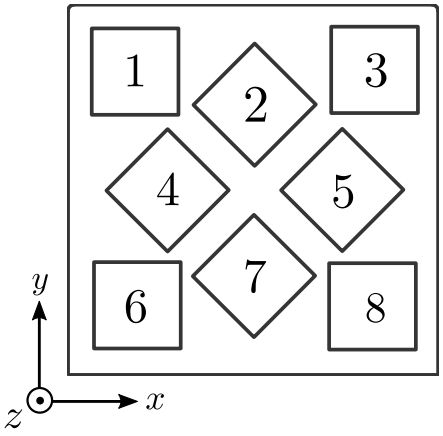


Figure 5.3: (a) The Anser electromagnetic tracking system [100]. (b) The arrangement of coils on the Anser EMT field generator. This arrangement was originally based on an optimised coil arrangement proposed by [102].

was feasible and to provide a reference for experimental measurements. For simulation, each transmitter coil of the tracking system can be considered as a set of individual straight copper traces, with each trace idealised as a current carrying filament [125]. The magnetic field (in Tesla) observed at a point $\boldsymbol{r}$ due to a single current carrying filament is given by (5.7), where I is the magnitude of the filament current, μ_0 is the magnetic permeability of free space and $\boldsymbol{a}$, $\boldsymbol{b}$ and $\boldsymbol{c}$ are vectors relating the location of the current filament to the observation point $\boldsymbol{r}$ as shown in Figure 3.17. The magnetic field due to each printed circuit board coil can then be modelled as a superposition of fields produced by all constituent current filaments [90, 125]. This approach is described in section 3.5.3 for the simple field generator design.

$$B(\boldsymbol{r}) = \frac{\mu_0 I}{4\pi}\left(\frac{\boldsymbol{c}\times\boldsymbol{a}}{|\boldsymbol{c}\times\boldsymbol{a}|^2}\right)\left(\frac{\boldsymbol{a}\cdot\boldsymbol{c}}{|\boldsymbol{c}|}-\frac{\boldsymbol{a}\cdot\boldsymbol{b}}{|\boldsymbol{b}|}\right) \tag{5.7}$$

The magnetic coupling between any two coils can be simulated by integrating the magnetic field of the primary coil over the area of the secondary coil. Since all transmitting coils are co-planar in the x-y plane, the total flux produced by a primary coil P intersecting a secondary coil S can be written as an area integral in (5.8), where $\boldsymbol{B}_P$ is the primary's magnetic field strength at location (x,y) and $d\boldsymbol{A}_S$ is a differential

An implementation of this equation can be found online: `https://osf.io/47q8q/`

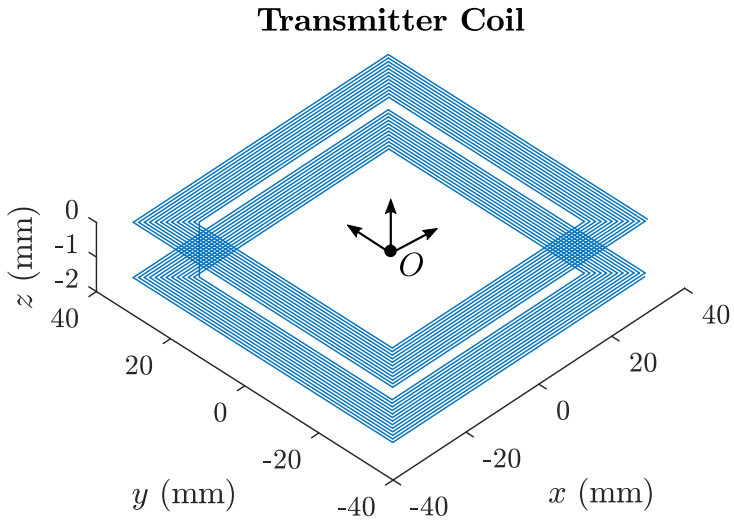


Figure 5.4: 3D model of the double-sided PCB traces of a single transmitter coil with the origin O located at its centre. Each straight-line trace can be considered a single current filament.

area element of the secondary coil.

$$\Phi_S = \int_{A_S} \boldsymbol{B}_P(x,y) \cdot d\boldsymbol{A}_S \tag{5.8}$$

The equation for the magnetic field is highly non-linear and must be numerically integrated as a discrete a sum over the length l and width w of the secondary coil. The total flux linkage λ_S is computed by scaling the result by the number of secondary coil turns N as shown in (5.9).

$$\lambda_S = N_S \Phi_S \simeq N_S \sum_l \sum_w \boldsymbol{B}_P(x,y) \cdot \Delta x \Delta y \tag{5.9}$$

In this work, numerical computation of the integrals was performed using Matlab (*MathWorks, MA, USA*). Consistent with the experimental design described previously [92], the coil integration area was approximated as 25 uniform turns of the mean coil side length of 66.75mm. Full coil dimensions are shown in Table 5.3. Acceleration of the calculations was performed using the *parfor* language feature of the Parallel Computing toolbox in Matlab. Through rearrangement of (5.1), the mutual inductance

between two coils α and β can be calculated using (5.10):

$$M_{\alpha\beta} = \frac{N_\alpha \Phi_\alpha}{I_\beta}\ , \tag{5.10}$$

where N_α and Φ_α are the turn count and magnetic flux respectively of the secondary coil and I_β is the current flowing in the primary coil. The resulting mutual inductance matrix is shown in Table 5.1. The colour-coding of the entries reveals that there are only four unique mutual inductance values for the field generator (ignoring the 10nH difference between 1.31µH and 1.32µH entries, which may be attributed to modelling error). These unique entries are a consequence of the square symmetry in the field generator design. Referring back to Figure 5.3 it can be expected that adjacent coils will experience the highest mutual inductance values, while the furthest separated coils will experience the lowest values. For example, coils 1 and 2 have a mutual inductance (indicated by M_{12}) of 1.32µH, while coils 1 and 8 have a comparatively low mutual inductance $M_{18} = 6$nH. Taking each entry for $M_{\alpha\beta}$, one can calculate the predicted induced voltage due to a sinusoidal time varying current $i(t)$. Assuming a sinusoidal coil current of amplitude $I_\beta = 160$mA [90] at a frequency of 20kHz, (5.11) provides the induced voltage for a given mutual inductance $M_{\alpha\beta}$;

$$v_{\alpha\beta} = M_{\alpha\beta}\frac{di_\beta}{dt} = \omega I_\beta M_{\alpha\beta} \tag{5.11}$$

where $\omega = 2\pi f$, the angular frequency of the primary coil current. Table 5.2 shows the matrix of predicted voltages for the different inductances shown in Table 5.1. On the order of millivolts, these induced voltages are well within acceptable sensing ranges enabling reliable measurements to be taken. The measurement hardware used to experimentally measure these voltages is now discussed in section 5.3.

$$\mathbf{M},\,(\mu\mathrm{H}) = \begin{array}{c} \begin{matrix} M_{\alpha 1} & M_{\alpha 2} & M_{\alpha 3} & M_{\alpha 4} & M_{\alpha 5} & M_{\alpha 6} & M_{\alpha 7} & M_{\alpha 8} \end{matrix} \\ \begin{pmatrix} - & 1.32 & 0.18 & 1.31 & 0.18 & 0.18 & 0.18 & 0.006 \\ 1.32 & - & 1.31 & 1.32 & 1.32 & 0.18 & 0.48 & 0.18 \\ 0.18 & 1.31 & - & 0.18 & 1.31 & 0.006 & 0.18 & 0.18 \\ 1.31 & 1.32 & 0.18 & - & 0.48 & 1.31 & 1.32 & 0.18 \\ 0.18 & 1.32 & 1.31 & 0.48 & - & 0.18 & 1.32 & 1.31 \\ 0.18 & 0.18 & 0.006 & 1.31 & 0.18 & - & 1.31 & 0.18 \\ 0.18 & 0.48 & 0.18 & 1.32 & 1.32 & 1.31 & - & 1.32 \\ 0.006 & 0.18 & 0.18 & 0.18 & 1.31 & 0.18 & 1.32 & - \end{pmatrix} \end{array} \begin{matrix} M_{1\beta} \\ M_{2\beta} \\ M_{3\beta} \\ M_{4\beta} \\ M_{5\beta} \\ M_{6\beta} \\ M_{7\beta} \\ M_{8\beta} \end{matrix}$$

Table 5.1: Simulated mutual inductance matrix for the eight coil PCB field generator of the Anser EMT system. The entries have units of microhenries (μH). Self inductances of each coil are omitted. Precision of entries have been truncated for clarity. Each coil area was subdivided into 4 million area elements for the integration process.

$$\mathbf{V},\,(\mathrm{mV}) = \begin{array}{c} \begin{matrix} v_{\alpha 1} & v_{\alpha 2} & v_{\alpha 3} & v_{\alpha 4} & v_{\alpha 5} & v_{\alpha 6} & v_{\alpha 7} & v_{\alpha 8} \end{matrix} \\ \begin{pmatrix} - & 26.5 & 3.62 & 26.3 & 3.62 & 3.62 & 3.62 & 0.12 \\ 26.5 & - & 26.3 & 26.5 & 26.5 & 3.62 & 9.66 & 3.62 \\ 3.62 & 26.3 & - & 3.62 & 26.3 & 0.12 & 3.62 & 3.62 \\ 26.3 & 26.5 & 3.62 & - & 9.66 & 26.3 & 26.5 & 3.62 \\ 3.62 & 26.5 & 26.3 & 9.66 & - & 3.62 & 26.5 & 26.3 \\ 3.62 & 3.62 & 0.12 & 26.3 & 3.62 & - & 26.3 & 3.62 \\ 3.62 & 9.66 & 3.62 & 26.5 & 26.5 & 26.3 & - & 26.5 \\ 0.12 & 3.62 & 3.62 & 3.62 & 26.3 & 3.62 & 26.5 & - \end{pmatrix} \end{array} \begin{matrix} v_{1\beta} \\ v_{2\beta} \\ v_{3\beta} \\ v_{4\beta} \\ v_{5\beta} \\ v_{6\beta} \\ v_{7\beta} \\ v_{8\beta} \end{matrix}$$

Table 5.2: Simulated induced peak-voltage matrix for the eight coil PCB field generator of the Anser EMT system based on the results in Table 5.1. The entries have units of millivolts (mV).

5.3 Experimental Setup

5.3.1 Modified Field Generator Design

The tracking system field generator consists of a planar transmitter coil array fabricated on a single printed circuit board as shown in Figure 5.3. The tight process accuracy of PCB fabrication ensures experimental repeatability and similar self-inductance val-

ues on each coil winding. The properties of each coil are shown in Table 5.3. This field generator design was modified with additional circuitry to enable the generator's mutual inductance to be experimentally calculated. Each coil circuit was modified to allow independent switching between modes of transmission (TX) and reception (RX). By selectively controlling each coil in this manner, the mutual inductances of the field generator can be experimentally acquired.

The ADG1436 analog switch (*Analog Devices, MA, USA*) was used to enable the switching functionality. This switch was chosen due to its small PCB footprint, high current carrying capacity of and low R_{on} resistance. The switch is controlled using a logic signal programmed by a microcontroller. In TX mode, the switch connects the coil to the driver circuit of the tracking system. In RX mode, the switch routes the induced coil signal to an instrumentation amplifier for conditioning and amplification. The INA163 (*Texas Instrument, TX, USA*) was selected for amplification due to its high input impedance and low noise characteristics. The gain of the amplifier was set to 81 using a resistor with 1% tolerance, resulting in a maximum gain deviation of ± 1.6 using the amplifier's gain equation (5.12). A simplified circuit diagram of the switching circuit can be found in Fig. 5.5a. The switch implementation for a single transmitter coil is shown in Figure 5.5b.

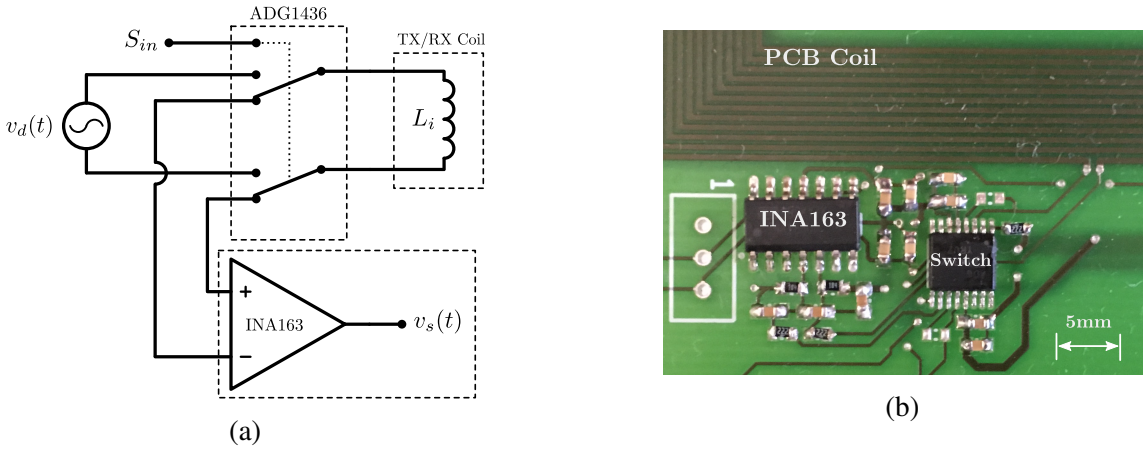
$$G = 1 + \frac{6000}{R_G} \tag{5.12}$$

5.3.2 Distorter Selection

A broad selection of metallic objects were chosen in order to investigate the effects of different materials on the mutual inductance of the field generator. Both ferrous and non-ferrous metal objects of various dimensions were chosen in order to simulate different scenarios in which distortion error may occur. A photograph of the tested distorters is shown in Figure 5.6a with the details of each distorter found in Table 5.4. Each object was placed at a known position beneath the field generator for each measurement. The distance between the distorter under test and field generator board was varied in fixed z-axis increments using Duplo bricks (*The Lego Group, Billund,*

Property	Value	Unit
Length (Max.)	70	mm
Width (Max.)	70	mm
Turns	25	-
Inductance	70	µH
Resistance (coil)	1.5	Ω
Resistance (switch)	3	Ω
Resistance (Total)	4.5	Ω
Trace Width	1.6	mm
Trace Spacing	0.25	mm

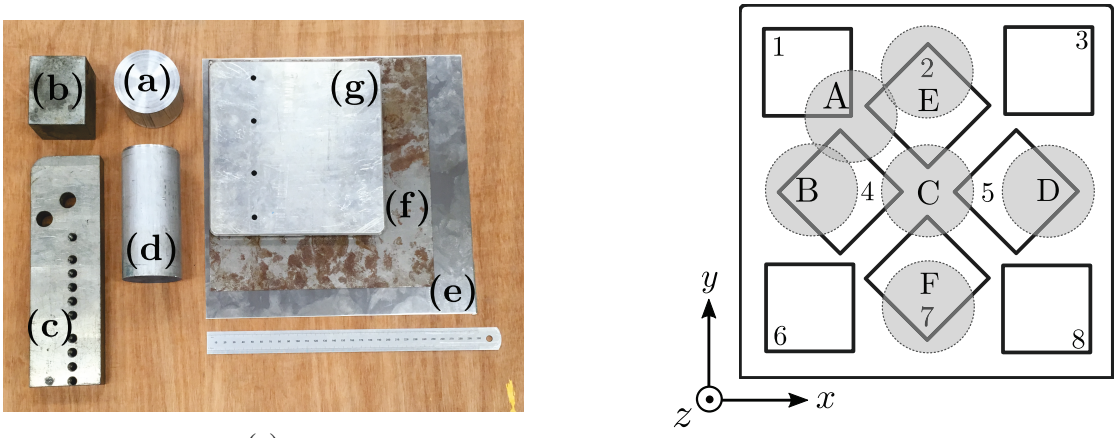
Table 5.3: Properties of EMT transmitter coils.



(a) (b)

Figure 5.5: (a) Simplified circuit diagram of the coil switching circuit. The ADG1436 behaves as a double-pole double throw (DPDT) switch enabling the coil to switch between TX and RX modes. S_{in} is the logic signal used to control the switch position. In TX mode (normal operation), the switch connects the driving source $v_d(t)$ to the coil to produce a stable time-varying magnetic field. In RX mode the INA163 is connected to the coil and is used to amplify the induced voltage signal to produce $v_s(t)$. (b) Layout of the switching circuit on the PCB.

Denmark), with each brick measuring 19.2mm in height as shown in Figure 5.7. The tight 10µm manufacturing tolerance of Duplo [163] ensures repeatability of the experiments while allowing accurate adjustment of the field generator height displacement. Locations of the distorters with respect to the field generator's *x*-*y* plane can be seen in Figure 5.6b. Large distorters span the length of the field generator and therefore lie underneath more than one labelled location. For example, the steel slab (c) spans lengthways from locations B to D while the sheet distorters span the entire area of the field generator.



(a) (b)

Figure 5.6: (a) Photograph of the metallic distorters used in the experiment. The properties of each distorter are shown in Table 5.4. (b) Illustrated top-down view of the field generator showing the locations of the distorters used in experiments.

5.3.3 Acquisition Hardware

A photograph of the experimental setup can be seen in Figure 5.8. An Anser EMT system unit was used to drive a constant amplitude alternating current through the transmitting coils. The embedded Teensy 3.2 microcontroller (*PJRC, Oregon, USA*) was used to automate the switching of the coils between TX and RX modes for the acquisition process. Each inductance measurement consisted of switching a single coil, α_i, to RX mode and setting an adjacent coil, β_i, to TX mode for a total of 56 independent inductance measurements. A National Instruments USB-6216 data acquisition

Label	Distorter Type	Name	Material	L (mm)	W (mm)	H (mm)	Locations
(a)	Small	Alu. Section	Aluminium	70	70	48	A, B, C
(b)	Small	Steel Block	Mild Steel	60	70	50	B, D
(c)	Medium	Steel Slab	Mild Steel	250	75	23	B-to-D, E-to-F
(d)	Medium	Alu. Cylinder	Aluminium	140	63	-	B-to-D, E-to-F
(e)	Sheet	Mu Sheet.	Mu Metal	300	300	1	Full coverage
(f)	Sheet	Alu. Sheet	Aluminium	195	195	6	Full coverage
(g)	Sheet	Steel Sheet	Mild Steel	265	250	1	Full coverage

Table 5.4: Properties of distorters used in experiments.

.

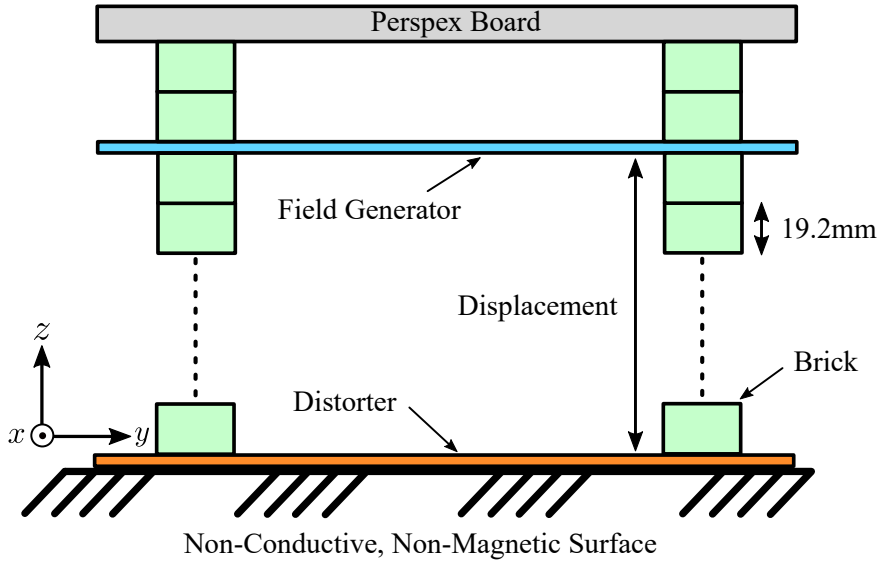


Figure 5.7: Side-view diagram of the modified field generator. The Duplo bricks allow adjustment of the displacement between the field generator and distorter in increments of 19.2mm. The perspex board height is also adjustable, although this was kept at a constant height during the position error experiments described in section 5.4.1. The experimental setup was placed on an all-wood table.

unit was used to record the received $v_s(t)$ signal of each RX coil, while simultaneously monitoring the TX coil current. The current signal was set to a frequency of 20kHz for all measurements. The DAQ was configured with a sampling rate of 50kHz. An acquisition frame length, $L = 5000$, was used for each individual signal measurement. A minimum signal-to-noise ratio (SNR) of 80dB was observed in the worst case when the furthest separated coil pairs (e.g. Coils 1 and 8) are transmitting and receiving respectively.

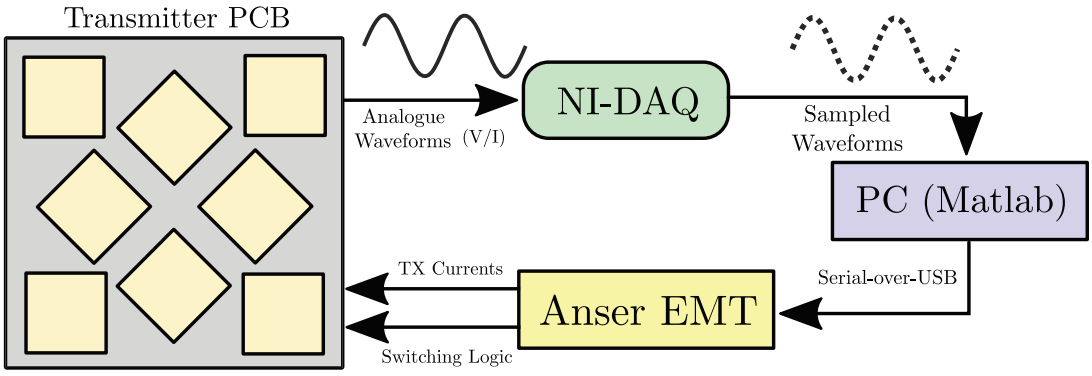


Figure 5.8: Block diagram of the experimental setup.

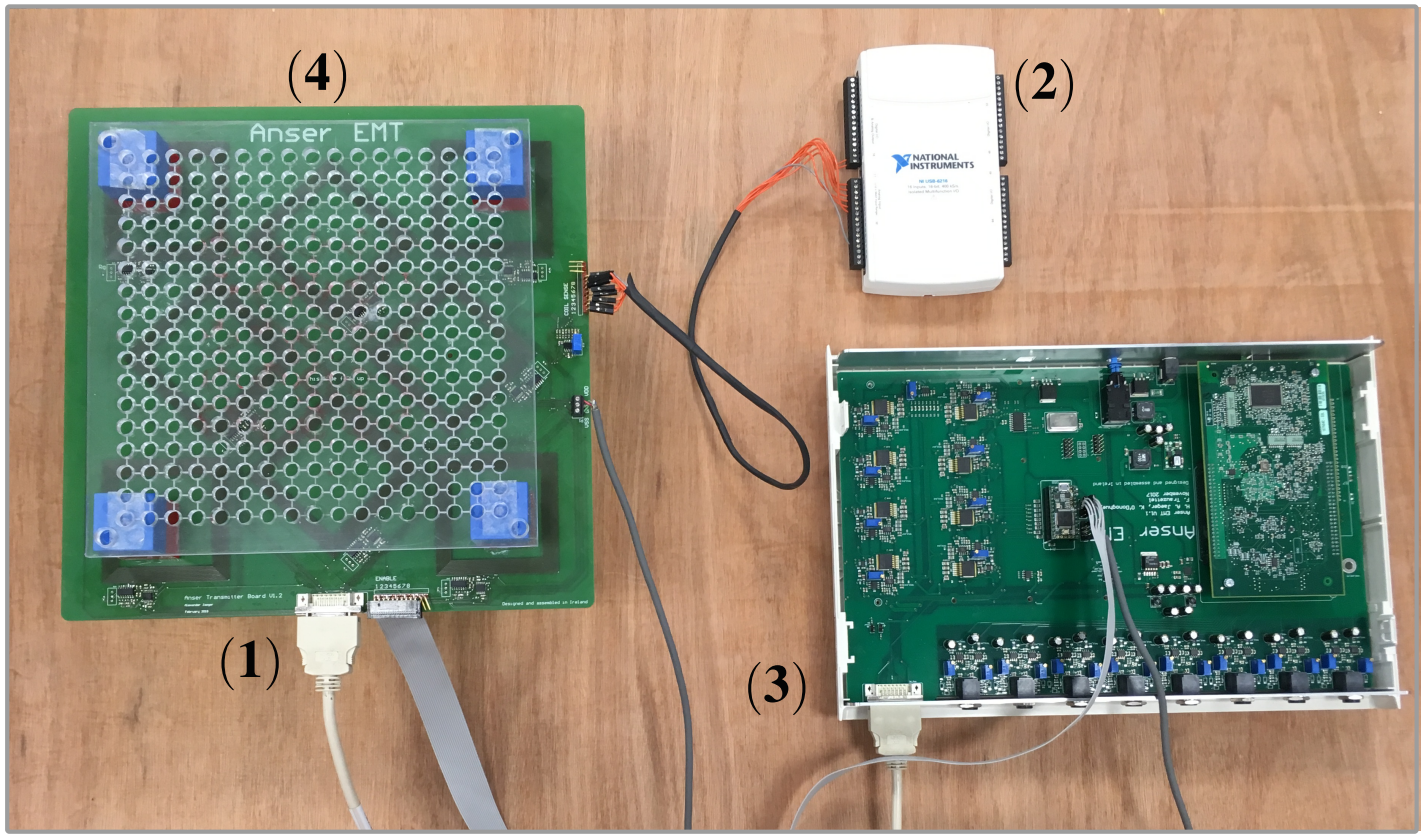


Figure 5.9: Photograph of the experimental setup of the modified field generator connected to the Anser EMT system. (1) The modified field generator with extra connections to enable coil switching. (2) The National Instruments DAQ connected to the instrumentation amplifier outputs of the field generator. (3) The Anser EMT tracking system unit with embedded Teensy 3.2 controller. (4) 6mm perspex planar board used for sensor position acquisitions.

5.4 Acquisition Methods

5.4.1 Mutual Inductance Measurement

Switching the EMT system transmitting coils between TX and RX modes was performed iteratively in order to measure the induced voltages on each coil with respect to every other coil. The algorithm outlined in Procedure (1) was applied to each distorter location in Table 5.4 at differing heights in multiples of 19.2mm as shown in Figure 5.7. The minimum heights in each case were limited by the size and shape of each distorter, with the lowest minimum height of one Duplo brick displacement (19.2mm) applied only to the sheet distorters (e)-(g). Distorters (a)-(d) required a minimum of three bricks of separation to avoid touching the field generator. The output of the procedure is a matrix of voltage amplitudes and phases corresponding to a particular distorter location and height. The phase information indicates the angle between the field generator (primary) coil current and induced (secondary) voltage waveforms. The procedure was implemented using Matlab and its Data Acquisition Toolbox. Total acquisition time was approximately 10 seconds for each distorter configuration. The mutual inductance matrix for the field generator was then calculated from the experimentally recorded voltage matrix $\mathbf{V}$ using (5.6).

5.4.2 Position acquisition

Position measurements were also acquired in the presence of each distorter in order to correlate the inductance and phase measurements with the position error experienced by the tracking system. This test requires that all transmitter coils are operating in TX mode with each transmitter coil emitting a unique frequency between 20kHz and 30kHz as described in chapter 3 [92, 100]. The planar perspex board shown in Figure 5.9 was set at a fixed height above the field generator. The positions were acquired by moving a commercial magnetic sensor (*Model No. 610099, Northern Digital Inc.*) in a 'scribbling' motion on the perspex board to acquire a planar array of x-y data points at a fixed z-displacement above the transmitting field generator. This was repeated for each distorter at the various distorter positions described in Table 5.4. One thousand random

Result: Matrices **V** and ϕ, where entry V(α,β) is the voltage on coil α due to coil β, and $\phi(\alpha,\beta)$ is the voltage phase angle of coil α relative to the current in coil β.

```
1  begin
2      T = no. of transmitter coils;
3      V = zeros(T, T);
4      φ = zeros(T, T);
5      for α ← 1 to T do
6          RXCoil ← α;
7          for β ← 1 to T do
8              if α == β then
9                  skip iteration since self inductance is not calculated;
10             end
11             else
12                 TXCoil ← β;
13                 V(α,β) ← DemodulateSignalAmplitude(RXCoil);
14                 φ(α,β) ← PhaseAngle(RXCoil) - PhaseAngle(TXCoil);
15             end
16         end
17     end
18 end
```

Procedure 1: Coil switching and acquisition procedure. Acquisition is skipped if indices $\alpha = \beta$ since this matrix entry represents a coil's self inductance.

position coordinates were recorded for each measurement. A control acquisition with no distorter present was also acquired.

5.5 Results

5.5.1 Mutual Inductance Matrix

The mutual inductance matrix calculation was carried out with no distorter present in order to verify the results of the simulation provided by Table 5.1. The experimental mutual inductance matrix was calculated using the measured voltages in (5.6) with the results shown in Table 5.5. The symmetry of this matrix matches closely with that of the simulated results. Four unique mutual inductance values can also be identified

using the colour-coding scheme used previously in Table 5.1.

$$\mathbf{M},\,(\mu\mathrm{H}) = \begin{array}{c} \begin{matrix} M_{\alpha 1} & M_{\alpha 2} & M_{\alpha 3} & M_{\alpha 4} & M_{\alpha 5} & M_{\alpha 6} & M_{\alpha 7} & M_{\alpha 8} \end{matrix} \\ \begin{pmatrix} - & 1.04 & 0.10 & 1.08 & 0.12 & 0.13 & 0.12 & 0.03 \\ 1.06 & - & 1.06 & 0.97 & 1.00 & 0.11 & 0.30 & 0.10 \\ 0.10 & 1.05 & - & 0.10 & 1.11 & 0.04 & 0.12 & 0.11 \\ 1.08 & 0.98 & 0.10 & - & 0.30 & 1.03 & 0.99 & 0.10 \\ 0.11 & 0.98 & 1.08 & 0.30 & - & 0.10 & 0.98 & 1.00 \\ 0.10 & 0.10 & 0.03 & 1.00 & 0.10 & - & 1.04 & 0.10 \\ 0.10 & 0.28 & 0.10 & 0.97 & 0.98 & 1.03 & - & 1.04 \\ 0.03 & 0.10 & 0.10 & 0.10 & 1.01 & 0.11 & 1.05 & - \end{pmatrix} \end{array} \begin{matrix} \\ M_{1\beta} \\ M_{2\beta} \\ M_{3\beta} \\ M_{4\beta} \\ M_{5\beta} \\ M_{6\beta} \\ M_{7\beta} \\ M_{8\beta} \end{matrix}$$

Table 5.5: Experimentally calculated mutual inductance matrix for the eight coil magnetic field generator of the Anser EMT system. All entries have units of microhenries (μH). The diagonal entries are left blank as the system is not built for measuring self-inductances. Results have been truncated and colour-coded for clarity.

It can be seen that the simulated and experimental results compare favourably, with corresponding matrix entries experiencing very similar inductance values. The absolute accuracy of the measurement is not critical due to the nature of the mutual inductance error calculation, as only changes in inductance are considered when calculating the error.

5.5.2 Inductance Error

The presence of a conductive or magnetic distorter near the system field generator will cause the mutual inductance between the coils to deviate from the control measurements of Table 5.5. The magnitude of the change is related to the severity of the distortion. This deviation from the control can be captured by calculating the mutual inductance error matrix $\mathbf{M_e}$ in (5.13) where $\mathbf{M_{distort}}$ is the measured mutual inductance matrix with a metallic distorter present and $\mathbf{M_{control}}$ is the measured inductance matrix with no distorter present. Normalising this error with respect to the control measurement in (5.14) gives the element-wise percentage mutual inductance error with respect

to the control measurement.

$$\mathbf{M_e} = \mathbf{M_{distort}} - \mathbf{M_{control}} \tag{5.13}$$

$$\mathbf{M_{e\%}} = (\mathbf{M_e}/\mathbf{M_{control}}) \times 100\% \tag{5.14}$$

The resulting matrix allocates a percentage inductance error to each mutual inductance measurement. The mutual inductance mean error (ME) per coil can be calculated by taking the column summation of $\mathbf{M_{e\%}}$ in (5.15). The mean error was used as opposed to the mean absolute error (MAE) so that net average increases and decreases in mutual inductance can be distinguished. Calculating the row summation is also correct since inductance matrices are symmetric by nature. The resulting mean error vector allocates each coil a signed mean percentage inductance error.

$$\textit{Mean Error \%} = \begin{bmatrix} \sum_{\beta=1}^{8} M_{e\%_{1\beta}} \\ \vdots \\ \sum_{\beta=1}^{8} M_{e\%_{8\beta}} \end{bmatrix} /8 \tag{5.15}$$

The inductance error of each coil was plotted against the distance of the distorter from the field generator for each distorter location. These locations are denoted in each plot using Fig 5.6b as a reference. Fig. 5.10 and 5.11 show the mean mutual inductance error experienced between transmitter coils in the presence of sheet metal and aluminium section distorters. The independent variable, *distorter distance*, is the vertical displacement between the distorter and the field generator PCB as shown in Fig. 5.8.

Results for the other remaining distorters can be found in appendix A.1.

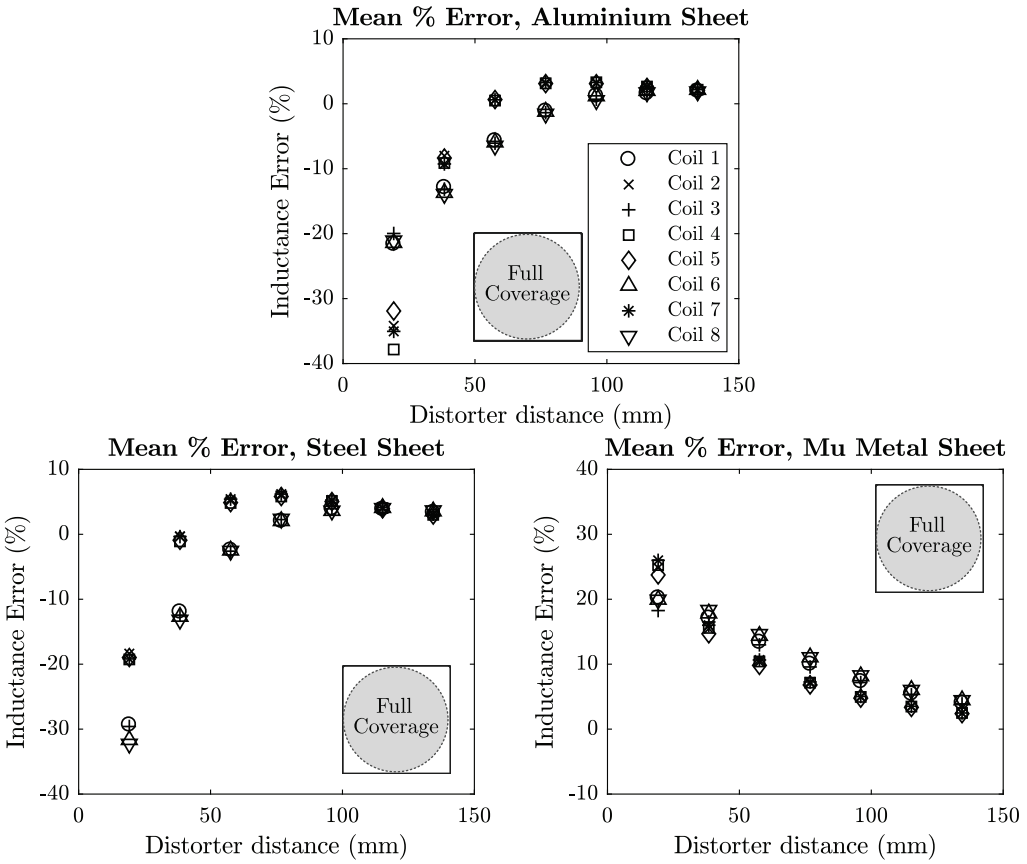


Figure 5.10: Mutual inductance error for planar sheet distorters. The Mu-metal sheet is the only material to consistently increase the mutual inductance of the transmitter coils.

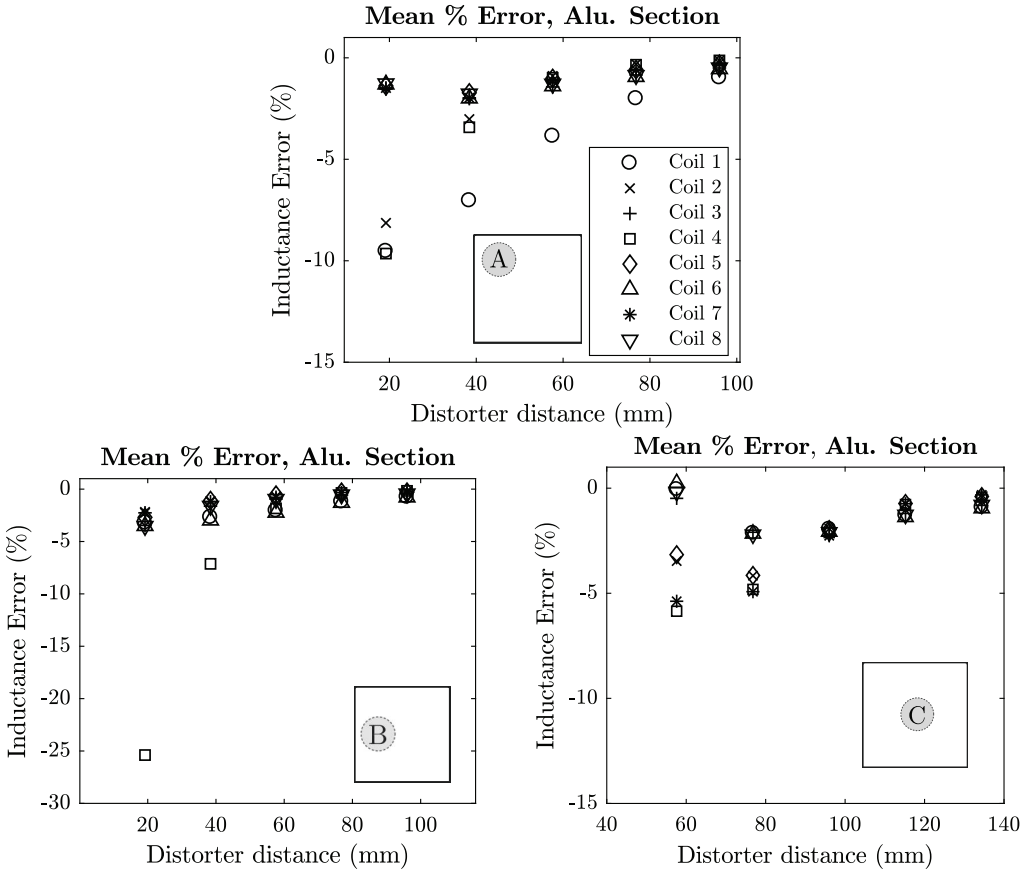


Figure 5.11: Mutual inductance error for the small aluminium section distorter in locations A, B and C. It can be seen that the location of the distorter decreases the mutual inductance of the coils in closest proximity.

5.5.3 Phase response

The demodulation process used to acquire the induced voltage signal magnitudes also yields the phase angle between the transmitter coil current and the corresponding mutually induced voltage waveforms. The phase angle θ between these current and voltage waveforms is ideally $\pi/2$ radians in the absence of distorters. This phase angle, similar to the inductance, will deviate depending on the magnitude of the distortion and the material of the distorting object. Subtracting the phase angle of the control measurement from the distortion measurement in (5.16) yields a matrix of phase differences for each mutual inductance entry. Fig. 5.12 and 5.13 show the mean phase angle error experienced between transmitter coils in the presence of sheet metal and aluminium section distorters. The independent variable, *distorter distance*, is the vertical displacement between the distorter and the field generator PCB as shown in Fig. 5.8. The phase plots for the remaining distorters can be found in appendix A.2.

$$\varphi_e = \theta_{distort} - \theta_{control} \tag{5.16}$$

where $\theta_{distort}$ is a matrix of calculated phase angles between the driving coil current and mutually induced voltages when a distorter is present and $\theta_{control}$ are the corresponding phase angles with no distorter present. The mean coil phase error φ_e is then calculated in (5.17).

$$\begin{bmatrix} \sum_{j=1}^{8} \varphi_{e_{1j}} \\ \vdots \\ \sum_{j=1}^{8} \varphi_{e_{8j}} \end{bmatrix} /8 \tag{5.17}$$

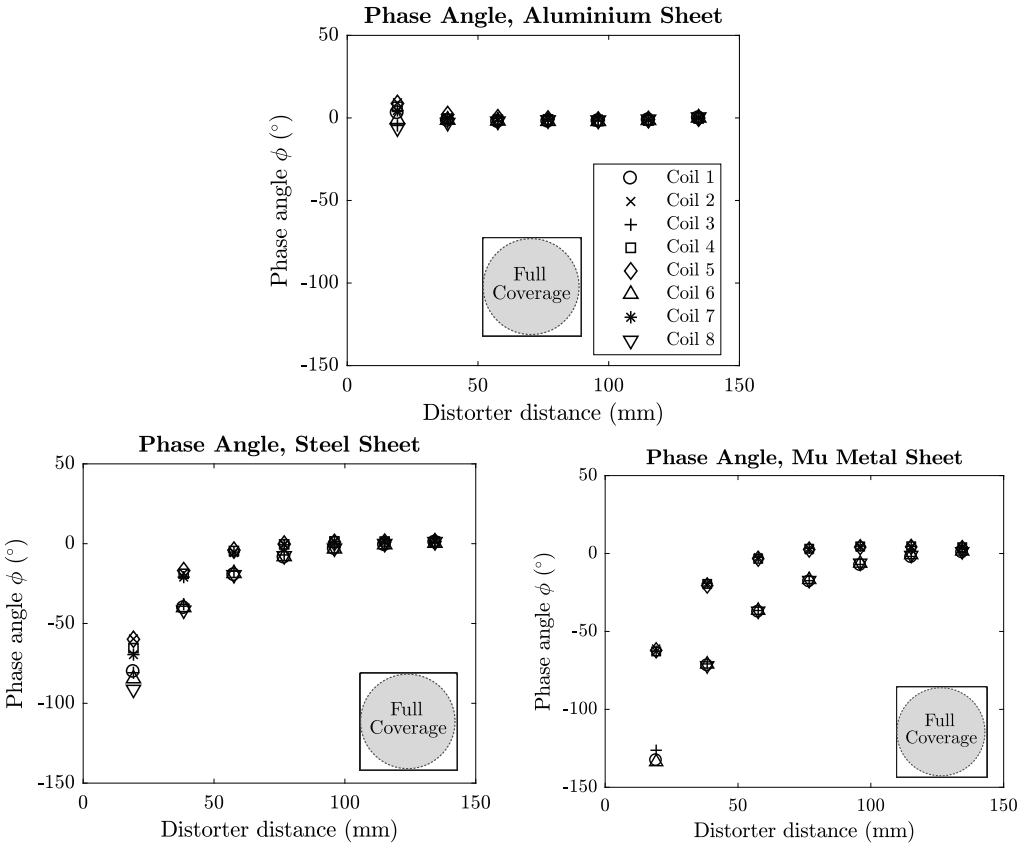


Figure 5.12: Phase error for the planar sheet distorters. The aluminium sheet contributes a small positive phase shift, while both steel and Mu-metal sheets contribute large negative phase shifts when in close proximity to the field generator.

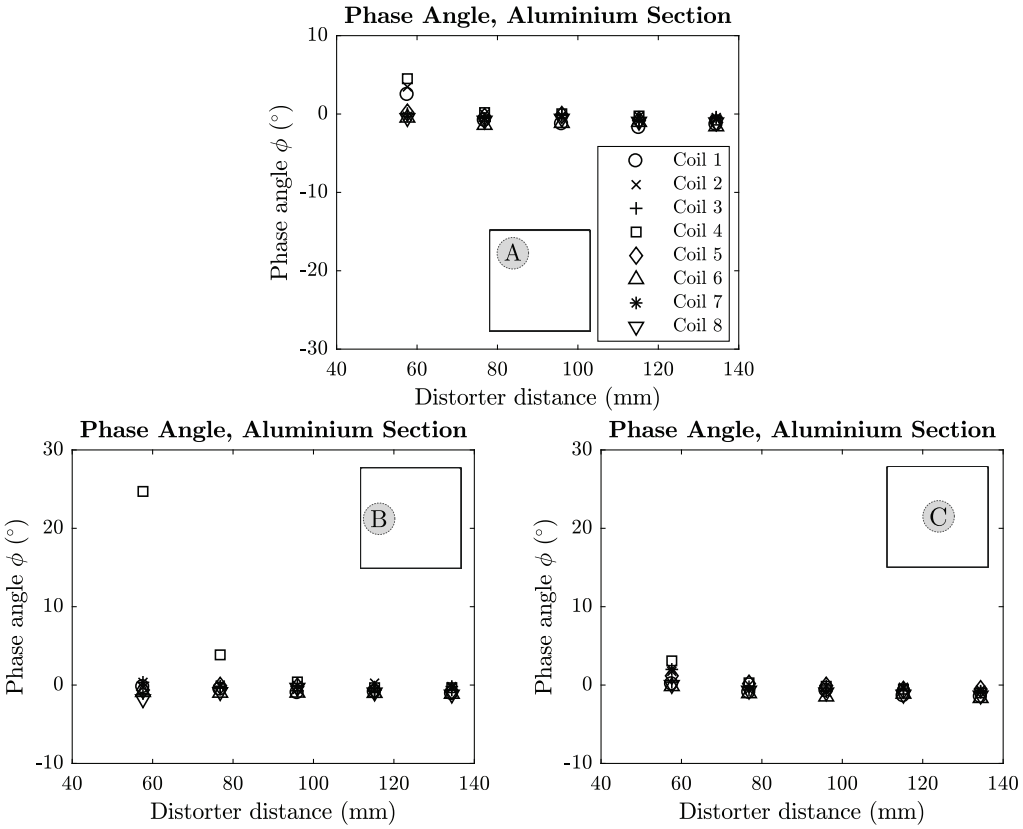


Figure 5.13: Phase error plots for small aluminium block distorter in locations A, B and C.

5.5.4 Position Error

The planar position acquisitions provided point clouds in the x-y plane of the field generator at a fixed z displacement. For a given distorter configuration, the mean z-axis error, e_z, with respect to the control, was calculated by subtracting the mean z value of the control, $\bar{z}_{control}$, from the distorted cloud positions z_i, and then averaging over N_{cloud} points in (5.18). The absolute error was not taken in order to preserve the sign of the error. The standard deviation of each distorted point cloud was calculated with respect to its own mean $\bar{z}_{distort}$ using (5.19).

$$e_z = \frac{1}{N}\sum_{i=0}^{N}(z_i - \bar{z}_{control}) \tag{5.18}$$

$$\sigma_z = \frac{1}{N}\sqrt{\sum_{i=0}^{N}(z_i - \bar{z}_{distort})^2} \tag{5.19}$$

The plots for both sheet and aluminium distorters are shown in Figures 5.14 and 5.15. High values of σ_z indicate large variances in the error when the distorter is near the field generator. The presence of the steel sheet results in unaccounted changes to the field generator's magnetic model. The field generator's magnetic model is discussed in section 3.5. Reported sensor positions tend to stray from the planar ground-truth in in the presence of the steel sheet as the real physics no longer adheres to the system's magnetic model. This error variance is visualised in the example point cloud plot in Figure 5.16 with and without the 1mm steel sheet, where its presence causes a large deviations in position compared to the control where no distorter is present. Position error plots for the remaining tested distorters can be found in appendix A.3.

5.6 Discussion

Comparing the data of both inductance matrix and position experiments highlights a number of useful relationships between the properties of the distorters and the mutual inductance measurements of the field generator transmitter coils.

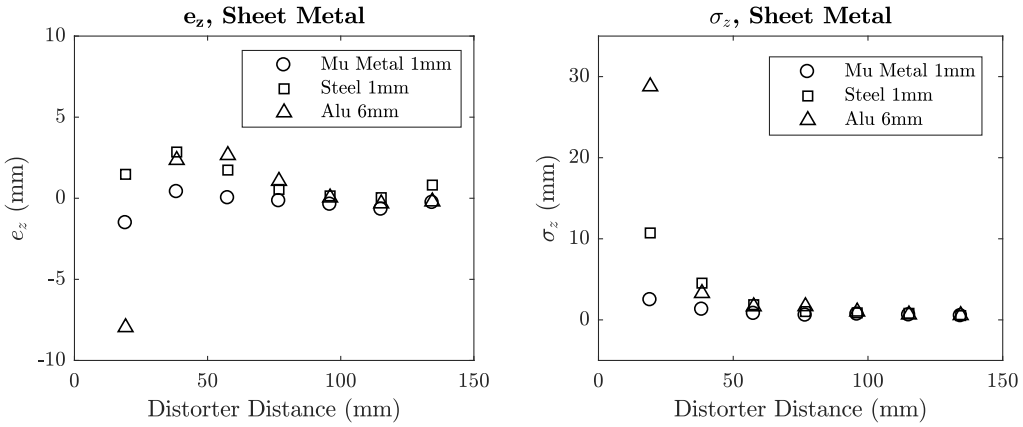


Figure 5.14: Mean error and standard deviation for sheet metal distorters

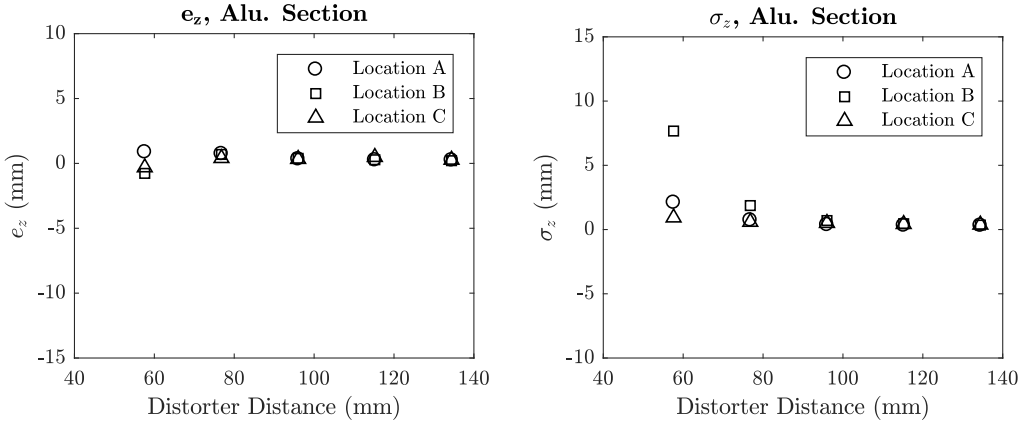


Figure 5.15: Mean error and standard deviation for aluminium section distorter in locations A, B and C.

5.6.1 Error versus Distance

There is an excellent correspondence between the measured inductance and positional error in relation to the distorter's distance from the field generator. In all cases it can be clearly seen that placing a distorter nearer to the field generator will increase both the inductance and positional errors. This is intuitively correct as a distorter's interaction with the field generator's magnetic field will become increasingly significant the closer it is placed to the field source. Steel and aluminium distorters tend to give rise to negative z-position errors, in which the distorter negatively impacts the mutual inductance of the field generator. However, it can be seen in Fig. 5.10 that a slight

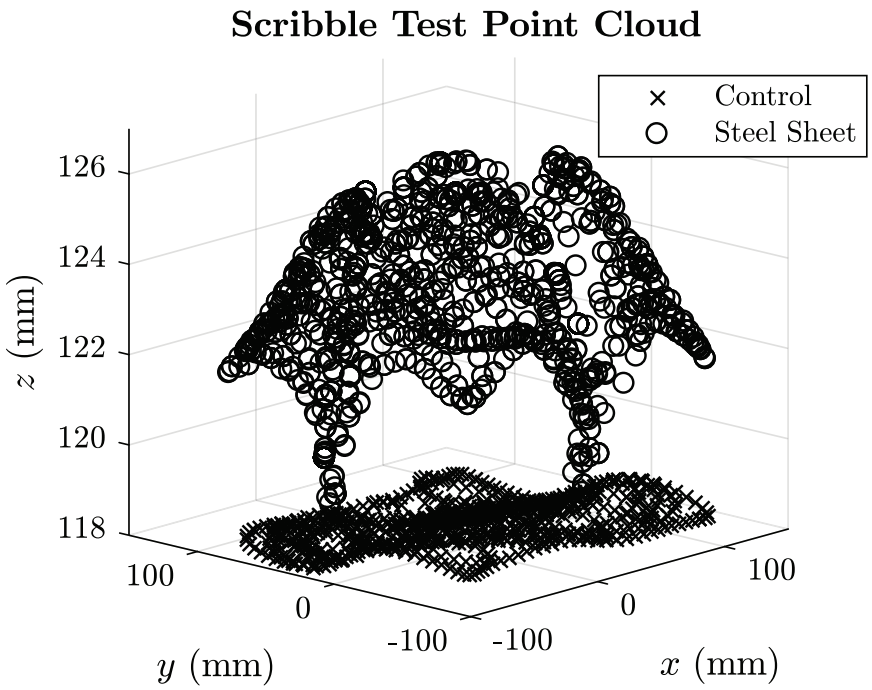


Figure 5.16: Point clouds a scribble test position acquisition for the 1mm steel sheet placed 57mm below the field generator PCB. The point cloud with steel present has a mean height of $\bar{z}_{steel}$ of 129.5mm and standard deviation of $\sigma_{z_{steel}} = 7.46$mm. The control point cloud is also shown for reference ($\bar{z}_{control} = 118.5$mm, $\sigma_{z_{control}} = 0.37$mm).

positive positive inductance contribution is evident for z-positions greater than 50mm. The Mu-metal sheet contributes positively to the field generator's mutual inductance for all z-positions. These results strongly agree with [157] in which the signal-to-noise ratio of the tracking system sensor is increased when a Mu-metal shield is used.

5.6.2 Phase Angle versus Material

A significant relationship can be found between the experimentally calculated phase angle and the material of the distorter. All steel distorters exhibited negative phase angles in these experiments, while the aluminium distorters experienced all positive phase angles. The mu-metal sheet distorter introduced very significant negative phase compared to the steel sheet, with a total phase angle of approximately -140°. Clearly the phase angle and permeability of the material have a positive correlation and can

be used to determine whether the distorter is ferromagnetic or purely conductive in nature. These results compare favourably with those of [161] which showed that purely conductive materials introduce opposing phase to that of ferrous materials. The degree of phase shift experienced in the presence of the distorter depends on the size, thickness and inductance and resistance of the distorter as well as the excitation frequency [164].

5.6.3 Inductance and Phase Error versus Distorter Location

A strong correlation was also shown between the location of a distorter and the error that it produces. This is particularly relevant to the small steel and aluminium distorters. In the case of the aluminium section and steel block distorters, the transmitter coils that are in closest proximity to the distorter experience the highest inductance (and phase) errors. This holds for the larger steel slab and aluminium cylinder distorters, although the relationship becomes less significant with increasing distance from the field generator. In particular, Figure 5.11 shows that the highest inductance errors for a distorter in position A are experienced by coils 1, 2 and 4 which are directly above the distorter as shown in Figure 5.6b. From these observations we can conclude that there is a correlation between the location of the distorter and the location of the coil(s) experiencing the highest inductance error. This relationship may be useful when initially placing the system field generator in order to minimise position errors from local distorters. Further more, the relationship may also enable EMT users to create quantitative measures of tracking confidence in the presence of distorters based on their location, in which specific portions or sub-volumes of the full EMT tracking volume are assigned a confidence score derived from the nearest transmitter coil's inductance error. It should be noted that the analysis presented in this chapter is most effective when distortions are of a static nature, as the method assumes the environment does not change during the induction measurement procedure.

5.7 Summary

Chapter 5 presented a novel electromagnetic tracking system field generator capable of characterising the nature of distortions in close proximity without the use of a stan-

dalone magnetic sensor. A mutual inductance model for the system field generator was developed, followed by an experimental amplitude and phase analysis of the system transmitter coils. The results allow the user to distinguish the size, severity and material (ferromagnetic or non-ferrous conductor) of the distorting objects in close proximity to the system field generator. The presented analyses can be readily applied to other electromagnetic tracking field generatorfield generator designs if induced voltages can be measured on all constituent transmitter coils. Achieving material discrimination in this manner may allow researchers to craft error compensation methods which are specifically designed for a particular distorter configuration.

Chapter 6

Modular and Tiled Field Generator Design

6.1 Introduction

The first electromagnetic tracking systems [99, 123, 165] were relatively large and suffered from significant positioning errors, but the technology has since advanced significantly to the point where they can employed in medical procedures [93].

Electromagnetic tracking systems invariably share two common components: a magnetic field generator and a magnetic receiver (sensor). The field generator, such as the planar generator used in the Anser system, produces a time-varying magnetic field such that each point in the vicinity of the generator has a unique magnetic signature dependant on the distance from the generator. Many field generator topologies exist and feature different magnetic field designs. Tri-axial generator designs as shown in Fig. 6.1(a) [120, 166–168] are by far the most common as they provide a sufficiently unique magnetic field distribution using three orthogonal coils. Generators using multiple planar coils as shown in Fig. 6.1(b) [92, 101, 102, 169] are also common as this

This chapter is based on H. A. Jaeger et al. "Electromagnetic Tracking using Modular, Tiled Field Generators", *IEEE Transactions on Instrumentation & Measurement*, 2018 (*under review*).

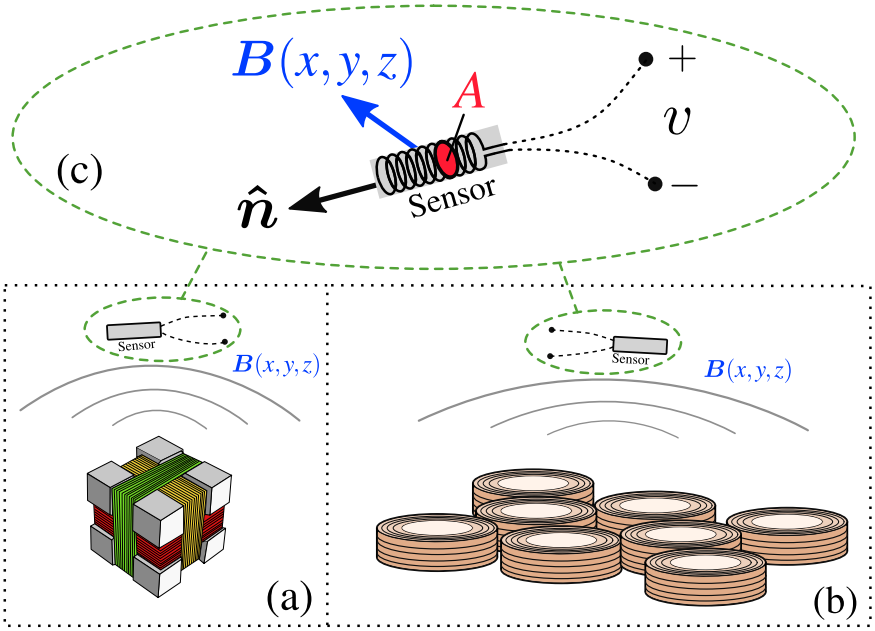


Figure 6.1: (a) Illustration of a tri-axial field generator consisting of 3 orthogonal windings on a cube former. (b) Illustration of a planar field generator design consisting of multiple circular coils. (c) The magnetic field sensor detects the component of the generated magnetic flux density $\boldsymbol{B}$ that is aligned axially with the sensor's cross-sectional area $A \cdot \hat{\boldsymbol{n}}$.

enables the field generator to be planar in shape allowing tracking over large areas, though this form factor requires a higher coil count to achieve a spatially unique magnetic field. In general, for the solenoidal tracking sensor receiver shown in Fig. 6.1(c), the induced voltage signal $v_s(t)$ is proportional the magnetic flux density $\boldsymbol{B}$ produced by the generator at the point (x,y,z) projected along the axis $\hat{\boldsymbol{n}}$ of the sensor. Section 3.5.4 explains the magnetic sensor physics in detail. Recent work [170] has shown that even a single uni-axial field generator can be used to successfully achieve six degree-of-freedom tracking, although this requires a relatively advanced sensor design capable of sensing both DC and AC magnetic signals.

As the applications of electromagnetic tracking continue to expand, the requirement for customisable tracking volumes becomes of particular interest. At present, the only commercially available systems that readily support expandable tracking volumes are the Liberty Latus and G4 tracking systems (*Polhemus Inc, Colchester, VT, USA*)

in which multiple field generators can work in tandem to form an aggregate tracking volume, but their modular tracking methods are proprietary and their associated sensor geometries are too large for many medical applications. Recent work [171–173] has described methods of achieving this functionality using discrete coils, though these do not produce a readily scalable design.

This chapter describes a method of constructing customised magnetic tracking volumes using multiple planar PCB field generators. The Anser electromagnetic tracking platform [100] described in chapter 3 is demonstrated with a configurable tracking volume using two such generators. The magnetic field model for the system is developed and experiments are performed for various generator configurations. Though only two field generators were used in experimental work, the method can be scaled for N_{FG} field generators to form larger tracking volumes.

6.2 Planar EM Tracking

The tracking system used in this work utilises a planar magnetic field generator implemented in a printed circuit board (PCB) and is capable of tracking a five degree-of-freedom (DoF) solenoidal coil sensor in a 25cm×25cm×25cm volume [174]. The induced voltage signals on the sensor are numerically fit to an analytical magnetic model of the field generator to yield the position and orientation of the sensor. This information can be represented as a 5-DoF vector as described in chapter 3.

Now consider a single field generator comprising multiple coils as shown in Fig. 6.2. For a tracking system containing M coils, transmitting M distinct frequencies, the full field generator magnetic model results in a $3 \times M$ matrix of magnetic flux densities given by (6.1).

$$\mathbf{B}_{\mathrm{FG}} = [\boldsymbol{B}_{coil_1}\ \boldsymbol{B}_{coil_2}\ \ldots\ \boldsymbol{B}_{coil_M}] \tag{6.1}$$

In order to compactly define the coil filament locations for each coil in the field generator, we define a $3 \times k$ coil matrix $\mathbf{P}_j$ in (6.2) which contains the consecutively ordered start and end points for each segment of the j^{th} coil of the generator in Fig. 6.2. A row

of ones is appended to allow manipulation of **P** using homogeneous transformations.

$$\mathbf{P}_j = [\boldsymbol{p}_1\ \boldsymbol{p}_2\ \ldots\ \boldsymbol{p}_k] = \begin{bmatrix} p_{x_1} & p_{x_2} & \cdots & p_{x_k} \\ p_{y_1} & p_{y_2} & \cdots & p_{x_k} \\ p_{z_1} & p_{z_2} & \cdots & p_{x_k} \\ 1 & 1 & \ldots & 1 \end{bmatrix} \tag{6.2}$$

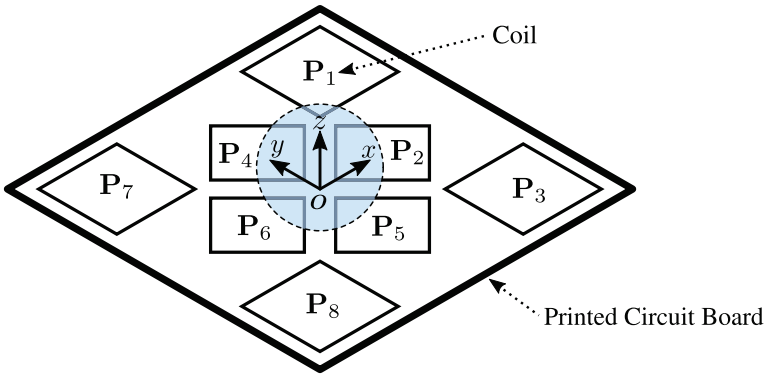


Figure 6.2: Diagram illustrating the location of each transmitter coil relative to the origin on the tracking system field generator.

6.2.1 Multi Field Generator Design

The shape and monolithic design of the system field generator coupled with the high manufacturing precision of printed circuit board process (10µm) allows multiple generators to be treated identically. It is then possible to place multiple field generators together and increase the overall system tracking volume. In this chapter we show results for two adjacent field generators, to increase the effective volume of the single field generator shown in Fig. 6.2.

We begin by introducing two identical field generators, A and B, as shown in Fig. 6.3. Generator B shares a common edge with A that is parallel to the y_A axis and is inclined at an angle β. The Euclidean distance between the origin of both field generators is given by the translation vector $\boldsymbol{t}$. Combining this information allows for the creation of a single 4×4 homogeneous transformation matrix which completely describes the location of field generator B with respect to A given by (6.3)

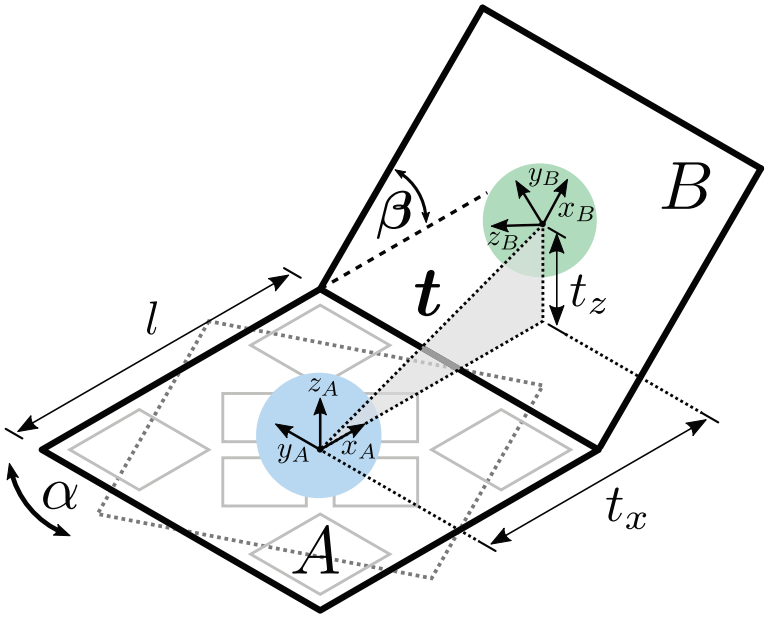


Figure 6.3: Diagram illustrating the spatial relationship between two square field generators A and B. The planar field generators are inclined at an angle β with respect to one another. If both generator boards touch at a common fulcrum then the translation vector $\boldsymbol{t}$ pointing from the origin of generator A to generator B can be readily calculated from the field generator PCB length l (30cm).

$$\mathbf{T}_B^A = \begin{bmatrix} \mathbf{R}_B^A & \boldsymbol{t}_B^A \\ \mathbf{0} & 1 \end{bmatrix} \tag{6.3}$$

where $\mathbf{R}_B^A$ describes the orientation of field generator B's origin with respect to A and $\boldsymbol{t}_B^A$ is the translation vector pointing from the origin of generator A to generator B, defined by (6.5). $\mathbf{R}_B^A$ is constructed using two elemental rotation matrices about the y and z axes of A respectively, and is shown in (6.6) and (6.7).

$$\mathbf{R}_B^A = \mathbf{R}_y \mathbf{R}_z \tag{6.4}$$

$$\mathbf{t}_B^A = \begin{bmatrix} t_x \\ t_y \\ t_z \end{bmatrix} = \begin{bmatrix} \frac{l}{2}\left(1+\cos(\beta)\right) \\ 0 \\ l\sin(\beta) \end{bmatrix} \tag{6.5}$$

$$\mathbf{R}_y = \begin{bmatrix} \cos(\beta) & 0 & \sin(\beta) \\ 0 & 1 & 0 \\ -\sin(\beta) & 0 & \cos(\beta) \end{bmatrix} \tag{6.6}$$

$$\mathbf{R}_z = \begin{bmatrix} \cos(\alpha) & -\sin(\alpha) & 0 \\ \sin(\alpha) & \cos(\alpha) & 0 \\ 0 & 0 & 1 \end{bmatrix} \tag{6.7}$$

The angle α which describes $\mathbf{R}_z$ is the initial rotation in the *x*-*y* plane of field generator *B* with respect to *A*, while the angle β of $\mathbf{R}_y$ describes the inclination of *B* relative to *A* as shown in Fig. 6.3. If both field generators share a common edge as shown, then α is restricted to angles of 0°, 90°, 180° and 270°. Angle β does not have this limitation and can be continuously varied whilst maintaining full contact along the common edge, although for experimental demonstration we restrict ourselves to angles between 0° and 90°.

With this transform defined, the matrices defining the coils coordinates of field generator *B* can be written in terms of those of *A*. Applying (6.3) to all coil matrices, $\mathbf{P}_j$, of field generator *A* yields the corresponding coil matrix of generator *B* (6.8).

$$\mathbf{P}_{jB} = \mathbf{T}_B^A \mathbf{P}_{jA} \tag{6.8}$$

This transformation allows the position of every coil to be defined in terms of the global reference frame of field generator *A*. The total magnetic field at any point $\boldsymbol{r}$ relative to generator *A* can now be calculated for each coil using (3.17) and (3.18). This modelling technique can be readily scaled for multiple field generators (*C, D,* ...) as shown in Fig. 6.4, to provide an arbitrarily large tracking area with the constraint that their origins be referenced with respect to the global reference *A*.

6.3 Field Generator Hardware

The open source electromagnetic tracking system [92, 100] described in chapter 3 was also used in this chapter to obtain experimental results.

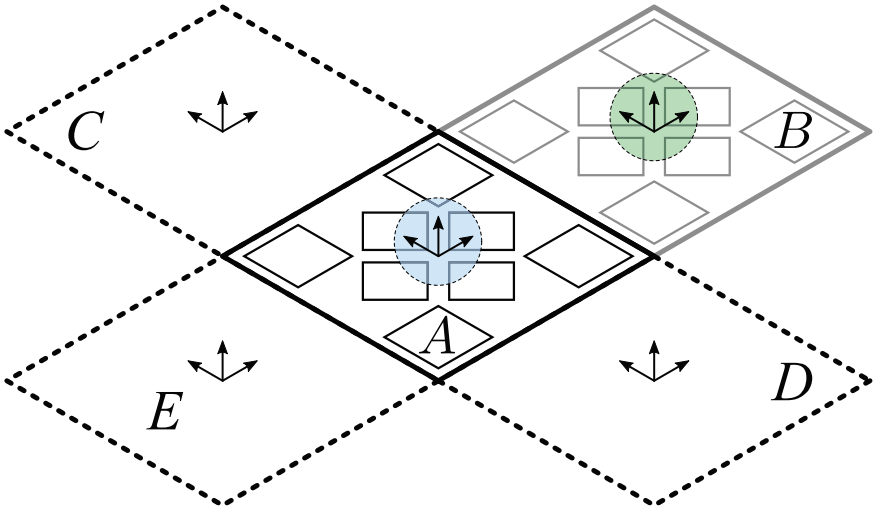


Figure 6.4: Multiple planar field generators can be tiled to form larger tracking volumes. All field generators share a common edge in order to preserve tracking continuity.

A commercial 5-DoF tracking sensor (*Model No. 610099, Northern Digital Inc, Waterloo, Ontario, Canada*) was used for experimental testing. The field generator current signal is also monitored in order to determine the phase angle between the transmitted magnetic field and the induced voltage signal. This angular information is used to resolve the axial orientation ambiguity associated with symmetric 5 degree-of-freedom magnetic sensors. Each base station is capable of driving an 8-coil field generator. This work uses two identical generators and thus required two base stations to operate. The coils of each field generator are excited by an AC signal at a unique frequency. Sixteen frequencies ranging from 18kHz to 33kHz with 1kHz spacing were chosen. The connectivity between the base stations is illustrated in Fig. 6.5.

Fig. 6.6 shows the experimental setup for two field generators labelled A and B. The origin of generator A is defined as the global reference frame. Generator B shares a common edge with A and is rotated by an angle α of 90° as indicated by the location of the cable connector. This orientation was chosen to minimise the mechanical warping of the circuit board due to the weight of the cable. Angle β can be adjusted to the desired value using the protractor. A precision machined polycarbonate test board with a thickness of 6mm is used to mechanically locate the tracking sensor in known positions. The height of the test board is adjusted using Duplo bricks (*The Lego Group,*

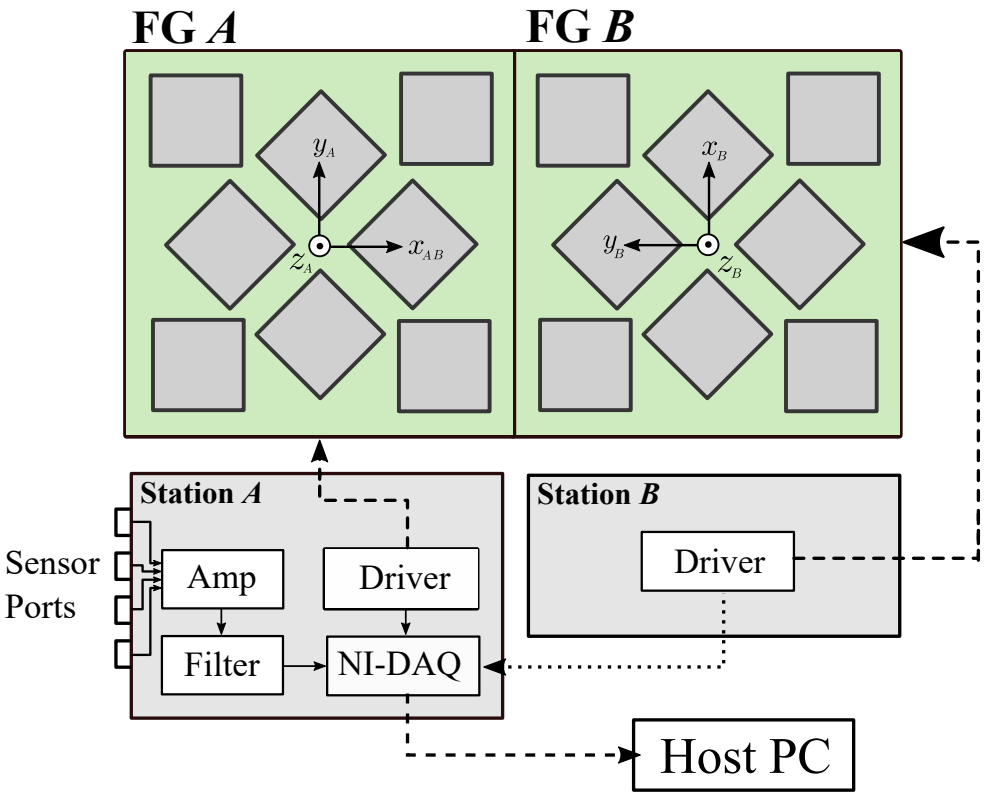


Figure 6.5: Diagram illustrating the connectivity between the two base stations. Each station powers a single field generator using an independent current driver circuit. Station *A* is used as the primary system for the tracking sensors. The DAQ of *A* is connected to the host PC and used for data acquisition. Station *B* is used solely as a current driver whose reference signal is fed back to the DAQ in station *A*.

Billund, Denmark) with each brick measuring 19.2mm in height with a manufacturing tolerance of 10µm [163].

6.4 Experimental Methods

Two experiments were undertaken to validate the effectiveness of the tiled field generator design. The first experiment investigates the use of a second field generator at a variable inclination angle on the overall precision (jitter) and position accuracy of the system. The second experiment investigates the continuity performance of the system at the tracking volume boundary when both generators are horizontally tiled.

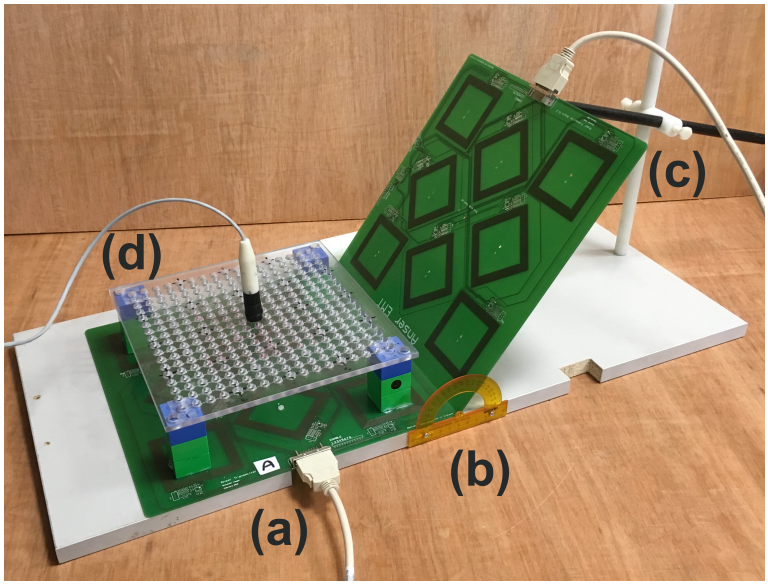


Figure 6.6: Photograph of the experimental field generator setup. (a) Generator A is mounted with plastic screws onto a planar wooden frame. (b) A protractor is mounted to the wooden frame such that the fulrum point is aligned with the edge of generator A. (c) The second generator, B, is mounted at an angle with respect to A using the protractor and an adjustable plastic rod. The configuration shown has $\alpha = 90^\circ$ and $\beta = 45^\circ$. (d) A precision machined polycarbonate test board is used in combination with Duplo to mechanically locate the test sensor at multiple locations above generator A.

6.4.1 Angle Experiment

The introduction of field generator B inclined to generator A provides additional magnetic fields whose spatial distribution is a function of the inclination angle β. Non-coplanar magnetic field generators, such as those used in orthogonal tri-axial magnetic tracking systems, require only three transmitting coils to provide a sufficiently spatially unique magnetic field. Intuitively the addition of generator B should increase the overall tracking accuracy of the system. The setup shown in Fig. 6.6 was used with test grid heights of 66mm, 162mm and 258mm. Adopting a similar testing technique to the compact field generator design in [149] described in chapter 3, the tracking sensor was placed at 9 equally spaced points on the test board's 3×3 point grid spaced 50mm apart. One hundred position measurements were acquired at each point. The acquisition is repeated for β angles of 0°, 20°, 45°, 70° and 90°. A typical plot of the

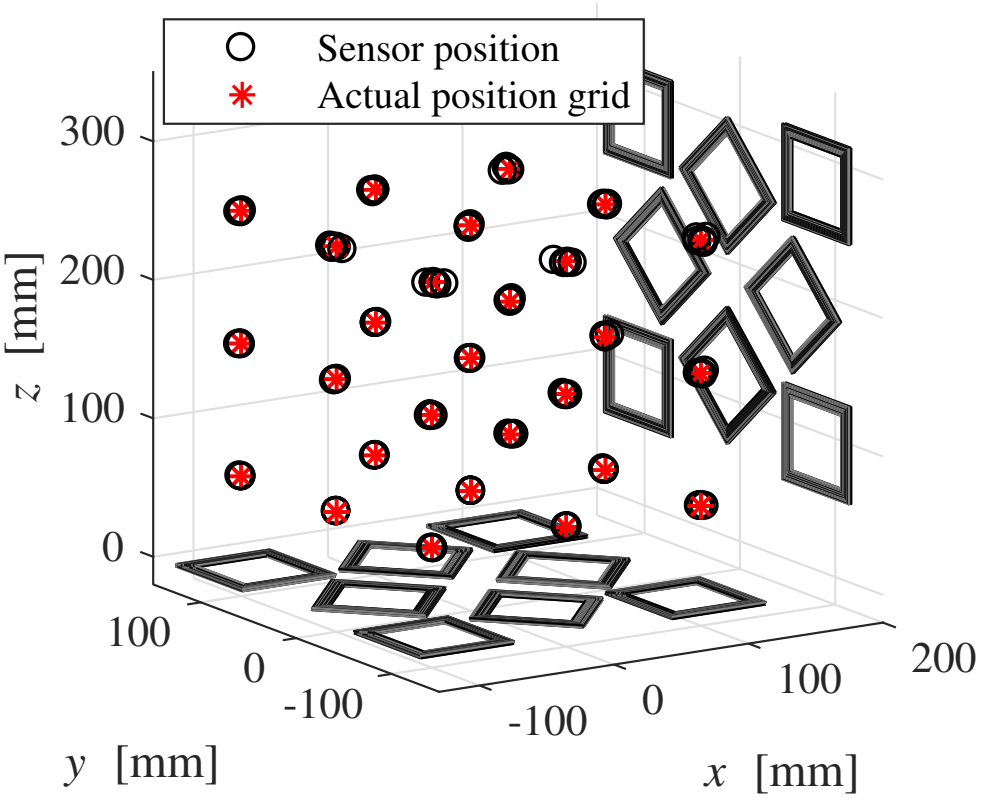


Figure 6.7: Plot of grid points gathered for $\beta = 90°$. The field generator coil filaments are also plotted for reference. Similar acquisitions were performed for angles $\beta = 0°$, 20°, 45° and 70°.

acquired position data for $\beta = 90°$ is shown in Fig. 6.7. A control measurement was also taken in which field generator *B* was switched off and removed from the position solving algorithm.

Error measurements were determined by calculating the fiducial registration error (FRE) for each grid of 9 points at $z = 66$mm, 162mm and 258mm. This method was adopted from [149] for testing the performance of a compact field generator tracking system in the absence of a ground truth measurement. Calculation of the FRE begins by determining the rigid registration transformation which best maps the acquired sensor position (*source*) points to the corresponding points in the test grid (*destination*) in a least-squares sense. This is performed using a well known closed form approach

[68]. The FRE for a grid height z is then defined as the root mean square Euclidean distance between corresponding *source* and *destination* points after registration has been applied to the *source* points according to (6.9) [175].

$$\text{FRE} = \sqrt{\frac{1}{P}\sum_{i=1}^{P} |\mathbf{T}_R \boldsymbol{p}_{s_i} - \boldsymbol{p}_{d_i}|^2} \tag{6.9}$$

where $\boldsymbol{p}_{s_i}$ and $\boldsymbol{p}_{d_i}$ are corresponding *source* and *destination* points, $\mathbf{T}_R$ is the best fit rigid registration matrix between the two sets of points in a least squared sense and $P = 9$ corresponding to the nine points on each x-y plane.

Calculation of the precision (or jitter) is another important metric when evaluating magnetic tracking systems [108]. The precision at each grid position $\boldsymbol{r}$ was calculated as the root-mean-square error of the reported sensor position measurements with respect to the sample mean as indicated by (6.10) where $\bar{\boldsymbol{p}}_{\boldsymbol{r}}$ is the sample mean over the $Q = 100$ acquired position measurements at a single position within the grid.

$$\sigma_{\boldsymbol{r}} = \sqrt{\frac{1}{Q}\sum_{j=1}^{Q} |\boldsymbol{p}_{\boldsymbol{r}_j} - \bar{\boldsymbol{p}}_{\boldsymbol{r}}|^2} \tag{6.10}$$

The jitter was calculated for heights of $z = 66$mm, 162mm and 258mm. The mean jitter for each grid height z was then calculated by taking the average of the 9 individual jitter calculations.

6.4.2 Scribble Experiment

The simultaneous use of multiple field generators allows for the creation of larger tracking volumes. In certain circumstances the common edge configuration shown in Fig. 6.3 may not be possible and a displacement may exist between the two field generators. The experimental setup used to investigate the effect of this displacement is shown in Fig. 6.8. The tracking sensor was randomly scribbled in a single plane on the test grid at a fixed height of 66mm above the two field generators. The test grid was centred on the gap d which is varied between 0mm and 30mm in steps of 5mm. One thousand random positions measurements were acquired for each value of

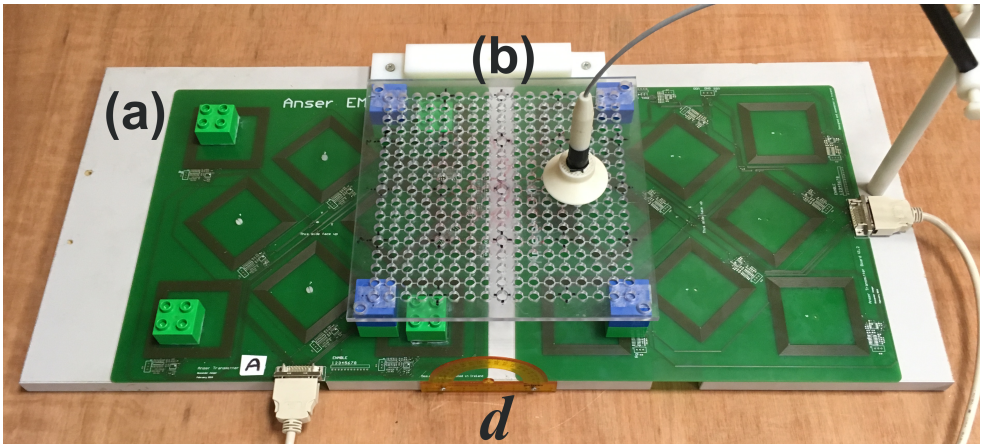


Figure 6.8: Photograph of the experimental field generator setup for acquisition of planar points during scribble testing. (a) Field generators A and B are placed in the same plane ($\beta = 0°$). (b) The machined test grid is placed in between both generators. A 3D-printed attachment allows the sensor to move smoothly on this plane. A displacement d exists between both generator boards and is adjusted from 0mm to 30mm with the planar test grid re-centred after each adjustment.

d. The error in z of each position measurement was calculated with respect to the $d = 0$ measurement using (6.11), where z_k is the current point and $\overline{z_0}$ is the mean value of z when $d = 0$.

$$\Delta z_k = z_k - \overline{z_0} \tag{6.11}$$

The RMS error and standard deviation of each point cloud was calculated from these data in (6.12) and (6.13) respectively.

$$\mathrm{RMSE}_z = \sqrt{\frac{1}{Q}\sum_{k=1}^{Q}(\Delta z_k)^2} \tag{6.12}$$

$$\sigma_z = \sqrt{\frac{1}{Q}\sum_{k=1}^{Q}(\Delta z_k - \overline{\Delta z_k})^2} \tag{6.13}$$

where $\overline{\Delta z_k}$ is the mean z coordinate over $Q = 1000$ position measurements for a particular point cloud.

6.5 Results

6.5.1 Error versus Angle β Results

Fig. 6.9 summarises the accuracy of the system at fixed heights of 66mm, 162mm and 258mm for different values of the inclination angle β. For heights of 66mm and 162mm above field generator A, the FRE remains below 2mm. The presence of field generator B becomes significant at a heights of 258mm above generator A. At this height the control measurement exhibits the highest FRE of 10.6mm, while the presence of an inclined generator B reduces the error to between 1.5mm and 2.3mm for angles between 45° and 90°. The observed trend shows that the FRE errors tend to reduce when generator B is inclined for large values of β, with the exception of $\beta = 90°$. Fig. 6.11 shows the frequency domain representation of the sampled sensor signal at a height of $z = 258$mm for two angle configurations of field generator B. The signal-to-noise ratio (SNR) of the frequency components produced by generator B are improved for $\beta = 90°$, as the Euclidean distance between generator B and the sensor is reduced. SNR differences of up to 40dB are observed between the two configurations.

6.5.2 Scribble Test Results

The scribble test results of Fig. 6.12 show how the separation between two field generators affects the overall system accuracy. A scatter plot of the results for $d = 0$mm, 15mm and 30mm is shown in Fig. 6.12. A bell-shape characteristic is observed for values of $d > 0$mm, with the peak value of the bell increasing with d. The relationship between d and the RMS error is plotted in Fig. 6.13.

6.6 Discussion

The results of Fig. 6.9 and Fig. 6.10 show that the addition of a secondary field generator increases the position tracking accuracy particularly at distances far from the primary field generator. The use of inclination angles between 45° and 90° appears to improve the accuracy of the tracking performance and decrease jitter above generator

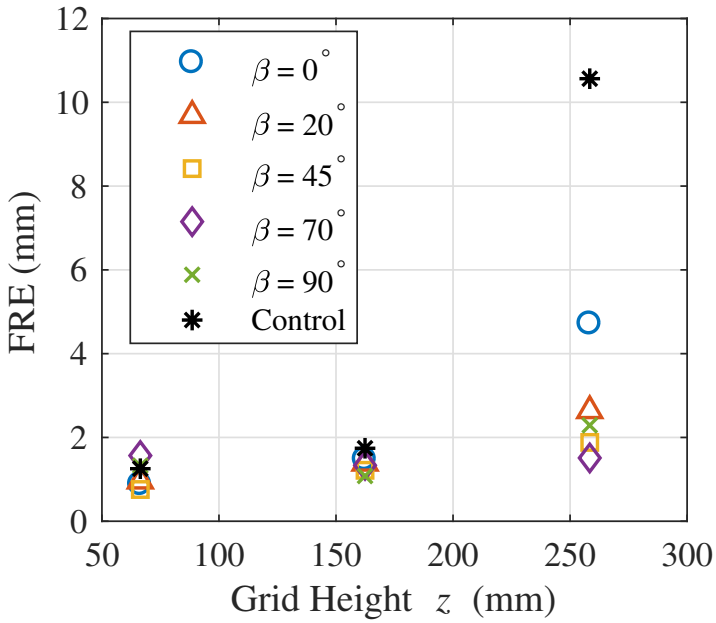


Figure 6.9: Fiducial registration error (FRE) calculated using (6.9) for grid heights of 66mm, 162mm and 258mm above field generator A for different angle configurations β of generator B. The control measurement with generator B powered off is also shown. The addition of field generator B significantly reduces the grid registration error at large values of z.

A. The reason for this is evident Fig. 6.11 which shows that the sensor experiences an improved signal-to-noise ratio at the fringes of the tracking volume when field generator B is inclined at 90°.

The scribble tests identify the continuity performance of the tracking system when two field generators are placed side-by-side in the same plane. The results of Fig. 6.12 show that any gap $d > 0$mm causes significant tracking error, where the maximum error occurs at the midpoint of the gap between the two field generators. The error characteristic is shown in Fig. 6.13 where it is clear the error increases with larger gap sizes. As expected, this result indicates that for tiled field generators of this particular design, neighbouring boards should physically touch along a common edge in order to preserve tracking continuity.

This work gathered results for two field generators. Expansion of this design for N_{FG} field generators is possible allowing larger customisable tracking volumes can be

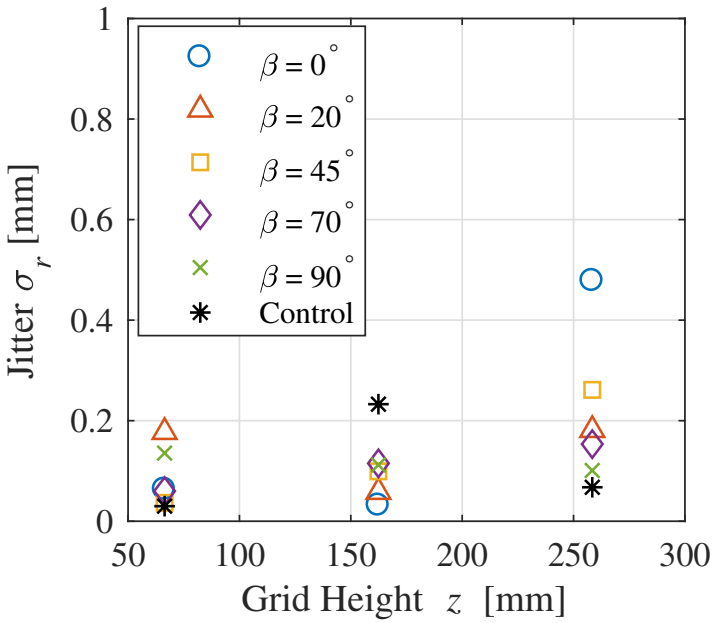


Figure 6.10: RMS jitter error σ_r calculated using (6.10) for grid heights of 66mm, 162mm and 258mm above field generator A for different angle configurations β of generator B. The control measurement with generator B powered off is also shown.

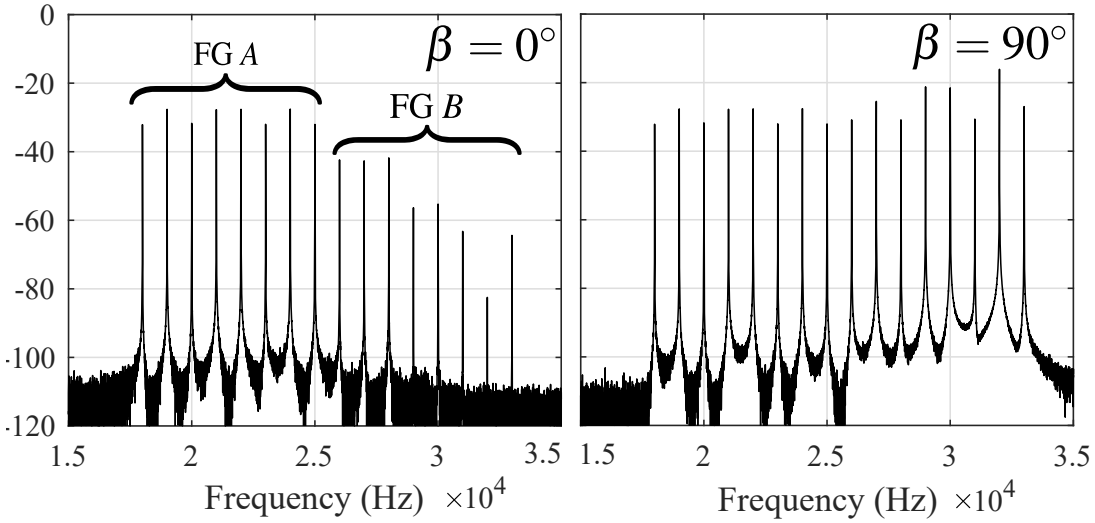


Figure 6.11: FFT of the tracking sensor signal for $\beta = 0^\circ$ and 90° after amplification. Each peak represents the induced voltage from a single field generator coil. The sensor was located in the center of the test grid at $z = 258$mm above generator A.

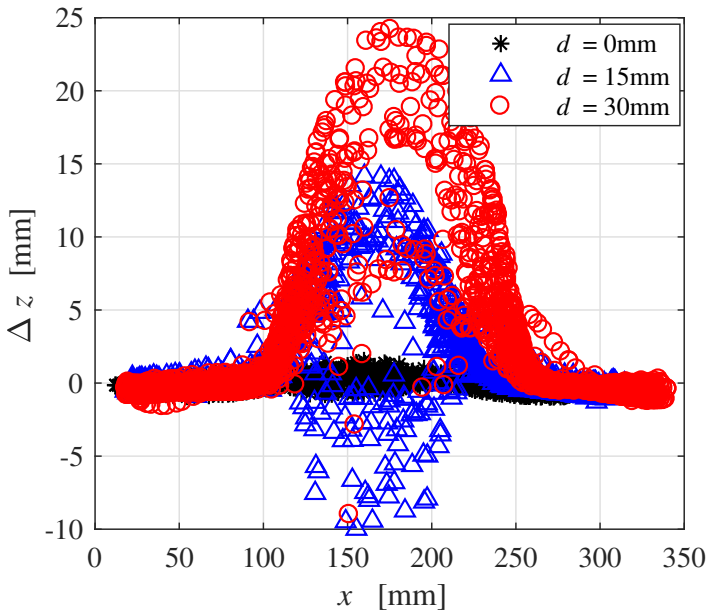


Figure 6.12: Sensor error point cloud for field generator separation distances of 0mm (black), 15mm (blue) and 30mm (red). The 3D coordinates are projected onto the x-z plane for clarity and are referenced to the origin of field generator A. The peaks of the point clouds shift in the positive x direction as the separation distance is adjusted by only displacing generator B.

constructed as shown in Fig. 6.4. Future work might study how to robustly implement a full tiling strategy whilst addressing limitations inherent in the current system design, such as transmission bandwidth and computational complexity. The system shown in this chapter requires 16 unique frequencies with a uniform spacing of 1kHz to achieve sufficient tracking performance. The requirement for all frequencies to be transmitted simultaneously (synchronous transmission) coupled with a system sampling rate of 100kHz (i.e. Nyquist 50kHz) results in bandwidth limitations occurring for $N_{FG} >$ 6 field generators, since all constituent coils must have their own distinct transmission frequency. Increasing the system sampling rate alleviates the issue, but this will eventually be limited by some hardware maximum. In this work the sampling rate limit is determined by the USB-6212 data acquisition unit which features a maximum sampling rate of 400kHz. Scaling the system in this manner also increases the computational load on the host PC as the number of filaments in the magnetic model scales

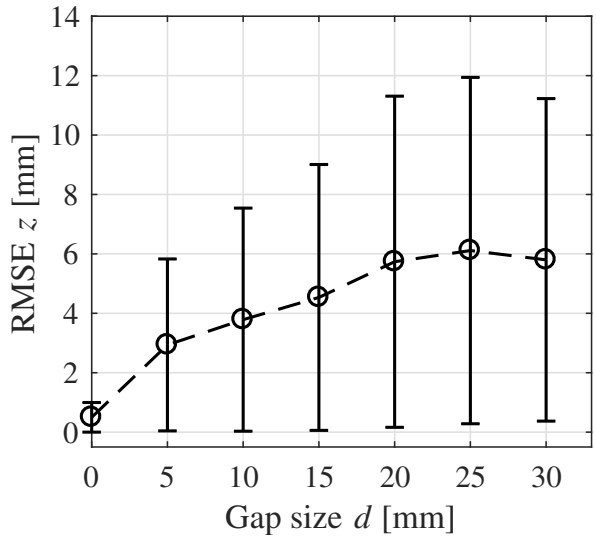


Figure 6.13: RMS error of the z coordinate data calculated using (6.12) plotted as a function of gap size d between 0mm and 30mm. Error bars indicate the standard deviation σ_z of each plot cloud's z coordinates calculated using (6.13).

linearly with the number of field generator current filaments as shown in (6.2). These constraints will need to be addressed when developing a full modular field generator tiling strategy. Notwithstanding these limitations, the current work may represent a significant milestone in extending the volume of accuracy of electromagnetic tracking technology, particularly in applications such as virtual reality and industrial robotics where low cost and modularity are beneficial.

6.7 Summary

A method of creating custom magnetic tracking volumes has been demonstrated using modular magnetic field generators in a tiled configuration. Static positional accuracy improvements occur when an inclination angle exists between the field generators. Tiling of this particular design shows that errors are minimised when a common edge is shared between both field generators. The system design may be easily scaled to create larger tracking volumes in applications such as medical instrument tracking, robotics and virtual reality.

Chapter 7

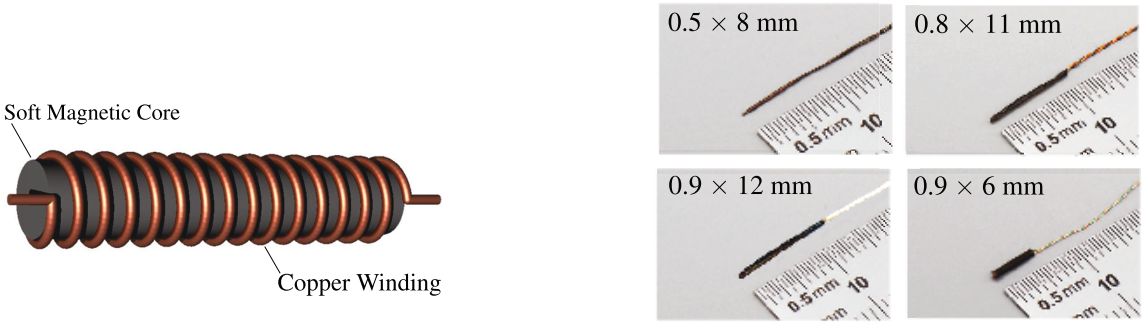
Bespoke Tracking Sensor Design

7.1 Introduction

Electromagnetic tracking (EMT) is the gold standard technology for tracking and navigation in image-guided interventions when there is no line of sight to the target. Clinical applications which currently exploit EMT for virtual navigation include bronchoscopy [8,176], neurosurgery [177] and ear,nose and throat surgery [178]. Commercial systems which use EMT for navigation include the Medtronic superDimension [179], the Veran SPiN system [35] and the Fiagon system [180]. EMT is also increasingly common in visualization systems used for surgical simulation and robotic surgery. A number of OEM EMT systems have been developed which are suitable for third-party use and research purposes. These include the NDI Aurora (Northern Digital Inc., Waterloo, Canada), the NDI Trakstar (*Northern Digital Inc., Waterloo, Canada*, formerly sold by *Ascension Technologies*) and the Polhemus Fastrak (*Polhemus Inc., Colchester, Vermont*).

Apart from the NDI Trakstar which operates on the principle of pulsed DC operation, all commercial EMT systems work on the principle of Faraday's law of electro-

This chapter is based on O. McVeigh, H. A. Jaeger et al. "Sensor design for electromagnetic tracking in image guided interventions", Submitted to IPCAI 2019



(a) (b)

Figure 7.1: **(a)** The typical electromagnetic sensor consists of copper winding of N turns. The coil may be air-cored or with a soft magnetic (ferrite) core, as shown here. **(b)** Commercially availble EMT sensors provide $x-y-z$ position, as well as pitch and yaw angular position (*i.e.*, 5 'degrees of freedom' or 5-DoF). 6-DoF sensors also provide angular roll position using 2 5-DoF sensors within a single sensor package.

magnetic induction, given by Equation (7.1) where $v_s(t)$ is the induced sensor voltage in Volts and Φ is the sensor magnetic flux in Webers.

$$v_s(t) = -\frac{d\Phi}{dt} \tag{7.1}$$

AC-based EMT systems tend to be more amenable to smaller sensor designs and are the basis of recent efforts to design open-source EMT architectures [92,100] which might address shortcomings in current systems such as electromagnetic distortion, proprietary interfaces and relatively high hardware costs.

The generalised form of (7.1) which is dependent on a function of the time derivative of the magnetic flux experienced by the sensor, is more specifically given by (7.2) for a coil-based inductive sensor of cross-sectional area, A_c, with N turns as shown in Figures 7.1a and 7.1b.

$$v_s(t) = -N\frac{d}{dt}\oint_{A_c} \mathbf{B}\cdot d\mathbf{A} \tag{7.2}$$

In EMT systems, the magnetic flux density $\mathbf{B}$, which is provided by the planar field generator board, is spatially and temporally varying and transmits has a number of unique frequency components (8 in the Anser EMT system, between 20 and 30 kHz)

which can be used to resolve the sensor position and orientation in the working volume around the field generator. For small sensors, such as those shown in Figure 7.1b, the variation in flux density across the sensor cross-section is usually small, so that (7.2) may be simplified to (7.3) where the flux density **B** is related to the field intensity **H** (in A/m) by the magnetic permeability of free space, $\mu_0 = 4\pi \times 10^{-7}$ for an air core and A_c is the coil's mean cross sectional area, approximated by (7.4) where d_i is the innermost winding diameter and d_o is the outermost winding diameter.

$$\mathbf{B} = \mu_0 \mathbf{H}$$

$$v_s(t) = -\mu_0 N A_c \frac{d\mathbf{H}}{dt} \tag{7.3}$$

$$A_c = \pi \left(\frac{d_o}{4} + \frac{d_i}{4} \right)^2 \tag{7.4}$$

In this work, larger sensor cross-sections require the use of the more general (7.2). The addition of a ferromagnetic core, as shown in Figure 7.1a, can significantly increase the received sensor voltage, v_s, particularly in the case of smaller sensor geometries. The presence of a ferromagnetic core tends to concentrate the magnetic flux lines so as to increase flux through the coil area, resulting in increased v_s. The apparent increase in magnetic permeability of the core, μ_a (compared to the air-core case), is related to the manufacturer-supplied relative permeability, μ_r, as given by (7.5) where k_d is the geometry-specific demagnetisation factor [181], resulting in a changed sensor voltage, v_s as indicated by (7.6).

$$\mu_a = \frac{\mu_r}{1 + k_d(\mu_r - 1)} \tag{7.5}$$

$$v_s(t) = -\mu_a \mu_0 N \frac{d}{dt} \oint_{A_c} \mathbf{H} \cdot d\mathbf{A} \tag{7.6}$$

The demagnetisation of the core, k_d, is a geometry dependant parameter which is used to determine the effective or apparent permeability, μ_a, of an object. The longer the core is in relation to its diameter, the lower the demagnetisation factor. In the limit-

ing case, as the length-to-width ration of the core tends to infinity, the demagnetisation factor approaches 0. This limiting case can be realised by using closed magnetic structures such as toroidal cores, which have a demagnetisation factor of 0. Such designs are used to maximise the energy storage capacity of electrical transformers while minimising magnetic field leakage. Magnetic sensors instead require an open core design in order to allow the external magnetic fields from the field generator to excite the sensor coil. The open core will increase the sensitivity of the received signal, although the resulting gain factor becomes a function of the material's relative permeability μ_r *and* the core's geometry. The demagnetisation factor, k_d, encapsulates this geometry dependency. By approximating the core to be elliptical in shape, the demagnetisation factor may be estimated using (7.7) where d_c is the diameter of the core, and l_c is the length of the core [181]. The apparent permeability of the material can then be calculated using (7.5).

$$k_d \approx \frac{d_c^2}{l_c^2}\left[\ln\left(\frac{2l_c}{d_c}\right) - 1\right] \tag{7.7}$$

The ferromagnetic core can dramatically increase the sensitivity of sensor. However, this comes at the cost of linearity. All ferromagnetic materials are inherently non-linear in nature, hence the output of the sensor will now have some non-linear behaviour which can depend on many factors such as frequency, temperature, field strength etc. [182]. Increased noise is also observed from ferromagnetic materials due to Barkhausen noise [181]. If the applied magnetic field to the sensor is sinusoidal in nature (as is typically the case for EMT systems), (7.6) can be further simplified to (7.9) where ω is the received field frequency in radians per second.

$$\mathbf{H} = \mathbf{H}_0(x,y,z)\sin\omega t \tag{7.8}$$

$$v_s(t) = -\mu_a\mu_0 N\omega\cos\omega t \oint_A \mathbf{H}_0(x,y,z)\cdot d\mathbf{A} \tag{7.9}$$

Equation (7.9) is the basis of the investigations in this chapter where $\mu_a = 1$ in the case of an air-core coil. To date, EMT sensors, such as those shown in Figure 7.1b, are commercially manufactured to specified sensitivities in fixed geometries. However,

with the increasing prevalence of EMT across image-guided interventions, the need for flexible sensor geometries and sensitivities has become more important. While bespoke sensor design is not feasible with proprietary systems, the Anser EMT system [100] facilitates new sensor geometries for specific applications such as laparoscopic instrument and endoscope tracking. In these applications, tracking accuracy may often be less important than ergonomic sensor geometries which easily integrate with the large instrument diameter (6-12 mm) without taking up the instrument channel of endoscopic instruments [183]. The goal of this chapter is to demonstrate the feasibility of bespoke sensor design, development and testing for the Anser EMT system, where variations in sensor accuracy with turn count, N_{turn}, and coil area, A_c are investigated, using both air and ferrite core geometries. The work represents the first attempt to demonstrate bespoke inductive sensor characterisation for electromagnetic tracking systems within the limits of hand-wound geometries and 5 degree of freedom (5 DoF) sensing.

7.2 Materials and Methods

7.2.1 Sensor Design

A series of air-core inductive sensors were wound on custom Delrin formers with varying turn count, N, coil length, l_c, inner coil diameter, d_i (to the innermost winding), outer coil diameter d_o (to the outermost winding), and wire diameter, d_w as indicated in Table 7.1.

Coil	N_{turn}	l_c [mm]	d_i [mm]	d_o [mm]	d_w [mm]	R [Ω]	L [μH](Air)
A	321	12	9	12.5	0.19	7.4	604
B	319	12	11	14.1	0.19	8.6	804
C	120	12	9	12.2	0.32	0.8	91
D	216	12	9	11.4	0.19	9.4	425
E	417	12	9	12.0	0.15	14.3	1018

Table 7.1: Properties of EMT sensor coils designed and tested in this work.

Each coil was carefully hand-wound with visual inspection and still photography

used to confirm turn count upon completion of each layer. A typical completed winding layer is shown in Figure 7.2a. One turn of magnet tape was used to fix each layer upon winding as shown in Figure 7.2b. Each former could facilitate insertion of a ferrite rod core also shown in Figure 7.2b for testing. The final wound sensor coil was terminated with twisted-pair cable as shown in Figure 7.2c, before connection to a miniXLR connector (*part no. RT5FC-B, Neutrik AG, Liechtenstein*). Ferrite core cylinders were investigated as magnetic cores in coils *C*, *D* and *E*. The cores measured 12 $\times$ 6 mm (length $\times$ diameter) and were made of 3C90 grade ferrite (*Ferroxcube, Eindhoven, The Netherlands*) with relative permeability μ_r of 2300.

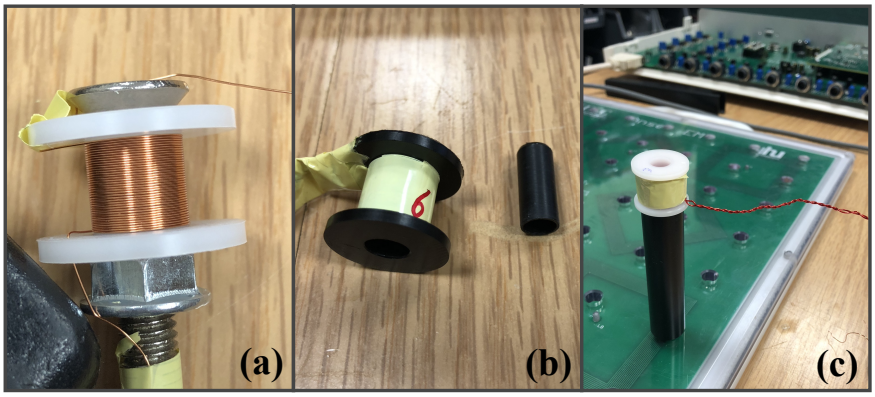


Figure 7.2: **(a)** Enamelled copper wire wound on the Delrin coil former. **(b)** Each completed winding layer was secured with magnet tape. Also shown is the removable ferrite core. The core may be inserted into the former's lumen. **(c)** The wound coil is located above the Anser EMT calibration board using the Delrin former during calibration and testing.

7.2.2 Sensor Calibration

Each sensor was calibrated for use with the Anser EMT system using the previously reported model-fitting routine [92] for sensor calibration. This involves a 7$\times$7 point-by-point calibration of the sensor and the Anser field generator (FG) shown in Figure 7.4. For 5-DoF sensor coil calibration, the coil is positioned at a fixed distance and orientation (z-oriented) relative to the field generator as shown in Figure 7.5. The induced sensor voltages at each point are processed to produce a vector of scalars which fit the magnetic model of the system FG to the sensor in a least-squares sense.

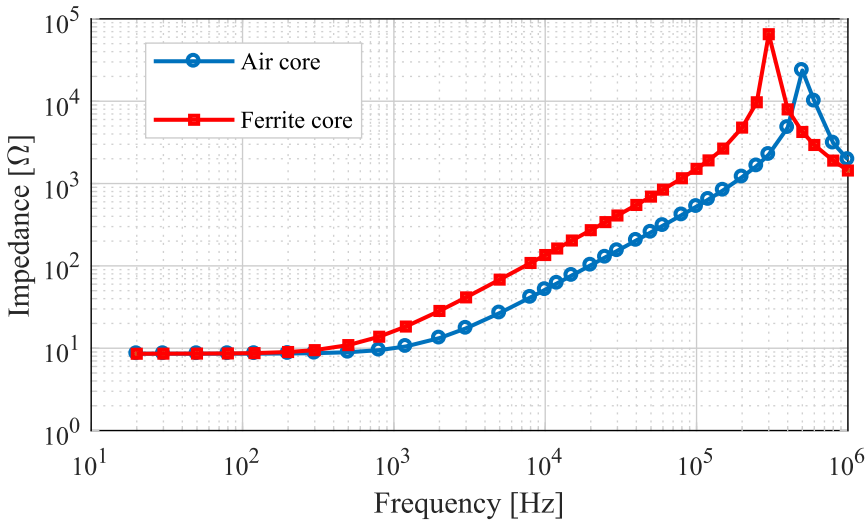


Figure 7.3: The typical impedance characteristic for an air-core and ferrite inductive sensor (*Coil B*) The coil exhibits linear impedance characteristics in the operating range of the Anser EMT system 20 and 30 kHz. The resonance frequency of the air coil is approximately 485 kHz, which is reduced to approximately 290 kHz due to the increase in coil inductance when the ferrite core is inserted.

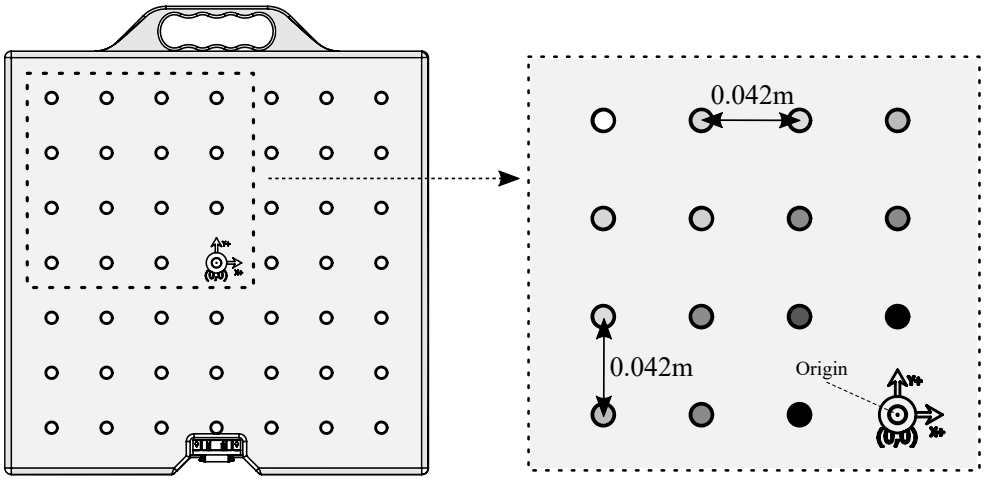


Figure 7.4: **(a)** Top-down view of Anser EMT field generator (FG) showing the 49 positions used for calibration and static position accurcy testing. **(b)** Zoomed in section of the top-left quadrant of the FG. Positions are shaded according to their (x, y, z) Euclidean distance from the FG origin $(0, 0, 0)$.

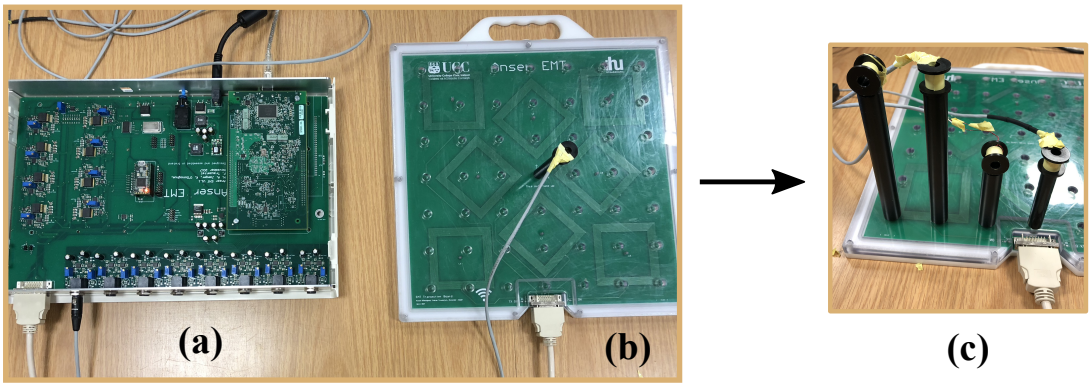


Figure 7.5: **(a)**-**(b)** Anser EMT base station and field generator (FG) used in experiments. The FG contains 8 field-generating coils below a 49 point grid of equispaced holes into which the coils may be inserted using a Delrin former. **(c)** Delrin formers of two heights were used in experiments. 49 position measurements are recorded with each former resulting in a total of 98 measurements per coil.

7.2.3 Static Accuracy Testing

The coils described in Table 7.1 were tested for static positional accuracy following calibration with previously described methods in chapter 3 [92, 100] for z-directed sensor coils using the 49 point grid shown in Figure 7.5 at fixed heights at 85.6 and 152 mm above the FG. The resultant scatter plots in Figure 7.6 show positional errors at 98 unique positions within the tracking volume. In each figure, the position error is shown as a function of the Euclidean distance from the sensor's absolute position to the centre-point of the transmitting board.

In general, it can be expected that points further from the centre-point of the transmitting board will give rise to the largest errors in position accuracy. The experimental positional errors are summarised in Tables 7.2 to 7.5. The associated point-by-point measurements are included in Fig. 7.8, 7.9 and 7.10. Static accuracy was determined by calculating the error between the reported sensor positions and the absolute position of the sensor above the field generator in a root-mean-squared (RMS) sense. Equation (7.10) was used to calculate the volume-averaged RMS error along each axis of the FG (*i.e.*, Δx_{RMS}, Δy_{RMS} and Δz_{RMS}) where x^i_{Meas} is the measured (x,y,z) position at the i^{th} point, x^i_{Ref} is the absolute x coordinate of the sensor coil and $N = 98$ is the total number test-points.

$$\Delta x_{RMS} = \sqrt{\frac{1}{N}\sum_{i=1}^{N}\left(x^i_{Meas} - x^i_{Ref}\right)^2}$$

$$\Delta y_{RMS} = \sqrt{\frac{1}{N}\sum_{i=1}^{N}\left(y^i_{Meas} - y^i_{Ref}\right)^2} \tag{7.10}$$

$$\Delta z_{RMS} = \sqrt{\frac{1}{N}\sum_{i=1}^{N}\left(z^i_{Meas} - z^i_{Ref}\right)^2}$$

The volume-averaged total RMS error by vector summation of the measured and reference positions at each experimental point is then given by (7.11)

$$Total_{RMS} = \sqrt{\Delta x^2_{RMS} + \Delta y^2_{RMS} + \Delta z^2_{RMS}} \tag{7.11}$$

7.2.4 Instrument Trajectory Tracking

One principle of application of the sensors developed in this work is in the tracking of instruments used in image-guided interventions. To demonstrate the utility of the sensors and in order to visualise real-time instrument trajectory tracking, two typical instruments were investigated. A therapeutic bronchoscope (Olympus BF-XT160, *Olympus Corp. Shinjuku, Tokyo*) with a 3.2 mm instrument channel was tracked using a 0.5 mm commercial 5-DoF sensor in the instrument channel. In addition, the bronchoscope was also tracked using *Coil B* from Table 7.1. A laparoscopic graspers (EndoClinch^{TM}, *Medtronic, Dublin, Ireland*) with an outer diameter of 5 mm was similarly attached with an identical 5-DoF commercial sensor to the bronchoscope as well as with *Coil B* from this study. Each instrument was then moved through the tracked volume and the position and orientation of both attached sensor coils was recorded. The resulting trajectory paths for both sensors is shown in Figure 7.12.

7.3 Results

7.3.1 Static Accuracy Testing

Fig .7.8 shows the total RMS error for coils A and B as a function of distance from the origin of the FG. The results are summarised in Table 7.2 which includes the different coil areas, A_c available for flux linkage (as given by (7.4)). Each coil has approximately equal turn count as noted in Table 7.1 and these coils were used to investigate the effect of increasing A_c on positional accuracy. No ferrite cores were used with coils A or B. The mean errors, Δx_{RMS}, Δy_{RMS} and Δz_{RMS}, as well as the total RMS error were calculated using (7.11).

Coil	A_c [mm^2]	Δx_{RMS} [mm]	Δy_{RMS} [mm]	Δz_{RMS} [mm]	σ_x	σ_y	σ_z	$Total_{RMS}$ [mm]
A	90.7	1.05	1.23	0.97	0.95	1.15	0.96	1.89
B	123.7	0.86	0.99	0.90	0.87	0.99	0.90	1.59

Table 7.2: Static accuracy of coils A and B with air-cores.

Figure 7.9 shows the total RMS error for coils C, D and E as a function of distance from the origin of the FG in the absence of any ferrite core. The results are summarised in Table 7.3 which includes the different turn counts, N. In this case, each coil has approximately equal core area, A_c as noted in Table 7.1 and these coils were used to investigate the effect of increasing N on positional accuracy in the absence of a ferrite core. As previously, the mean errors, Δx_{RMS}, Δy_{RMS} and Δz_{RMS}, as well as the total RMS error were calculated using (7.11).

Coil	N	Δx_{RMS} [mm]	Δy_{RMS} [mm]	Δz_{RMS} [mm]	σ_x	σ_y	σ_z	$Total_{RMS}$ [mm]
C	120	1.57	1.50	1.52	1.50	1.17	1.17	2.48
D	216	1.14	1.08	1.26	1.21	1.01	1.01	1.98
E	417	0.99	1.09	0.84	0.98	1.09	0.83	1.70

Table 7.3: Static accuracy of coils C, D and E with air-cores.

Figure 7.9 also shows the effect of inserting the ferrite core described in section 7.2.1 into cores C, D and E. The results described for this case are summarised in Table 7.4 where a 4.5 mm 3C90 ferrite core is present.

Coil	N	Δx_{RMS} [mm]	Δy_{RMS} [mm]	Δz_{RMS} [mm]	σ_x	σ_y	σ_z	$Total_{RMS}$ [mm]
C	120	1.04	0.89	1.31	1.03	0.78	0.8	1.90
D	216	1.13	0.73	0.91	0.94	0.73	0.91	1.62
E	417	0.86	1.04	0.81	0.74	1.03	0.76	1.58

Table 7.4: Static accuracy of coils *C*, *D* and *E* with ferrite cores.

For comparison, the NDI coil used in subsequent trajectory tracking experiments was also tested for static accuracy and the results are included in Figure 7.10 and summarised in Table 7.5.

Coil	Δx_{RMS} [mm]	Δy_{RMS} [mm]	Δz_{RMS} [mm]	σ_x	σ_y	σ_z	$Total_{RMS}$ [mm]
NDI	1.19	1.12	0.73	0.98	1.11	0.73	1.79

Table 7.5: Static accuracy test results for the NDI coil.

The effect of the ferrite core is more clearly demonstrated in the results of Figure 7.11 which showns the Fast Fourier Transform (FFT) of the sensor voltage at a fixed position $\{x,y,z\} = \{0,0,85\}$ mm from the FG where each voltage peak corresponds to the induced voltage due to one of the 8 transmitting coils of the FG shown in Figure 7.5b. The plot shows that the ferrite core increases the sensor voltage by approximately 10 dB for the four transmitting coils located closest to the origin of the FG.

7.3.2 Instrument Trajectory Tracking

In the absence of a gold standard for instrument position tracking, the error during instrument trajectory tracking is calculated relative to the position measurement of the NDI sensor (part no. 610099, *Northern Digital Inc., Waterloo, Canada*) used in previous investigations [92, 100]. In the case of the bronchoscope, the NDI sensor is concentrically located inside the scope's working channel as shown in Figure 7.7b. In the case of the laparoscopic graspers, the NDI sensor is located between the instrument and the inner diameter of the coil former concentric to the sensor coil's diameter as shown in Figure 7.7b. Due to the coil and NDI sensors not being located in the same position in each instrument, a constant displacement r will exist between the two reported

sensor positions. This offset remains physically constant as both sensors are rigidly fastened to the instrument, but tracking system imperfections and interference due to the metal content of the instruments will result in variations occurring in the reported offset measurement. The instrument moves through the spiral trajectories shown in Figure 7.12. Δr_{RMS} is calculated as the root-mean-square position difference between the two sensors over the N acquired points. The RMS offset in each principle axis (*i.e.,* Δx_{RMS}, Δy_{RMS} and Δz_{RMS}) was calculated using (7.12) and total RMS offset calculated using (7.13) where x^i_{coil} and x^i_{NDI} are i^{th} corresponding reported x coordinates of the coil and NDI sensor resolved at the same instant in time and N_{cloud} is the total number of acquired points.

$$\begin{aligned}
\Delta x_{RMS} &= \sqrt{\frac{1}{N}\sum_{i=1}^{N}\left(x^i_{Coil} - x^i_{NDI}\right)^2} \\
\Delta y_{RMS} &= \sqrt{\frac{1}{N}\sum_{i=1}^{N}\left(y^i_{Coil} - y^i_{NDI}\right)^2} \\
\Delta z_{RMS} &= \sqrt{\frac{1}{N}\sum_{i=1}^{N}\left(z^i_{Coil} - z^i_{NDI}\right)^2}
\end{aligned} \tag{7.12}$$

$$\Delta r_{RMS} = \sqrt{\Delta x^2_{RMS} + \Delta y^2_{RMS} + \Delta z^2_{RMS}} \tag{7.13}$$

The standard deviation σ_r was calculated using (7.14).

$$\sigma_r = \sqrt{\frac{1}{N}\sum_{i=1}^{N}\left(r_i - \bar{r}\right)^2} \tag{7.14}$$

where r_i is the i^{th} absolute offset between the wound coil and the NDI sensor and $\bar{r}$ is the sample mean of all absolute offsets over N_{cloud} position measurements.

7.4 Discussion

7.4.1 Coil Design Theory and Practice

The coil geometries in this work are limited to geometries which were practical for hand-winding without automation. Significantly smaller coils capable of 5-DoF and 6-DoF sensing could be achieved with automated coil winding. However, the resultant coil geometries provide excellent inductance properties over the frequency range of the Anser EMT system, as indicated by Fig. 7.3. The resultant voltage gain was approximately tripled (+10 dB) using the ferrite core as shown in the voltage response in Figure 7.11. Referring to (7.3), this corresponds to an apparent magnetic permeability $\mu_a \approx 3$. This experimental result may be compared with the expected value based on an estimated demagnetising factor, $k_d \approx 0.1$ using the core's dimensions (12 mm $\times$ 6 mm) and (7.7), leading to an apparent magnetic permeability, $\mu_a \approx 10$ using (7.5). It should be noted that recent work [184] indicates that for $l_c/d_c = 2$, Parker's equation (given by (7.7)) may significantly underestimate k_d and a value of 0.2 is correct. This would effectively decrease the apparent magnetic permeability to $\mu_a \approx 5$. The remaining difference between the experimental and theoretical values for μ_a might be explained by the mechanical machining of the ferrite core to decrease its length to fit inside the former which likely also increased demagnetisation within the core volume. The core's large manufacturing tolerance ($\pm 20\%$) and failure to degauss the core during use in order to avoid any potential for inadvertent magnetic saturation are other potential sources for the error. However, the result highlights a simple design methodology which can be used to predict the approximate increase in sensed voltage which can be achieved with a ferrite core. Clearly, as the dimensional ratio l_c/d_c increases, the apparent magnetic permeability of the core will also increase resulting in larger sensor voltages.

7.4.2 Static Accuracy Testing

Static accuracy measurements were completed for each sensor and, in the case of coils C, D, and E, these results were compared with and without the addition of the ferrite

core.

Table 7.2 details the effect of increasing coil area, A_c, on total tracking error. As predicted by (7.9), increasing coil area, results in significant improvement in the total tracking accuracy. This is because, as the area of the coil increases, the induced voltage is due to an increased flux density crossing the coil's cross-section. Clearly, care needs to be taken in the numerical calculation of the expected **B** field across A_c to account for spatial variations which can generally be disregarded with small point-based sensors such as the NDI probe included in Table 7.5.

The results of Tables 7.3 shows the effect of turn count, N on tracking accuracy. Clearly, as N increases, the total tracking error decreases. This is to be expected since the associated induced voltage, v_s given by (7.9), increases linearly with N. As v_s increases, the signal-to-noise ratio increases correspondingly with resultant improvement in tracking accuracy. It is also noted that calculation of the total tracking error (as given by (7.11)) is required to avoid anomolies in the single-axis errors (e.g., Δx_{RMS}, Δy_{RMS} etc.) which is due to the significant variance across each axis, as indicated by the results for σ_x, σ_y, and σ_z.

The addition of a magnetic core to the coil improved tracking accuracy in the case of all 3 coils as might be expected. Table 7.4 shows a reduction in the total RMS error of $\{0.58, 0.36, 0.12\}$ mm or $\{23.4, 18.2, 7.1\}\%$ for coils C, D and E respectively in the presence of the ferrite core.

One general comment relates to the static position accuracy of small electromagnetic tracking sensors which is intrinsically limited by the radial dimension of the coil geometry. So, for example, the RMS error of the 0.5 mm NDI coil used in this work (reported here as 1.85 mm but previously reported as 0.8 mm [149]), is inherently limited to the diameter of the sensor coil due to the point-based approximation used in the magnetic field model (see (7.3)). However, larger diameter coils such as those used in this work, which require spatial integration of the magnetic field across the coil's cross-section (see (7.9)) do not have this limitation and can resolve positions with errors significantly smaller than their diameter, where the resolved position corresponds to the coil's geometric centre. For this reason, the total RMS errors in all cases investigated in this work are substantially smaller than the coil diameter.

7.4.3 Instrument Trajectory Tracking

Trajectory tracking of two separate instruments was demonstrated without a gold standard reference such as optical tracking. In the absence of such a reference, the results of Figure 7.12 should be treated with some care as error sources other than tracking errors may account for the discrepancy. These sources include the inevitable shielding and Eddy current effects in the outer sensor (and the bronchoscope shaft in the case of the bronchoscope) on the inner NDI sensor which may cause distortion of the detected magnetic field for the inner sensor. A second source of error is the off-centre positioning of the inner NDI sensor relative to the outer wound coil sensor. Notwithstanding these caveats, the overall trajectory mapping between the two sensors is reasonable with reported difference errors of 7 ± 1mm in the case of the bronchoscope and 7 ± 2mm in the case of the laparoscopic graspers. It will be noted that in many clinical scenarios (e.g., colonoscopy and endoscopy), a tracking resolution of 5-10mm may be sufficiently accurate to resolve position within the patient anatomy. It is supposed that in the presence of a gold-standard for tracked instrument trajectory, the reported error would be significantly closer to the static position errors of 1.59 mm and 1.70 mm reported for coils E and B respectively with an air core.

The principle advantage of the current design approach for instrument tracking is the improved form factor of the sensors which makes it easy to integrate a wound-coil around the outer diameter of the existing instrument shaft and, in the case of the bronchoscope, maintain the instrument channel of the scope free for clinical investigations. Future work might look to integrate such a sensor design within the instrument shaft, thus eliminating the requirement to fix the sensor ends to the outside of the instrument. It is also conceivable to include a high μ_r material within the instrument core in order to increase the sensed voltage.

7.5 Summary

This work represents the first investigation of bespoke sensor designs for medical applications of electromagnetic tracking with reported static RMS errors of 1.58 to 2.48 mm. As expected, errors are decreased by the use of larger diameter coils, addi-

tional winding turns and the presence of a ferrite core. The devices used to validate the prototype inductive sensors used in this work were limited to tracking of large laparoscopic and endoscopic instruments. However, the principles and experimental results indicate the approach of this chapter can easily be used to produce highly-integrated bespoke sensors using automated coil winding for miniature instrument tracking with reasonable prediction of sensor voltage gain based on simple theoretical calculations.

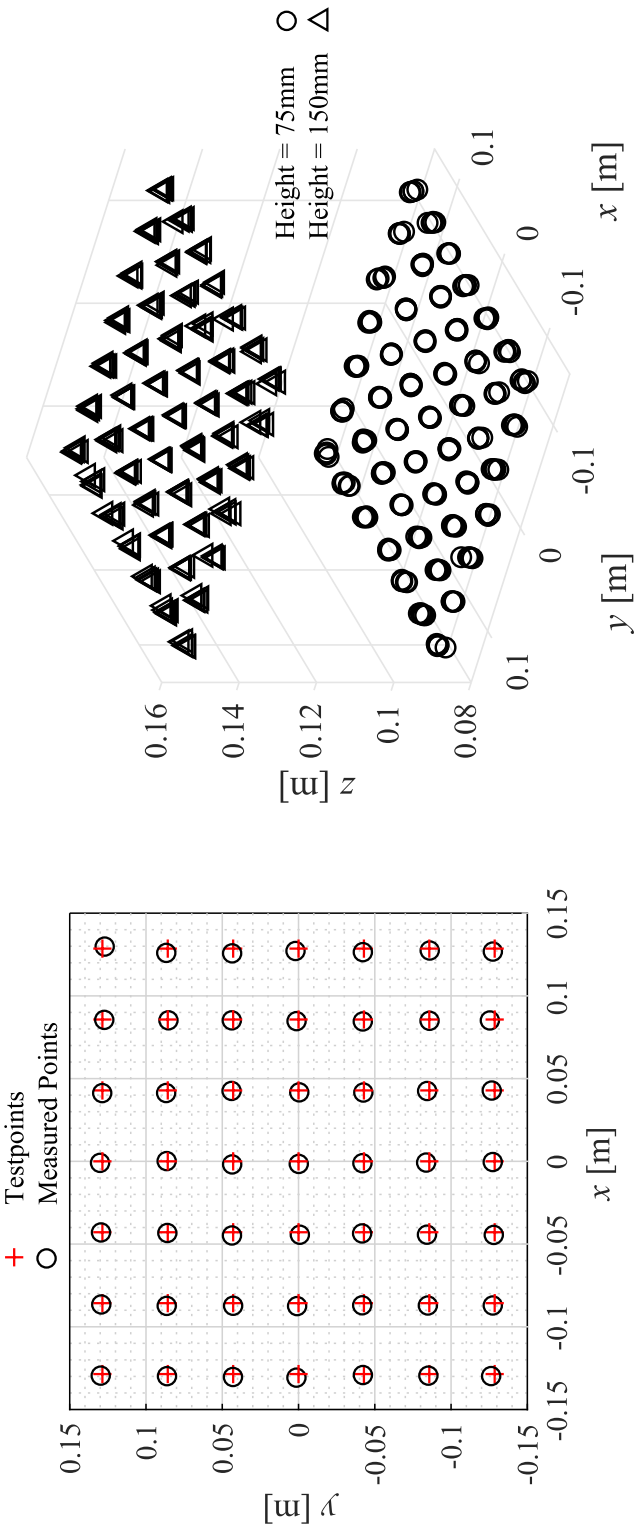


Figure 7.6: **(a)** Static accuracy position plot showing the test-point position and reported tracking system measurements for a height $h = 85.6$mm. **(b)** Position plot showing reported position measurements $h = 85.6$mm and 152mm.

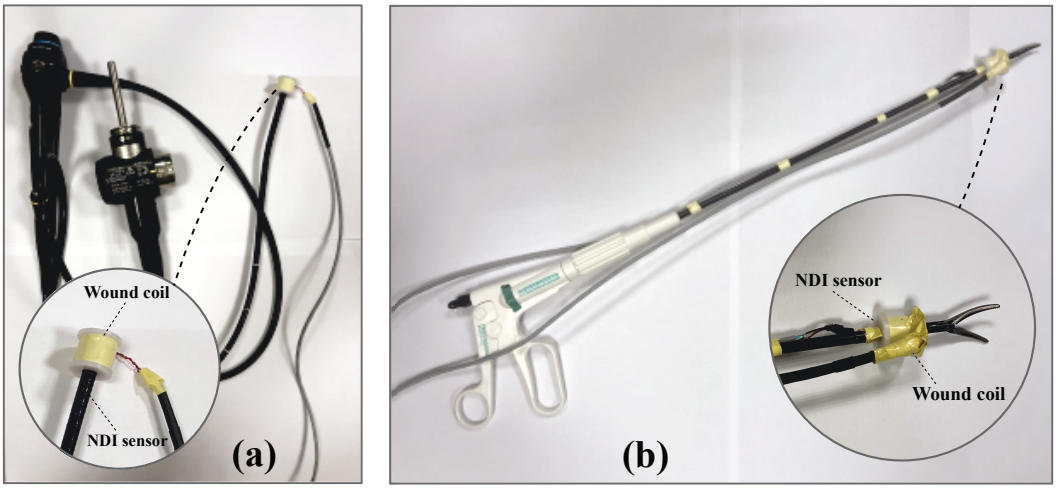


Figure 7.7: **(a)** Olympus BF-XT160 therapeutic bronchoscope using both the commercial NDI 5-DoF sensor and *Coil B* described in this study. The NDI sensor is inserted through the working channel and advanced to the tip of the bronchoscope **(b)** Tracking of the laparoscopic graspers using both the commercial NDI 5-DoF sensor and *Coil B* described in this study. The NDI sensor is fixed to the tip of the graspers using insulation tape.

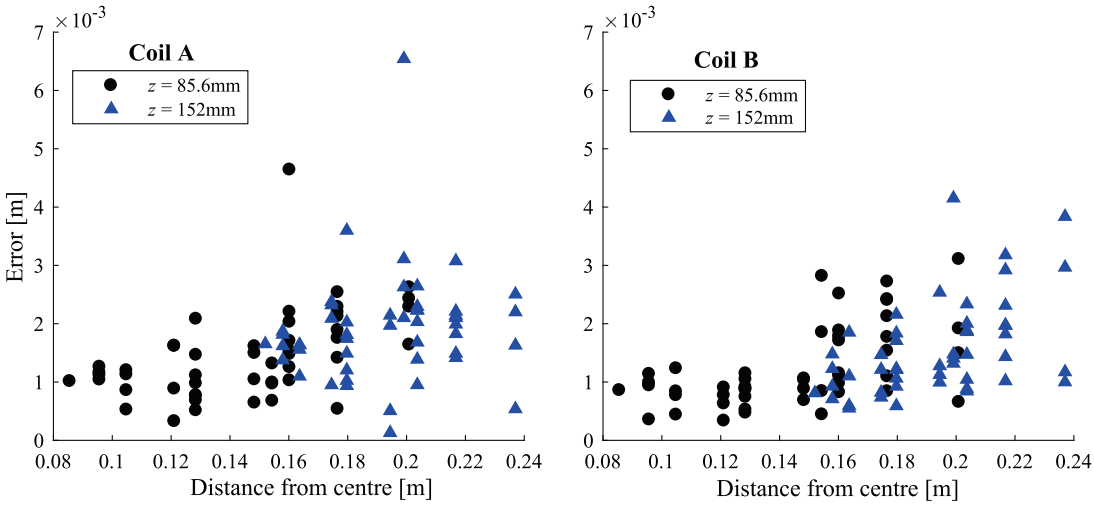


Figure 7.8: Error plots for coils *A* and *B*.

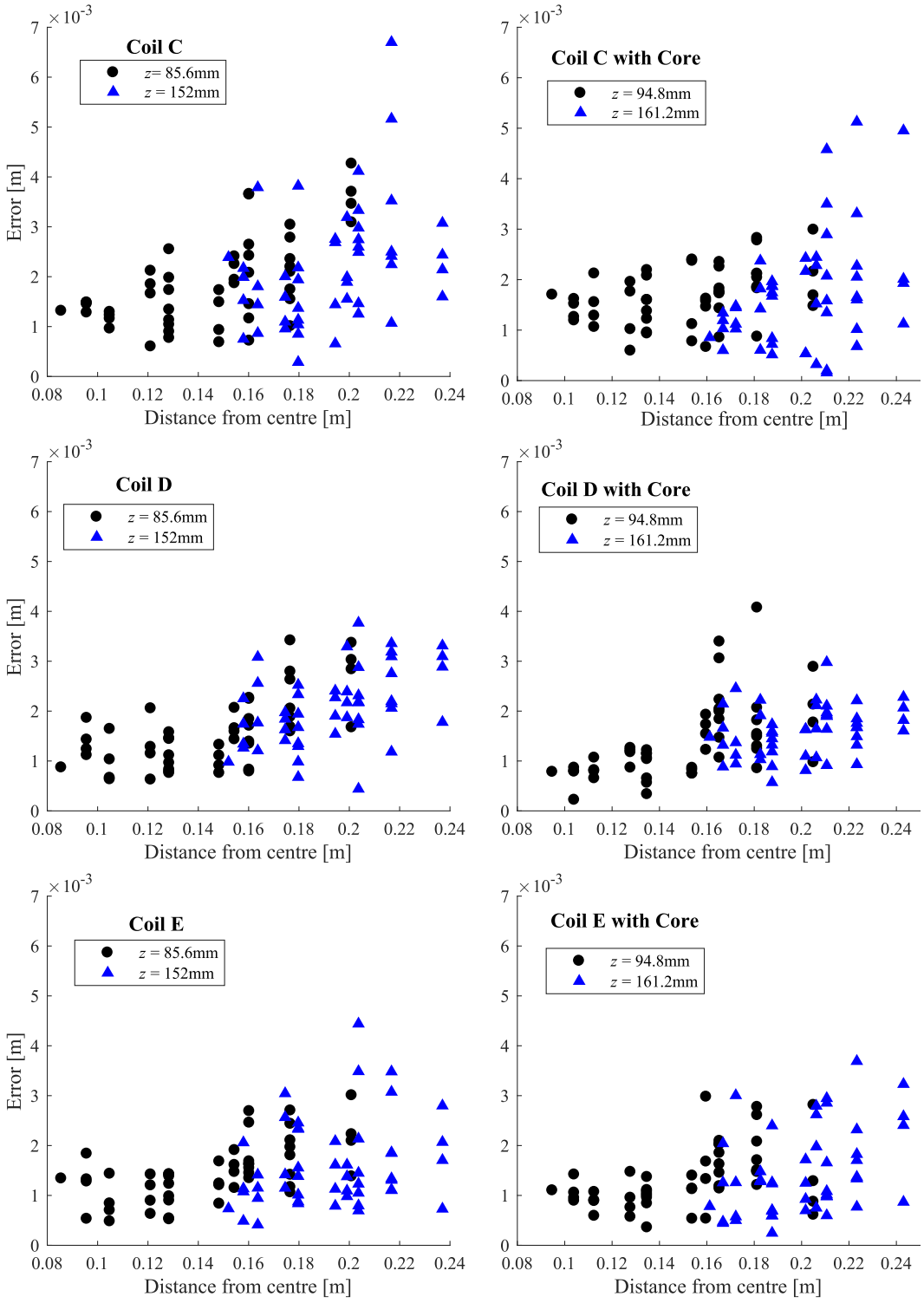


Figure 7.9: Error plots for coils *C*, *D* and *E* with and without ferrite cores.

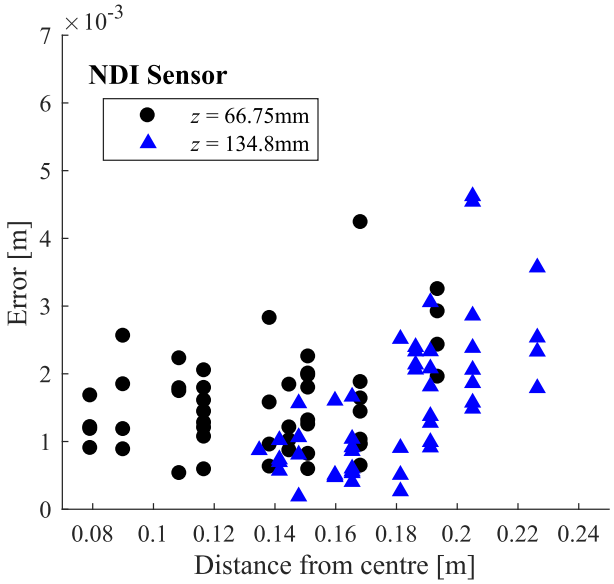


Figure 7.10: Error plot for the NDI coil.

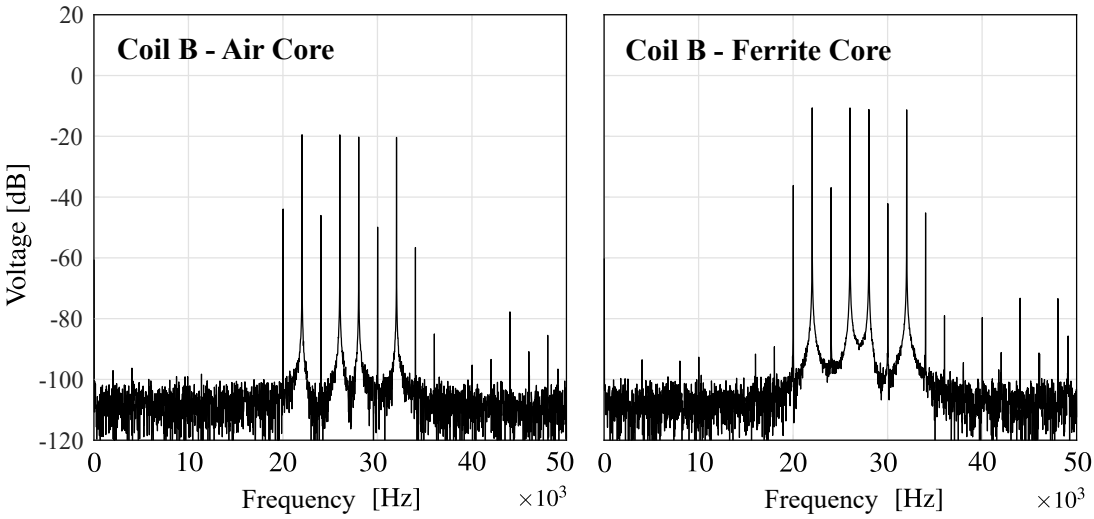


Figure 7.11: Fast Fourier Transform of the sensed voltage in coil *B* with air and ferrite cores. Voltage units are in decibels (dB) with respect to 1 Volt.

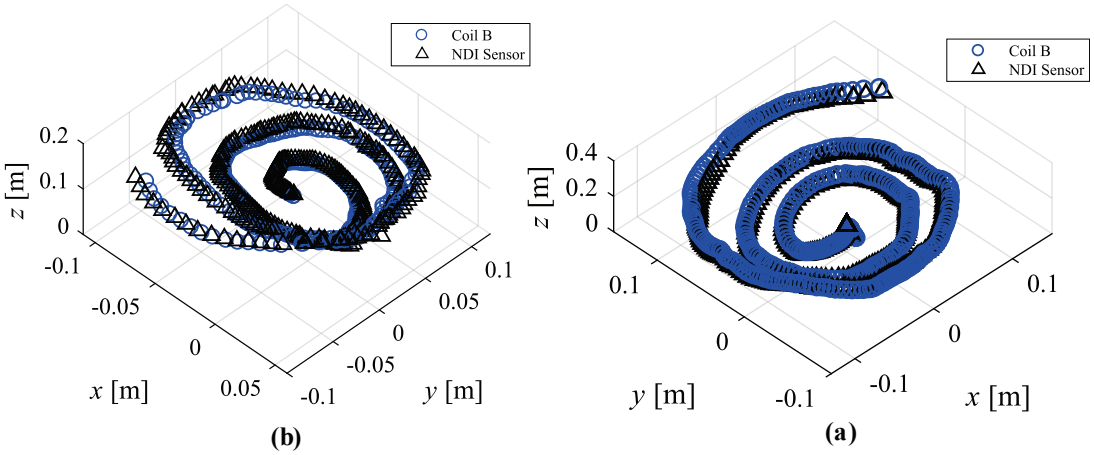


Figure 7.12: **(a)** Trajectory plot of sensor tracking using *Coil B* and NDI sensors with the Olympus bronchoscope ($r_{offset_{RMS}}$ =7 mm, σ_r =1 mm) **(b)** Trajectory plot of sensor tracking using *Coil B* and the NDI sensor with the Medtronic graspers (Δr_{RMS} =7 mm, σ_r =2 mm).

Chapter 8

Pre-clinical Evaluation with Anser EMT

This chapter discusses how the Anser EMT system was integrated as part of an image-guided solution for bronchoscopy, and tested in a live pre-clinical evaluation. The design and development of a novel electromagnetically tracked catheter is then discussed as well as the procedure used for testing the accurate targeting of simulated cancer tumours in the outer airways.

8.1 Open Navigation System Design

To advance the field of electromagnetic navigation bronchoscopy (ENB), open-source approaches to both navigated bronchoscopy [64] and electromagnetic tracking [174] were combined. The rationale is that by enabling open-source access to the underlying technology and visualisation tools behind ENB, current technical bottlenecks and shortcomings described in chapter 2 can be collaboratively tackled by the research community, eventually resulting in more reliable, low-cost methods of diagnosing lung cancer. This chapter describes the design, development and pre-clinical testing of an

This chapter is based on H. A. Jaeger et al. "Peripheral tumour targeting using open-source virtual bronchoscopy with electromagnetic tracking", *Minimally Invasive Therapy & Allied Technologies*, 2018 (*in press*)

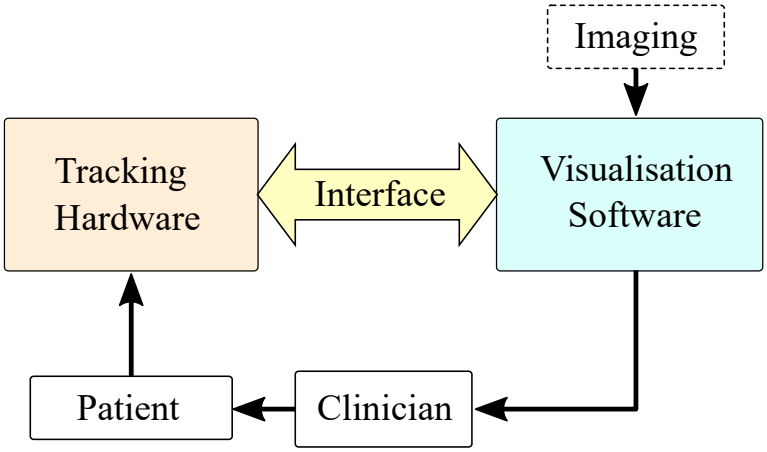


Figure 8.1: Generalised block diagram of a surgical navigation system. As the clinician navigates in the patient these actions are monitored using the tracking hardware. The tracking data is transferred to a visualisation software package and combined with either prior or real-time patient imaging for viewing by the clinician. Compatibility with the PLUS system [95] is discussed in chapter 9.

open-source navigated bronchoscopy visualisation tool.

Successful ENB requires the integration of tracking hardware and visualisation software in order to function. The Anser system described in chapters 3 and 4 provides the real-time instrument position and orientation (pose) information. The visualisation software utilises this information to guide the clinician using the patient CT scan as a reference. A block diagram of a generalised navigation system is shown in Fig. 8.1.

8.1.1 Tracking Hardware

The tracking hardware provides the position and orientation reference for the instruments being used in a medical procedure. Electromagnetic tracking (EMT) tracks the position of a magnetic sensor by providing the Cartesian coordinates and rotation angles (8.1) of a tracking sensor with respect to the magnetic field generator. Alternatively the angles may be represented as a rotation matrix $\mathbf{R}$ or quaternion $\boldsymbol{q}$. A thorough discussion of the Anser EMT system design is discussed in chapters 3 and 4.

$$\text{Position} = [x, y, z], \quad \text{Orientation} = [\theta, \varphi] \tag{8.1}$$

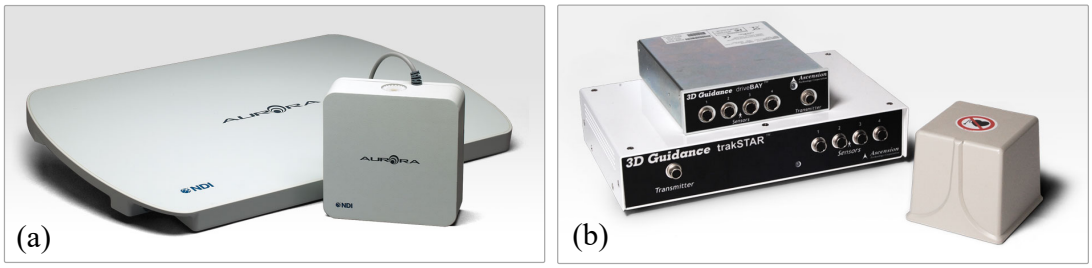


Figure 8.2: Commercial proprietary OEM electromagnetic tracking systems approved for clinical use. (a) The *Aurora* system and (b) the *Trakstar* system.

Commercially available tracking systems include the Northern Digital *Aurora* and Ascension Technology *Trakstar* systems shown in Fig. 8.2. While these companies do offer regulatory approved tracking systems as original equipment manufacturers (OEMs), the proprietary nature of their design limits their applicability in research, as fundamental system parameters (e.g. transmission frequencies, analog-to-digital converter sampling rate) cannot be adjusted. The Anser EMT system was created as an open-source alternative to begin to overcome some of these limitations [92, 100] and was used in the development the open-source bronchoscopy tools in this chapter.

8.1.2 Visualisation Software

Visualisation of the instrument position and orientation during electromagnetic navigation bronchoscopy is necessary as the use of cameras is not be feasible. The software's main function is to combine the position and orientation data of the tracking hardware with patient imaging data to create a computer-rendered representation for interpretation by the clinician. Many open-source tools exist to accomplish this task. CustusX, MITK and 3D Slicer [64, 132, 151] are the three major open-source medical imaging packages currently under development. The main difference between these software packages are in terms of user interface and software plug-in architecture, but underneath they all rely on similar software libraries, including:

- The Insight Segmentation & Registration Toolkit (ITK) [185], used for manipulating and processing image data, with an emphasis on medical imaging such as from MRI and CT scanners.

- The Visualization Toolkit (VTK) [186], used for rendering and visualising image data.
- Qt [187], used for the graphical user interface of all programs and plug-ins

CustusX is an image-guided diagnostics and therapy research platform dedicated to intraoperative navigation and imaging. The package has the flexibility to be utilised in a wide range of clinical settings including neurosurgery, laparoscopic surgery [188], vascular surgery [189] and bronchoscopy [71, 153]. The developers' current research focus on bronchoscopy [63, 65] made it an ideal candidate for developing a full airway navigation system, and it was chosen as the visualisation environment for this work as a result. An example visualisation palette from the virtual bronchoscopy toolkit is shown in Fig. 8.3.

8.1.3 Communication Interface

The OpenIGTLink standard [96] is an open-source network communication protocol created to standardise communication protocols between hardware and software of medical imaging navigation systems. The standard defines a number of standard *message* types allowing different computer systems and architectures may communicate and exchange data with one another reliably without data corruption. This library is utilised heavily in this work to establish connectivity between Anser EMT and CustusX. It should be noted that a newer software library, the Public software Library for Ultrasound (PLUS) [95] exists which combines OpenIGTLink and hardware specific libraries in an all-in-one solution for interfacing with ultrasound, camera-based and electromagnetic tracking hardware. Anser EMT is not yet usable with this toolkit, although it is envisaged it will become compatible in the future.

8.2 Tracked Instrument Design

Diagnosing lung cancer in the outer airways requires extending the reach of the bronchoscope using an extended working channel. Commercially available electromagnet-

CustusX is available at `https://www.custusx.org`

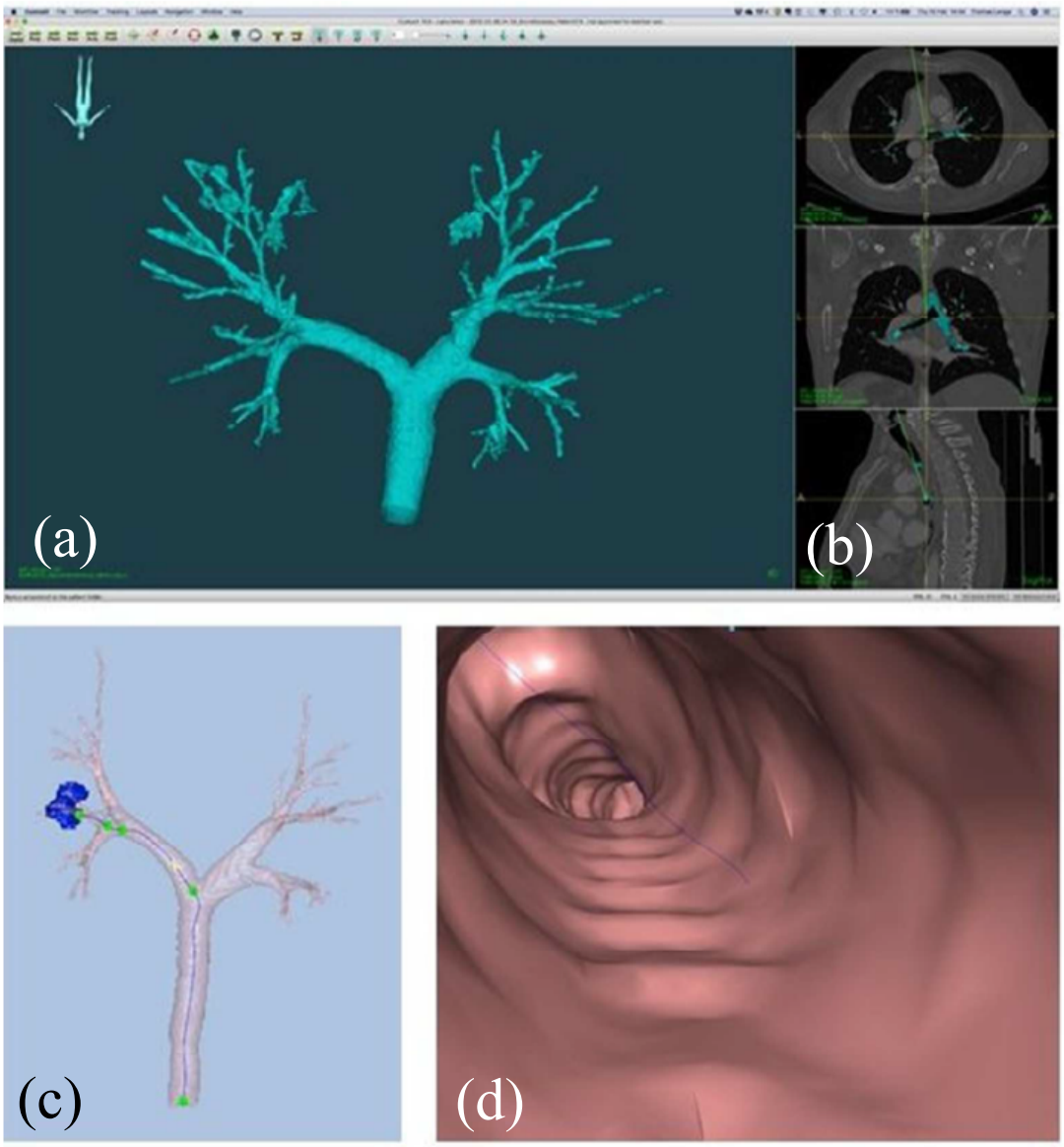


Figure 8.3: Screenshot of the interface palette of CustusX configured for bronchoscopy navigation. (a) 3D airway segmentation of the patient pre-operative CT scan. (b) Axial, coronal and sagital views of the pre-operative CT with position overlay. (c) 3D segmentation of the airway with tumour highlighted (blue) and route to target (green). (d) Virtual bronchoscopy view of the airway from the perspective of the targeting instrument.

ically tracked tools exist and are described in chapter 2 in Fig. 2.14 and 2.15 , but their proprietary sensor interface means that they are not readily compatible with the

Anser EMT system. A custom tracked catheter was designed for this work based on a previous design [174] and recent work by [190], in order to showcase the open nature of the system.

8.2.1 Bronchial Catheter Specification

An extended working channel behaves as an extension to the bronchoscope, allowing the clinician to navigate the outer airways and access the fine bronchiole structures at the lung periphery. Once the extended working has reached the region of interest it acts as a conduit for biopsy brushes, needles and forceps as shown in Fig. 8.4. The catheter design must adequately fulfil this role according to a number of constraints. The catheter must:

- Maintain compatibility with commercially available bronchoscopes. The catheter must pass smoothly through the working channel of the bronchoscope.
- Contain tracking sensors to enable electromagnetic navigation (EMN)
- Provide a working channel which is capable of passing commercially available biopsy instruments.

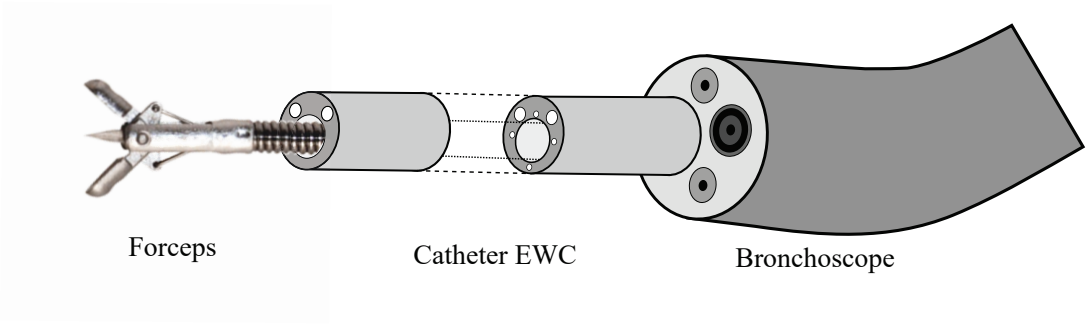


Figure 8.4: Diagram showing the extended working channel functionality of the catheter. The catheter extends beyond the tip of the bronchoscope providing a path for biopsy tools such as forceps, cytology brushes and needles.

The designed catheter was designed and manufactured in partnership with Teleflex OEM (*Annacotty, Co. Limerick, Ireland*). A diagram showing the catheter specification

is shown in Fig. 8.5. Photographs of the proximal and distal ends of the manufactured catheter are shown in Fig. 8.8. The 3.0mm outer diameter of the catheter provides compatibility with a range of therapeutic bronchoscopes including the Olympus BF-XT160, Pentax EB-1970TK and Fujifilm EB-530XT which all feature a 3.2mm working channel. A 1.5mm central lumen provides extended working channel capabilities to the catheter. The length of the catheter was specified at 105cm. This dimension was chosen to allowing biopsy instruments to protrude from the tip of the catheter, as it lies between the channel length of the bronchoscope (60cm) and the length of biospy instruments (110cm).

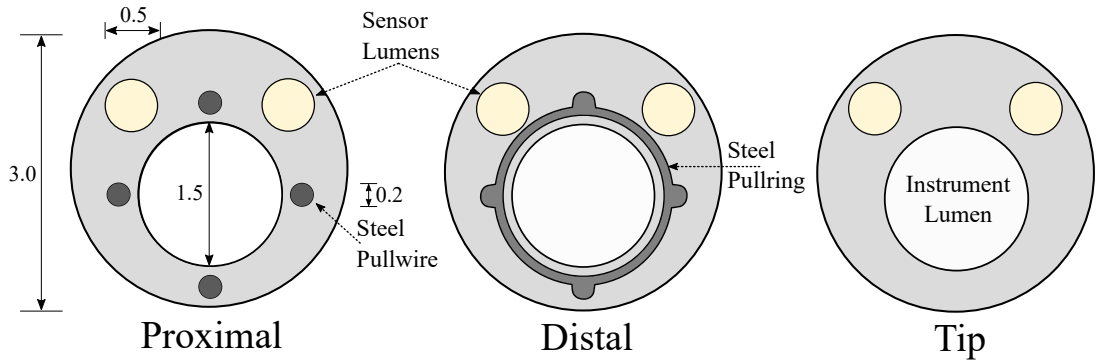


Figure 8.5: Diagram of the proximal, distal and tip sections of the catheter shaft. All dimensions are in millimeters (mm).

8.3 Experimental Procedure

In order to provide a quantitative *in vivo* measure of tracking accuracy, an innovative methodology of tumour targeting was used as follows;

1. Injection of the tumour model by percutaneous needle injection
2. Imaging with CT scan to determine position and volume of each tumour model after the animal is placed in the Anser field generator.
3. Registration and navigation to each target tumour model using electromagnetic navigation bronchoscopy
4. Deployment of a marking coil (embolization coil) at the site of the tumour model. Using the subsequent 3D x-ray, distance from the tumour model to the marking coil was measured.

8.3.1 Tumour Model Deployment

The radiopaque tumour model was obtained through a proprietary process (IRCAD France, Strasbourg) based on reported efforts [191] to form a homogeneous solution suitable for needle injection. In each case, a total model volume of 1.5ml was injected percutaneously at each 'tumour' site. In the two pre-clinical animal investigations, four lung sites were targeted in each of the two animals; the caudal (lower) left lobe, the cranial (upper) right lobe, the middle right lobe and the caudal (lower) right lobe. Tumour models were injected to an approximate depth of 2 cm via a 1.5mm double-lumen needle. Following injection of the tumour models in each of the two animals, a follow-up CT image was obtained with identical imaging parameters to that of the initial CT. This second CT confirmed the absence of pneumothorax and was also used to characterise tumour model position and volume. The results are summarised in Table 8.1 where each tumour model site (x, y) position is measured from the centre of the CT image while z position is measured from the top of the CT topogram. The tumour dimensions ($x \times y \times z$ in mm) upon deployment were measured from the same

CT image and these are also included in Table 8.1. The tumour marker labels A1-B4 correspond to the eight models placed where the *A* and *B* labels indicate distinct clinical end-users and animal subjects.

8.3.2 Segmentation, Registration and Mark-up

At the beginning of the procedure the animal was placed on the table, with the Anser field generator located beneath the animal, and centred on the animal's sternum. A second CT image was acquired after the tumour injection, and was used to perform a segmentation of the lung volume using previously reported methods [63] and the Virtual Bronchoscopy plugin to CustusX. Semi-automatic registration was achieved using the CloudCompare tool [192]: Initially the Bronchoscopy Registration plugin of CustusX was used to perform a balanced bronchoscopy airway survey, with an EM sensor in the scope channel, to acquire a coordinate point cloud in the animal's reference frame. A corresponding point cloud of the airways was generated from the airway image segmentation. The two resulting point clouds, corresponding to the image reference frame and patient reference frame, were registered by manual alignment followed by an automatic iterative-closest-point (ICP) registration [70]. A single rigid registration transformation matrix (see chapter 2) was calculated during this process. Time domain compensation for errors due to breathing motion was not performed in this study. Following registration, the four injected tumour models were marked with fiducials in CustusX to provide targets for virtual navigation as shown in Fig. 8.7.

8.3.3 Virtual navigation

Each clinical user sequentially navigated to each of the four virtual targets corresponding to the site of the percutaneous tumour model injection. Endobronchial navigation was performed using the novel 4-tendon catheter shown in Fig. 8.8) with two 5-DOF electromagnetic sensors embedded in the tip as indicated in Fig 8.5. The catheter had an outer diameter of 3 mm to fit the 3.2 mm working channel of a standard therapeutic endoscope (Pentax EB-1970TK) with a 1.5 mm working lumen for instrument and

marker delivery. Once the user achieved minimal separation from the virtual fiducial marker (see Figure 8.9), an embolization coil (Fig. 8.10(a)) was deployed to mark the target site. In each case, the closest Euclidean distance between the tool tip and the virtual fiducial marker was recorded at the point of marker coil deployment (see Table 8.1). The marker coil was a 0.035" MReye embolization coil (*Cook Medical, Limerick, Ireland*) with a coiled embolus diameter of 2-5 mm and an extended embolus length of 2-4 cm after deployment [193]. The marker was deployed by means of the working lumen within the tracked catheter shown in Fig. 8.8. The marker coil was advanced and deployed from the distal tip using closed endobronchial forceps. Deployment was verified by the inserted length of the forceps.

8.3.4 Measuring targeting accuracy

Targeting accuracy of marker coil deployment was measured using subsequent 3D x-ray (*Artis Zeego, Siemens Healthineers, Erlangen, Germany*) as indicated in Figure 8.10(b). While one goal of electromagnetic navigation is to reduce reliance on real-time imaging, the use of x-ray in this study was to facilitate accuracy measurements of the electromagnetic targeting. The closest, furthest and centre-to-centre distance from the tumour model to the centre of the deployed coil was measured (see Table 8.1). Indicative measurements for tumour model A3 are shown in Fig. 8.10(b) where *d4* corresponds to the centre-to-centre distance, *d5* is the closest distance and *d6* is the furthest distance between the marker coil and the tumour model. A similar procedure was completed for all eight tumour models in the two live animal studies. All animals were humanely euthanised using a potassium chloride injection under anaesthesia immediately following the procedure.

8.4 Results

8.4.1 Tumour model results

Following percutaneous injection of the four tumour models in each of the two reported live studies, no evidence of pneumothorax was seen in the subsequent CT images.

Tumour model position was successful at the four targets. A single tumour model was deployed in each middle left lobe to avoid excessive manipulation. The remaining three targets were successfully deployed in the cranial, middle and caudal right lobes in each of the two studies.

The tumour dimensions recorded from subsequent CT (see Table 8.1) are representative of the injected volume of 1.5 ml, albeit model A1 appears larger than expected due to syringe slippage during injection. Major axis lengths for the deployed tumour models ranged from 21.1 mm (labelled A1) to 15.5 mm (labelled A3). The models are representative of stage IA2-3 lung carcinoma non-small cell lung peripheral airway nodules as defined in the TNM classification guidelines [194]. The headings for Table 8.1 are detailed below.

Tumour label- Label applied to specific tumour throughout studies

Lobe location- Anatomic of tumour within lung

Tumour Position on CT- Coordinates of tumour location in CT volume

Tumour Size- Size of tumour using CT volume coordinate system

Closest Dist.- Closest distance between tumour and marker on DynaCT

Centre Dist.- Distance between centre of tumour and marker on DynaCT

Farthest Dist. Farthest distance between tumour and marker on DynaCT

Virtual Dist. Distance between tumour and marker as reported by the virtual bronchoscopy software

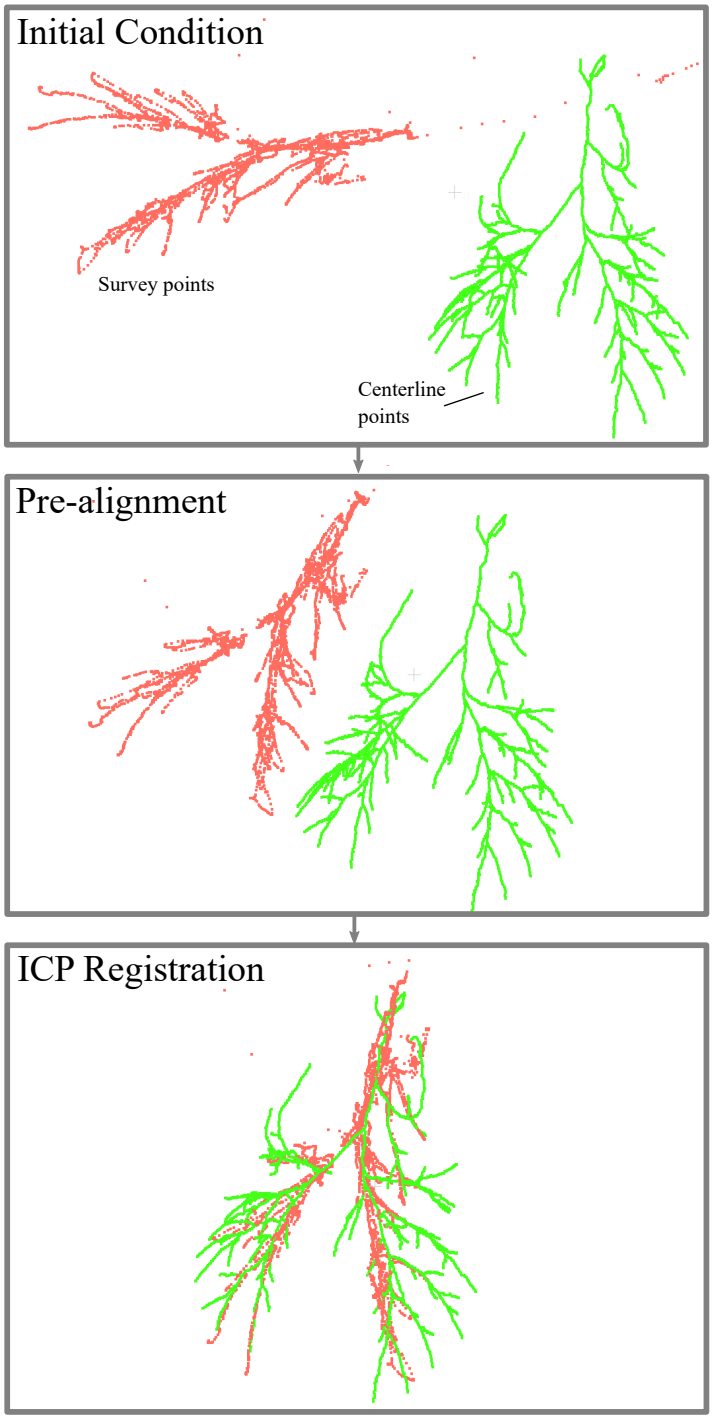


Figure 8.6: Screenshots of CloudCompare [192] during the registration process. The balanced survey of the lungs using the electromagnetic tracker provides a set point cloud of in the patient frame (red). This is the *source* point cloud. The airway centerline points (green) are obtained from the 3D airway model and and forms the *destination* cloud in the image frame. Manual alignment is performed by manipulating the *source* cloud to the same approximate rotation of the *destination*. The ICP algorithm [70] is invoked to perform the final registration.

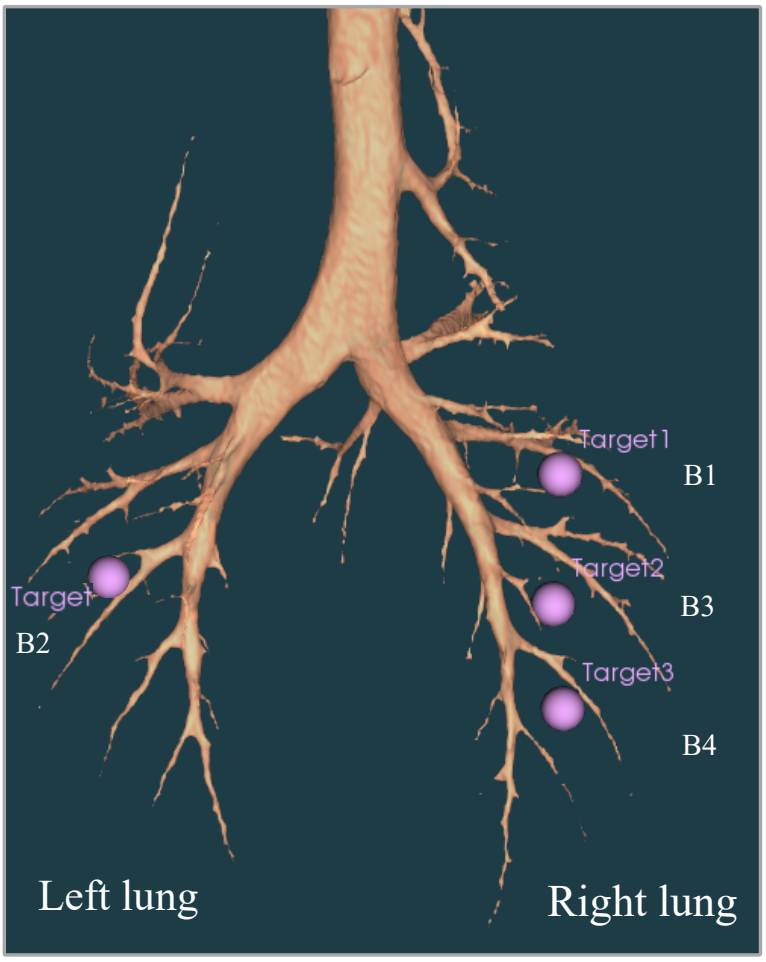


Figure 8.7: Screenshot of CustusX showing the marked up tumour model locations B1-B4. The exact locations are described in Table 8.1.

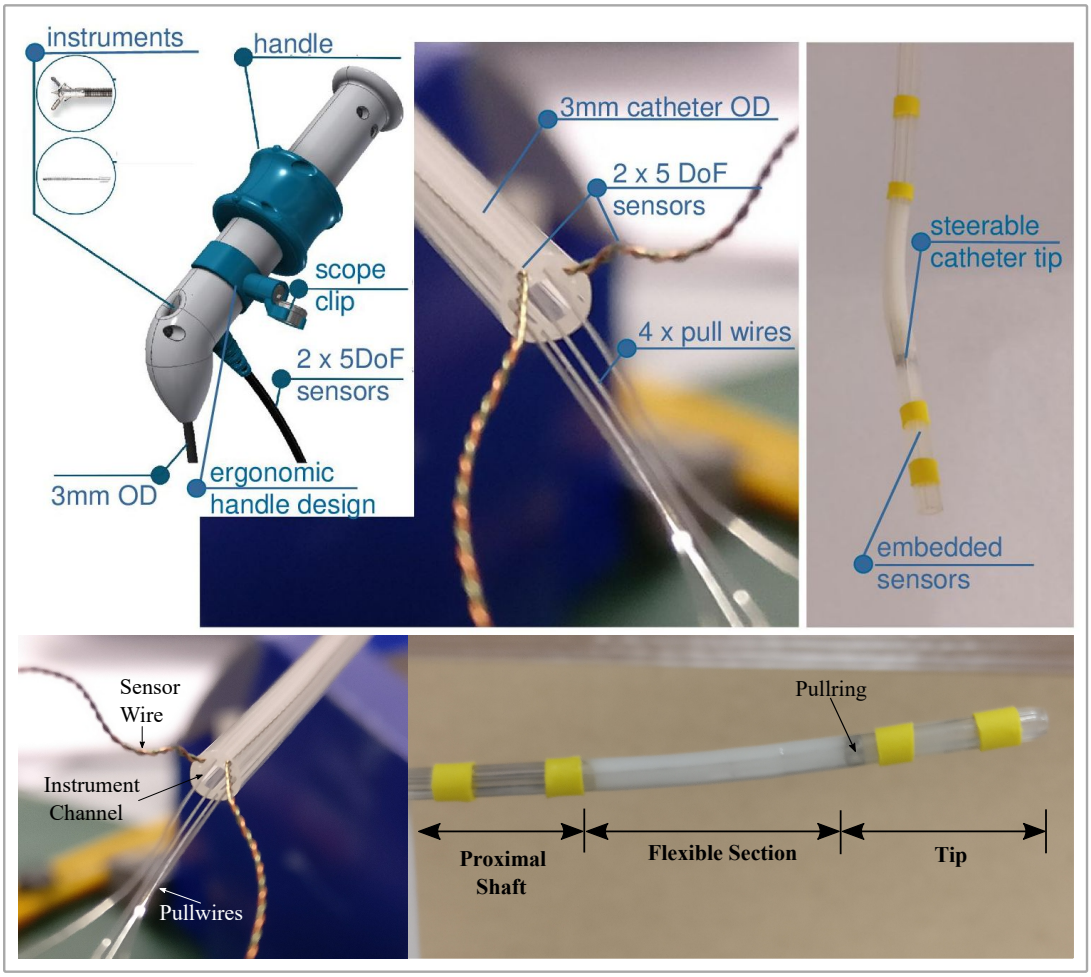


Figure 8.8: Custom four tendon catheter with attached handle used in bronchoscopy procedures. The handle design allows continuous deflection of the catheter while providing an instrument port for the insertion of biopsy instruments.

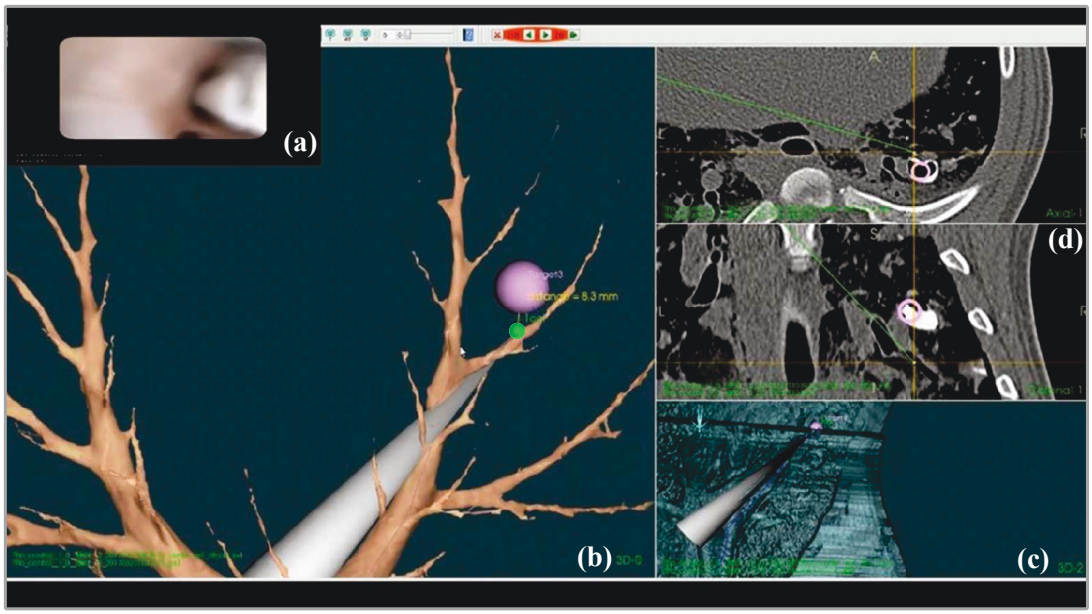


Figure 8.9: Screenshot of the CustusX screen during navigation with the airway. (a) Live bronchoscope camera feed. (b) 3D model of the airway showing the catheter tip location (green) and the tumour target (pink). (c) Alternative 3D view of the sensor position within the lung [63]. (d) CT scan slices indicating the location of the catheter tip using crosshairs.

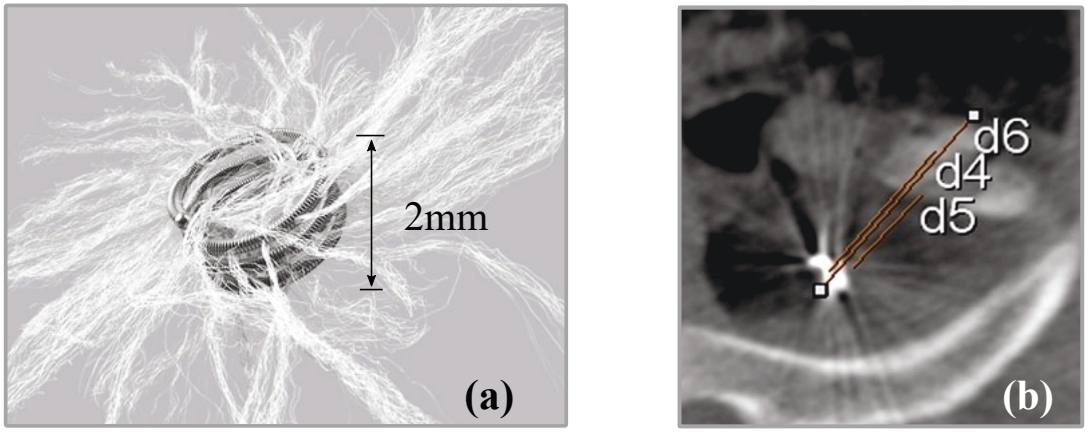


Figure 8.10: (a) MReye embolization coil (*Cook Medical, Limerick, Ireland*). In its deployed state the coil measures less than 1mm in diameter. The integrated fibres allow to coil to successfully lodge within the outer airway when it is deployed. (b) Distance calculations between an embolisation coil and the injected tumour model., used to calculate the overall accuracy of the electromagnetic navigation system.



Figure 8.11: Photograph of the clinical setup of the animal study performed in *IHU Strasbourg*. The electromagnetic field generator lies beneath the pig. The pulmonologist navigates the airway using the ENB catheter through the working channel of the bronchoscope. The overhead screen displays the CustusX navigation panel, indicating the live catheter tip location within the 3D airway model. The live bronchoscope camera feed and CT scan slices are also displayed.

8.4.2 Targeting accuracy results

Post-imaging segmentation and registration of the post-injection CT image with the Anser EMT platform was achieved in each study. All eight tumour models deployed in this study lay outside segmented airways. In each case, the user navigated without the assistance of the virtual pathway planner available in the CustusX platform. The tool tip roll-angle orientation was not enabled. Expert users noted that the use of 6-DOF sensing at the tool tip would not improve accuracy in targeting the tumour models in this study. Virtual distances from the tool-tip to virtual tumour fiducial between 3.6 mm (label B4) and 18.7 mm (label A3) were reported in Table 8.1. Given the small cohort, statistical analysis was not attempted. However, it was noted that the closest virtual distance to the tumour fiducial for both users was for targets in the caudal right lobe. The furthest distance to the tumour fiducials occurred in the caudal left (label B2) and middle right (label A3) lobes where the A and B labels indicate distinct clinical users. Therefore, centre-to-centre and furthest distance measures are also included in the results of Table 8.1.

Following deployment of the marking coils, the closest distance from deployed marker coil to the injected tumour model was found to be between 1.39 mm (model B4) and 12.04 mm (model B2). In one of eight instances (B2), the distance between the tumour model and the deployed marker exceeded 10 mm. Furthest distance measurements varied between 14.87 mm (model B1) and 30.96 mm (model A4). There was weak statistical correlation between the virtual distance to the tumour at marker deployment and the closest distance to the tumour marker from subsequent x-ray images ($r = 0.55$). However, the shortest virtual distance (model B4) did correspond to the minimum closest distance to the tumour model measured by x-ray. Furthermore, in all cases, the virtual distance to the tumour model measured at marker deployment was within the range of the closest and furthest distances to the tumour marker as measured with subsequent x-ray. Edited video footage of this study is available at `https://youtu.be/5S8pvGGAV8Q`.

Tumour Label	Lobe location	Tumour Position on CT [mm]	Tumour size [mm]	Closest dist. [mm]	Centre dist. [mm]	Furthest dist. [mm]	Virtual dist. [mm]
A1	Cranial right	$(-43.5, -5.0, -652)$	$21.1 \times 14.3 \times 10.9$	2.48	13.13	25.28	9.4
A2	Caudal left	$(64.5, -7.5, -694.1)$	$18 \times 11.8 \times 12.1$	6.95	16.23	23.55	12.8
A3	Middle right	$(-42.9, -10.8, -682.2)$	$15.5 \times 16.5 \times 19.3$	3.79	16.88	28.23	18.7
A4	Caudal right	$(-49.2, -17.6, -706)$	$16.2 \times 12.7 \times 15.9$	8.07	18.98	30.96	8.3
B1	Cranial right	$(-68.8, -10, -583.5)$	$16.7 \times 10.7 \times 12.3$	1.97	7.19	14.87	9.0
B2	Caudal left	$(49.5, -3.0, -578.6)$	$18.3 \times 10.1 \times 0.98$	12.04	19.76	28.51	18.4
B3	Middle right	$(-53.2, -23.1, -533.8)$	$16.7 \times 15.8 \times 13.7$	5.54	17.1	29.12	8.7
B4	Caudal right	$(-72.1, -27.9, -594.7)$	$15.6 \times 9.6 \times 15.3$	1.39	11.15	22.88	3.6

Table 8.1: Names, locations, sizes and distances from the marking embolisation coil to the targeted tumour are shown for each of the eight deployed tumour models. All dimensions are in millimeters [mm].

Chapter 9

Summary and Future Work

This thesis presents the design and development of an open-source electromagnetic tracking system for clinical applications. The theory of operation, software and hardware design of an exemplary electromagnetic tracking system is presented. The effectiveness of the system for developing novel sensing applications is demonstrated through the creation of a novel metal distorter detection technique and a scalable field generator scaling design. The system is also demonstrated to facilitate experiments for the design of bespoke magnetic sensors for medical instruments. Finally the system is applied to virtual bronchoscopy navigation in the pre-clinical setting to demonstrate the first fully open-source electromagnetic navigation bronchoscopy suite. The novel contributions of the thesis are summarised here.

1. *Open-source electromagnetic navigation.* The design and development of a fully open-source electromagnetic navigation system, Anser EMT, is presented in Chapter 3 and 4 [91, 100]. A novel hardware design was refined with improvements in power supply and current driver design. The system designs are open and can be manufactured at scale using standard circuit fabrication techniques. An accompanying open software platform was developed for the system. The structure of the system allows for future modification and refinement by researchers in the field. The performance of the proposed system was evaluated and compared using a standardised testing protocol. The system's accuracy and precision metrics compare favourably with commercial electromagnetic tracking

systems.

2. *Magnetic distortion detection.* A novel magnetic field generator design was designed, developed and demonstrated to effectively detect and distinguish metal distorters in the vicinity of the electromagnetic tracking system tracking volume [154]. Chapter 5 provides a detailed analysis of the construction of the field generator the switching circuit design. Experimental data on the discriminative capabilities of the metal detection system is provided. Distorters comprising of ferrous material exhibit significantly different phase shift characteristics compared to non-ferrous materials. The approximate location of the distortion can be localised by measuring the net change in mutual inductance experienced by proximal transmitter coils. Such an approach using mutual inductance measurements has not been proposed for distortion identification in EMT.

3. *Scalable tracking volumes.* Chapter 6 details a novel method of creating scalable tracking volumes for electromagnetic tracking systems using low-cost printed circuit board field generators [195]. Experiments using angled and planar configurations of two field generators are demonstrated using fiducial registration error as a measure of accuracy. Improved system accuracy is demonstrated with when two field generators are angled with respect to one another. Tiled planar configurations are shown to experience significant error on the mutual boundary unless both field generators share a common edge. This work represents the first reported modular field generator design for electromagnetic tracking systems.

4. *Bespoke sensor design.* The proposed tracking system was used for the design and experimentation of customised magnetic induction coils for tracking medical instruments in chapter 7 [196]. The theory of induction coil design was detailed followed by the construction of a number of hand-wound coils. Experiments were performed to analyse the effects of turn count and cross sectional area on the positional accuracy of the sensors. The effect of a soft ferrite core was also demonstrated. Positional performance of the coils compares favourably with commercially available tracking sensors. The feasibility of integrating such sensors into medical instruments is demonstrated by tracking both a laparoscopic

graspers and bronchoscope using a commercial sensor as a reference. This work represents a first step towards developing customised magnetic sensors for minimally invasive surgical instruments.

5. *Electromagnetic navigation bronchoscopy suite.* The proposed tracking system was demonstrated in the pre-clinical setting for electromagnetic navigation bronchoscopy [197]. Successful tracking of a custom bronchial catheter demonstrated use of the tracking system in combination with the open-source visualisation and planning tool, CustusX. This represents the first reported electromagnetic navigation bronchoscopy study performed solely with open-source tooling and software visualisation.

9.1 Proposals for Future Work

This thesis provides many avenues for future work in the area of electromagnetic tracking and navigation. This section provides suggestions for future work on the topics discussed in this thesis.

9.1.1 A scalable and robust field generator topology

The work in Chapter 6 discusses how two or more field generators may be used in combination to form a larger aggregate tracking volume for magnetic sensors. Scaling of this idea for more than two generators requires careful consideration of many system parameters such as frequency selection and cost function optimisation. Forcing every transmitter coil of the field generators to transmit a unique frequency quickly utilises analogue signal bandwidth due to the large signal separation required for high position update rates. As-is, the complexity of the system cost function will also increase linearly with the number of transmitter coils in active use. A proposed method of addressing this scaling problem is the creation of an intelligent switching system, analogous to that of the *handover* process in a cellular phone network, where a sensor would be *handed over* from one field generator to another whilst crossing the boundary between two adjacent field generators. Signal bandwidth would be preserved while

maintaining a constant complexity system cost function. It may possible to achieve this handover process in a more granular manner, where individual transmitter coils become the focus of the handover process, rather than entire field generators sets.

9.1.2 Integration with toolkits

Commercially available tracking systems are currently interfaced using the Public Library for Ultrasound Imaging (PLUS) [95], which manages the interoperation of multiple tracking and imaging platforms in a single software package. Future work will see integration of the Anser EMT platform as part of this interface system.

9.1.3 Distortion detection and compensation

The effect of distorters on the mutual inductance of the field generator coils and tracking performance discussed in this thesis may provide a foundation for more advanced distortion compensation techniques. Building on the work of chapter 5, a first step would be integrating inductive sensing technology as an integral part of the open source tracking system design. This may facilitate the creation of a *smart field generator* that is capable of detecting the severity of distortion in the vicinity in real-time, allowing the user to quickly optimise placement of the field generator during the system setup phase. Intelligent selection of field generator frequencies based on the material of the distorter may also be possible, as lower frequency magnetic fields suffer less distortion with non-ferrous materials at these frequencies.

9.1.4 Improved sampling

The sampling scheme used by the proposed tracking system is limited by the use of the National Instruments data acquisition unit. By acquiring raw electrical samples in hardware and then performing DFT processing in software, the position solver is required to wait until a finite number of samples are acquired to constitute an *acquisition frame*. The number of samples in an acquisition frame and the sampling frequency of the DAQ then determine the minimum latency and position update rate of the system. Minimum latency may be significantly reduced if both sample acquisition and DFT processing

are performed in hardware. A *sliding window* scheme could be implemented removing the need for a finite size acquisition frame. While the minimum system latency is still determined by the window size in this case, the theoretical update rate of the system becomes equivalent to the sampling period of the analogue-to-digital converter being used. Implementation of such a sampling scheme can be performed on a digital signal processing microcontroller and field programmable gate arrays. Fully coherent sampling is then achievable, which would significantly enhance DFT performance.

9.1.5 Simplified calibration using machine learning

The advent of advanced machine learning techniques in recent years has led to a plethora of network models capable of analysing speech, text and image data to an extremely high accuracy, and in many cases better than traditional model based approaches. An investigation into whether machine learning can be applied to electromagnetic tracking should be conducted with particular focus on the calibration process of these systems. Current calibration techniques for the proposed electromagnetic tracking system rely on the acquisition of a fixed set of predefined position measurements at a fixed height above the field generator. The process is cumbersome and must be repeated for each new sensor in order to be used in the system. For example, each sensor in chapter 7 was individually calibrated before experimental data were acquired. An alternative calibration technique may take the form of a trained neural network whose training data consists of a set of labelled magnetic field strength values from the magnetic sensor. Labels in this case could be obtained from an optical tracking system, whose measurements are unaffected by metal distorters and thus can be treated as a ground truth source. The resulting machine learning model would represent a coupled magnetic model of both the magnetic field (due to the field generator) *and* the sensor model (flux intersecting the sensor) in a single network. A sufficiently trained network may allow for the calibration of any sensor without the requirement for a set of predefined points (i.e. a random set of magnetic field data from an un-calibrated sensor may yield sufficient information for the network to resolve the system calibration coefficients.)

9.1.6 Persistent calibration

Anser EMT currently requires calibration of each new sensor used with the system. Calibration is also necessary when the field generator transmitter current amplitude and frequency parameters are adjusted. If the current-sense voltage can be measured, as demonstrated in chapter 3, then it may be possible to create a persistent calibration model for each sensor, taking into account the transmitter coil currents' frequency and magnitude. Assuming linearity, a look-up table scheme may be constructed which encapsulates an individual sensor's frequency response over a certain frequency range. This response, when combined with real-time current sensing, may provide sensors with a persistent system calibration over a pre-defined operating bandwidth. The current drift issue discussed in chapter 4 will need to be addressed in this case.

9.1.7 Miniaturised sensor design

Wound induction coil sensors, such as those used with the Anser EMT system, reach a scaling limit beyond which they cannot be manufactured any smaller via traditional spool-based, tension-controlled machine winding techniques. For example, the smallest commercially available induction coil sensor measures 0.5 mm in diameter [17]. Advances in the semiconductor industry, particularly in the area of on-chip magnetics, may provide a solution to this problem. Recent advances in integrated magnetics technology [198, 199] may allow densely packed copper turns, in the order of microns, to be manufactured on a silicon die. The physical behaviour of such a sensor can be readily simulated to very high precision using state-of-the-art magnetic simulation tooling. The creating of sensors at such a scale could enable magnetic tracking in many more surgical instruments than there are available today. The first step in this process would be an in-depth Helmholtz coil characterisation of the hand-wound coils presented in chapter 7. This should provide an understanding of the minimum coil sensitivities required for accurate and consistent electromagnetic tracking. To this end, an improved mechanical strain relief could be developed to facilitate robust electrical connectivity for these sensor designs.

Appendix A

Extended Results

This chapter contains extended results of the experiments described in chapter 5. The inductance, phase and position error plots for all tested distorters in Table 5.4 are shown.

A.1 Inductance Error Plots

The inductance error plots for the sheet and aluminium section distorters were shown in Fig. 5.10 and 5.11. These plots are repeated here along with the remaining mutual inductance error plots for the distorters in Table 5.4. In almost all cases, the mean mutual inductance error calculated using (5.15) decreases with decreasing distance between the distorter and field generator. It can also be seen that the smaller distorters cause the highest percentage error in the transmitter coils which are in closest proximity to one another.

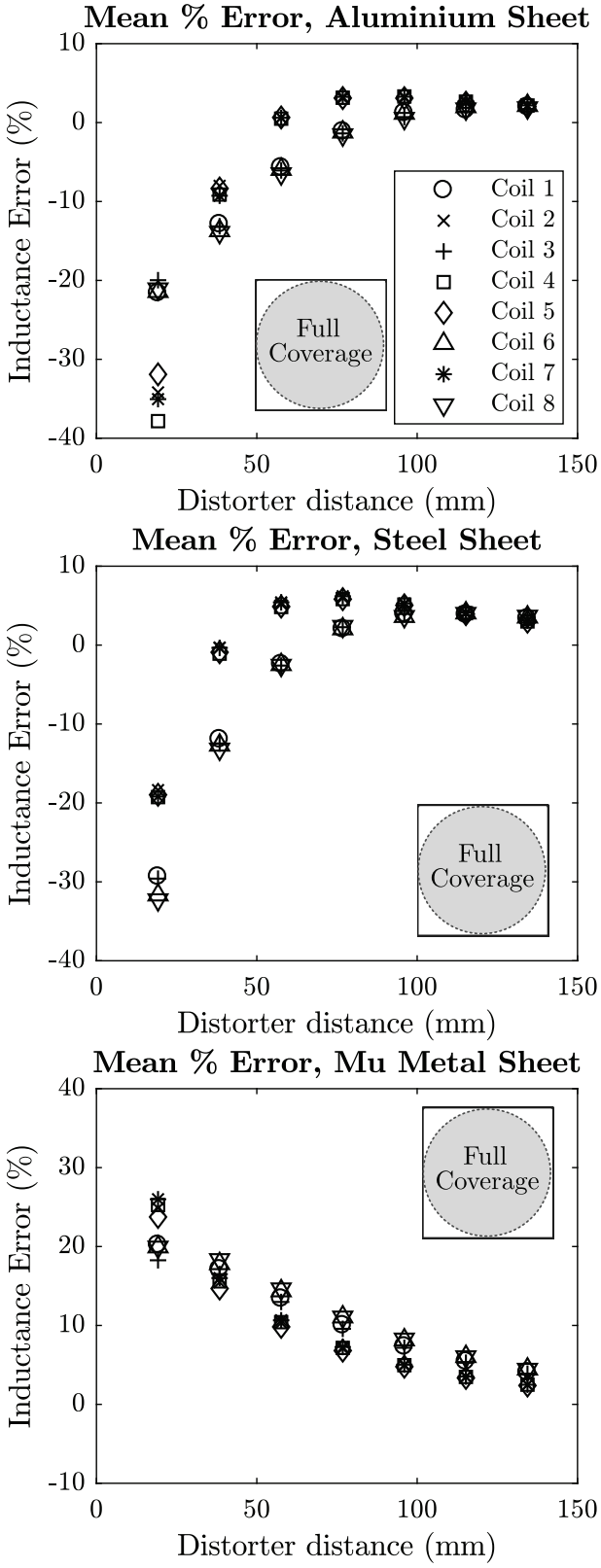


Figure A.1: Mutual inductance error plots for planar sheet distorters spanning the area of all transmitter coils. The mu-metal sheet contributes positively to the overall inductance of the field generator over all distances.

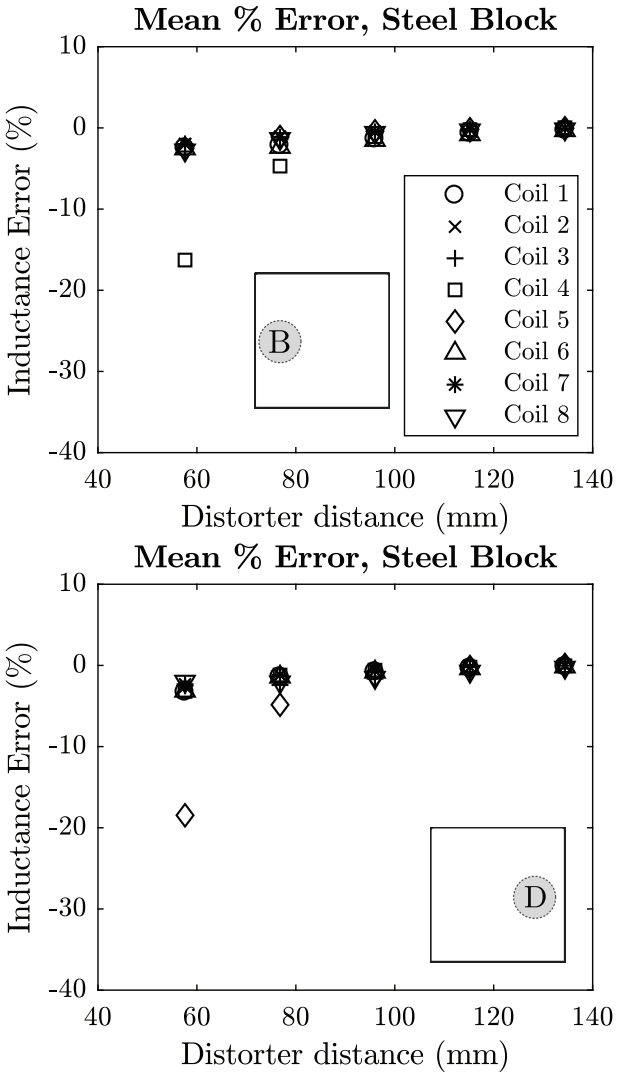


Figure A.2: Mutual inductance error plots for small steel block distorter in locations B and D, with the corresponding coils 4 (closest to position B) and 5 (closest to position D) respectively experiencing the largest mutual inductance error.

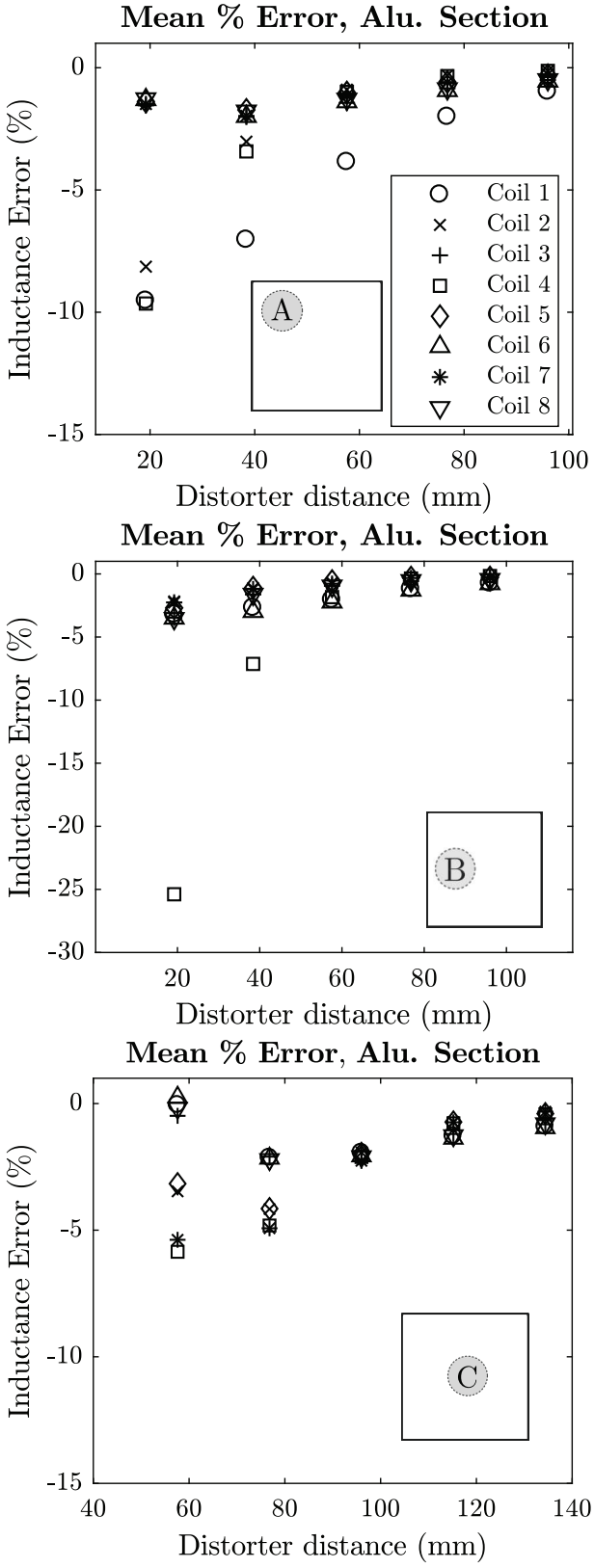


Figure A.3: Mutual inductance error for small aluminium section distorter in locations A, B and C. The distorter placed at locations A and B experience the largest errors in their nearest respective coils, 1 and 4. The centrally placed distorter at location C causes the central transmitter coils 2,4,5 and 7 to experience the largest mutual inductance errors.

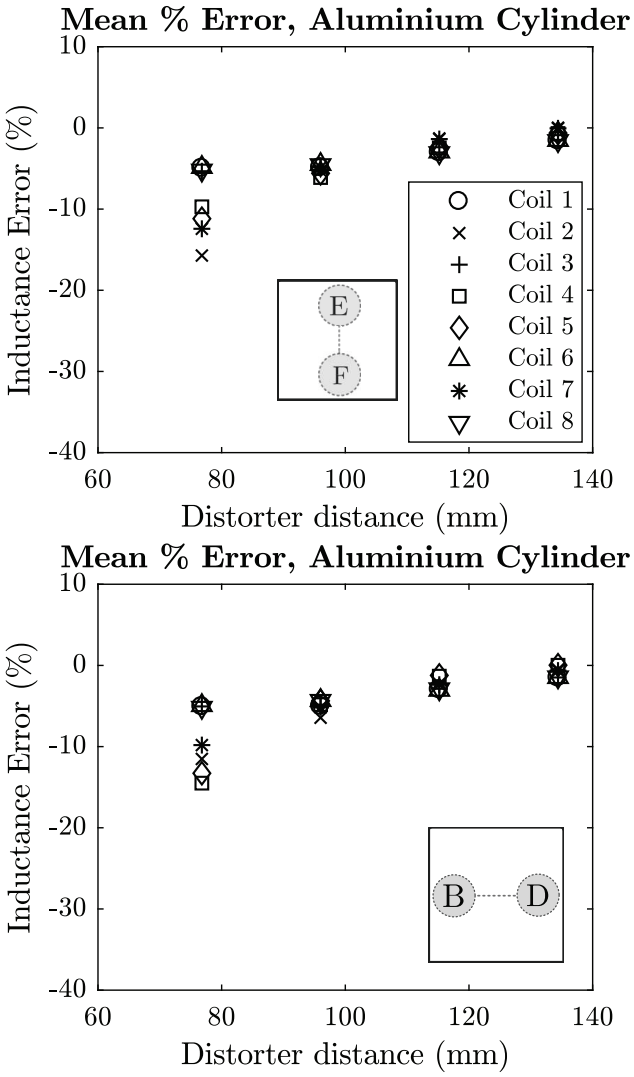


Figure A.4: Mutual inductance error plots for large aluminium cylinder in locations E to F and B to D. The cylinder spans the length of the field generator. The highest mutual inductance errors correspond to the coils to the distorter.

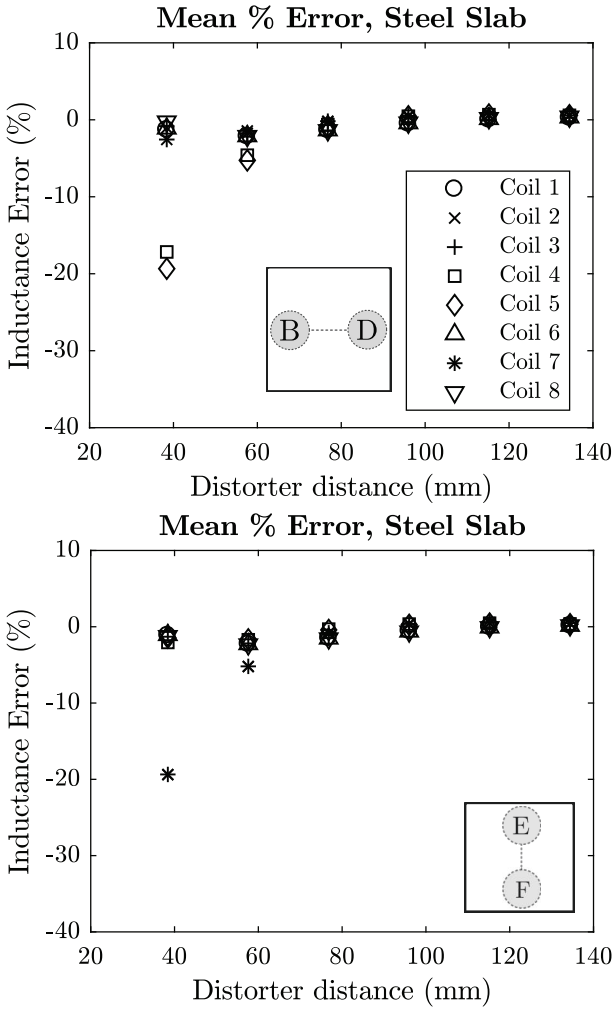


Figure A.5: Mutual inductance error plots for steel slab in locations B to D and E to F. The effect is similar to that of the aluminium cylinder, with the highest error experienced by the coils closest to the distorter.

A.2 Phase Angle Plots

The phase angle error plots for the sheet and aluminium section distorters were shown in Fig, 5.12 and 5.13. These plots are repeated here along with the remaining phase error plots for the distorters in Table 5.4 calculated using (5.16) and (5.17). The resulting angle allows for a clear differentiation between materials. Aluminium distorters cause a positive phase error in all cases, while steel distorters cause negative phase error.

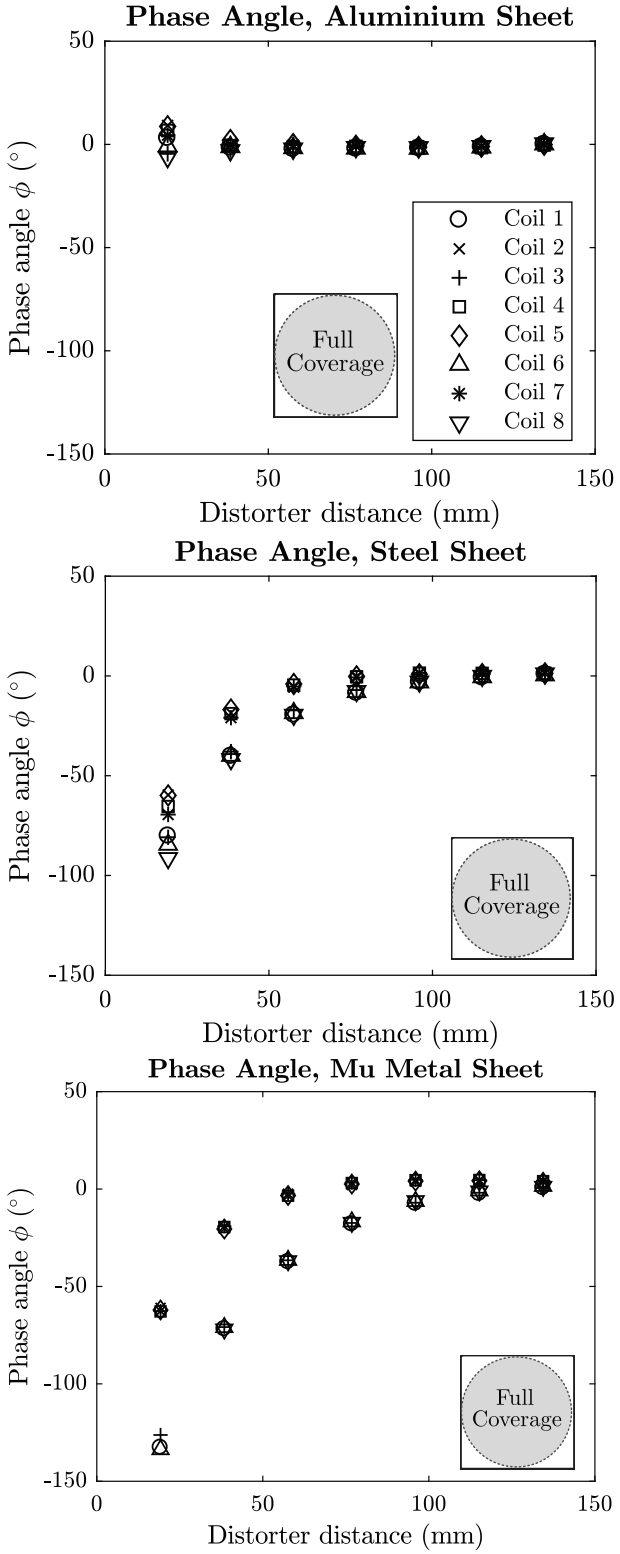


Figure A.6: Phase error for planar sheet distorters. The aluminium sheet causes a small positive phase error of approximately 10° when placed very close to the field generator, but quickly returns to zero with increasing distance. The steel sheet initially causes very large negative phase errors when close to the field generator but returns to zero at approximately 120mm from the field generator. The mu-metal sheet phase error is an exaggerated version of that of the steel sheet, with maximum errors of approximately 140°.

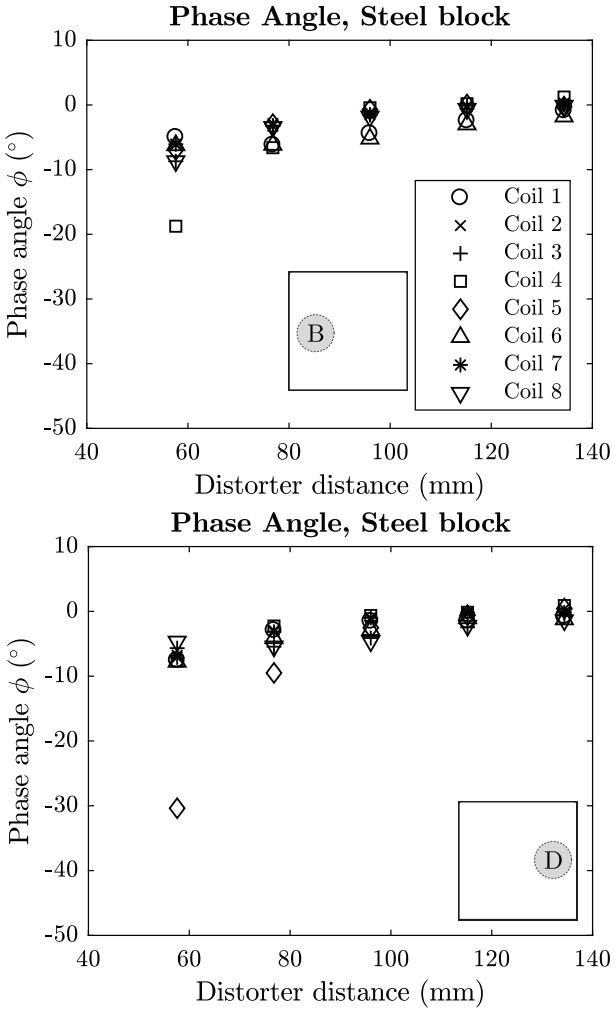


Figure A.7: Phase error plots for small steel block distorter in locations B and D. The largest errors are experienced by coils 4 and 5 since these coils are closest to locations B and D respectively. Negative phase error is experienced in both locations.

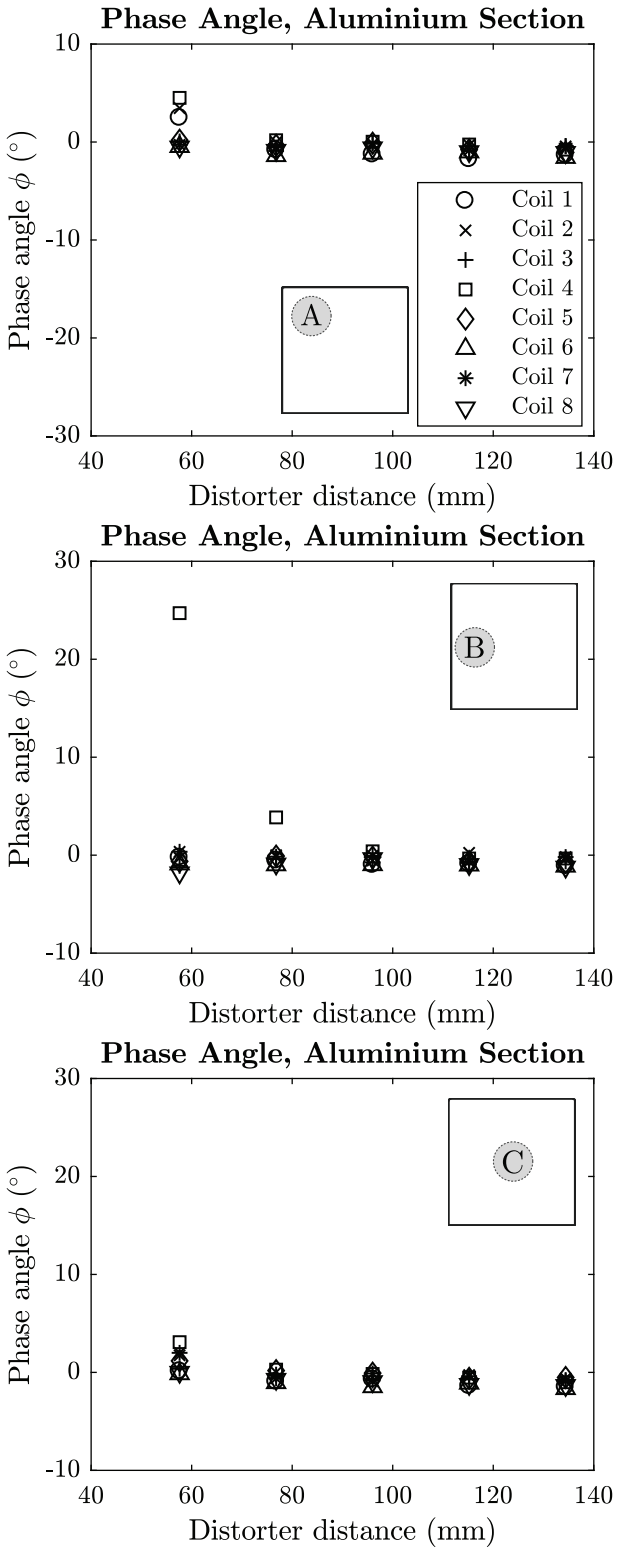


Figure A.8: Phase error plots for small aluminium block distorter in locations A, B and C. The largest phase errors are experienced by the coils closest to locations A, B and C. Positive phase error is experienced in all cases.

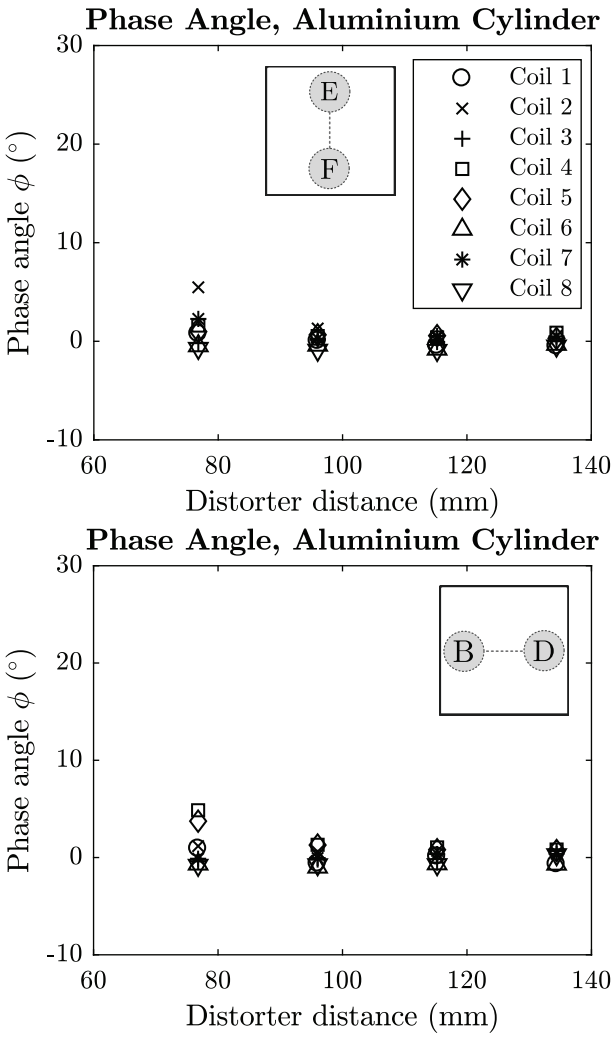


Figure A.9: Phase error plots for large aluminium cylinder in locations E to F and B to D. The cylinder spans the length of the field generator. The highest phase errors correspond to the positions of the distorter. Positive phase error is experienced in each case.

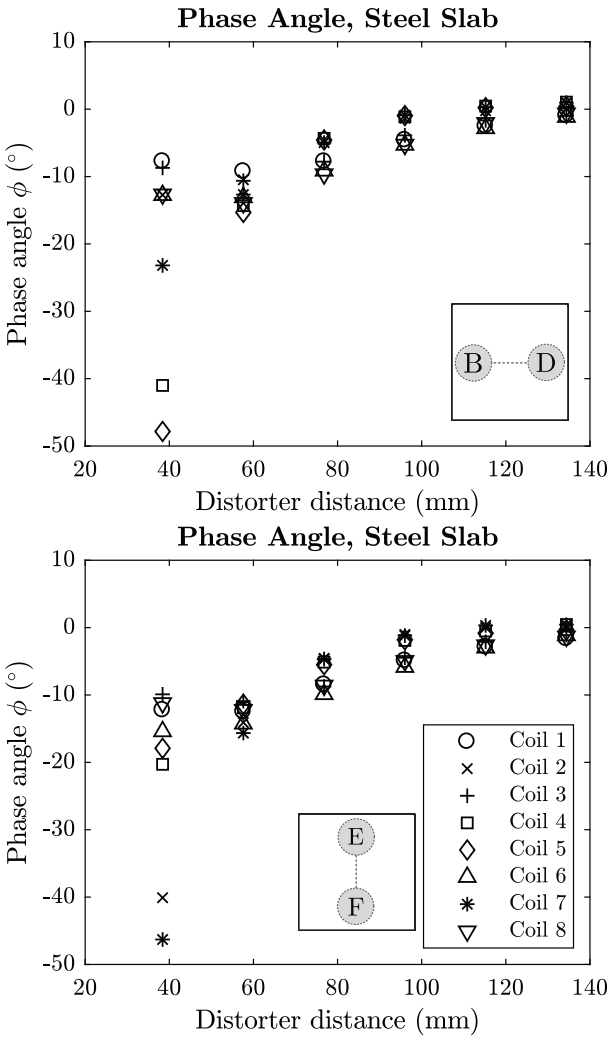


Figure A.10: Phase error plots for steel slab in locations B to D and E to F. Negative phase is experienced in each case, with the highest phase error experienced by the coils in closest to the distorter.

A.3 Position Error Plots

The position error plots for the sheet and aluminium section distorters were shown in Fig 5.14 and 5.15. These plots are repeated here with the remaining position error plots for the distorters in Table 5.4. (5.18) and (5.19) were used to extract the mean error e_z and standard deviation σ_z from each planar point cloud. The resulting errors show how the different distorters effect the tracking performance of the Anser EMT system.

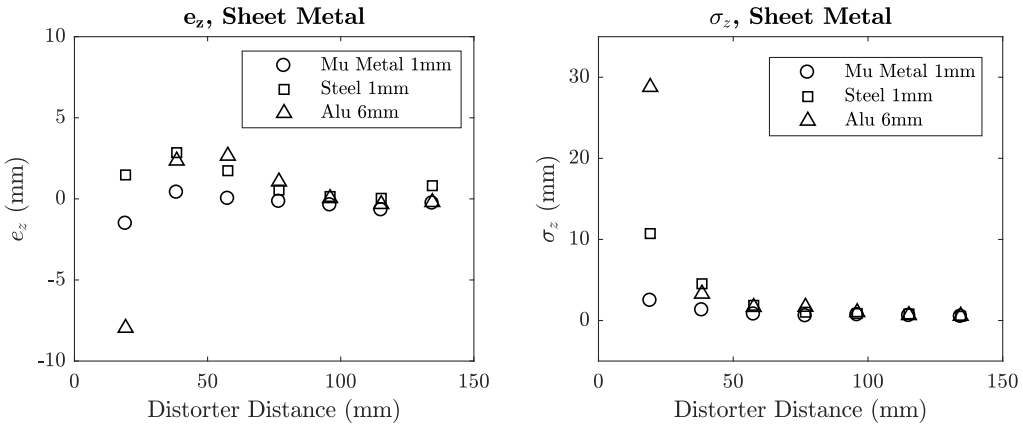


Figure A.11: Position error plots for sheet metal distorters. Aluminium causes the most severe position error and highest standard deviation. A cross-over point is seen at approximately 100mm in which the errors are minimised, before increasing for distances $>$100mm.

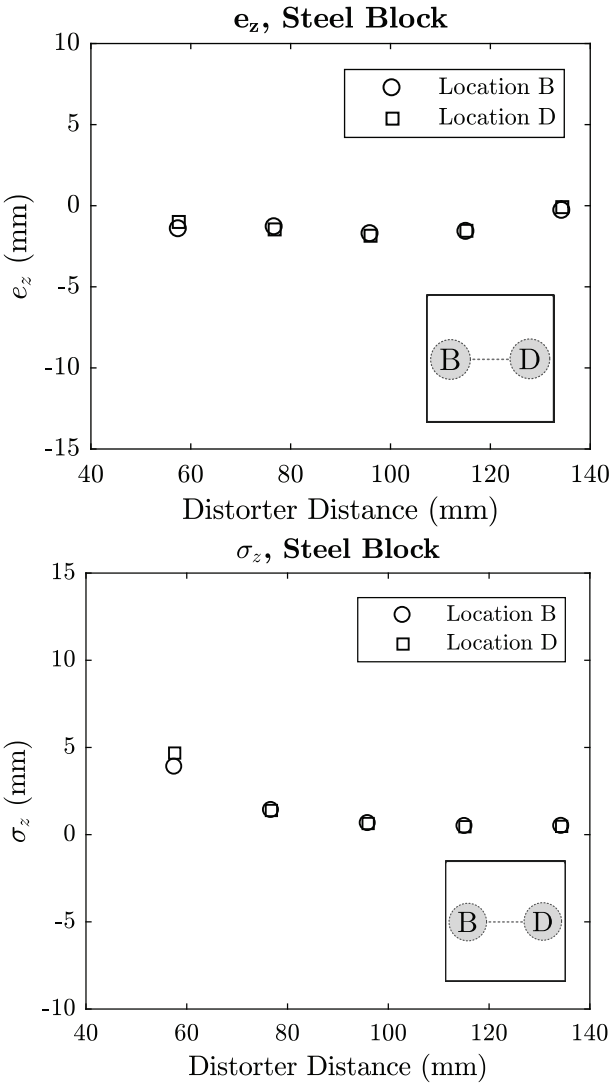


Figure A.12: Position error plots for the steel block at locations B and D.

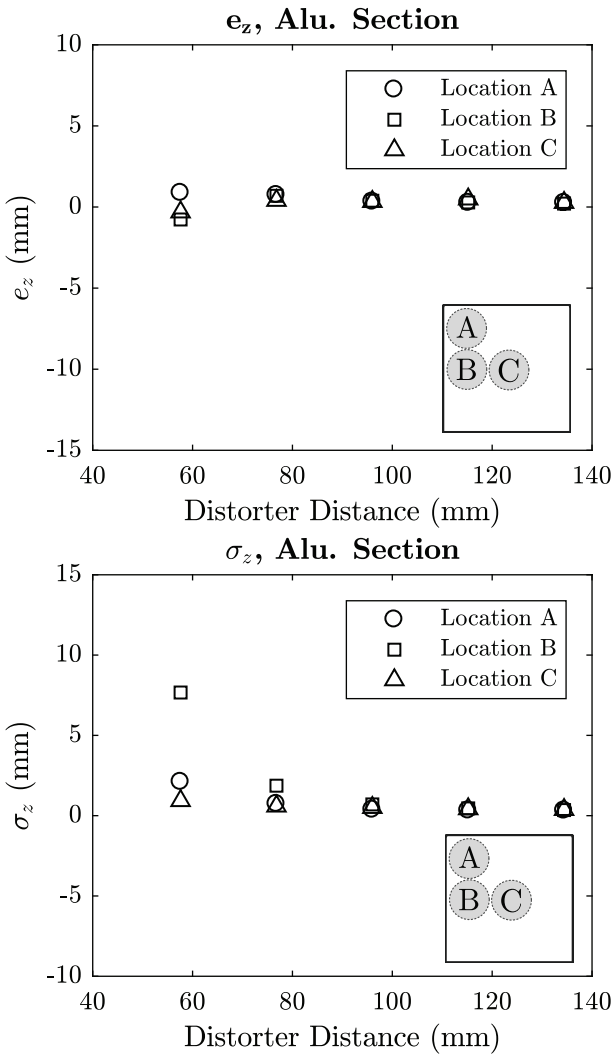


Figure A.13: Position error plots for aluminium section in locations A, B and C. Location B causes the highest positioning error and standard deviation as the aluminium section is placed directly below transmitter coil 4.

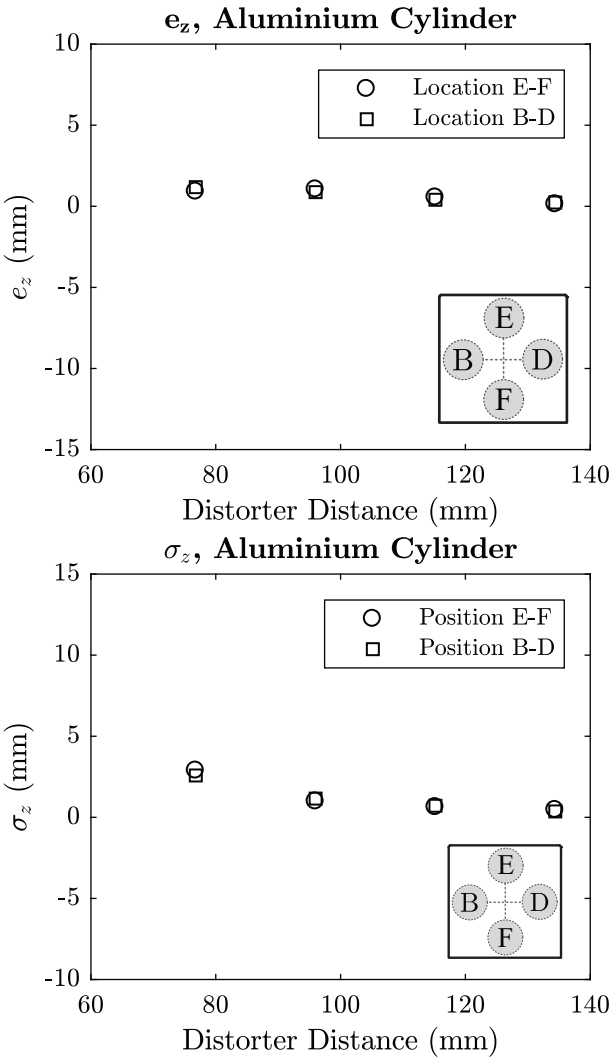


Figure A.14: Position error plots for aluminium cylinder at locations B and D and E to F.

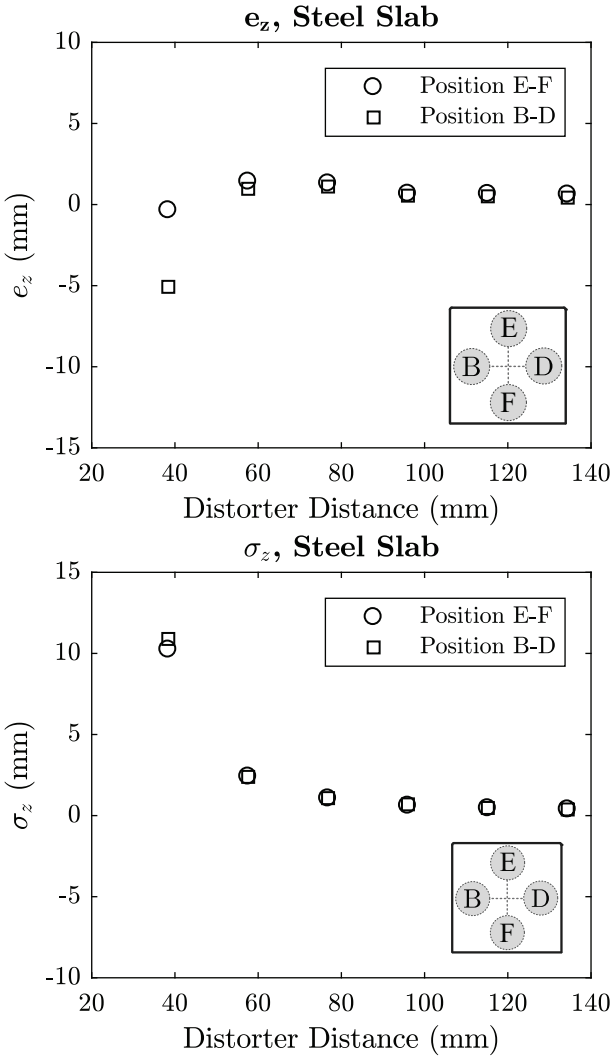


Figure A.15: Position error plots for steel slab at locations B and D and E to F.

Bibliography

[1] Global Cancer Observatory, "Cancer Incidence and Mortality Worldwide," 2018. [Online]. Available: http://gco.iarc.fr/. Date accessed: 14/01/2019.

[2] F. Bray, J. S. Ren, E. Masuyer, and J. Ferlay, "Global estimates of cancer prevalence for 27 sites in the adult population in 2008," *International Journal of Cancer*, vol. 132, DOI 10.1002/ijc.27711, no. 5, pp. 1133–1145, 2013.

[3] NIH National Cancer Institute, "Lung Cancer," 2018. [Online]. Available: https://visualsonline.cancer.gov. Date accessed: 14/01/2019.

[4] Olympus Medical America, "BF-P190 Bronchoscope," 2018. [Online]. Available: http://medical.olympusamerica.com. Date accessed: 14/01/2019.

[5] R. Guteanu, A. Bobocea, M. Dumitrescu, and B. Miron, "The role of mediastinoscopy for diagnosis of isolated mediastinal lymphadenopathies," *Journal of Clinical and Investigative Surgery*, vol. 2, DOI 10.25083/2559.5555.22.120125, no. 2, pp. 120–125, 2017.

[6] C. Gilbert, J. Akulian, R. Ortiz, H. Lee *et al.*, "Novel bronchoscopic strategies for the diagnosis of peripheral lung lesions: Present techniques and future directions," *Respirology*, vol. 19, DOI 10.1111/resp.12301, no. 5, pp. 636–644, 2014.

[7] F. J. Herth, R. Eberhardt, and A. Ernst, "The future of bronchoscopy in diagnosing, staging and treatment of lung cancer," *Respiration*, vol. 73, DOI 10.1159/000093369, no. 4, pp. 399–409, 2006.

[8] K. A. Khan, P. Nardelli, A. Jaeger, C. O'Shea *et al.*, "Navigational Bronchoscopy for Early Lung Cancer: A Road to Therapy," *Advances in Therapy*, vol. 33, DOI 10.1007/s12325-016-0319-4, no. 4, pp. 580–596, 2016.

[9] Medtronic, "SuperDimension Navigation System." [Online]. Available: http://superdimension.com/. Date accessed: 14/01/2019.

[10] H. Himberg and Y. Motai, *Latency and Distortion of Electromagnetic Trackers for Augmented Reality Systems*, A. Spanias, Ed., vol. 6, no. 1. Williston, VT: Morgan & Claypool Publishers, 2014.

[11] H. Sadjadi, K. Hashtrudi-zaad, and G. Fichtinger, "Simultaneous Electromagnetic Tracking and Calibration for Dynamic Field Distortion Compensation," *IEEE Transactions on Biomedical Engineering*, vol. 63, DOI 10.1109/TBME.2015.2502138, no. 8, pp. 1771–1781, 2016.

[12] A. Vaccarella, E. De Momi, A. Enquobahrie, and G. Ferrigno, "Unscented Kalman filter based sensor fusion for robust optical and electromagnetic tracking in surgical navigation," *IEEE Transactions on Instrumentation and Measurement*, vol. 62, DOI 10.1109/TIM.2013.2248304, no. 7, pp. 2067–2081, 2013.

[13] W. Birkfellner, F. Watzinger, F. Wanschitz, G. Enislidis *et al.*, "Systematic distortions in magnetic position digitizers Evaluation of a miniature electromagnetic position tracker Systematic distortions in magnetic position digitizers," *Medical Physics J. Appl. Phys. Med. Phys*, vol. 25, DOI 10.1118/1.1508377, no. 29, pp. 2242–66 112, 1998.

[14] G. Zachmann, "Distortion Correction of Magnetic Fields for Position Tracking," *Computer Graphics International*, DOI 10.1109/CGI.1997.601306, pp. 213–220, 251, 1997.

[15] M. Li, C. Hansen, and G. Rose, "A software solution to dynamically reduce metallic distortions of electromagnetic tracking systems for image-guided surgery," *International Journal of Computer Assisted Radiology and Surgery*, vol. 12, DOI 10.1007/s11548-017-1546-0, no. 9, pp. 1621–1633, 2017.

[16] T. Bien, M. Li, Z. Salah, and G. Rose, "Electromagnetic tracking system with reduced distortion using quadratic excitation," *International Journal of Computer Assisted Radiology and Surgery*, vol. 9, DOI 10.1007/s11548-013-0925-4, no. 2, pp. 323–332, 2014.

[17] Northern Digital Inc., "NDI Tools and Sensors." [Online]. Available: https://www.ndigital.com/medical/products/tools-and-sensors/. Date accessed: 14/01/2019.

[18] Auris Health, "Robotic Endoscopy," 2018. [Online]. Available: https://www.aurishealth.com. Date accessed: 14/01/2019.

[19] R. L. Drake, W. Vogl, and A. W. M. Mitchell, "Thorax," in *Gray's Anatomy for Students*, 3rd ed., ch. 3, pp. 167–183. Elsevier, 2015.

[20] Wikimedia Commons, "The human respiratory system," 2007. [Online]. Available: https://en.wikipedia.org/wiki/File:Respiratory_system_complete_en.svg. Date accessed: 14/01/2019.

[21] H. Hansen, *Textbook of Lung Cancer*, 2nd ed. Boca Raton, FL: CRC Press, 2008.

[22] M. Andolfi, R. Potenza, R. Capozzi, V. Liparulo *et al.*, "The role of bronchoscopy in the diagnosis of early lung cancer: A review," *Journal of Thoracic Disease*, vol. 8, DOI 10.21037/jtd.2016.11.81, no. 11, pp. 3329–3337, 2016.

[23] D. R. Aberle, A. M. Adams, C. D. Berg, W. C. Black *et al.*, "Reduced lung-cancer mortality with low-dose computed tomographic screening." *The New England journal of medicine*, vol. 365, DOI 10.1056/NEJMoa1102873, no. 5, pp. 395–409, 2011.

[24] A. Ernst, "Airway Anatomy for the Bronchoscopist," in *Introduction to Bronchoscopy*, pp. 38–45. Cambridge University Press, 2009.

[25] L. Niu, K. Xu, and F. Mu, "Cryosurgery for lung cancer," *Journal of Thoracic Disease*, vol. 4, DOI 10.3978/j.issn.2072-1439.2012.07.13, no. 4, pp. 408–419, 2012.

[26] Y. X. Wang, G. G. Lo, J. Yuan, P. E. Larson *et al.*, "Magnetic resonance imaging for lung cancer screen," *Journal of Thoracic Disease*, vol. 6, DOI 10.3978/j.issn.2072-1439.2014.08.43, no. 9, pp. 1340–1348, 2014.

[27] F. Laurent, M. Montaudon, and O. Corneloup, "CT and MRI of lung cancer," *Respiration*, vol. 73, DOI 10.1159/000091528, no. 2, pp. 133–142, 2006.

[28] A. A. Memon, B. Weber, M. Winterdahl, S. Jakobsen *et al.*, "PET imaging of patients with non-small cell lung cancer employing an EGF receptor targeting drug as tracer," *British Journal of Cancer*, vol. 105, DOI 10.1038/bjc.2011.493, no. 12, pp. 1850–1855, 2011.

[29] E. Van Cutsem, A. Cervantes, B. Nordlinger, D. Arnold *et al.*, "Metastatic colorectal cancer: ESMO clinical practice guidelines for diagnosis, treatment and follow-up," *Annals of Oncology*, vol. 25, DOI 10.1093/annonc/mdu260, pp. 1–9, 2014.

[30] J. Zhu, W. Li, J. Zhou, Y. Chen *et al.*, "The diagnostic value of narrow-band imaging for early and invasive lung cancer: a meta-analysis," *Clinics*, vol. 72, DOI 10.6061/clinics/2017(07)09, no. 07, pp. 438–448, 2017.

[31] B. Zaric and B. Perin, "Use of narrow-band imaging bronchoscopy in detection of lung cancer," *Expert Review of Medical Devices*, vol. 7, DOI 10.1586/erd.10.12, no. 3, pp. 395–406, 2010.

[32] M. Gomez and G. A. Silvestri, "Endobronchial Ultrasound for the Diagnosis and Staging of Lung Cancer," *Proceedings of the American Thoracic Society*, vol. 6, DOI 10.1513/pats.200808-081LC, no. 2, pp. 180–186, 2009.

[33] B. Canneto, G. Ferraroli, G. Falezza, and M. V. Infante, "Ideal conditions to perform EBUS-TBNA," *Journal of Thoracic Disease*, vol. 9, DOI 10.21037/jtd.2017.04.64, no. Suppl 5, pp. S414–S417, 2017.

[34] K. G. Tournoy, R. C. Rintoul, J. P. van Meerbeeck, N. R. Carroll *et al.*, "EBUS-TBNA for the diagnosis of central parenchymal lung lesions not visible at routine bronchoscopy," *Lung Cancer*, vol. 63, DOI 10.1016/j.lungcan.2008.04.004, no. 1, pp. 45–49, 2009.

[35] D. H. Yu and D. Feller-Kopman, "Interventional bronchoscopy in adults," *Expert Review of Respiratory Medicine*, vol. 12, DOI 10.1080/17476348.2018.1429922, no. 3, pp. 239–248, 2018.

[36] K. L. Yu, T. H. Tsai, C. C. Ho, W. Y. Liao *et al.*, "The value of radial endobronchial ultrasound-guided bronchial brushing in peripheral non-squamous non-small cell lung cancer," *Scientific Reports*, vol. 8, DOI 10.1038/s41598-018-24300-7, no. 1, pp. 1–8, 2018.

[37] Olympus Medical America, "EBUS Bronchoscope (BF-UC180F)," 2018. [Online]. Available: http://medical.olympusamerica.com/products/bf-uc180f-ebus-bronchoscope. Date accessed: 14/01/2019.

[38] J. F. de Boer, R. Leitgeb, and M. Wojtkowski, "Twenty-five years of optical coherence tomography: the paradigm shift in sensitivity and speed provided by Fourier domain OCT [Invited]," *Biomedical Optics Express*, vol. 8, DOI 10.1364/BOE.8.003248, no. 7, p. 3248, 2017.

[39] A. F. Fercher, "Optical Coherence Tomography," *Journal of Biomedical Optics*, vol. 1, DOI 10.1117/12.231361, no. 2, pp. 157–173, 1996.

[40] D. Huang, E. A. Swanson, C. P. Lin, J. S. Schuman *et al.*, "Optical Coherence Tomography," *Science. November*, vol. 254, DOI 10.1002/jcp.24872, no. 5035, pp. 1178–1181, 1991.

[41] X. Luo, K. Mori, and T. M. Peters, "Advanced Endoscopic Navigation: Surgical Big Data, Methodology, and Applications," *Annual Review of Biomedical*

Engineering, vol. 20, DOI 10.1146/annurev-bioeng-062117-120917, no. 1, pp. 221–251, 2018.

[42] L. P. Hariri, M. Mino-Kenudson, M. Lanuti, A. J. Miller *et al.*, "Diagnosing lung carcinomas with optical coherence tomography," *Annals of the American Thoracic Society*, vol. 12, DOI 10.1513/AnnalsATS.201408-370OC, no. 2, pp. 193–201, 2015.

[43] C. Manley, L. Hariri, D. Adams, M. Lanuti *et al.*, "Optical Coherence Tomography Imaging for the Diagnosis of Airway Tumors In Vivo," *Chest*, vol. 148, DOI 10.1378/chest.2260159, no. 4, p. 561A, 2015.

[44] R. G. Michel, G. T. Kinasewitz, K.-M. Fung, and J. I. Keddissi, "Optical Coherence Tomography as an Adjunct to Flexible Bronchoscopy in the Diagnosis of Lung Cancer," *Chest*, vol. 138, DOI 10.1378/chest.10-0753, no. 4, pp. 984–988, 2010.

[45] M. Tsuboi, A. Hayashi, N. Ikeda, H. Honda *et al.*, "Optical coherence tomography in the diagnosis of bronchial lesions," *Lung Cancer*, vol. 49, DOI 10.1016/j.lungcan.2005.04.007, no. 3, pp. 387–394, 2005.

[46] R. Hou, T. Le, S. D. Murgu, Z. Chen *et al.*, "Recent advances in optical coherence tomography for the diagnoses of lung disorders," *Expert Review of Respiratory Medicine*, vol. 5, DOI 10.1586/ers.11.59, no. 5, pp. 711–724, 2011.

[47] R. S. Winokur, B. B. Pua, B. Sullivan, and D. C. Madoff, "Percutaneous lung biopsy: Technique, efficacy, and complications," *Seminars in Interventional Radiology*, vol. 30, DOI 10.1055/s-0033-1342952, no. 2, pp. 121–127, 2013.

[48] T. Lin, L. I. Cerviño, X. Tang, N. Vasconcelos *et al.*, "Fluoroscopic tumor tracking for image-guided lung cancer radiotherapy," *Physics in Medicine and Biology*, vol. 54, DOI 10.1088/0031-9155/54/4/011, no. 4, pp. 981–992, 2009.

[49] M. S. Linet, T. L. Slovis, D. L. Miller, R. Kleinerman *et al.*, "Cancer Risks Associated with External Radiation From Diagnostic Imaging Procedures," *CA: A Cancer Journal for Clinicians*, vol. 62, DOI 10.3322/caac.21132, no. 2, pp. 75–100, 2012.

[50] R. Eberhardt, D. Anantham, F. Herth, D. Feller-Kopman *et al.*, "Electromagnetic navigation diagnostic bronchoscopy in peripheral lung lesions." *Chest*, vol. 131, DOI 10.1378/chest.06-3016, no. 6, pp. 1800–1805, 2007.

[51] E. van Beek and E. Hoffman, "Functional imaging: CT and MRI," *Clinics in chest medicine*, vol. 29, DOI 10.1016/j.ccm.2007.12.003, no. 1, pp. 195–216, 2008.

[52] G. T. Herman, *Fundamentals of Computerized Tomography*. Berlin: Springer, 2009.

[53] P. R. Smith, T. M. Peters, and R. H. Bates, "Image reconstruction from finite numbers of projections," *Journal of Physics A: General Physics*, vol. 6, DOI 10.1088/0305-4470/6/3/011, no. 3, pp. 361–382, 1973.

[54] Schoolphysics, "Computerised axial tomography (CAT or CT)," 2018. [Online]. Available: http://www.schoolphysics.co.uk/age16-19/Medicalphysics/text/CT_scanning/index.html. Date accessed: 14/01/2019.

[55] P. Nardelli, K. A. Khan, A. Corvò, N. Moore *et al.*, "Optimizing parameters of an open-source airway segmentation algorithm using different CT images." *Biomedical engineering online*, vol. 14, DOI 10.1186/s12938-015-0060-2, no. 1, p. 62, 2015.

[56] E. Smistad, T. L. Falch, M. Bozorgi, A. C. Elster *et al.*, "Medical image segmentation on GPUs - A comprehensive review," *Medical Image Analysis*, vol. 20, DOI 10.1016/j.media.2014.10.012, no. 1, pp. 1–18, 2015.

[57] I. Bankman, *Handbook of Medical Image Processing and Analysis*, 2nd ed. Amsterdam: Elsevier, 2008.

[58] P. Nardelli, A. Jaeger, C. O'Shea, K. A. Khan *et al.*, "Pre-clinical validation of virtual bronchoscopy using 3D Slicer," *International Journal of Computer Assisted Radiology and Surgery*, vol. 12, DOI 10.1007/s11548-016-1447-7, no. 1, pp. 25–38, 2016.

[59] P. Nardelli, "Open-source Virtual Bronchoscopy for Image Guided Navigation," PhD thesis, University College Cork, 2016.

[60] A. Mehnert and P. Jackway, "An improved seeded region growing algorithm," *Pattern Recognition Letters*, vol. 18, DOI 10.1016/S0167-8655(97)00131-1, no. 10, pp. 1065–1071, 1997.

[61] Z. Bian, J.-P. Charbonnier, J. Liu, D. Zhao *et al.*, "Small airway segmentation in thoracic computed tomography scans: a machine learning approach," *Physics in Medicine and Biology*, vol. 63, DOI 10.1088/1361-6560/aad2a1, 2018.

[62] Q. Meng, T. Kitasaka, Y. Nimura, M. Oda *et al.*, "Automatic segmentation of airway tree based on local intensity filter and machine learning technique in 3D chest CT volume," *International Journal of Computer Assisted Radiology and Surgery*, vol. 12, DOI 10.1007/s11548-016-1492-2, no. 2, pp. 245–261, 2017.

[63] P. J. Reynisson, E. F. Hofstad, H. O. Leira, C. Askeland *et al.*, "A new visualization method for navigated bronchoscopy." *Minimally invasive therapy & allied technologies*, vol. 27, DOI 10.1080/13645706.2017.1327870, no. 2, pp. 119–126, Apr. 2018.

[64] C. Askeland, O. V. Solberg, J. B. L. Bakeng, I. Reinertsen *et al.*, "CustusX: an open-source research platform for image-guided therapy," *International Journal of Computer Assisted Radiology and Surgery*, vol. 11, DOI 10.1007/s11548-015-1292-0, no. 4, pp. 505–519, 2016.

[65] P. J. Reynisson, M. Scali, E. Smistad, E. F. Hofstad *et al.*, "Airway segmentation and centerline extraction from thoracic CT - Comparison of a new method to state of the art commercialized methods," *PLoS ONE*, vol. 10, DOI 10.1371/journal.pone.0144282, no. 12, pp. 1–20, 2015.

[66] I. Wegner, J. Biederer, R. Tetzlaff, I. Wolf *et al.*, "Evaluation and extension of a navigation system for bronchoscopy inside human lungs," *Proc. SPIE 6509, Medical Imaging 2007: Visualization and Image-Guided Procedures*, vol. 6509, DOI 10.1117/12.708199, 2007.

[67] S. B. Solomon, P. White, C. M. Wiener, J. B. Orens *et al.*, "Three-dimensional CT-guided bronchoscopy with a real-time electromagnetic position sensor: A comparison of two image registration methods," *Chest*, vol. 118, DOI 10.1378/chest.118.6.1783, no. 6, pp. 1783–1787, 2000.

[68] B. K. P. Horn, "Closed-form solution of absolute orientation using unit quaternions," *Journal of the Optical Society of America A*, vol. 4, DOI 10.1364/JOSAA.4.000629, no. 4, p. 629, 1987.

[69] T. Klein, J. Traub, H. Hautmann, A. Ahmadian *et al.*, "Fiducial-free registration procedure for navigated bronchoscopy." *International Conference on Medical Image Computing and Computer-Assisted Intervention, MICCAI*, vol. 10, no. Pt 1, pp. 475–82, 2007.

[70] P. Besl and N. McKay, "A Method for Registration of 3-D Shapes," *IEEE Transactions on Pattern Analysis and Machine Intelligence*, vol. 14, DOI 10.1109/34.121791, no. 2, pp. 239–256, 1992.

[71] E. F. Hofstad, H. Sorger, H. O. Leira, T. Amundsen *et al.*, "Automatic registration of CT images to patient during the initial phase of bronchoscopy: a clinical pilot study." *Medical physics*, vol. 41, DOI 10.1118/1.4866884, no. 4, p. 41903, 2014.

[72] D. Deguchi, M. Feuerstein, T. Kitasaka, Y. Suenaga *et al.*, "Real-time marker-free patient registration for electromagnetic navigated bronchoscopy: A phantom study," *International Journal of Computer Assisted Radiology and Surgery*, vol. 7, DOI 10.1007/s11548-011-0626-9, no. 3, pp. 359–369, 2012.

[73] X. Luo, Y. Wan, X. He, and K. Mori, "Adaptive marker-free registration using a multiple point strategy for real-time and robust endoscope electromagnetic navigation," *Computer Methods and Programs in Biomedicine*, vol. 118, DOI 10.1016/j.cmpb.2014.11.008, no. 2, pp. 147–157, 2015.

[74] Veran Medical Technologies Inc. USA, "Veran Medical Technologies vs. superDimension," 2018. [Online]. Available: https://www.veranmedical.com/spin-system/comparison/. Date accessed: 14/01/2019.

[75] Medtronic, "Edge Firm Tip Navigation Catheter," 2018. [Online]. Available: https://superdimension.com/innovations/navigation-catheters/. Date accessed: 14/01/2019.

[76] Veran Medical Technologies Inc. USA, "Always-On Tip Tracked Instruments," 2018. [Online]. Available: https://www.veranmedical.com/spin-system/always-on-tip-tracked-instruments/. Date accessed: 14/01/2019.

[77] W. D. Bolton, H. Howe, and J. E. Stephenson, "The utility of electromagnetic navigational bronchoscopy as a localization tool for robotic resection of small pulmonary nodules," *Annals of Thoracic Surgery*, vol. 98, DOI 10.1016/j.athoracsur.2014.04.085, no. 2, pp. 471–476, 2014.

[78] J. R. Rojas-Solano, L. Ugalde-Gamboa, and M. MacHuzak, "Robotic Bronchoscopy for Diagnosis of Suspected Lung Cancer: A Feasibility Study," *Journal of Bronchology and Interventional Pulmonology*, vol. 25, DOI 10.1097/LBR.0000000000000499, no. 3, pp. 168–175, 2018.

[79] D. Fielding, F. Bashirzadeh, J. H. Son, M. Todman *et al.*, "First Human Use of a New Robotic-Assisted Navigation System for Small Peripheral Pulmonary Nodules Demonstrates Good Safety Profile and High Diagnostic Yield," *Chest*, vol. 152, DOI 10.1016/j.chest.2017.08.892, no. 4, p. A858, 2017.

[80] F. S. Fuchs, S. Zirlik, K. Hildner, J. Schubert *et al.*, "Confocal laser endomicroscopy for diagnosing lung cancer in vivo," *European Respiratory Journal*, vol. 41, DOI 10.1183/09031936.00062512, no. 6, pp. 1401–1408, 2013.

[81] A. Goud, C. Dahagam, D. P. Breen, and S. Sarkar, "Role of electromagnetic navigational bronchoscopy in pulmonary nodule management," *Journal of Thoracic Disease*, vol. 8, DOI 10.21037/jtd.2016.02.73, no. 6, pp. 501–S08, 2016.

[82] R. Eberhardt, D. Anantham, A. Ernst, D. Feller-Kopman *et al.*, "Multimodality bronchoscopic diagnosis of peripheral lung lesions: a randomized controlled trial." *American journal of respiratory and critical care medicine*, vol. 176, DOI 10.1164/rccm.200612-1866OC, no. 1, pp. 36–41, 2007.

[83] D. Makris, A. Scherpereel, S. Leroy, B. Bouchindhomme *et al.*, "Electromagnetic navigation diagnostic bronchoscopy for small peripheral lung lesions." *The European respiratory journal*, vol. 29, DOI 10.1183/09031936.00165306, no. 6, pp. 1187–1192, 2007.

[84] D. E. Ost, A. Ernst, X. Lei, K. L. Kovitz *et al.*, "Diagnostic Yield and Complications of Bronchoscopy for Peripheral Lung Lesions. Results of the AQuIRE Registry." *American journal of respiratory and critical care medicine*, vol. 193, DOI 10.1164/rccm.201507-1332OC, no. 1, pp. 68–77, 2016.

[85] P. J. Reynisson, H. O. Leira, T. N. Hernes, E. F. Hofstad *et al.*, "Navigated bronchoscopy: a technical review." *Journal of bronchology & interventional pulmonology*, vol. 21, DOI 10.1097/LBR.0000000000000064, no. 3, pp. 242–264, 2014.

[86] A. K. Mahajan, S. Patel, D. K. Hogarth, and R. Wightman, "Electromagnetic navigational bronchoscopy: an effective and safe approach to diagnose peripheral lung lesions unreachable by conventional bronchoscopy in high-risk patients." *Journal of bronchology & interventional pulmonology*, vol. 18, DOI 10.1097/LBR.0b013e318216cee6, no. 2, pp. 133–137, 2011.

[87] L. M. Seijo, J. P. de Torres, M. D. Lozano, G. Bastarrika *et al.*, "Diagnostic yield of electromagnetic navigation bronchoscopy is highly dependent on the presence of a Bronchus sign on CT imaging: results from a prospective study." *Chest*, vol. 138, DOI 10.1378/chest.09-2708, no. 6, pp. 1316–1321, 2010.

[88] S. J. Khandhar, M. R. Bowling, J. Flandes, T. R. Gildea *et al.*, "Electromagnetic navigation bronchoscopy to access lung lesions in 1,000 subjects: First results of the prospective, multicenter NAVIGATE study," *BMC Pulmonary Medicine*, vol. 17, DOI 10.1186/s12890-017-0403-9, no. 1, pp. 1–9, 2017.

[89] E. F. Hofstad, H. Sorger, J. B. L. Bakeng, L. Gruionu *et al.*, "Intraoperative localized constrained registration in navigated bronchoscopy," *Medical Physics*, vol. 44, DOI 10.1002/mp.12361, no. 8, pp. 4204–4212, 2017.

[90] K. O'Donoghue, "Electromagnetic Tracking and Steering for Catheter Navigation," PhD thesis, University College Cork, 2014.

[91] H. A. Jaeger, S. Hinds, and P. Cantillon-Murphy, "An Open Framework Enabling Electromagnetic Tracking in Image-Guided Interventions," in *Medical Image Computing and Computer Assisted Intervention – MICCAI 2018*, DOI 10.1007/978-3-030-00937-3_20, pp. 168–175. Granada, Spain: Springer International Publishing, 2018.

[92] K. O'Donoghue, D. Eustace, J. Griffiths, M. O'Shea *et al.*, "Catheter position tracking system using planar magnetics and closed loop current control," *IEEE Transactions on Magnetics*, vol. 50, DOI 10.1109/TMAG.2014.2304271, no. 7, pp. 1–9, 2014.

[93] A. M. Franz, A. Seitel, N. Bopp, C. Erbelding *et al.*, "First clinical use of the EchoTrack guidance approach for radiofrequency ablation of thyroid gland nodules," *International Journal of Computer Assisted Radiology and Surgery*, vol. 12, DOI 10.1007/s11548-017-1560-2, no. 6, pp. 931–940, 2017.

[94] I. Paolucci, M. Schwalbe, G. A. Prevost, A. Lachenmayer *et al.*, "Design and implementation of a dynamic navigation technique for laparoscopic ablation of liver tumors based on electromagnetic tracked ultrasound (submitted)," *Surgical Endoscopy*, DOI 10.1007/s00464-018-6088-1, pp. 1–10, 2018.

[95] A. Lasso, T. Heffter, A. Rankin, C. Pinter *et al.*, "PLUS: Open-source toolkit for ultrasound-guided intervention systems," *IEEE Transactions on Biomedical Engineering*, vol. 61, DOI 10.1109/TBME.2014.2322864, no. 10, pp. 2527–2537, 2014.

[96] J. Tokuda, G. S. Fischer, X. Papademetris, Z. Yaniv *et al.*, "OpenIGTLink: An open network protocol for image-guided therapy environment," *International Journal of Medical Robotics and Computer Assisted Surgery*, vol. 5, DOI 10.1002/rcs.274, no. 4, pp. 423–434, 2009.

[97] A. Enquobahrie, P. Cheng, K. Gary, L. Ibanez *et al.*, "The Image-Guided Surgery Toolkit IGSTK: An open source C++ software toolkit," *Journal of Digital Imaging*, vol. 20, DOI 10.1007/s10278-007-9054-3, no. SUPPL. 1, pp. 21–33, 2007.

[98] P. Traneus Anderson, "Open Source Electromagnetic Trackers," 2014. [Online]. Available: https://www.na-mic.org/wiki/Open_Source_Electromagnetic_Trackers. Date accessed: 14/01/2019.

[99] F. H. Raab, E. B. Blood, T. O. Steiner, and H. R. Jones, "Magnetic Position and Orientation Tracking System," *IEEE Transactions on Aerospace and Electronic Systems*, vol. 5, DOI 10.1109/TAES.1979.308860, no. 5, pp. 709–718, 1979.

[100] H. A. Jaeger, A. M. Franz, K. O'Donoghue, A. Seitel *et al.*, "Anser EMT: the first open-source electromagnetic tracking platform for image-guided interventions," *International Journal of Computer Assisted Radiology and Surgery*, vol. 12, DOI 10.1007/s11548-017-1568-7, no. 6, pp. 1059–1067, 2017.

[101] J. Huang, T. Mori, K. Takashima, S. Hashi *et al.*, "IM6D : Magnetic Tracking System with 6-DOF Passive Markers for Dexterous 3D Interaction and Motion," *ACM Transactions on Graphics*, vol. 34, DOI 10.1145/2816795.2818135, no. 6, pp. 1–10, 2015.

[102] A. Plotkin, O. Shafrir, E. Paperno, and D. M. Kaplan, "Magnetic eye tracking: A new approach employing a planar transmitter," *IEEE Transactions on Biomedical Engineering*, vol. 57, DOI 10.1109/TBME.2009.2038495, no. 5, pp. 1209–1215, 2010.

[103] A. Plotkin, E. Paperno, G. Vasserman, and R. Segev, "Magnetic tracking of eye motion in small, fast-moving animals," *IEEE Transactions on Magnetics*, vol. 44, DOI 10.1109/TMAG.2008.2002187, no. 11, pp. 4492–4495, 2008.

[104] M. Li, T. Bien, and G. Rose, "FPGA based electromagnetic tracking system for fast catheter navigation," *International Journal of Scientific & Engineering Research*, vol. 4, DOI 10.14299/ijser.2013.09.001, no. 9, 2013.

[105] National Instruments, "NI USB-6212," 2018. [Online]. Available: http://www.ni.com/en-ie/support/model.usb-6212.html. Date accessed: 14/01/2019.

[106] L. Ramadoss and J. Y. Hung, "A study on universal serial bus latency in a real-time control system," in *IECON Proceedings (Industrial Electronics Conference)*, DOI 10.1109/IECON.2008.4757930, pp. 67–72, Orlando, FL, 2008.

[107] C. E. Shannon, "Communication in the Presence of Noise (Classic Paper)," *Proceedings of the IRE*, vol. 37, DOI 10.1109/JPROC.1998.659497, no. 1, pp. 10 – 21, 1949.

[108] A. M. Franz, D. Schmitt, A. Seitel, M. Chatrasingh *et al.*, "Standardized accuracy assessment of the calypso wireless transponder tracking system," *Physics in Medicine and Biology*, vol. 59, DOI 10.1088/0031-9155/59/22/6797, no. 22, p. 6797, 2014.

[109] K. O'Donoghue and P. Cantillon-Murphy, "Low Cost Super-Nyquist Asynchronous Demodulation for Use in EM Tracking Systems," *IEEE Transactions on Instrumentation and Measurement*, vol. 64, DOI 10.1109/TIM.2014.2343431, no. 2, pp. 458–466, 2015.

[110] K. R. Rao and P. C. Yip, *The Transform and Data Compression Handbook*, 1st ed. CRC Press, 2001.

[111] Wikimedia Commons, "Fourierop rows only," 2018. [Online]. Available: https://commons.wikimedia.org/wiki/File:Fourierop_rows_only.png. Date accessed: 14/01/2019.

[112] S. Haykin and B. Van Veen, "Fourier Representations of Signals and Linear Time-Invarient Systems," in *Signals and Systems*, 2nd ed., ch. 3. Hoboken, NJ: Wiley, 2003.

[113] J. Harris, "On the Use of Windows with the Discrete for Harmonic Analysis Fourier Transform," *Proc. IEEE*, vol. 66, DOI 10.1109/PROC.1978.10837, no. 1, pp. 51–83, 1978.

[114] Renesas, "A Tutorial in Coherent and Windowed Sampling with A/D Converters," pp. 1–9, 1997. [Online]. Available: https://www.intersil.com/content/dam/Intersil/documents/an96/an9675.pdf

[115] Texas Instruments, "TI Precision Labs – ADCs: Coherent Sampling and Filtering to Improve SNR and THD," 2018. [Online]. Available: https://training.ti.com/ti-precision-labs-adcs-coherent-sampling-and-filtering. Date accessed: 14/01/2019.

[116] S. W. Smith, "Windowed Sinc Filters," in *The Scientist and Engineer's Guide to Digital Signal Processing*, ch. 16, p. 285. San Diego, CA: California Technical Publishing, 1997.

[117] G. Heinzel, a. Rüdiger, R. Schilling, and T. Hannover, "Spectrum and spectral density estimation by the Discrete Fourier transform (DFT), including a comprehensive list of window functions and some new flat-top," *Max Plank Institute*, DOI 395068.0, pp. 1–84, 2002.

[118] Maxim Integrated, "Coherent Sampling vs. Window Sampling," pp. 1–7, 2002. [Online]. Available: https://pdfserv.maximintegrated.com/en/an/AN1040.pdf

[119] D. K. Cheng, "The Magnetic Dipole," in *Field and Wave Electromagnetics*, 2nd ed., p. 239. Reading, MA: Addison-Wesley, 1989.

[120] W. Kim, J. Song, and F. C. Park, "Closed-Form Position and Orientation Estimation for a Three-Axis Electromagnetic Tracking System," *IEEE Transactions on Industrial Electronics*, vol. 65, DOI 10.1109/TIE.2017.2760244, no. 5, pp. 4331–4337, 2018.

[121] S. Song, C. Hu, B. Li, X. Li *et al.*, "An electromagnetic localization and orientation method based on rotating magnetic dipole," *IEEE Transactions on Magnetics*, vol. 49, DOI 10.1109/TMAG.2012.2211375, no. 3, pp. 1274–1277, 2013.

[122] Xin Ge, Yifeng Wang, Ning Ding, Xiaomei Wu *et al.*, "An Electromagnetic Tracking Method Using Rotating Orthogonal Coils," *IEEE Transactions on Magnetics*, vol. 48, DOI 10.1109/TMAG.2012.2203917, no. 12, pp. 4802–4810, 2012.

[123] J. B. Kuipers, "SPASYN - An Electromagnetic Relative Position and Orientation Tracking System," *IEEE Transactions on Instrumentation and Measurement*, vol. 29, DOI 10.1109/TIM.1980.4314980, no. 4, pp. 462–466, 1980.

[124] Y. Chu, "Numerical calculation for the magnetic field in current-carrying circular arc filament," *IEEE Transactions on Magnetics*, vol. 34, DOI 10.1109/20.661481, no. 2, pp. 502 –504, 1998.

[125] C. L. W. Sonntag, M. Sprée, E. A. Lomonova, J. L. Duarte *et al.*, "Accurate Magnetic Field Intensity Calculations for Contactless Energy Transfer Coils," in *Proceedings of the 16th International Conference on the Computation of Electromagnetic Fields, Achen, Germany*, pp. 1–4, Aachen, Germany, 2007.

[126] Northern Digital Inc., "3D Guidance driveBAY and trakSTAR." [Online]. Available: https://www.ndigital.com/msci/products/drivebay-trakstar/. Date accessed: 14/01/2019.

[127] K. Levenberg, "A Method for the Solution of Certain Non-Linear Problems in Least Squares," *Quarterly of Applied Mathematics*, vol. 2, pp. 164–168, 1944.

[128] R. Byrd, R. Schnabel, and G. Shultz, "A Trust Region Algorithm for Nonlinearly Constrained Optimization," *SIAM Journal on Numerical Analysis*, vol. 24, DOI 10.1137/0724076, no. 5, pp. 1152–1170, 1987.

[129] P. Cladé, "PyDAQmx : a Python interface to the National Instruments DAQmx driver." [Online]. Available: http://pythonhosted.org/PyDAQmx/

[130] T. E. Oliphant, "Python for scientific computing," *Computing in Science and Engineering*, vol. 9, DOI 10.1109/MCSE.2007.58, no. 3, pp. 10–20, 2007.

[131] D. Hiversen, "PyIGTLink: A Python implementation of OpenIGTLink," 2016. [Online]. Available: https://github.com/Danielhiversen/pyIGTLink. Date accessed: 14/01/2019.

[132] S. Pieper, B. Lorensen, W. Schroeder, and R. Kikinis, "The NA-MIC Kit: ITK, VTK, Pipelines, Grids and 3D Slicer as An Open Platform for the Medical Image Computing Community," *3rd IEEE International Symposium on Biomedical Imaging: Macro to Nano, 2006.*, DOI 10.1109/ISBI.2006.1625012, pp. 698–701, 2006.

[133] J. Hummel, M. Figl, W. Birkfellner, M. R. Bax *et al.*, "Evaluation of a new electromagnetic tracking system using a standardized assessment protocol," *Physics in Medicine and Biology*, vol. 51, DOI 10.1088/0031-9155/51/10/N01, no. 10, pp. N205–N210, 2006.

[134] A. M. Franz, T. Haidegger, W. Birkfellner, K. Cleary *et al.*, "Electromagnetic tracking in medicine -A review of technology, validation, and applications," *IEEE Transactions on Medical Imaging*, vol. 33, DOI 10.1109/TMI.2014.2321777, no. 8, pp. 1702–1725, 2014.

[135] Analog Devices, "AD9833 programmable waveform generator," 2018. [Online]. Available: http://www.analog.com/media/en/technical-documentation/data-sheets/AD9833.pdf. Date accessed: 14/01/2019.

[136] L. Riordan, "Programming the AD9833/AD9834," pp. 1–4, 2010. [Online]. Available: http://www.analog.com/media/en/technical-documentation/application-notes/AN-1070.pdf. Date accessed: 14/01/2019.

[137] Texas Instruments, "LM7171 High Speed Voltage Amplifier," 2018. [Online]. Available: http://www.ti.com/lit/ds/symlink/lm7171.pdf. Date accessed: 14/01/2019.

[138] Texas Instruments, "LMH6321: 300 mA High Speed Buffer," 2018. [Online]. Available: http://www.ti.com/lit/ds/symlink/lmh6321.pdf. Date accessed: 14/01/2019.

[139] Texas Instruments, "INA128 Instrumentation Amplifier," 2018. [Online]. Available: http://www.ti.com/lit/ds/symlink/ina128.pdf. Date accessed: 14/01/2019.

[140] Texas Instruments, "INA163 Instrumentation Amplifier," 2018. [Online]. Available: http://www.ti.com/lit/ds/symlink/ina163.pdf. Date accessed: 14/01/2019.

[141] P. Horowitz and W. Hill, "Instrumentation Amplifiers," in *The Art Of Electronics*, 3rd ed. Cambridge University Press, 2015.

[142] International Electrotechnical Commision, "Medical electrical equipment - Part 1-2: General requirements for basic safety and essential performance - Collateral Standard: Electromagnetic disturbances - Requirements and tests," IEC, Tech. Rep., 2014.

[143] Texas Instruments, "1.5-A Wide Input Adjustable Buck-Boost Switching Converter," 2018. [Online]. Available: http://www.ti.com/lit/ds/slts246b/slts246b.pdf. Date accessed: 14/01/2019.

[144] Texas Instruments, "TPS7A33 Ultralow-Noise Negative Voltage Regulator." 2018. [Online]. Available: http://www.ti.com/lit/ds/symlink/tps7a33.pdf. Date accessed: 14/01/2019.

[145] Texas Instruments, "TPS7A47 RF LDO Voltage Regulator," 2018. [Online]. Available: http://www.ti.com/lit/ds/symlink/tps7a47.pdf. Date accessed: 14/01/2019.

[146] Beta Layout, "PCB Pool Process Specifications," 2018. [Online]. Available: https://uk.beta-layout.com/pcb/technology/specifications/. Date accessed: 14/01/2019.

[147] OKW, "OKW Instrument Enclosures," 2018. [Online]. Available: https://www.okw.com/en/Plastic-enclosures/Euro-Case.htm. Date accessed: 14/01/2019.

[148] American National Standard Institute, "ANSI/IEEE 488.2-1992 - IEEE Standard Codes, Formats, Protocols, and Common Commands For Use with ANSI/IEEE Std 488.1-1987 IEEE Standard Digital Interface for Programmable Instrumentation," American National Standards Institute (ANSI), Tech. Rep., 2004.

[149] L. Maier-Hein, A. M. Franz, W. Birkfellner, J. Hummel *et al.*, "Standardized assessment of new electromagnetic field generators in an interventional radiology setting," *Med Phys*, vol. 39, DOI 10.1118/1.4712222, no. 6, pp. 3424–3434, 2012.

[150] J. B. Hummel, M. R. Bax, M. L. Figl, Y. Kang *et al.*, "Design and application of an assessment protocol for electromagnetic tracking systems," *Medical Physics*, vol. 32, DOI 10.1118/1.1944327, no. 7, pp. 2371–2379, 2005.

[151] I. Wolf, M. Vetter, I. Wegner, T. Böttger *et al.*, "The medical imaging interaction toolkit," *Medical Image Analysis*, vol. 9, DOI 10.1016/j.media.2005.04.005, no. 6, pp. 594–604, 2005.

[152] J. Much, "Error Classification and Propagation for Electromagnetic Tracking," Master's Thesis, Technical University of Munich, 2008.

[153] A. M. Franz, K. März, J. Hummel, W. Birkfellner *et al.*, "Electromagnetic tracking for US-guided interventions: Standardized assessment of a new compact field generator," *International Journal of Computer Assisted Radiology and Surgery*, vol. 7, DOI 10.1007/s11548-012-0740-3, no. 6, pp. 813–818, 2012.

[154] H. A. Jaeger and P. Cantillon-Murphy, "Distorter Characterisation Using Mutual Inductance in Electromagnetic Tracking," *Sensors*, vol. 18, DOI 10.3390/s18093059, no. 9, pp. 1–25, 2018.

[155] W. Birkfellner, J. Hummel, and E. Wilson, "Tracking Devices," in *Image-Guided Interventions: Technology and Applications*, pp. 23–45, 2008.

[156] D. K. Cheng, "Time-Varying Fields and Maxwell's Equations," in *Field and Wave Electromagnetics*, 2nd ed., ch. 7, p. 314. Reading, MA: Addison-Wesley, 1989.

[157] K. O'Donoghue and P. Cantillon-Murphy, "Planar Magnetic Shielding for Use With Electromagnetic Tracking Systems," *IEEE Transactions on Magnetics*, vol. 51, DOI 10.1109/TMAG.2014.2352344, no. 2, pp. 1–12, 2015.

[158] D. K. Cheng, *Field and Wave Electromagnetics*, 2nd ed. Addison-Wesley, 1989.

[159] C. T. Tsai and W. Y. Yip, "An experimental technique for full package inductance matrix characterization," *IEEE Transactions on Components Packaging and Manufacturing Technology Part B*, vol. 19, DOI 10.1109/96.496037, no. 2, pp. 338–343, 1996.

[160] R. Dutta, M. F. Rahman, and L. Chong, "Winding inductances of an interior permanent magnet (IPM) machine with fractional slot concentrated winding," *IEEE Transactions on Magnetics*, vol. 48, DOI 10.1109/TMAG.2012.2203140, no. 12, pp. 4842–4849, 2012.

[161] S. Yamazaki, H. Nakane, S. Member, and A. Tanaka, "Basic Analysis of a Metal Detector," *IEEE Trans. Instrum. Meas.*, vol. 51, no. 4, pp. 810–814, 2002.

[162] M. S. Sharawi and M. I. Sharawi, "Design and implementation of a low cost VLF metal detector with metal-type discrimination capabilities," in *ICSPC 2007 Proceedings - 2007 IEEE International Conference on Signal Processing and Communications*, DOI 10.1109/ICSPC.2007.4728360, no. November, pp. 480–483, 2007.

[163] The LEGO Group, "Company Profile, An introduction to the LEGO Group," Billund, p. 8, 2010.

[164] W. Yin and A. J. Peyton, "Thickness measurement of metallic plates with an electromagnetic sensor using phase signature analysis," *IEEE Transactions on Instrumentation and Measurement*, vol. 57, DOI 10.1109/TIM.2008.923777, no. 8, pp. 1803–1807, 2008.

[165] H. P. Kalmus, “A New Guiding and Tracking System,” *IRE Transactions on Aerospace and Navigational Electronics*, DOI 10.1109/TANE3.1962.4201833, no. 2, pp. 7–10, 1962.

[166] M. N. Islam and A. J. Fleming, “An Algorithm for Transmitter Optimization in Electromagnetic Tracking Systems,” *IEEE Transactions on Magnetics*, vol. 53, DOI 10.1109/TMAG.2017.2703653, no. 8, 2017.

[167] C. Hu, S. Song, X. Wang, M. Q. Meng *et al.*, “A novel positioning and orientation system based on three-axis magnetic coils,” *IEEE Transactions on Magnetics*, vol. 48, DOI 10.1109/TMAG.2012.2188537, no. 7, pp. 2211–2219, 2012.

[168] C. Schilstra and J. H. Van Hateren, “Using miniature sensor coils for simultaneous measurement of orientation and position of small, fast-moving animals,” *Journal of Neuroscience Methods*, vol. 83, DOI 10.1016/S0165-0270(98)00069-7, no. 2, pp. 125–131, 1998.

[169] S. Hashi, S. Yabukami, H. Kanetaka, K. Ishiyama *et al.*, “Wireless magnetic position-sensing system using optimized pickup coils for higher accuracy,” *IEEE Transactions on Magnetics*, vol. 47, DOI 10.1109/TMAG.2011.2154313, no. 10, pp. 3542–3545, 2011.

[170] H. Dai, S. Song, X. Zeng, S. Su *et al.*, “6-D Electromagnetic Tracking Approach Using Uniaxial Transmitting Coil and Tri-Axial Magneto-Resistive Sensor,” *IEEE Sensors Journal*, vol. 18, DOI 10.1109/JSEN.2017.2779560, no. 3, pp. 1178–1186, 2018.

[171] D. Ning, W. Yifeng, and W. Xiaomei, “Novel Calibration Method for Magnetic Source in Magnetic Tracking System,” in *Proceedings of the 11th IEEE International Conference on Electronic Measurement & Instruments ICEMI’2013*, Harbin, China, 2013.

[172] W. F. Loke, T. Y. Choi, T. Maleki, L. Papiez *et al.*, “Magnetic tracking system for radiation therapy,” *IEEE Transactions on Biomedical Circuits and Systems*, vol. 4, DOI 10.1109/TBCAS.2010.2046737, no. 4, pp. 223–231, 2010.

[173] X. Ge, D. Lai, X. Wu, and Z. Fang, “A novel non-model-based 6-DOF electromagnetic tracking method using non-iterative algorithm,” in *Proceedings of the 31st Annual International Conference of the IEEE EMBS*, DOI 10.1109/IEMBS.2009.5332723, pp. 5114–5117, Minneapolis, 2009.

[174] H. A. Jaeger, P. Nardelli, C. O’Shea, J. Tugwell *et al.*, “Automated Catheter Navigation With Electromagnetic Image Guidance,” *IEEE Transactions on*

Biomedical Engineering, vol. 64, DOI 10.1109/TBME.2016.2623383, no. 8, pp. 1972–1979, 2017.

[175] J. M. Fitzpatrick and J. B. West, "The distribution of target registration error in rigid-body point-based registration," *IEEE Transactions on Medical Imaging*, vol. 20, DOI 10.1109/42.952729, no. 9, pp. 917–927, 2001.

[176] J. P. Díaz-Jimenez and A. N. Rodriguez, *Interventions in pulmonary medicine*. Springer, 2017.

[177] E. J. Hermann, H.-H. Capelle, C. A. Tschan, and J. K. Krauss, "Electromagnetic-guided neuronavigation for safe placement of intraventricular catheters in pediatric neurosurgery," *Journal of Neurosurgery: Pediatrics*, vol. 10, DOI 10.3171/2012.7.PEDS11369, no. 4, pp. 327–333, 2012.

[178] F. Kral, E. J. Puschban, H. Riechelmann, F. Pedross *et al.*, "Optical and electromagnetic tracking for navigated surgery of the sinuses and frontal skull base," *Rhinology*, vol. 49, DOI 10.4193/Rhino10.177, no. 3, 2011.

[179] E. E. Folch, M. R. Bowling, T. R. Gildea, K. L. Hood *et al.*, "Design of a prospective, multicenter, global, cohort study of electromagnetic navigation bronchoscopy," *BMC Pulmonary Medicine*, vol. 16, DOI 10.1186/s12890-016-0228-y, no. 1, pp. 1–11, 2016.

[180] K. Lam, J.-L. Bigcas, A. Luong, W. Yao *et al.*, "Flexible microsensor technology for real-time navigation tracking in balloon sinus ostial dilation." *Allergy & rhinology (Providence, R.I.)*, vol. 8, DOI 10.2500/ar.2017.8.0193, no. 1, pp. 20–24, 2017.

[181] S. Tumanski, "Induction coil sensors - A review," *Measurement Science and Technology*, DOI 10.1088/0957-0233/18/3/R01, 2007.

[182] K. Kuang, *Magnetic Sensors - Principles and Applications*, K. Kuang, Ed. New York: InTechOpen, 2012.

[183] I. R. Stavroula Pelitari and P. B. Praful Patel, "Magnetic Endoscopic Imaging: A Useful Ally in Colonoscopy," *Journal of Gastrointestinal & Digestive System*, vol. 5, DOI 10.4172/2161-069X.1000342, no. 342, 2015.

[184] B. K. Pugh, D. P. Kramer, and C. H. Chen, "Demagnetizing factors for various geometries precisely determined using 3-D electromagnetic field simulation," *IEEE Transactions on Magnetics*, vol. 47, DOI 10.1109/TMAG.2011.2157994, no. 10, pp. 4100–4103, 2011.

[185] W. J. Schroeder and K. M. Martin, "The visualization toolkit," in *Visualization Handbook*, 2005.

[186] T. S. Yoo, M. J. Ackerman, W. E. Lorensen, W. Schroeder *et al.*, "Engineering and algorithm design for an image processing Api: a technical report on ITK–the Insight Toolkit." *Studies in health technology and informatics*, vol. 85, DOI 10.3233/978-1-60750-929-5-586, pp. 586–92, 2002.

[187] "The Qt Company." [Online]. Available: https://www.qt.io. Date accessed: 14/01/2019.

[188] T. Lango, G. A. Tangen, R. Marvik, B. Ystgaard *et al.*, "Navigation in laparoscopy–prototype research platform for improved image-guided surgery." *Minimally invasive therapy & allied technologies : MITAT : official journal of the Society for Minimally Invasive Therapy*, vol. 17, DOI 10.1080/13645700701797879, no. 1, pp. 17–33, 2008.

[189] F. Manstad-Hulaas, G. A. Tangen, L. G. Gruionu, P. Aadahl *et al.*, "Three-dimensional endovascular navigation with electromagnetic tracking: ex vivo and in vivo accuracy." *Journal of endovascular therapy : an official journal of the International Society of Endovascular Specialists*, vol. 18, DOI 10.1583/10-3301.1, no. 2, pp. 230–240, Apr. 2011.

[190] F. Trauzettel, "Design and Development of a Catheter Actuation System," Master's thesis, University College Cork, 2018.

[191] A. Blandino, M. Macias, and D. Canter, "Formation of Calcium Alginate Gel Capsules : Influence of Sodium Alginate and CaC12 Concentration on Gelation Kinetics," *Journal of Bioscience*, vol. 88, DOI http://dx.doi.org/10.1016/S1389-1723(00)87103-0, no. 6, pp. 686–689, 1999.

[192] D. Girardeau-Montaut, "CloudCompare - 3D point cloud and mesh processing software," 2018. [Online]. Available: https://www.danielgm.net/cc/

[193] K. Karaman, A. M. Dokdok, O. Karadeniz, C. Ceylan *et al.*, "Intravascular Placement of Metallic Coils as Lung Tumor Markers for CyberKnife Stereotactic Radiation Therapy." *Korean journal of radiology*, vol. 16, DOI 10.3348/kjr.2015.16.3.626, no. 3, pp. 626–631, 2015.

[194] F. C. Detterbeck, D. J. Boffa, A. W. Kim, and L. T. Tanoue, "The Eighth Edition Lung Cancer Stage Classification." *Chest*, vol. 151, DOI 10.1016/j.chest.2016.10.010, no. 1, pp. 193–203, 2017.

[195] H. A. Jaeger and P. Cantillon-Murphy, "Electromagnetic Tracking using Modular, Tiled Field Generators," *IEEE Transactions on Instrumentation and Measurement*, 2018, *(under review)*.

[196] E. de Kater, O. McVeigh, S. Hinds, H. A. Jaeger *et al.*, "Sensor design for electromagnetic tracking in image guided interventions," *Information Processing in Computer Assisted Interventions*, *(submitted to IPCAI 2019)*.

[197] H. A. Jaeger and P. Cantillon-Murphy, "Peripheral tumour targeting using open-source virtual bronchoscopy with electromagnetic tracking: a multi-user preclinical study," *Minimally Invasive Therapies and Allied Technologies*, 2018, *(in press)*.

[198] H. Thanh Le, Y. Nour, Z. Pavlovic, C. O'Mathuna *et al.*, "High-Q 3D Microfabricated Magnetic-core Toroidal Inductors for Power Supplies in Package," *IEEE Transactions on Power Electronics*, vol. 34, DOI 10.1109/TPEL.2018.2847439, no. 1, pp. 74–85, 2018.

[199] C. Ó. Mathúna, N. Wang, S. Kulkarni, and S. Roy, "Review of integrated magnetics for Power Supply on Chip (PwrSoC)," *IEEE Transactions on Power Electronics*, vol. 27, DOI 10.1109/TPEL.2012.2198891, no. 11, pp. 4799–4816, 2012.